UNIVERSITAT DE BARCELONA

Bottom-up Engineering of Chalcogenide Thermoelectric Nanomaterials

Yu Liu

Tesi doctoral

Bottom-up Engineering of Chalcogenide Thermoelectric Nanomaterials

Autor:

Yu Liu

Directors:

Prof. Andreu Cabot i Prof. Doris Cadavid

UNIVERSITAT DE BARCELONA

Bottom-up Engineering of Chalcogenide Thermoelectric Nanomaterials

Memòria presentada per optar al grau de doctor per la

Universitat de Barcelona

Programa de doctorat en Nanociències

Autor:
Yu Liu
Directors de la tesis:
Prof. Andreu Cabot i Prof. Doris Cadavid

Tutora de la tesis:
Dra. Anna Vilà

Lloc on s'ha dut a terme la tesi

Institut de Recerca en Energia de Catalunya (IREC)

UNIVERSITAT DE BARCELONA

Contents

Acknowledgements

Time flies! Until now I still cannot believe that four years have been passed, and in my mind, I still undoubtedly remember all the details when I first time set foot on this amazing city-Barcelona, it was just like yesterday. At that time, I planned in my heart I would cherish every moment and make it unforgettable here in my life. Now, I have become accustomed to living here, known many nice people. Of course, the most important my beloved friends and kind colleagues at IREC, especially the people in Functional Nanomaterials Group. So here, I would like to extend my deep appreciation to all those who have offered me practical, sincere and unselfish support in these four years.

First and foremost, I would like to give my deepest gratitude to my supervisors Prof. Andreu Cabot and Doris Cadavid. Thank you for both guiding me the fantastic world of thermoelectric as my research project during these years. Thanks Andreu, I can still feel that exciting moment, who offered the opportunity to join the Functional Nanomaterials Group at IREC 4 years ago. You opened the door for me in a deeper understanding of thermoelectric based on my master study, guided my projects and helped me to address the difficulties that I met in science. Your critical way of thinking, inspiring insight and logical rigor have impressed me a lot and will exert a profound influence on a young PhD student to grow into a scientific researcher. About Doris, I always say thanks to you because you have walked me through all the stages of my PhD projects. I cannot image how it will go without your constant encouragement and illuminating instruction. You helped and taught me not only including my first colloidal synthesis, first hot press, equipment training, experiments design, data analysis, presentation preparation, paper writing, etc., but also the attitude to life, e.g. always hard-working, optimism, confidence and kindness. Of course, the above should not be enough, although you are not at IREC in the last year of my PhD, and you have been always close to discuss with me every week by skype and help me in whatever matter. So, I am very lucky that you both help me to make the seemingly boring and difficult in science much more colorful.

Secondly, I would like to express my sincere gratitude to all the members of Functional Nanomaterials Group at IREC: Alex, Raquel, Alejandro, Michaela, Taisiia, Oleksandr, Evgenii, Marcos Batista, Pablo. Marcos Sanles, Gihan, and Arash. I will never forget many memorable funny moments in these years. In particular, I cannot forget our thermoelectric team: my dears Silvia & Doris, my bro and best friends Mike & Peter. We are really a great team for sure. I cannot say we are the best team, but we are the most active team in our group. I will always remember for all the hours' hard-working together in the lab and coffee break time, etc. But only Peter and I are still in this team now, Doris left in last June 2017, Mike left in last July 2017 and Silvia left in this March 2018. Although it is known that sometimes reality is cruel and there is no never-ending feast, friends for all my life.

Also, I would like to give a special thanks to the big Chinese Community at IREC, Zhishan Luo, Haibing Xie, Junfeng Liu, Xiaoting Yu, Kai Pan, Yu Zhang, Junshan Li, Yong Zuo, Pengyi Tang, Qin Shi, Chaoqi Zhang, Mengyao Li, Congcong Xing and Ruifeng Du. Never forget the “lunch time” every day. I am really happy and proud to have been working with you in abroad. We come from all corners of China, is the fate lets your me gather in this, causes us to become the friend, and I will remember all of you. It’s also very special meaning for me that I introduced most of you and joined our Functional Nanomaterials group.

I would like to give my special thanks to Prof. Maria Ibáñez, who has performed many measurements from ETH for me, e. g. NMR, Hall or the corrections of the paper work and many valuable comments. Thank you as always for your help.

Furthermore, I am also grateful to Prof. Jordi Arbiol’s group, including Sara Martí Sánchez, Albert Grau Carbonell and María de la Mata for checking the wonderful HRTEM of my samples. Those nice HRTEM images really play an important role in my project and publications. Thank you very much for all your help.

I wish to express my acknowledgement to all the researchers from Universidad Politécnica de Madrid (Prof. Perla Wahnón, Dr. Gregorio García and Dr. Jinyu Lu) and Shanghai University (Prof. Wenqing Zhang, Dr. Lili Xi) who have helped us for the simulation and DFT calculations in Cu_3SbSe_4 system. Thank you very much for all your nice work.

I would also thank Dr. Chaochao Dun from Wake Forest University who has performed the measurements of heat capacity and XPS of all my Cu_3SbSe_4 samples.

I also need to thank the “China Scholarship Council” for providing me the financial support that I am able to focus on my PhD research work abroad.

Ultimately, I also want to thank my family: my parents, my brother and 2 lovely nieces and my only 12-months-old nephew, whose care and support motivate me to move on and make me want to be a better person. Home is the harbor of my soul, no matter where I am, my heart always goes with all of you. Specifically, to my wife Tingting Li (李婷婷), thank you for being part of my life, you always support me to do everything. We have kept this kind of long-distance love for almost 4 years. Thanks for all the persistence. There will be a romantic wedding for you very soon, I promise! I LOVE YOU!

Barcelona, Spain
April, 2018

List of publications

My PhD research work have been included in five publications, four that have already been published in peer-reviewed journals and one that is currently in the peer review process. A full copy of each of the publications can be found in the Annex part. The following is the list of publications included in this thesis:

1. **Y. Liu,** D. Cadavid, M. Ibáñez, J. D. Roo, S. Ortega, O. Dobrozhan, M. V Kovalenko, A. Cabot. *Colloidal $AgSbSe_2$ nanocrystals: Surface analysis, electronic doping and processing into thermoelectric nanomaterials. J. Mater. Chem. C, 2016,4, 4756-4762.*
2. **Y. Liu,** G. García, S. Ortega, D. Cadavid, P. Palacios, J. Y. Lu, M. Ibáñez, L. L. Xi, J. De Roo, A. M. López, S. Martí-Sánchez, I. Cabezas, M. Mata, Z. S. Luo, C. Dun, O. Dobrozhan, D. L. Caroll, W. Zhang, J. Martins, M. V. Kovalenko, J. Arbiol, G. Noriega, J. Song, P. Wahnón and A. Cabot. *Solution-Based Synthesis and Processing of Sn- and Bi-Doped Cu_3SbSe_4 Nanocrystals, Nanomaterials and Ring-Shaped Thermoelectric Generators. J. Mater. Chem. A, 2017, 5, 2592–2602.*
3. **Y. Liu,** D. Cadavid, M. Ibáñez, S. Ortega, S. Martí-Sánchez, O. Dobrozhan, M.V. Kovalenko, J. Arbiol, A. Cabot. *Thermoelectric properties of semiconductor-metal composites produced by particle blending. APL Mater. 2016, 4,104813.*
4. **Y. Liu,** Y. Zhang, S. Ortega, M. Ibáñez, K. H. Lim, A. Grau Carbonell, S. Martí-Sànchez, K. M. Ng, J. Arbiol and M. V. Kovalenko, D. Cadavid, A. Cabot. *Crystallographically Textured Nanomaterials Produced from the Liquid Phase Sintering of $Bi_xSb_{2-x}Te_3$ Nanocrystal Building Blocks. Nano Lett., 2018, 18, 2557-2563.*
5. **Y. Liu,** Y. Zhang, K. H. Lim, M. Ibáñez, S. Ortega, M. Li, J. David, S. Martí-Sánchez, K. M. Ng, J. Arbiol, M. V. Kovalenko, D. Cadavid, A. Cabot. *High Thermoelectric Performance in Crystallographically Textured n-type $Bi_2Te_{3-x}Se_x$ Produced from Asymmetric Colloidal Nanocrystals. Submitted.*

In addition to the publications listed above, I have contributed to some other projects during my PhD that resulted in other publications that are not included in the thesis. They are listed as follows.

1. S. Ortega, M. Ibáñez, **Y. Liu,** Y. Zhang, M. V Kovalenko, D. Cadavid, A. Cabot. *Bottom-up engineering of thermoelectric nanomaterials and devices from solution-processed nanoparticle building blocks. Chem. Soc. Rev., 2017, 46, 3510-3528.*
2. M. Ibáñez, R. Hasler, **Y. Liu,** O. Dobrozhan, O. Nazarenko, D. Cadavid, A. Cabot, M. V. Kovalenko. *Tuning P-type Transport in Bottom-Up-Engineered Nanocrystalline Pb Chalcogenides Using Alkali Metal Chalcogenides as Capping Ligands. Chem. Mater., 2017 29, 7093-7097.*
3. M. Ibáñez, Z. S. Luo, A. Genç, L. Piveteau, S.Ortega, D. Cadavid, O. Dobrozhan, **Y. Liu,** M. Nachtegaal, M. Zebarjadi, J. Arbiol, M. V. Kovalenko, A. Cabot. *High-performance thermoelectric nanocomposites from nanocrystal building blocks. Nat. Commun., 2016, 7, 10766.*
4. Z. S. Luo, E. Irtem, M. Ibáñez, R. Nafria, S. Marti, A. Genç, M. Mata, **Y. Liu,** D. Cadavid, J. Llorca, J. Arbiol, T. Andreu, J. R. Morante, A. Cabot. *Mn_3O_4@$CoMn_2O_4$-Co_xO_y Nanoparticles: Partial Cation Exchange Synthesis and Electrocatalytic Properties toward the Oxygen Reduction and Evolution Reactions. ACS Appl. Mater. Interfaces 2016, 8, 17435–17444.*

Authors' contributions

The work within this thesis was carried out at the Advanced Material Research Department in the Catalonia Institute for Energy Research. Yu Liu, as PhD student, contributed to the experimental work, data analysis and manuscript writing for all the publications presented in this thesis. The contributions of co-authors for each article are shown below this paragraph. The impact factor in 2017 of the journals where the manuscripts were published is provided. All of the publications belong to the 1st quartile according to the Science Citation Index. None of these papers has been previously presented in any other PhD thesis. In all the publications, Andreu Cabot and Doris Cadavid conceived and guided the projects, participated in the experiment design and manuscript writing.

Chapter 2:

Y. Liu, D. Cadavid, M. Ibáñez, J. D. Roo, S. Ortega, O. Dobrozhan, M. V Kovalenko, A. Cabot. *Colloidal $AgSbSe_2$ nanocrystals: Surface analysis, electronic doping and processing into thermoelectric nanomaterials.* *J. Mater. Chem. C, 2016, 4, 4756-4762.*

Impact factor 2017: 5.256

In this work, Y. Liu designed the experiments, produced the nanomaterials and wrote the first draft of the manuscript. Y. Liu, S. Ortega and O. Dobrozhan performed the thermoelectric characterization. M. Ibáñez and J. D. Roo performed Hall and NMR measurements and analyzed the results. D. Cadavid and A. Cabot conceived and guided the project and supervised the work. The manuscript was corrected and improved by all authors.

Chapter 3:

Y. Liu, G. García, S. Ortega, D. Cadavid, P. Palacios, J. Y. Lu, M. Ibáñez, L. L. Xi, J. De Roo, A. M. López, S. Martí-Sánchez, I. Cabezas, M. Mata, Z. S. Luo, C. Dun, O. Dobrozhan, D. L. Caroll, W. Zhang, J. Martins, M. V. Kovalenko, J. Arbiol, G. Noriega, J. Song, P. Wahnón and A. Cabot. *Solution-Based Synthesis and Processing of Sn- and Bi-Doped Cu_3SbSe_4 Nanocrystals, Nanomaterials and Ring-Shaped Thermoelectric Generators.* *J. Mater. Chem. A, 2017, 5, 2592–2602.*

Impact factor 2017: 8.867

In this work, J. Song, D. Cadavid and A. Cabot conceived and supervised the work. Y. Liu and D. Cadavid designed the experiments, produced the nanomaterials, performed the thermoelectric characterization and wrote the first draft of the manuscript. S. Ortega, A. M. López, G. Noriega and I. Cabezas designed and fabricated the device test station and tested the device. M. Ibáñez, J. De Roo and J. Martins performed Hall and NMR measurements and analyzed the results. S. Martí-Sánchez, M. Mata, and J. Arbiol performed of HRTEM and EELS and discussed these results. G. García, P. Palacios, J. Y. Lu, P. Wahnón L. Xi and W. Zhang performed and discussed detailed DFT calculations. C. Dun and D. L. Caroll performed the C_p characterization. O. Dobrozhan and Z. Luo measured and discussed XPS data. The manuscript was corrected and improved by all authors.

Chapter 4:

Y. Liu, D. Cadavid, M. Ibáñez, S. Ortega, S. Martí-Sánchez, O. Dobrozhan, M. V. Kovalenko, J. Arbiol, A. Cabot. *Thermoelectric properties of semiconductor-metal composites produced by particle blending. APL Mater. 2016, 4,104813.*

Impact factor 2017: 4.335

In this work, D. Cadavid and A. Cabot conceived and guided the project. Y. Liu designed the experiments, produced the nanomaterials and wrote the first draft of the manuscript. Y Liu and S. Ortega performed the thermoelectric characterization. M. Ibáñez performed Hall measurements and analyzed the results. S. Martí-Sánchez and J. Arbiol performed HRTEM and discussed the results. The manuscript was corrected and improved by all authors.

Chapter 5:

Y. Liu, Y. Zhang, S. Ortega, M. Ibáñez, K. H. Lim, A. Grau Carbonell, S. Martí-Sànchez, K. M. Ng, J. Arbiol and M. V. Kovalenko, D. Cadavid, A. Cabot. *Crystallographically Textured Nanomaterials Produced from the Liquid Phase Sintering of* $Bi_xSb_{2-x}Te_3$ *Nanocrystal Building Blocks. Nano Lett., 2018, 18, 2557-2563.*

Impact factor 2017: 12.712

In this work, D. Cadavid and A. Cabot guided the project and supervised the work. Y. Liu, D. Cadavid, M. Ibáñez, M. V. Kovalenko and A. Cabot conceived and prepared the manuscript. Y. Liu, S. Ortega and D. Cadavid designed the experiments, produced the nanomaterials, and performed the thermoelectric characterization. Y. Zhang and K. Lim produced the bulk samples. M. Ibáñez, K. Lim and K. Ng performed Hall measurement and analyzed the results in this manuscript. A. Grau Carbonell, S. Martí-Sànchez, and J. Arbiol performed HRTEM and STEM-EELS and discussed these results. The manuscript was corrected and improved by all authors.

Chapter 6:

Y. Liu, Y. Zhang, K. H. Lim, M. Ibáñez, S. Ortega, M. Li, J. David, S. Martí-Sánchez, K. M. Ng, J. Arbiol, M. V. Kovalenko, D. Cadavid, A. Cabot. *High Thermoelectric Performance in Crystallographically Textured n-type $Bi_2Te_{3-x}Se_x$ Produced from Asymmetric Colloidal Nanocrystals. Submitted.*

In this work, D. Cadavid and A. Cabot conceived the project and supervised the work. Y. Liu, D. Cadavid, M. Ibáñez, M. V. Kovalenko and A. Cabot prepared the manuscript. Y. Liu and S. Ortega designed the experiments, produced the nanomaterials, and performed the thermoelectric characterization. Y. Zhang and K. Lim produced the bulk samples. M. Ibáñez, K. Lim and K. Ng performed Hall measurement and analyzed the results in this manuscript. J. David, S. Martí-Sànchez, and J. Arbiol performed HRTEM and STEM-EELS and discussed these results. The manuscript was corrected and improved by all authors.

Prof. Andreu Cabot

and Prof. Doris Cadavid

certify the information provided above is true.

Barcelona, 29th of April 2018

Preface

The chapters included in this PhD thesis cover the work developed by the PhD candidate Yu Liu at the Catalonia Institute for Energy Research (IREC) in Sant Adrià de Besòs, Barcelona, in the period 2014-2018, supported by China Scholarship Council (No. 201406500003). The thesis is particularly focused on the development of high performance thermoelectric (TE) nanomaterials by means of the bottom-up assembly of nanocrystals (NCs) with finely tuned properties obtained by cost-effective and scalable colloidal synthesis routes.

The thesis is structured into 6 chapters. In the first chapter, a general introduction of the different objectives and topics is presented. Experimental work is included in chapters 2 to 6. Within the general framework of optimizing thermoelectric nanomaterials from NC-based bottom up processes, the work carried out in this thesis focuses on 3 main research directions related to 3 main challenges of the strategy used: 1) control of stoichiometry and ionic doping in NCs to optimize charge carrier concentration; 2) modulation doping in nanocomposites; 3) production of crystallographically textured nanomaterials. The first block, chapter 2 and 3, starts with the production of ternary I−V−VI semiconductors, using $AgSbSe_2$ and Cu_3SbSe_4 model systems. Their TE performances have been significantly enhanced by tuning their compositions carefully during the synthesis. The second block is included as chapter 4, where semiconductor-metal nanocomposites are developed. In particularly we blended PbS NCs with Cu/Sn metal NCs to improve the electrical transport property by means of controlling the injection of electrons from the metal to semiconductor host. The last block, chapter 5 and 6, addresses the production of crystallographically textured nanomaterials with improved TE performance using Bi_2Te_3-based materials as a model system.

Summary of results

Colloidal NCs exhibit excellent properties for different applications, including energy conversion, catalysis, electronic and optoelectronic devices, medicine, etc. The colloidal synthesis of NCs shows various advantages, such as: i) fine control of size, shape and composition at nanoscale; ii) low reaction temperature; and iii) no need for high-cost specialized equipment.

This project focuses on the rational design and engineering of high performance thermoelectric (TE) nanostructured materials by the bottom-up assembly of colloidal NCs. Currently, bottom-up approaches to produce TE nanomaterials are drawing attention due to the advantages they can offer. Particularly, enhanced TE performance by means of reduction of the thermal conductivity due to the increasing of the phonon scattering is easily accomplished. Although nanostructuring has proven an effective strategy to improve the TE properties, it still has some major challenges: i) the tuning of the surface chemistry, that includes the development of different procedures to remove the organic molecules attached to the NCs, which can affect the electronic transport of the material; ii) the precise control of the charge carrier concentration; and iii) The production of precisely crystallographically textured materials with strong anisotropic properties. In this thesis several methods are proposed to overcome these major challenges.

This thesis is divided in 6 chapters. The first one is the introduction. Chapters 2 and 3 correspond to the study of synthetic routes to produce high quality chalcogenide NCs that are doped at the NC synthesis step to control the charge carrier concentrations. Furthermore, with the aim of an efficient transport of charge carriers, the organic ligands were removed before compacting the NCs into high density TE nanomaterials. The systems studied were I−V−VI chalcogenide semiconductors, specifically $AgSbSe_2$ and Cu_3SbSe_4, which show very attractive and yet to be exploited functional properties for energy conversion applications, particularly thermoelectricity. A low-cost, high-yield and scalable colloidal synthesis route to produce monodisperse and narrow size and shape distributions of $AgSbSe_2$ and Cu_3SbSe_4 NCs was obtained. After ligand displacement, the NCs were used as building blocks to produce TE nanomaterials. Additionally, by means of substitutional doping during colloidal synthesis, a large increment in the power factor and relatively lower thermal conductivities were observed. We presented a complete characterization of the TE nanomaterials obtained after the densification of the NCs by using a hot–press technique. The preliminary optimization of the doping concentration resulted in a TE figure of merit ZT of 1.10 at 640 K for $AgSb_{0.98}Bi_{0.02}Se_2$, and of 1.26 at 673 K for $Cu_3Sb_{0.88}Sn_{0.10}Bi_{0.02}Se_4$, which represents a significant increase beyond the state of the art in Te-free multinary Ag/Cu-based chalcogenide materials made of relatively abundant, safe and environmental friendly materials. Finally, the best performance sample of $Cu_3Sb_{0.88}Sn_{0.10}Bi_{0.02}Se_4$ was further used to fabricate ring-shaped TE generators to be coupled to hot pipes and which provided 1 mW of electric power per TE element with a 160 °C of temperature gradient. This bottom-up engineering colloidal NCs building blocks for the fabrication of a shape-adaptable TE generator shows the real potential of applications in near future. The results presented in chapter 2 and 3 were published in *Journal of Materials Chemistry C* in 2016 and *Journal of Materials Chemistry A* in 2017, respectively.

Chapter 4 constitutes the second block of the thesis. In this chapter, the work of PbS-metal (Cu and Sn) nanocomposites produced by a versatile nanoparticle blending procedure is presented. For these materials, the low work function metal is able to inject electrons to the intrinsic PbS matrix, which is another strategy to control the charge carrier concentration. The power factor is dramatically enhanced due to the increase of the electrical conductivity in the TE nanocomposites. Consequently, the maximum ZT was remarkably enhanced by two times as compared with the pristine PbS host. Furthermore, we also compared the TE performance of microcrystalline composites with the same composition as in nanocrystalline composites; commercial PbS host with Cu particles. The results revealed that with the same metal addition, higher electrical conductivities were obtained in the nanocomposite, but higher Seebeck coefficients were maintained in the microcomposite. Both results were associated to a more efficient charge transfer from the metal to the semiconductor in the nanocrystalline materials. Moreover, higher thermal conductivities were also obtained in the microcomposite. Finally, the figure of merit ZT were higher for the microcomposite system in the low temperature range, but much lower in the higher temperature range compared with the nanocomposites system. This project is a follow up of the previous PbS-Ag system (*Nature Communications 2016*), in which the final figure of merit can reach to 1.7 at 850 K for PbS-4.4%Ag. The results obtained and presented in this chapter were published in *APL materials* in 2016.

In the last block, chapters 5 and 6, the process of production of crystallographically textured materials is presented. We face here the challenge of bottom-up approaches to control the crystallographic alignment of nanograins. The production of nanostructured p-type $Bi_xSb_{2-x}Te_3$ and n-type $Bi_2Te_{3-x}Se_x$ alloys is presented. This can be done with controlled stoichiometry by solution-processing, and crystallographic texture by liquid-phase sintering using multiple pressure and release steps at 480 °C, above the tellurium melting point. Additionally, we explain the possible mechanism to produce the highly textured nanomaterials. This strategy results in record TE figures of merit: ZT=1.83 at 420 K for $Bi_{0.5}Sb_{2.5}Te_3$ and ZT=1.31 for $Bi_2Te_{2.7}Se_{0.3}$ at 440 K when averaged over 5 materials, respectively. These figures of merit were obtained in the *c* direction, in contrast with most previous works measuring or assuming better TE performances in the *ab* plane. These high figures of merit extended over a wide temperature range, from 320 K to 500 K, which results in energy conversion efficiencies a 50% higher than commercial ingots in the similar temperature range. The results in Chapter 5 has been published in *Nano Letters* in 2018, and the results of Chapter 6 have been recently submitted.

Finally, the main conclusions of this thesis and some perspectives for future work are presented in the last chapter.

Resumen de Resultados

Los nanocristales (NCs) coloidales tienen excelentes propiedades para diferentes aplicaciones, incluyendo la conversión de energía, la catálisis, los dispositivos electrónicos y optoelectrónicos, y la medicina, entre otros. La síntesis coloidal de NCs presenta varias ventajas, tales como: i) excelente control del tamaño, forma y composición a nivel de la nanoescala; ii) bajas temperaturas de reacción; y iii) que no hay necesidad de equipos especializados. Este proyecto se concentra en el diseño racional y la ingeniería de materiales termoeléctricos (TE) nanoestructurados de alto rendimiento, usando la estrategia del ensamblado ascendente (bottom-up) de NCs coloidales, los cuales se utilizan como los elementos de construcción.

Actualmente, las estrategias ascendentes para producir nanomateriales termoeléctricos llaman la atención debido a las ventajas que pueden ofrecer este tipo de rutas en la optimización de dichos materiales. En particular, usando estrategias ascendentes es casi inmediato lograr un incremento de la eficiencia termoeléctrica por medio de la reducción de la conductividad térmica, esto debido también al incremento en el bloqueo de fonones en el material. A pesar de que la nanostructuración ha probado ser una estrategia efectiva para mejorar las propiedades termoeléctricas, este camino todavía tiene varios retos importantes: i) Ajustar la química de superficie, lo cual incluye el desarrollo de diferentes procedimientos para remover las moléculas orgánicas que se enlazan a la superficie de los NCs, lo cual afecta el transporte electrónico en el material; ii) el control preciso de la concentración de portadores de carga; iii) la producción de materiales texturizados cristalográficamente con fuertes propiedades anisotrópicas. En esta tesis se proponen varios métodos para superar estos retos.

Esta tesis está dividida en 6 capítulos. El primero es la introducción, en la cual se presentan los conceptos básicos de la termoelectricidad y el procesamiento en solución de NCs. Los capítulos 2 y 3 corresponden al estudio de las rutas sintéticas para producir NCs de calcogenuros de alta calidad que se doparon durante el proceso de síntesis, con el objetivo de controlar la concentración de portadores. Además, con el propósito de obtener un transporte eficiente de portadores de carga, se removieron los ligandos antes de compactar los NCs en nanomateriales TE altamente densos. El sistema estudiado fue el de los calcogenuros semiconductores I-V-VI, específicamente $AgSbSe_2$ y Cu_3SbSe_4, los cuales muestran propiedades funcionales muy atractivas y que aún no se han podido explicar completamente para las aplicaciones en conversión de energía, específicamente en termoelectricidad. Se diseñó una ruta de síntesis de bajo costo, alto rendimiento y con las cual se obtuvieron NCs de $AgSbSe_2$ y Cu_3SbSe_4 con distribuciones de tamaño y forma muy estrechas. Después del intercambio de ligandos, los NCs se usaron como elementos de construcción para la producción de los nanomateriales TE. Adicionalmente, por medio del dopaje durante la síntesis de los NCs, se produjo un gran incremento en el factor de potencia TE, así como valores relativamente bajos de la conductividad térmica, en los materiales obtenidos. Se presenta una caracterización completa de los nanomateriales TE que resultaron después de la densificación de los NCs por medio de la técnica de prensado en caliente. La optimización preliminar de la concentración de dopaje resultó en valores para la figura de mérito TE, ZT, de 1.10 a 640 K para $AgSb_{0.98}Bi_{0.02}Se_2$, y de 1.26 at 673 K para $Cu_3Sb_{0.88}Sn_{0.10}Bi_{0.02}Se_4$, lo cual representa un incremento significativo, más allá del estado del arte de los calcogenuros multinarios, basados en Ag/Cu, libres de Te y hechos con elementos relativamente abundantes, seguros y ambientalmente amigables. Finalmente, el material que presentó mejor comportamiento TE, fue el $Cu_3Sb_{0.88}Sn_{0.10}Bi_{0.02}Se_4$, el cual se usó después para la producción de un generador TE en forma de anillo. El objetivo de este dispositivo era poder acoplarlo a los tubos de escape de gases y fue posible obtener una potencia eléctrica de 1mW por elemento TE con una diferencia de temperatura de 160 °C, lo cual es un resultado bastante prometedor. Esta ingeniería ascendente de NCs coloidales como elementos de construcción para la fabricación de generadores TE, de forma adaptable, deja ver el gran potencial para diversas aplicaciones en un futuro cercano. Los resultados presentados en el capítulo 2 y 3 fueron publicados en el *Journal of Materials Chemistry C* en 2016 y en el *Journal of Materials Chemistry A* in 2017, respectivamente.

El capítulo 4 constituye el segundo bloque de esta tesis. En este capítulo, se presenta el trabajo de la producción de nanocopuestos de PbS-metal (Cu y Sn) usando un procedimiento versátil de mezcla de NCs. Para estos materiales, la función de trabajo del metal es capaz de inyectar electrones a la matriz intrínseca de PbS, lo cual constituye otra estrategia de control de concentración de portadores de carga. El factor de potencia TE, se ve dramáticamente incrementado debido al aumento en la conductividad eléctrica en los nanocompuestos TE. Consecuentemente, el valor máximo de ZT se vio excepcionalmente incrementado por el doble del valor comparado con el material original

PbS. Además, también se comparó el desempeño TE de los compositos nanocristalinos, con compositos microcristalinos, que fueron producidos usando PbS comercial como matriz y nanopartículas de Cu. Estos resultados revelan que con la misma adición de metal, para los nanocompositos se obtienen valores de conductividad eléctrica mayores comparados con los microcompositos. Asi mismo, se obtienen valores de coeficiente Seebeck mayores para los microcompositos. Ambos resultados, fueron asociados a la transferencia de carga más eficiente desde el metal al semicondutor en los materiales nanocristalinos. Finalmente, el valor para la figura de mérito ZT fue mayor para el sistema del microcomposito en el rango de temperatura bajo, pero mucho más grande para el sistema del nanocompuesto en el rango de altas temperaturas. Este proyecto es la continuación de un trabajo previo que se realizó en el grupo de investigación con el sistema PbS-Ag (*Nature Communications 2016*), en el cual, el valor de la figura de mérito final alcanzó a llegar a 1.7 a 850 K para el PbS-4.4%Ag. Los resultados obtenidos en el presenta capítulo fueron publicados en *APL materials* en 2016.

En el último bloque, capítulos 5 y 6, se presenta el proceso de producción de materiales texturizados cristalográficamente. En este trabajo enfrentamos el reto de controlar el alineamiento cristalográfico de los nanogranos usando la estrategia ascendente. Se presenta la producción de materiales nanoestructurados de aleaciones tipo p $Bi_xSb_{2-x}Te_3$ y tipo n $Bi_2Te_{3-x}Se_x$. Esto se pudo realizar, controlando la estequiometria del procesamiento en solución y la textura cristalográfica, por medio de la sinterización en fase líquida con un procedimiento de múltiples pasos de presión y relajación a una temperatura de 480°C, la cual está por encima de la temperatura de fisión del Te. Adicionalmente, nosotros explicamos cómo es el posible mecanismo que se da para la obtención de nanomateriales altamente texturizados. Este fue un resultado estratégico con valores de la figura de mérito TE record de: ZT=1.83 a 420 K para $Bi_{0.5}Sb_{2.5}Te_3$ y ZT=1.31 para $Bi_2Te_{2.7}Se_{0.3}$ a 440 K realizando promedio sobre 5 diferentes muestras, respectivamente. Estos valores de la figura de mérito fueron obtenidos para la dirección *c*, en contraste con la mayoría de los trabajos previos que asumían y/o medían desempeños termoeléctricos mejores en la dirección del plano *ab*. Los valores altos de la figura de mérito se extendieron sobre todo el rango de temperatura, desde 320 K a 500 K, lo cual se traduce en eficiencias de conversión de energía un 50% mayor que las de los materiales comerciales en un rango de temperatura similar. Los resultados del capítulo 5 fueron publicados en *Nano Letters* en 2018 y los resultados del capítulo 6 fueron sometidos a una revista recientemente.

Finalmente, en el último capítulo, se presentan las conclusiones principales y las perspectivas del trabajo futuro de esta tesis.

Chapter 1

General Introduction

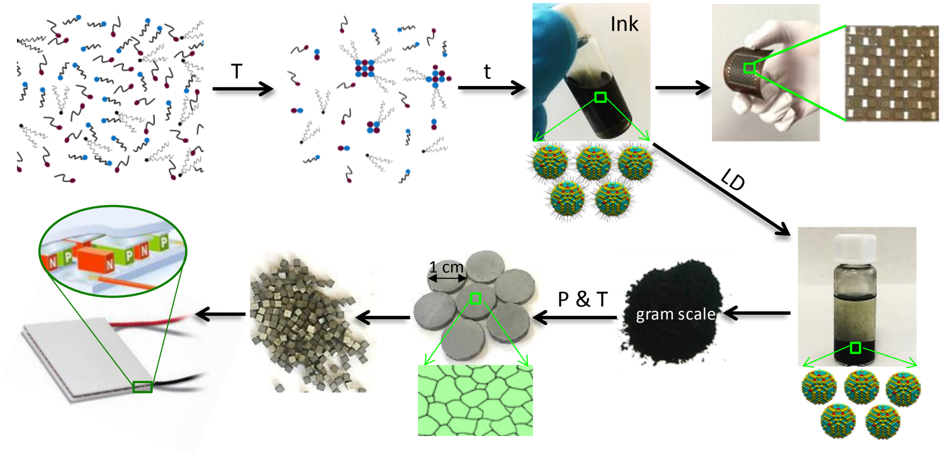

1.1 The Energy challenges

A main challenge facing mankind in the 21st century is to make compatible the unprecedented increase in human numbers with the accessibility to sufficient amounts of energy and the conservation of the environment. The fossil fuel consumption and greenhouse gas production have reached a record high in history. In addition to environmental issues, developing countries have experienced their own energy crisis because their energy consumption has soared as the economy boomed in the last two or three decades.

Currently, fossil fuels provide around 80% of the world's energy demand.[1] Taking the total Unite States primary energy consumption in 2016 as an example (Figure 1.1), petroleum-37%, natural gas-29% and coal-15% accounted for the most of the country’s energy production. Additionally, in developing countries the percentage of fossil fuels in the total primary energy consumption should be even higher than in the world's largest economy, Unite States. For decades to come, global energy demand is expected to continuously grow, by 50% until 2035 (Figure 1.2),[2] and it is expected to triple by the end of this century.[3] There's no denying it that we will run out of all fossil fuels at some point. At the present consumption rate all known reserves of fossil fuels will be extinguished before the end of the present century.[4]

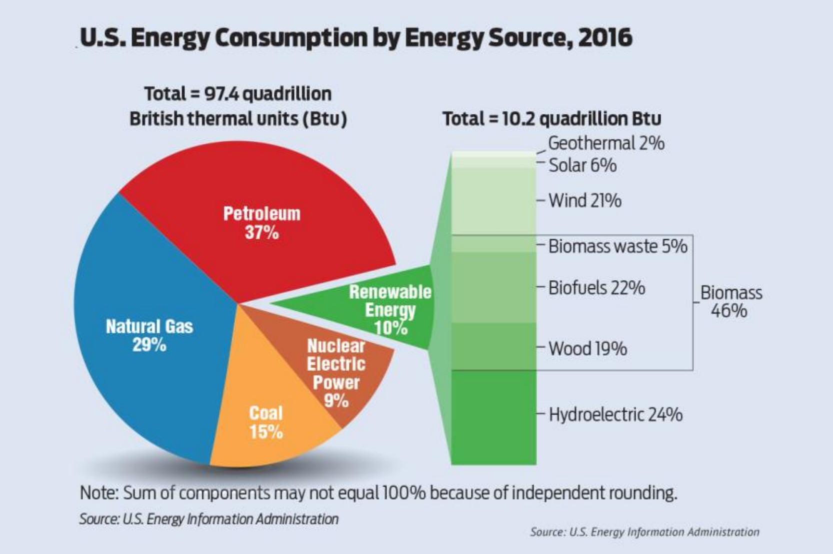

Figure 1.1. Total U.S. primary energy consumption in 2016, source, U.S. Energy Information Administration, Monthly Energy Review, Table 1.3 and 10.1, April 2017, preliminary data.

Energy is essential to humans, as important as food, air and water, that is why we talk energy all the time. It is now time to overcome the energy challenge and turn it into an opportunity. The age of low carbon has come, by 2050 all industrial and domestic processes and transportation need to be low carbon by means of industrial restructuring, more efficient fossil fuel use and a shift to clean energy sources.[5]

Renewable energy conversion technologies, e.g. photovoltaics, fuel cells and wind mills, will play a key role for resolving the current energy challenge. Besides, energy efficiency of industrial and domestic processes and in transportation will need to be optimized. Currently, more than 60% of the word's energy consumption is wasted in the form of heat. Thermoelectric (TE) technology is a clean energy conversion technique, it can be used to harvest any thermal source including industrial waste heat and solar, to directly produce useful electricity without any pollution.[6-8] Consequently, TE materials can play an important role in the development of sustainable energy-efficient and environmental-friendly technologies.

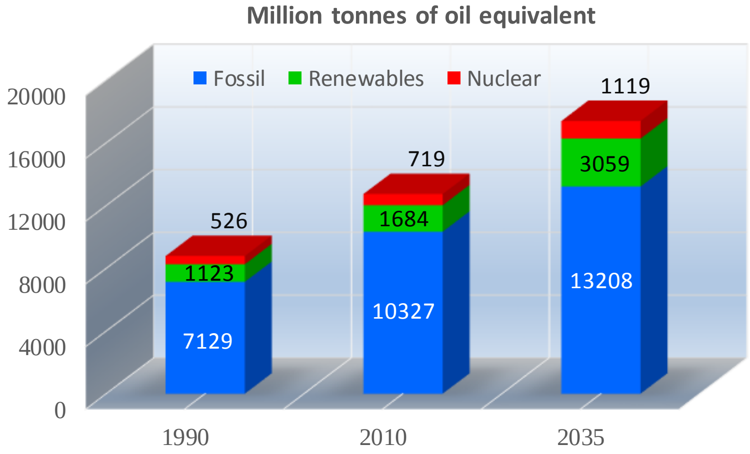

Figure 1.2. Global energy and power demand is underpinned by fossil fuels. Primary energy demand by fuel source (million tonnes of oil equivalent), Source: IEA, 2012. World Energy Outlook (WEO) 2012 and IEA, 2013. WEO 2013 (New Policies scenario).

1.2 Thermoelectricity

1.2.1 Background of thermoelectricity

Thermoelectricity, allowing the solid-state conversion between thermal and electric energy, has a huge potential to develop competitive products in a wide range of application fields, e.g. climate control, energy recovery and energy harvesting. TE devices exhibit numerous advantages, e.g. direct energy conversion without moving parts or fluids, long lifetime and silent operations, reduced volume, and a very flexible design with large size/power adaptability.[6, 7, 9-11]

In 1821, Thomas J. Seebeck discovered the phenomenon that a circuit made from two dissimilar materials produced a voltage when their junctions were at different temperatures.[12] This became known as the "Seebeck effect" and it is used for creating TE power generators. He found that the voltage is proportional to the temperature difference between the hot and cold sides of the material. The proportionality factor, the Seebeck coefficient (S), changes with material and operating temperature:

$$S = -\frac{\Delta \mathrm{V}}{\Delta \mathrm{T}} \tag{1}$$

In equation (1), ΔV and ΔT are, respectively, the voltage and temperature difference between the hot and cold sides. The minus sign comes from the negative charge of the electron and the convention of the current flow. A negative Seebeck coefficient is generally associated with electrons being the dominant charge carriers, n-type materials, whereas holes are the dominant carrier in p-type materials with a positive Seebeck coefficient.[7]

Jean C.A. Peltier first discovered the phenomenon that passing an electric current through two dissimilar materials produces heating or cooling at their junction in 1834,[12] which is known as the "Peltier effect". This is the foundation for TE cooling and temperature control, the widest applications of TE devices currently.[7]

TE devices can work reversely in both power generation configurations and cooling, as shown in Figure 1.3.

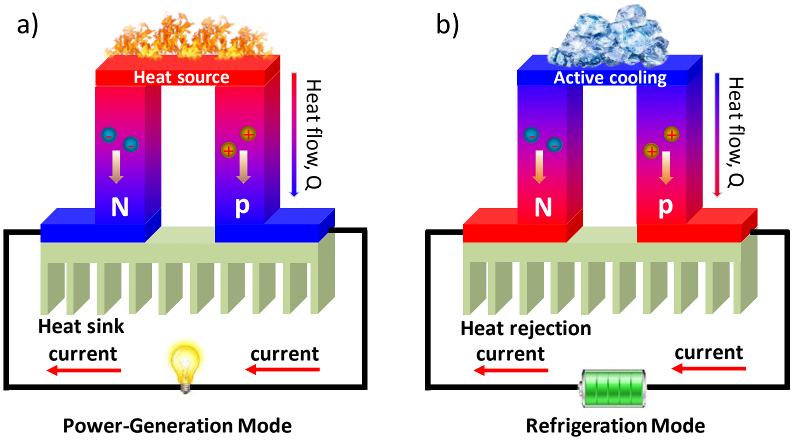

Figure 1.3. Reversible models of a TE module: a) Seebeck of power generation mode and b) Peltier of refrigeration mode.

The practical TE device is generally composed of tens to hundreds of p- and n-type elements coupled together electrically in series and thermally in parallel, as shown in Figure 1.4. These devices are sold by many companies and are being further developed in numerous laboratories.[8, 9, 13-15]

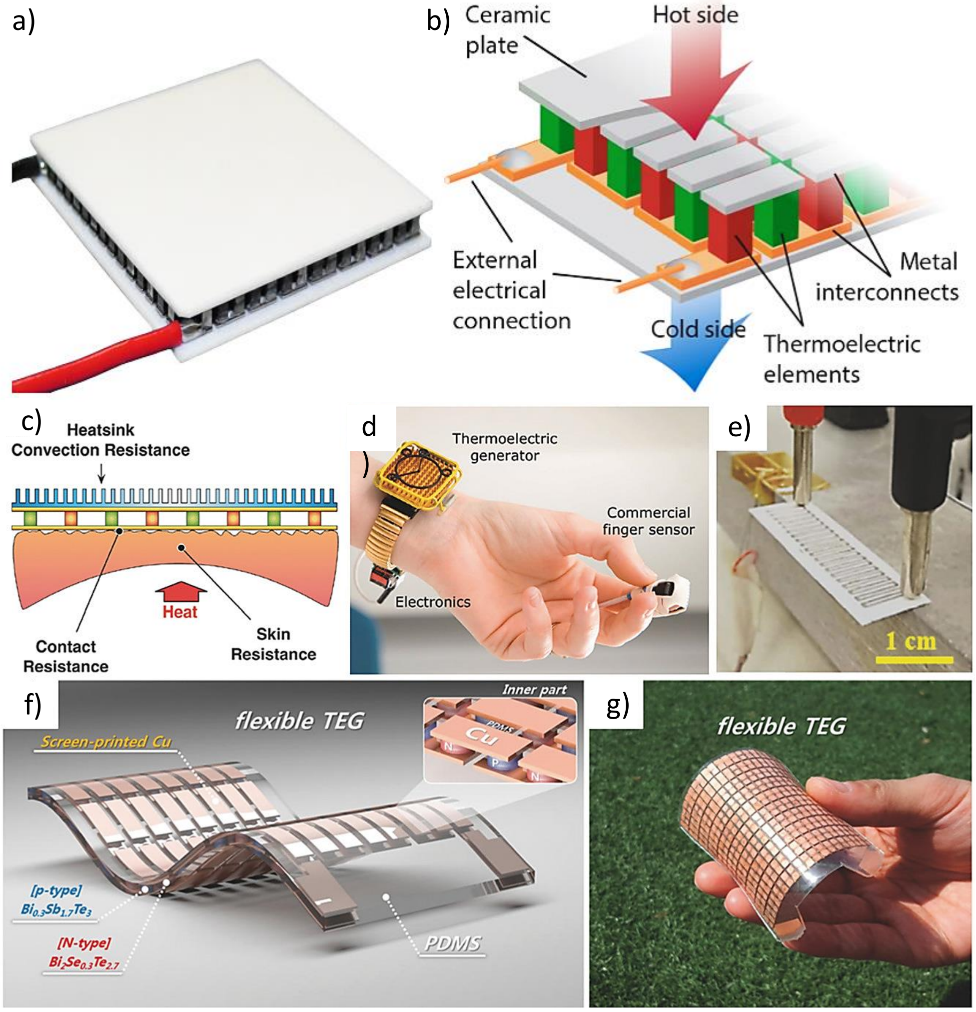

Figure 1.4. (a)-(b) Traditional TE device; a) typical commercial TE module, b) many of *pn*-couples are arranged in series in a commercial module.[8] (c)-(g) Flexible TE device;[15] c) Schematic of the working principle of wearable TE device.[14] d) An example of TE-powered wearable device.[16] e) Paper-based TE device.[17] f) Schematic of a flexible TE device assembled using inorganic modules and g) a photo of the flexible TE device.[18]

1.2.2 The efficiency of thermoelectric device

The maximum coefficient of performance (COP) and power conversion efficiency (η) of a TE device depend on the temperature at the cold (T_c) and hot side (T_h) and can be analytically expressed with the following relationships:

$$COP = \frac{T_c}{\Delta T}\frac{\sqrt{1+ZT_a}-\frac{T_h}{T_c}}{\sqrt{1+ZT_a}+1} \tag{2}$$

$$\eta = \frac{\Delta T}{T_h}\frac{\sqrt{1+ZT_a}-1}{\sqrt{1+ZT_a}+\frac{T_c}{T_h}} \tag{3}$$

where $\Delta T = T_h - T_c$ is the temperature difference, $T_a = \Delta T/2$ is the average temperature, and Z is named as the thermoelectric figure of merit and has dimensions of T^{-1}.[6, 19, 20] As seen in the equation 4 below, the dimensionless figure of merit ZT depends on three tightly interrelated material parameters,[6, 8, 9, 19, 21] the Seebeck coefficient (S), electrical conductivity (σ) and thermal conductivity (κ).

$$ZT = \frac{\sigma S^2}{\kappa} T \qquad (4)$$

There is no known limitation to ZT and thus, except for the Carnot limit, to the energy conversion efficiency of a TE device.

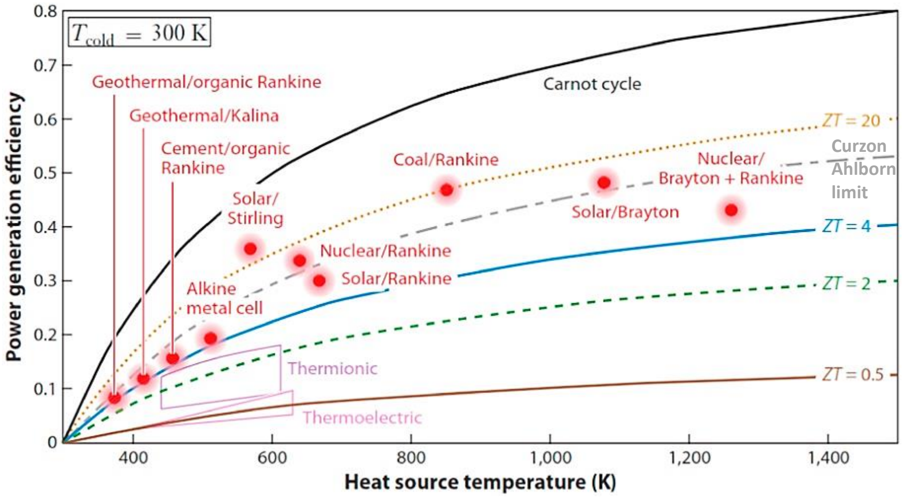

Figure 1.5. Comparison with current competing technologies and efficiency expressed for power generation with different values of ZT.[22]

In the past decades, Bi_2Te_3-based alloys, with ZT close to 1, have been the only material used for industrial TE devices.[6] Figures of merit ZT>2 are required to have efficiencies above 10% in practical temperature gradients.[23, 24] A comparison of TE efficiency with other established current competing technologies is shown in Figure 1.5.

1.2.3 Challenges and determining parameters of thermoelectric

At present, the low efficiency is the main obstacles to the commercialization of TE devices. To improve the efficiency of a TE device one needs to optimize the electrical and thermal transport properties. Generally speaking, a good TE material behaves as a "phonon-glass/electron-crystal" material with efficient electrical transport performance as in a crystalline material and poor thermal transport property as in a glass-like material.

The power factor (PF) is another comprehensive parameter determining performance of a TE material:

$$PF = \sigma S^2 = ne\mu S^2 \quad (5)$$

$$\sigma = ne\mu \quad (6)$$

where n is the charge carrier concentration, e is the electron charge and μ is the mobility of the carrier. For the degenerate semiconductor, the Seebeck coefficient is given by

$$S = \frac{8\pi^2\kappa_B^2}{3eh^2} m^* T \left(\frac{\pi}{3n}\right)^{\frac{2}{3}} \quad (7)$$

where κ_B is the Boltzmann constant, h is the Planck's constant and m^* is the effective mass. It can be seen that the Seebeck coefficient is directly proportional to the effective mass. However, increasing m^* will reduce the carrier mobility μ, and thus electrical conductivity.

The thermal conductivity includes two factors, a lattice contribution and an electronic contribution:

$$\kappa = \kappa_L + \kappa_e \quad (8)$$

The lattice thermal conductivity κ_L can be expressed as follows:

$$\kappa_L = \lambda C_p \rho \quad (9)$$

where λ is the thermal diffusivity, C_p is the specific heat, and ρ is the density of the material. Diminishing lattice thermal conductivity has been extensively endeavored to realize a large figure of merit ZT. The lattice thermal conductivity depends on the ability of phonons to propagate through the material and it is essential to enhance the phonon scattering in order to reduce it.

κ_e is proportional to the electrical conductivity and related to carrier concentration by the Wiedemann–Franz law;[25]

$$\kappa_e = L_o \sigma T = ne\mu L_o T \quad (10)$$

where L_o is the Lorenz number.

To maximize ZT, the optimization of the carrier concentration has become a key parameter, as not only the electrical conductivity, but also the Seebeck coefficient and the electronic contribution to the thermal conductivity depend on it (Figure 1.6). Overall, maximum figures of merit are reached with relatively high charge carrier concentrations, around 10^{19} cm^{-3}.

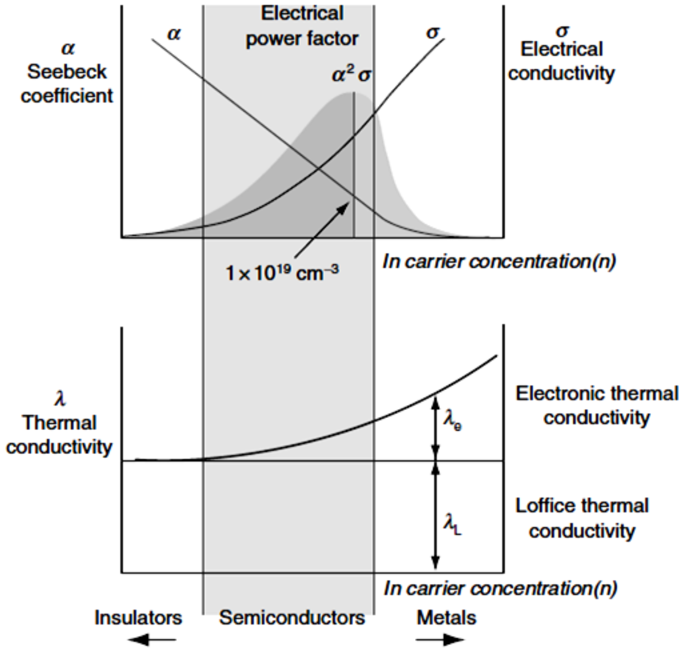

Figure 1.6. Dependence of the figure of merit ZT-related properties with carrier concentration.[20]

1.2.4 Figure of merit ZT improvement

Numerous strategies, e. g. doping, alloying and nanocomposites, have been used to enhance ZT. The most effective approaches are to optimize carrier concentration, to engineer the electronic band structure of the material and to maximize phonon scattering. Generally, the carrier concentration is tuned by means of extrinsic doping or intrinsic defects.[26] Alternatively, modulation toping strategies can be used. Additionally, doping approaches to modify the density of states (DOS) at the Fermi level, increasing the number of energy valleys participating in the transport of majority carriers by forcing band convergence for instance, are considered to increase Seebeck.[27] An alternative strategy to significantly increase Seebeck is energy filtering by rationally designing the band alignment in the nanocomposite interfaces, selectively blocking minority and low energy majority carriers, thus reducing bipolar effects and increasing the average energy per majority charge carrier.[28-30 31 32-34]

On the other hand, nanostructuring is found to be effective in reducing the thermal conductivity through efficient phonons scattering at the high density of grain boundaries.[15, 19, 26, 35]

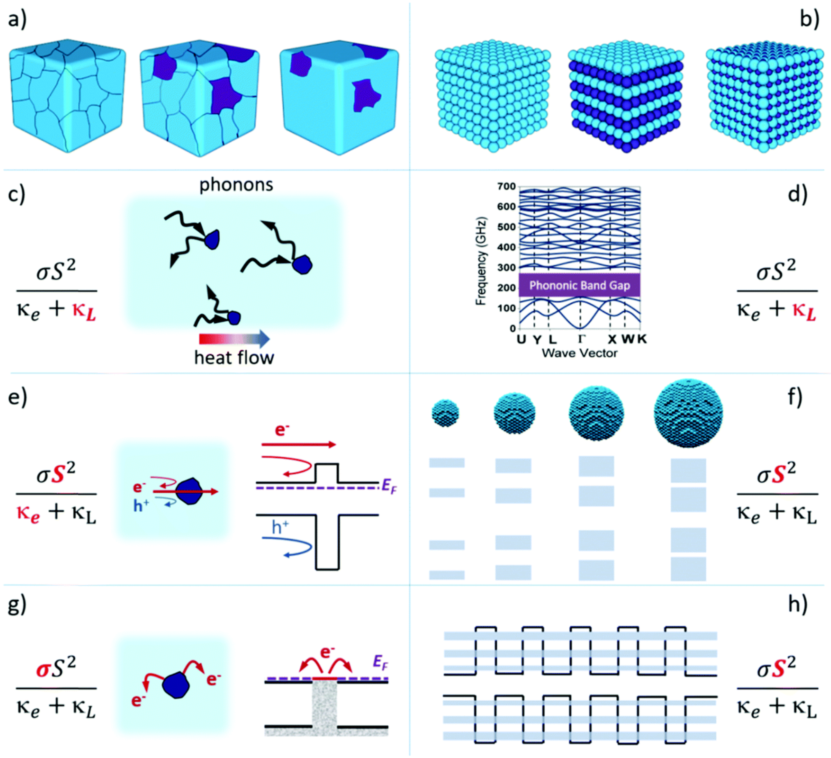

Figure 1.7. Cartoons of different types of disorganized and organized nanomaterials (a) and (b) schemes of the effect of nanostructures on the TE figure of merit: (c) phonon scattering; (d) phononic band gap; (e) charge carrier type- and energy-dependent filtering; (f) DOS modification by quantum confinement in quantum dots; (g) modulation doping; (h) DOS modification within quantum dot superlattices.[19]

To sum up, nanomaterials and particularly nanocomposites can help enhancing the figure of merit ZT by increasing electrical conductivity through modulation doping, increasing Seebeck by manipulating the density of states or filtering charge carriers according to their sign and energy, and decreasing thermal conductivity via scattering of phonons and minority charge carriers (Figure 1.7).

1.3 Bottom-up thermoelectric materials

1.3.1 Bulk thermoelectric materials

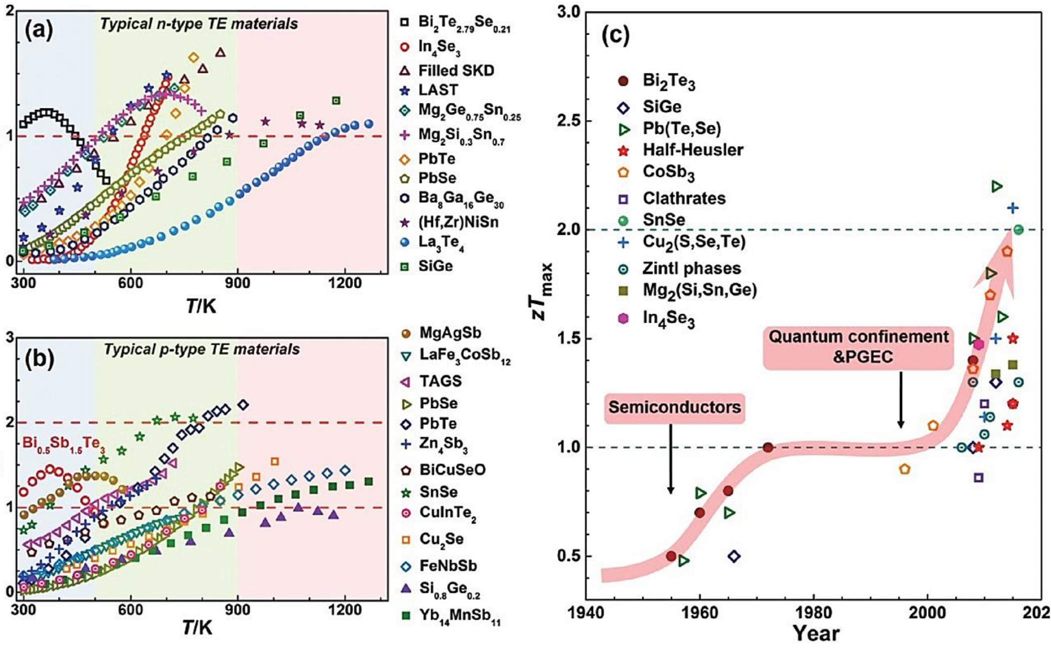

Figure 1.8. Temperature dependence of figure of merit ZT values for some typical classes of a) n-type, and b) p-type bulk TE materials, respectively. c) Evolution of the maximum ZT values for some typical TE materials.[25]

TE materials generally belong to certain material families, including intermetallics, skutterudites, half-Heusler, oxides, Zintl-phase materials and their superlattice architectures.[36] The temperature dependence of the state-of-art figure of merit ZT of some typical classes of n-type and p-type bulk TE materials are shown in Figures 1.8a-c. With the continuous efforts of researchers, the performance of the existing TE materials has been greatly improved. Some TE materials have reached ZT values above 2, which is an exciting result for practical applications.[26]

All these promising TE materials can be synthesized by chemical and physical approaches, and in crystalline or nanocrystalline form. Conventional crystal growth strategies are used to produce crystalline TE bulk materials. Nanomaterials are generally produced by mechanical alloying or ball milling. To produce nanomaterials from mechanical alloying, elemental powders are mixed in stoichiometric ratios and ground in a very high-energy ball mill to produce a fine powder. Then this powder needs to be processed into bulk pellets by hot press or spark plasma sintering (SPS). Some typical TE materials, e.g. PbTe,[37-40] PbSe[41-44] and Bi_2Te_3-based[45-48], are produced by ball milling for a long period of time (commonly more than 10 h), and the resulting nanopowders are loaded into a graphite die and processed by hot press at high temperature, respectively. Although such ball milling strategy provides the simple and large-scale production of materials, a poor level of control over nanomaterial parameters is obtained. Moreover, these strategies are highly time and energy consuming, thus reducing cost-effectiveness.[19]

1.3.2 Bottom-up thermoelectric nanomaterials from solution process

In order to overcome limitations of traditional strategies to produce nanomaterials, alternative approaches are needed. The bottom-up engineering of nanomaterials from solution processed nanocrystals (NCs) is based on a material growth by atomic or molecular addition, which can potentially provide the technology with a precise control over composition, size and shape at nanoscale. It also requires low processing temperatures and short reaction time, what can also reduce device processing cost. NC-based bottom-up approaches are also compatible with the production of flexible devices, by printing techniques, enabling new applications in wearable energy conversion devices.[49-51]

1.3.3 Colloidal synthesis

Colloidal synthesis routes allow producing NCs with excellent control over their properties using low amounts of energy and low capital cost equipment.[52-54] Elemental, binary, ternary, quaternary and even quinary NCs can be prepared via reaction or decomposition of multiple precursors or single-molecule sources. Reactions are usually performed under inert atmosphere in high boiling point solvents, e.g. oleylamine (OLA), octadecene (ODE), oleic acid (OA), hexadecylamine (HDA), trioctylphosphine (TOP), trioctylphosphine oxide (TOPO) or dodecanethiol (DDT). Elemental S, thiourea, elemental Se, SeO_2, TOP-Se and TOP-Te are the most commonly used anion sources to produce chalcogenide NCs. The typical synthesis route to produce colloidal NCs at the laboratory scale uses a Schlenk line as shown in Figure 1.9.

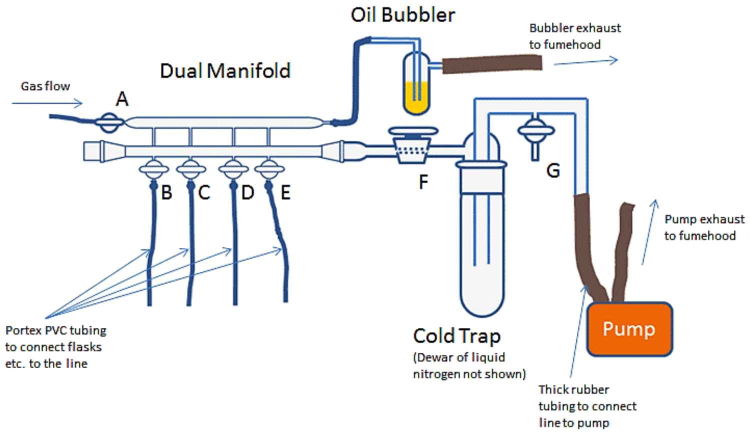

Figure 1.9. Complete colloidal synthesis Schlenk line set-up.[55]

1.3.3.1 Parameters control in colloidal synthesis

Colloidal NC parameters can be modified to affect structural, chemical and physical properties of the resultant particles, e.g. size, shape, composition, phase, absorption, emission and conductivity.[53, 56-59] The progress to this nanoscale level of control has resulted in successful exploitation for numerous applications, particularly in the energy conversion field. [56, 60, 61] In TE applications, tuning the crystal domain sizes in the proper range plays an important role in determining transport properties and allows modifying the electronic band structure through quantum confinement effects.[19, 62]

In particular, the following reaction parameters are important to control the size and shape of colloidal NCs: i) the reaction temperature and time, ii) the injection temperature of the reactant in the case of hot-injection methods, iii) the reactivity and the concentration of precursors, iv) the ratio of the concentration of the chemicals and pH.[63, 64] In order to improve the size distribution of NCs, the hot-injection method is often used. Figure 1.10 represents some examples of inorganic NCs with different size and morphologies synthesized by colloidal technique in this thesis.

Furthermore, composition and phase-controlled by colloidal synthesis approach can also be implemented. NCs with the multinary compositions can be produced by selecting suitable precursors and adjusting the reaction conditions. Substitution reactions are also especially powerful to control the composition of the NCs, and even to create materials with new crystallographic phases. The composition of pre-grown NCs can be also adjusted by subtractive reactions.[19]

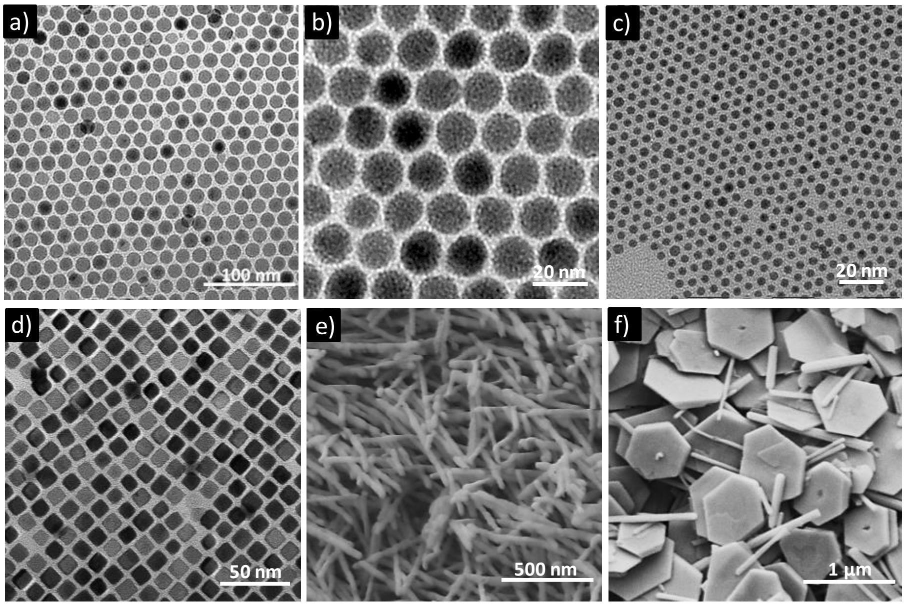

Figure 1.10. Examples of NCs produced by means of colloidal synthesis with different size and shapes in this thesis. a) $AgSbSe_2$ spheres (chapter 2); b) Cu_3SbSe_4 spheres (chapter 3); c) Cu NCs (chapter 4); d) PbS nanotubes (chapter 4); e) Bi_2Te_3 nanowires (chapter 5) and f) nanocomposites of $Bi_2Te_{2.5}Se_{0.5}$ nanoplates-Te nanowires (chapter 6).

1.3.4 Bottom-up thermoelectric nanomaterials challenges

Colloidal NCs have an inorganic core possessing useful properties that is stabilized by a layer of organic surface surfactants. The stability of the colloidal NCs in the solvents is accomplished through this layer of surface ligands.[53] Unfortunately, these organic ligands block charge transport between NCs in TE nanomaterials.[61, 65]

Nanoparticle purification: Generally, the widely used approach to remove the organic ligands is based on thermal decomposition by means of an annealing process. The organics can be cracked during high temperature annealing process, but the process can potentially modify the NC size and shape, and even the phase due to their own low intrinsic phase transition temperature. Another problem is the residual carbon layer after annealing that may have a big influence on their final TE properties. So, in order to minimize this influence, the surface ligands can be displaced with shorter and weak coordinating molecules or some inorganic salts, such as hydrazine,[66, 67] $NOBF_4$,[68] ammonia NH_4SCN,[69] NH_4S,[65] $NaNH_2$,[70] and even halide anions Cl^-, Br^- and I^-,[71-74] etc.

These ligands chemically attached to surface should be considered as part of the nanoparticle, resulting in the potential modification of stoichiometry and valence balance of the overall NCs.

Charge carrier concentrations controlling: The carrier concentration adjustment is essential to optimize TE performance, thus to precisely control the charge carrier concentration become the second big challenge for bottom-up TE nanomaterials. In fact, this important parameter can be tuned at different processing steps (Figure 1.11). In this thesis, I have tried to overcome this challenge by doping during the synthesis (chapter 2 and 3) and by modulation doping (chapter 4).

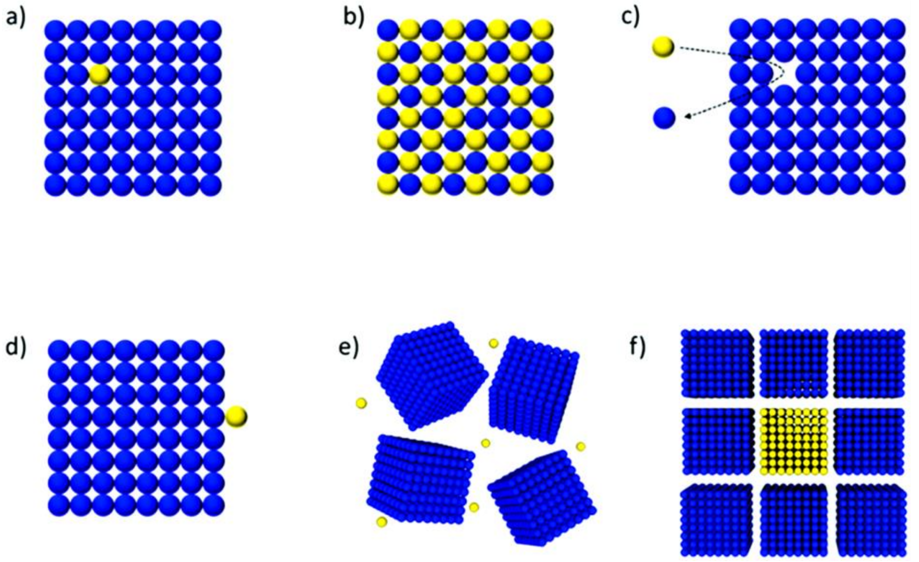

Figure 1.11. Scheme of possible strategies to tune doping in nanoparticle-based solution-processed nanomaterials: (a) extrinsic dopants during synthesis; (b) stoichiometry control; (c) post-synthesis atomic substitution; (d) surface chemistry; (e) dopant additives during consolidation; and (f) modulation doping.[19]

The most widely used strategy to control charge carrier concentration is to introduce the suitable amount of a dopant precursor in the initial reaction solution.[69, 70, 75-77] However, it is not easy to select of the proper dopants, precursors, coordinating ligands and even reaction conditions to enable an effective doping of the NCs. In principle, the reactivity of the dopant precursor need to be very similar to that of the host precursor.[19]

In general, modulation doping strategies are applied by combining two different types of NCs of different materials.[78-80] The charge injecting phase should be homogeneously distributed throughout the matrix, hold very high charge carrier concentrations and a proper electronic band structure for them to spill over the matrix.[19] This strategy has been successfully implemented to optimize the TE performance of PbS-Ag/Cu/Sn nanocomposites.[78, 79] For example, the power factor of PbS–Ag nanocomposites can be significantly enhanced by the electrons injection from the low work function metal Ag NCs to the PbS matrix, as shown in Figure 1.12.[79,78] However, this strategy has been proved effective only to produce n-type matrix with the low work function metal NCs, and it still need to be established for materials potentially obtained by blending a p-type semiconductor matrix with high enough work function metal NCs. Anyway, modulation doping offers an alternative and effective strategy to design nanocomposites with excellent TE performance.

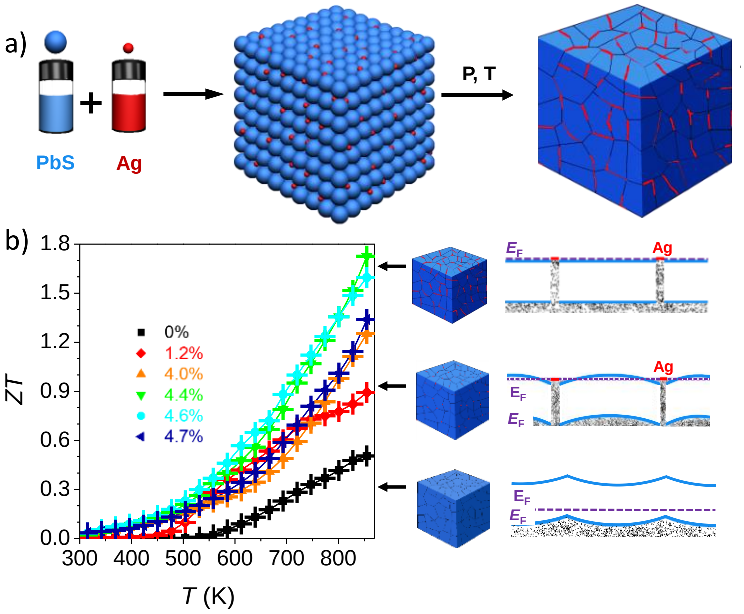

Figure 1.12. a) Bottom-up assembly process to produce PbS–Ag nanocomposites from the assembly of PbS and Ag NCs; b) Figure of merit and schematic representation of the electron energy band alignment.[79]

In addition, there are some other methods that can be effectively used to adjusting the carrier concentrations, e.g. doping during consolidation or surface doping.

NC consolidation into dense and crystallographically textured nanomaterials: Additional challenges are the consolidation of the NCs into a high density bulk nanomaterial that has a proper crystallographic texture. Some TE materials are highly anisotropic, e.g. Bi–Sb–Se–Te alloys[8, 26, 75, 81] and SnSe.[82-84] Bottom-up strategies have conventionally lacked control over the crystallographic alignment of nanograins.[81, 85-92] In order to overcome this challenge, in this thesis (chapter 5 and 6) we produced nanomaterials by combining Bi_2Te_3-based nanoplates (p-type: $Bi_xSb_{2-x}Te_3$ alloys, n-type: $Bi_2Te_{3-x}Se_x$ alloys) with tellurium nanowires, and hot pressed them using multiple pressure and release steps at a temperature above the Te melting point.

This is a very young and in large part unexplored research field using NCs as building blocks to produce nanostructured materials, which is also an area of high potential to develop the high performance TE nanomaterials that will be used in future technologies.

1.4 Objectives

The aim of this thesis is to produce high performance TE nanomaterials by means of the bottom-up approach using finely tuned NCs obtained by cost-effective and scalable colloidal synthesis routes. To achieve the goals of the thesis, it will be required to overcome several main challenges encountered when aiming at the production of nanomaterials and devices using bottom-up engineering. These include the purification of the NCs, the control of the carrier concentration, and the consolidation of the NCs into dense and texturized bulk nanomaterials. To deal with these challenges, in this thesis the following specific objectives have been defined:

i) To develop solution synthesis strategies to produce high quality NCs of three relevant thermoelectric materials: $AgSbSe_2$, Cu_3SbSe_4 and Bi_2Te_3-based alloys.

ii) To develop reliable electronic and modulation doping strategies to control the charge carrier concentration of colloidal NC-based nanomaterials.

iii) To develop assembly and consolidation strategies that allow controlling the composition and crystallographically alignment of nanograins within colloidal NC-based nanomaterials.

iv) To produce TE nanomaterials with controlled charge carrier concentration and crystallinity reaching figures of merit ZT up to ~2 by the bottom-up assembly of NCs.

v) To develop strategies to fabricate TE devices with versatile form factors using these colloidal NC-based nanomaterials.

1.5 References

1. Conti, J.; Holtberg, P.; Diefenderfer, J.; LaRose, A.; Turnure, J. T.; Westfall, L. Washington, DC (United States). Office of Energy Analysis: 2016.
2. Hightower, M.; Pierce, S. A. *Nature* **2008,** 452, (7185), 285.
3. DESA, U., World population projected to reach 9.7 billion by 2050. 2015.
4. Grant, L. *Negative Population Growth* **2004**, 1-12.
5. Foxon, T. *The Energy Journal* **2012,** 33, (2), 225-227.
6. Champier, D. *Energy Conversion and Management* **2017,** 140, 167-181.
7. Callen, H. B. Wiley: 1985.
8. Snyder, G. J.; Toberer, E. S. *Nature materials* **2008,** 7, (2), 105.
9. Mahan, G. *APL Materials* **2016,** 4, (10), 104806.
10. Winder, E. J.; Ellis, A. B.; Lisensky, G. C. *Journal of chemical education* **1996,** 73, (10), 940.
11. Riffat, S. B.; Ma, X. *Applied thermal engineering* **2003,** 23, (8), 913-935.
12. Rowe, D. M. In *CRC Handbook of thermoelectrics*, CRC press: 1995; 31-37.
13. Zhou, W.; Fan, Q.; Zhang, Q.; Cai, L.; Li, K.; Gu, X.; Yang, F.; Zhang, N.; Wang, Y.; Liu, H. *Nature communications* **2017,** 8, 14886.
14. Suarez, F.; Nozariasbmarz, A.; Vashaee, D.; Öztürk, M. C. *Energy & Environmental Science* **2016,** 9, (6), 2099-2113.
15. Yang, L.; Chen, Z. G.; Dargusch, M. S.; Zou, J. *Advanced Energy Materials* **2017**, 8, (6), 1701797.
16. Leonov, V.; Vullers, R. J. *Journal of Renewable and Sustainable Energy* **2009,** 1, (6), 062701.
17. Rojas, J. P.; Conchouso, D.; Arevalo, A.; Singh, D.; Foulds, I. G.; Hussain, M. M. *Nano Energy* **2017,** 31, 296-301.
18. Kim, S. J.; Lee, H. E.; Choi, H.; Kim, Y.; We, J. H.; Shin, J. S.; Lee, K. J.; Cho, B. J. *ACS nano* **2016,** 10, (12), 10851-10857.
19. Ortega, S.; Ibáñez, M.; Liu, Y.; Zhang, Y.; Kovalenko, M. V.; Cadavid, D.; Cabot, A. *Chemical Society Reviews* **2017,** 46, (12), 3510-3528.
20. Rowe, D. M., *Thermoelectrics handbook: macro to nano*. CRC press: 2005.
21. Li, J.-F.; Liu, W.-S.; Zhao, L.-D.; Zhou, M. *NPG Asia Materials* **2010,** 2, (4), 152.
22. Shakouri, A.; Zebarjadi, M., Springer: 2009; 225-299.
23. Hsu, K. F.; Loo, S.; Guo, F.; Chen, W.; Dyck, J. S.; Uher, C.; Hogan, T.; Polychroniadis, E.; Kanatzidis, M. G. *Science* **2004,** 303, (5659), 818-821.
24. Biswas, K.; He, J.; Blum, I. D.; Wu, C.-I.; Hogan, T. P.; Seidman, D. N.; Dravid, V. P.; Kanatzidis, M. G. *Nature* **2012,** 489, (7416), 414.
25. Jonson, M.; Mahan, G. *Physical Review B* **1980,** 21, (10), 4223.

26. Zhu, T.; Liu, Y.; Fu, C.; Heremans, J. P.; Snyder, J. G.; Zhao, X. *Advanced Materials* **2017**, 29, (14), 1605884.
27. Zeier, W. G.; Zevalkink, A.; Gibbs, Z. M.; Hautier, G.; Kanatzidis, M. G.; Snyder, G. J. *Angewandte Chemie International Edition* **2016,** 55, (24), 6826-6841.
28. Shakouri, A. *Annual Review of Materials Research* **2011,** 41.
29. Martin, J.; Wang, L.; Chen, L.; Nolas, G. *Physical review B* **2009,** 79, (11), 115311.
30. Heremans, J. P.; Thrush, C. M.; Morelli, D. T. *Journal of Applied Physics* **2005,** 98, (6), 063703.
31. Joshi, G.; Lee, H.; Lan, Y.; Wang, X.; Zhu, G.; Wang, D.; Gould, R. W.; Cuff, D. C.; Tang, M. Y.; Dresselhaus, M. S. *Nano letters* **2008,** 8, (12), 4670-4674.
32. Zhang, Q.; Ai, X.; Wang, L.; Chang, Y.; Luo, W.; Jiang, W.; Chen, L. *Advanced Functional Materials* **2015,** 25, (6), 966-976.
33. Soni, A.; Shen, Y.; Yin, M.; Zhao, Y.; Yu, L.; Hu, X.; Dong, Z.; Khor, K. A.; Dresselhaus, M. S.; Xiong, Q. *Nano letters* **2012,** 12, (8), 4305-4310.
34. Ko, D.-K.; Kang, Y.; Murray, C. B. *Nano letters* **2011,** 11, (7), 2841-2844.
35. Zheng, Y.; Luo, Y.; Du, C.; Zhu, B.; Liang, Q.; Hng, H. H.; Hippalgaonkar, K.; Xu, J.; Yan, Q. *Materials Chemistry Frontiers* **2017,** 1, (12), 2457-2473.
36. Gayner, C.; Kar, K. K. *Progress in Materials Science* **2016,** 83, 330-382.
37. Pei, Y.; LaLonde, A. D.; Heinz, N. A.; Shi, X.; Iwanaga, S.; Wang, H.; Chen, L.; Snyder, G. J. *Advanced materials* **2011,** 23, (47), 5674-5678.
38. Fu, L.; Yin, M.; Wu, D.; Li, W.; Feng, D.; Huang, L.; He, J. *Energy & Environmental Science* **2017,** 10, (9), 2030-2040.
39. Królicka, A. K.; Mirowska, A.; Materna, A.; Piersa, M. *Crystal Research and Technology* **2017,** 52, (8).
40. Papageorgiou, C.; Hatzikraniotis, E.; Lioutas, C. B.; Frangis, N.; Valassiades, O.; Paraskevopoulos, K.; Kyratsi, T. *Journal of electronic materials* **2010,** 39, (9), 1665-1668.
41. Zhang, Q.; Wang, H.; Liu, W.; Wang, H.; Yu, B.; Zhang, Q.; Tian, Z.; Ni, G.; Lee, S.; Esfarjani, K. *Energy & Environmental Science* **2012,** 5, (1), 5246-5251.
42. Wu, C.-F.; Wei, T.-R.; Li, J.-F. *APL Materials* **2016,** 4, (10), 104801.
43. Zhang, Q.; Cao, F.; Lukas, K.; Liu, W.; Esfarjani, K.; Opeil, C.; Broido, D.; Parker, D.; Singh, D. J.; Chen, G. *Journal of the American Chemical Society* **2012,** 134, (42), 17731-17738.
44. Achimovičová, M.; Baláž, P.; Ďurišin, J.; Daneu, N.; Kováč, J.; Šatka, A.; Feldhoff, A.; Gock, E. *International Journal of Materials Research* **2011,** 102, (4), 441-445.
45. Liu, W. S.; Zhang, Q.; Lan, Y.; Chen, S.; Yan, X.; Zhang, Q.; Wang, H.; Wang, D.; Chen, G.; Ren, Z. *Advanced Energy Materials* **2011,** 1, (4), 577-587.
46. Kuo, C.-H.; Hwang, C.-S.; Jeng, M.-S.; Su, W.-S.; Chou, Y.-W.; Ku, J.-R. *Journal*

of alloys and compounds **2010,** 496, (1-2), 687-690.

47. Kanatzia, A.; Papageorgiou, C.; Lioutas, C.; Kyratsi, T. *Journal of electronic materials* **2013,** 42, (7), 1652-1660.
48. Pacheco, V.; Görlitz, H.; Peranio, N.; Aabdin, Z.; Eibl, O. *Thermoelectric Bi* **2015,** 2.
49. Ding, D.; Lu, C.; Tang, Z. *Advanced Materials Interfaces* **2017,** 4, (20), 1700517.
50. Liang, L.-X.; Deng, Y.; Wang, Y.; Gao, H.-L.; Cui, J. *Journal of nanoparticle research* **2014,** 16, (9), 2575.
51. Madan, D.; Wang, Z.; Chen, A.; Juang, R.-c.; Keist, J.; Wright, P. K.; Evans, J. W. *ACS applied materials & interfaces* **2012,** 4, (11), 6117-6124.
52. Sperling, R. A.; Parak, W. J. *Physical and Engineering Sciences* **2010,** 368, (1915), 1333-1383.
53. Yin, Y.; Alivisatos, A. P. *Nature* **2004,** 437, (7059), 664.
54. You, H.; Yang, S.; Ding, B.; Yang, H. *Chemical Society Reviews* **2013,** 42, (7), 2880-2904.
55. Millar, S. *Wiley-VCH Verlag GmbH & Co. KGaA, Weinheim* **2013**.
56. Talapin, D. V.; Lee, J.-S.; Kovalenko, M. V.; Shevchenko, E. V. *Chemical reviews* **2009,** 110, (1), 389-458.
57. Li, H.; Zanella, M.; Genovese, A.; Povia, M.; Falqui, A.; Giannini, C.; Manna, L. *Nano letters* **2011,** 11, (11), 4964-4970.
58. Mokari, T.; Sztrum, C. G.; Salant, A.; Rabani, E.; Banin, U. *Nature Materials* **2005,** 4, (11), 855.
59. Peng, X. *Advanced Materials* **2003,** 15, (5), 459-463.
60. Wang, J.-j.; Liu, P.; Seaton, C. C.; Ryan, K. M. *Journal of the American Chemical Society* **2014,** 136, (22), 7954-7960.
61. Kovalenko, M. V.; Scheele, M.; Talapin, D. V. *Science* **2009,** 324, (5933), 1417-1420.
62. Ibáñez, M.; Zamani, R.; LaLonde, A.; Cadavid, D.; Li, W.; Shavel, A.; Arbiol, J.; Morante, J. R.; Gorsse, S.; Snyder, G. J.; Cabot. A. *Journal of the American Chemical Society* **2012,** 134, (9), 4060-4063.
63. Chang, J.; Waclawik, E. R. *RSC Advances* **2014,** 4, (45), 23505-23527.
64. El-Sayed, M. A. *Accounts of chemical research* **2004,** 37, (5), 326-333.
65. Nag, A.; Kovalenko, M. V.; Lee, J.-S.; Liu, W.; Spokoyny, B.; Talapin, D. V. *Journal of the American Chemical Society* **2011,** 133, (27), 10612-10620.
66. Scheele, M.; Oeschler, N.; Meier, K.; Kornowski, A.; Klinke, C.; Weller, H. *Advanced Functional Materials* **2009,** 19, (21), 3476-3483.
67. Song, J.-M.; Liu, Y.; Niu, H.-L.; Mao, C.-J.; Cheng, L.-J.; Zhang, S.-Y.; Shen, Y.-H. *Journal of Alloys and Compounds* **2013,** 581, 646-652.
68. Dong, A.; Ye, X.; Chen, J.; Kang, Y.; Gordon, T.; Kikkawa, J. M.; Murray, C. B.

Journal of the American Chemical Society **2010,** 133, (4), 998-1006.

69. Liu, Y.; García, G.; Ortega, S.; Cadavid, D.; Palacios, P.; Lu, J.; Ibáñez, M.; Xi, L.; De Roo, J.; López, A.; Martí-Sánchez, S.; Cabezas, I.; Mata, M.; Luo, Z.; Dun, C.; Dobrozhan, O.; Carroll, D.; Zhang, W.; Martins, J.; Kovalenko, M.; Arbiol, J.; Noriega, G.; Song, J.; Wahnon, P.; Cabot, A. *Journal of Materials Chemistry A* **2017,** 5, (6), 2592-2602.
70. Liu, Y.; Cadavid, D.; Ibánez, M.; De Roo, J.; Ortega, S.; Dobrozhan, O.; Kovalenko, M. V.; Cabot, A. *Journal of Materials Chemistry C* **2016,** 4, (21), 4756-4762.
71. Ning, Z.; Ren, Y.; Hoogland, S.; Voznyy, O.; Levina, L.; Stadler, P.; Lan, X.; Zhitomirsky, D.; Sargent, E. H. *Advanced Materials* **2012,** 24, (47), 6295-6299.
72. Tang, J.; Kemp, K. W.; Hoogland, S.; Jeong, K. S.; Liu, H.; Levina, L.; Furukawa, M.; Wang, X.; Debnath, R.; Cha, D. *Nature materials* **2011,** 10, (10), 765.
73. Zhitomirsky, D.; Furukawa, M.; Tang, J.; Stadler, P.; Hoogland, S.; Voznyy, O.; Liu, H.; Sargent, E. H. *Advanced materials* **2012,** 24, (46), 6181-6185.
74. Ibáñez, M.; Korkosz, R. J.; Luo, Z.; Riba, P.; Cadavid, D.; Ortega, S.; Cabot, A.; Kanatzidis, M. G. *Journal of the American Chemical Society* **2015,** 137, (12), 4046-4049.
75. Liu, Y.; Zhang, Y.; Ortega, S.; Ibáñez, M.; Lim, K. H.; Grau Carbonell, A.; Martí-Sànchez, S.; Ng, K. M.; Arbiol, J.; Kovalenko, M. V.; Cadavid D.; Cabot. A. *Nano letters* **2018**, 18, (4), 2557-2563
76. Stavrinadis, A.; Konstantatos, G. *ChemPhysChem* **2016,** 17, (5), 632-644.
77. Buonsanti, R.; Milliron, D. J. *Chemistry of Materials* **2013,** 25, (8), 1305-1317.
78. Liu, Y.; Cadavid, D.; Ibáñez, M.; Ortega, S.; Martí-Sánchez, S.; Dobrozhan, O.; Kovalenko, M. V.; Arbiol, J.; Cabot, A. *APL Materials* **2016,** 4, (10), 104813.
79. Ibáñez, M.; Luo, Z.; Genç, A.; Piveteau, L.; Ortega, S.; Cadavid, D.; Dobrozhan, O.; Liu, Y.; Nachtegaal, M.; Zebarjadi, M.; Arbiol, J.; Kovalenko, M.V.; Cabot, A. *Nature communications* **2016,** 7, 10766.
80. Zebarjadi, M.; Joshi, G.; Zhu, G.; Yu, B.; Minnich, A.; Lan, Y.; Wang, X.; Dresselhaus, M.; Ren, Z.; Chen, G. *Nano letters* **2011,** 11, (6), 2225-2230.
81. Jiang, J.; Chen, L.; Bai, S.; Yao, Q.; Wang, Q. *Scripta Materialia* **2005,** 52, (5), 347-351.
82. Zhao, L.-D.; Tan, G.; Hao, S.; He, J.; Pei, Y.; Chi, H.; Wang, H.; Gong, S.; Xu, H.; Dravid, V. P. *Science* **2015**, aad3749.
83. Zhao, L.-D.; Lo, S.-H.; Zhang, Y.; Sun, H.; Tan, G.; Uher, C.; Wolverton, C.; Dravid, V. P.; Kanatzidis, M. G. *Nature* **2014,** 508, (7496), 373.
84. Duong, A. T.; Nguyen, V. Q.; Duvjir, G.; Kwon, S.; Song, J. Y.; Lee, J. K.; Lee, J. E.; Park, S.; Min, T.; Lee, J. *Nature communications* **2016,** 7, 13713.
85. Kitagawa, H.; Takimura, K.; Ido, S.; Morito, S.; Kikuchi, K. *Journal of Alloys and*

Compounds **2017,** 692, 388-394.

86. Seo, J.; Lee, C.; Park, K. *Journal of materials science* **2000,** 35, (6), 1549-1554.
87. Yan, X.; Poudel, B.; Ma, Y.; Liu, W.; Joshi, G.; Wang, H.; Lan, Y.; Wang, D.; Chen, G.; Ren, Z. *Nano letters* **2010,** 10, (9), 3373-3378.
88. Kimura, T.; Takahashi, T.; Tani, T.; Saito, Y. *Journal of the American Ceramic Society* **2004,** 87, (8), 1424-1429.
89. Zhao, L.; Zhang, B.-P.; Li, J.-F.; Zhang, H.; Liu, W. *Solid State Sciences* **2008,** 10, (5), 651-658.
90. Bhame, S. D.; Pravarthana, D.; Prellier, W.; Noudem, J. G. *Applied Physics Letters* **2013,** 102, (21), 211901.
91. Hu, L.; Liu, X.; Xie, H.; Shen, J.; Zhu, T.; Zhao, X. *Acta Materialia* **2012,** 60, (11), 4431-4437.
92. Suzuki, A.; Kitagawa, H.; Ido, S.; Pham, A. H.; Morito, S.; Etoh, T.; Kikuchi, K. *Journal of Alloys and Compounds* **2018,** 742, 240-247.

Chapter 2

Colloidal $AgSbSe_2$ Nanocrystals: Surface Analysis, Electronic Doping and Processing into Thermoelectric Nanomaterials

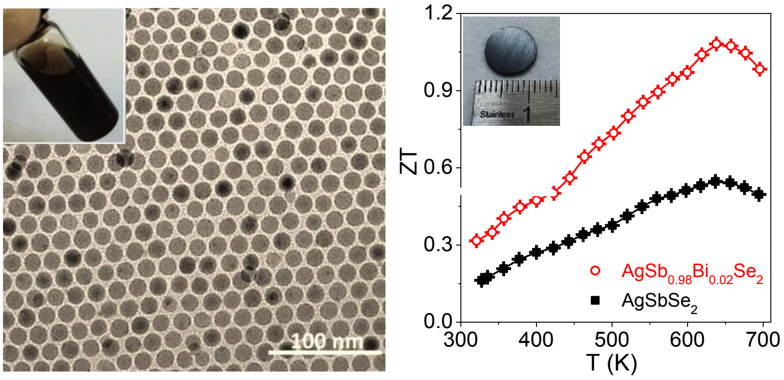

2.1 Abstract

We present a high-yield and scalable colloidal synthesis to produce monodisperse $AgSbSe_2$ nanocrystals (NCs). Using nuclear magnetic resonance (NMR) spectroscopy, we characterized the NC surface chemistry and demonstrate the presence of surfactants in dynamic exchange, which controls the NC growth mechanism. In addition, these NCs were electronically doped by introducing small amounts of bismuth. To demonstrate the technological potential of such processed material, after ligand removal by means of $NaNH_2$, $AgSbSe_2$ NCs were used as building blocks to produce thermoelectric (TE) nanomaterials. A preliminary optimization of the doping concentration resulted in a thermoelectric figure of merit (ZT) of 1.1 at 640 K, which is comparable to the best ZT values obtained with a Pb- and Te-free material in this middle temperature range, with the

additional advantage of the high versatility and low cost associated with solution processing technologies.

2.2 Introduction

I-V-VI_2 semiconductors, particularly $AgSbSe_2$, show very attractive and yet to be exploited functional properties. $AgSbSe_2$, with a rock-salt crystal structure, is highly suited, for instance, as phase change recording material in rewritable optical memories due to drastic resistance drop upon crystallization from amorphous state.[1-6] Within the $AgSbSe_2$ structure, Ag and Sb are generally assumed to randomly occupy the Na sites of the NaCl–type lattice,[7-10] which is consistent with ab initio calculations showing the total energies of the various ordered structures to be very close, thus allowing the presence of a significant density of disorder defects and mixed phases. A careful structural characterization has shown domains of ordering, not only in $AgSbSe_2$,[11] but also in the related $AgSbTe_2$,[12] correlating well with calculations showing a rhombohedral ordering to be the most energetically favorable in $AgSbSe_2$.[13] Atomic ordering within the $AgSbSe_2$ crystal has a significant impact on the electronic structure near the band gap, which dominates the electronic properties[14] and provides the material with ferroelectric properties.[11]

$AgSbSe_2$ is a narrow, indirect band-gap semiconductor (0.03–0.10 eV) showing p-type conductivity.[15] However, an apparent optical bandgap of 0.6–1.1 eV,[5, 15-18] and a high optical absorption coefficient (10^4 cm^{-1}) have also motivated the use of $AgSbSe_2$ for photovoltaic applications. [5, 17, 19-21]

The $AgSbSe_2$ band structure is characterized by a multi-peak valence band maximum, which potentially results in a high effective mass for holes and thus a high Seebeck coefficient. In addition, $AgSbSe_2$ features a strong anharmonic bonding arrangement associated to the Sb $5s^2$ lone pair, which translates into strong phonon-phonon interactions that reduce the lattice thermal conductivity to values close to the amorphous limit. This intrinsically low thermal conductivity and the appropriate electronic band structure make $AgSbSe_2$ and $AgSbTe_2$ promising candidates for TE applications in the intermediate temperature range (500–700K).[16, 22-28] While $AgSbTe_2$ exhibits higher electrical conductivity,[29, 30] and its nanostructured alloys with GeTe (TAGS) and PbTe (LAST–m) are well known for their remarkable ZT values, $AgSbSe_2$ is advantageous in terms of thermal stability, abundance of constituting elements and cost. Bulk $AgSbSe_2$ is typically produced by the solid-state reaction of its highly purified elements at temperatures above 1000 K. A relatively large variety of extrinsic electronic dopants, introduced as pure elements in the reaction mixture, has been tested, including substitution of Sb^{3+} by monovalent Na^{+},[28] divalent Pb^{2+},[16] Zn^{2+},[23] Sn^{2+},[24] Cd^{2+},[26] Mg^{2+},[27] Ba^{2+},[27] and peculiarly by trivalent Bi^{3+}.[16] Extrinsic dopants can also introduce additional disorder and point defect scattering reducing the material thermal conductivity. In some cases, e.g. Na^{+}, Zn^{2+} and Ba^{2+}, can also introduce nanoprecipitates with modified stoichiometry, e.g. Na-rich $AgSbSe_2$ or even of secondary phases, e.g. ZnSe and $BaSe_3$, which further reduce thermal conductivity and allow reaching ZT values up to ~1.1.[23, 27] Besides, intrinsic doping strategies based on tuning the material stoichiometry by modifying for instance the Sb content[25] and reaching ZT values up to ~1 has been also tested by solid state reaction methods.

The preparation of $AgSbSe_2$ with controlled properties by means of solution processing methods is especially appealing to investigate the structural and compositional dependent functional properties, optimize the material for relevant applications and develop high performance cost-effective products. In particular, the availability of $AgSbSe_2$ NCs with tuned size, shape, composition and phase would allow high density data storage systems, cost effective photovoltaic devices and high performance thermoelectric modules to be produced by highly versatile, low-cost, high-throughput and high-yield solution-based bottom-up technologies.[31-36] However, to the best of our knowledge, no synthesis protocol to produce colloidal $AgSbSe_2$ NCs is currently available.

Here, in this chapter we detail the first colloidal synthesis of monodisperse $AgSbSe_2$ NCs on the gram scale, determine the NC surface composition by NMR and demonstrate the possibility of electronically doping this material with controlled amounts of bismuth. Finally, we elaborate upon a procedure to remove organic ligands and demonstrate the suitability of these NCs to produce high performance thermoelectric nanomaterials.

2.3 Experimental Section

Chemicals and solvents: Silver nitrate ($AgNO_3$, ≥99%), antimony (III) chloride ($SbCl_3$, 99%), selenium powder (Se, 99.5%), bismuth (III) acetate ($Bi(CH_3CO_2)_3$, >99.99%), sodium amide ($NaNH_2$, 95%) dodecanethiol (DDT, 98%), oleic acid (OA, 90 %), 1-octadecene (ODE, 90%), and oleylamine (OLA, 70%) were purchased from Sigma-Aldrich. Analytical grade acetone and chloroform were obtained from various sources. All chemicals were used as received without further purification. Syntheses were carried out using a standard vacuum/dry argon Schlenk line.

Selenium precursor stock solution: A 0.5 M selenium stock solution was prepared by dissolving selenium powder (1.5792 g, 20 mmol) in 20 ml OLA and 20 ml DDT at room temperature, cycled between vacuum and argon to remove the oxygen in the flask, and then stirred under Ar atmosphere until Se powder was completely dissolved.

Synthesis of $AgSbSe_2$ NCs: In a typical synthesis, $AgNO_3$ (5 mmol, 0.849 g), $SbCl_3$ (5 mmol, 1.141 g), 70 ml OLA and 10 ml OA were mixed in a 250 ml three-neck flask at room temperature under magnetic stirring for 30 min in order to remove low boiling point impurities. Afterwards, the solution was maintained at 80 °C under vacuum for 60 min. At around 70 °C the solution became yellowish and changed from ivory yellow to yellowish-brown during the time at 80 °C. Then the solution was heated to 120°C for another 10 min under vacuum. After these steps, argon was introduced and the reaction was rapidly heated to 220 °C. At this temperature, 20 ml of a 0.5 M selenium solution were quickly injected. After injection, the color of the solution changed immediately from yellowish-brown to dark brown, indicating the NCs nucleation. NCs were allowed to grow for 30 min at 220 °C. Afterwards, the colloidal solution was rapidly cooled to room temperature through water bath. The resultant dark brown solution was cleaned by centrifugation at 6000 rpm for 5 min using chloroform as solvent and acetone as a non-solvent.

Synthesis of Bi-doped $AgSbSe_2$ NCs: Bi–doped $AgSbSe_2$ NCs were synthesized by using the same process that the pristine NCs but replacing the desired amount of $SbCl_3$ by $Bi(CH_3CO_2)_3$. To produce $AgSb_{0.98}Bi_{0.02}Se_2$, the precursor molar ratio was $SbCl_3/Bi(CH_3CO_2)_3=0.98/0.02$ (4.9 mmol/0.1 mmol).

Nuclear Magnetic Resonance (NMR): NMR measurements were recorded on a Bruker Avance III HD Spectrometer operating at a ^1H frequency of 500.26 MHz and equipped with a BBFO-Z probe. The sample temperature was set to 298.2 K. One dimensional (1D) ^1H and 2D NOESY (Nuclear Overhauser Effect Spectroscopy) spectra were acquired using standard pulse sequences from the Bruker library. For the quantitative 1D ^1H measurements, 64k data points were sampled with the spectral width set to 20 ppm and a relaxation delay of 30 sec. The NOESY mixing time was set to 300 ms and 4096 data points in the direct dimension for 512 data points in the indirect dimension were sampled, with the spectral width set to 12 ppm. Diffusion measurements (2D DOSY) were performed using a double stimulated echo sequence for convection compensation and with monopolar gradient pulses.[37] Smoothed rectangle gradient pulse shapes were used throughout. The gradient strength was varied quadratically from 2-95 % of the probe's maximum value in 64 increments, with the gradient pulse duration and diffusion delay optimized to ensure a final attenuation of the signal in the final increment of less than 10 % relative to the first increment. For 2D processing, the spectra were zero filled until a 4096 - 2048 real data matrix. Before Fourier transformation, the 2D spectra were multiplied with a squared cosine bell function in both dimensions, the 1D spectra were multiplied with an exponential window function. Concentrations were obtained using the Digital ERETIC method, as provided in the standard software of Bruker. The diffusion coefficients were obtained by fitting the appropriate Stejskal-Tanner equation to the signal intensity decay.[38]

NCs Ligand displacement (LD): $NaNH_2$ was used to displace organic ligands from the $AgSbSe_2$ and $AgSb_{0.98}Bi_{0.02}Se_2$ NCs surface. In a typical procedure, $AgSbSe_2$ NCs (500 mg) were dispersed in 15 ml of chloroform and mixed at room temperature with 5 ml of $NaNH_2$ solution (0.02 M) in methanol. The solution was shacked during 1~2 min to displace the organic ligands attached to the NCs surface. This process was repeated twice. Afterward, NCs were precipitated by centrifugation and they were thoroughly purified using chloroform and acetone to remove the remaining organic surfactants and excess $NaNH_2$. Finally, $AgSbSe_2$ NCs were precipitated and dried under vacuum to obtain a fine nanopowder.

Bulk nanomaterials: $AgSbSe_2$ and $AgSb_{0.98}Bi_{0.02}Se_2$ nanopowders obtained from drying 15 nm NCs were loaded into graphite dies and compacted into pellets (Ø10 mm × ~1.5 mm) in an Ar atmosphere using a custom-made hot press. The process temperature was maintained between 350 °C and 360 °C for 30 min and the pressure was set to 70 MPa. In this system, the heat is provided by an induction coil operated in the RF range applied directly to a graphite die, which acts as a susceptor, resulting in a heating ramp of about 20 °C/second. The density of the pressed pellets was always higher than 93% of their theoretical value.

Structural and chemical characterization: X-ray diffraction analyses were carried out on Bruker AXS D8 ADVANCE X-ray diffractometer with Cu-Kα radiation ($\lambda = 0.15406$ Å). Size and shape of initial NCs were examined by transmission electron microscopy (TEM) using a ZEISS LIBRA 120, operating at 120 kV. High resolution TEM (HRTEM) images were recorded using JEOL JEM-2200FS microscope operated at 200 kV. For TEM analysis colloidal nanoparticles in chloroform were supported by drop casting the solution on a carbon-coated copper grid at room temperature and ambient atmosphere. For HRTEM characterization of the pellets, we manually grinded a piece of the measured pellet and mixed the obtained powder with TCE (tetrachloroethylene). The powder suspension was drop casted onto a carbon coated copper grid at room temperature and ambient atmosphere. Field-emission scanning electron microscopy (SEM) was carried out on an Auriga Zeiss at 5.0 kV. Quantitative elemental analysis was made by means of an energy dispersive X-ray spectroscopy (EDX) detector attached to SEM.

Thermoelectric measurements: Seebeck coefficient was measured by using a static DC method. Electrical resistivity data was obtained by a standard four-probe method. Both the Seebeck coefficient and the electrical resistivity were measured simultaneously in a LSR-3 LINSEIS system in the range between room temperature and 700 K, under helium atmosphere. XFA 600 Xenon Flash equipment was used to determine the thermal diffusivities of the samples. The carrier concentration and mobility were measured using the Hall measurement system (PPMS-9T, Quantum Design Inc., USA) at room temperature under a magnetic field of 2 T. The thermal conductivity was calculated by $\kappa = \lambda C_P \rho$, where λ is the thermal diffusivity, C_P is the heat capacity, and ρ is the mass density of the specimen. The specific heat (C_P) was measured by means of a differential scanning calorimeter method (DSC model T2000 TA Instruments), and the density (ρ) values used here were calculated using the Archimedes' method.

2.4 Results and discussion

Figure 2.1a shows a representative TEM micrograph of the spherical 15 ± 1 nm $AgSbSe_2$ NCs obtained following the above procedure. NCs could be dispersed in non-polar solvents such as toluene, hexane or chloroform to form a stable, dark brown dispersion (Figure 2.1b). XRD analysis showed $AgSbSe_2$ NCs to have a cubic structure with a $Fm\bar{3}m$ space group (a = 5.78 Å) (Figure 2.1d, JCPDS card No. 00-012-0379). No order between the Ag and Sb ions could be discerned from the XRD patterns, which is consistent with the similar scattering factors of Ag and

Sb ions. Importantly, no secondary phases were detected in the XRD pattern, pointing towards the phase purity of the synthesized NCs. EDX analysis showed the silver, antimony, and selenium composition to be consistent with stoichiometric $AgSbSe_2$, within the experimental error of ~2 % (Figure 2.2).

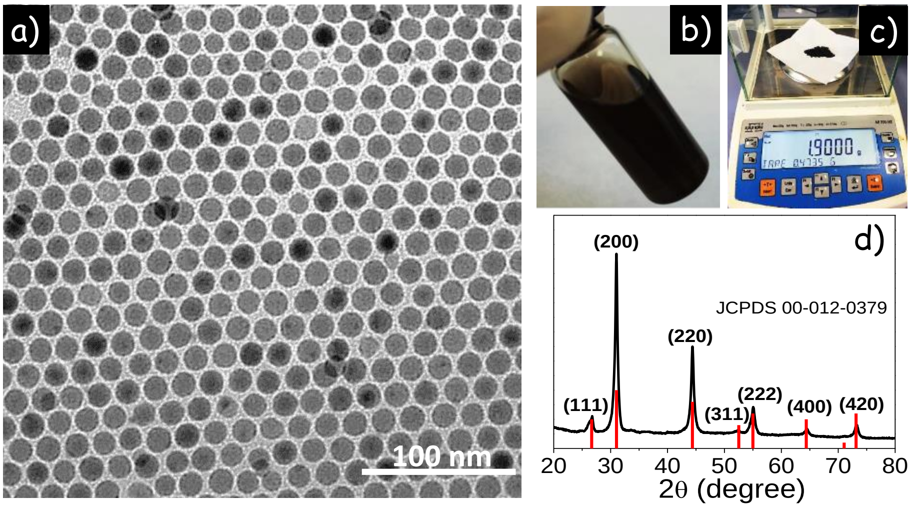

Figure 2.1. (a) TEM micrograph of the $AgSbSe_2$ NCs. (b) NCs dispersed in chloroform. (c) Amount of NCs produced per batch. (d) XRD pattern of $AgSbSe_2$.

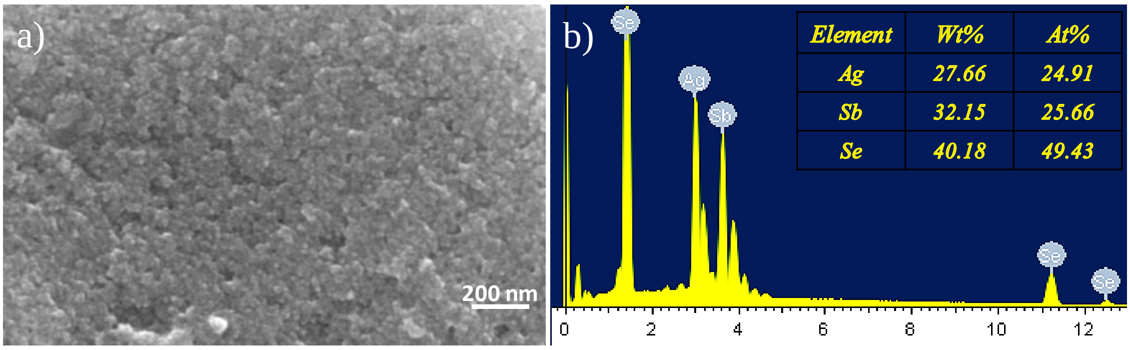

Element	Wt%	At%
Ag	27.66	24.91
Sb	32.15	25.66
Se	40.18	49.43

Figure 2.2. (a) and (b) SEM micrograph of the $AgSbSe_2$ NCs and EDX spectrum of $AgSbSe_2$ NCs, respectively.

The presence of OLA and OA in the precursor solution was required to dissolve $AgNO_3$ and $SbCl_3$, respectively.[39] The absence of OA prevented the incorporation of Sb and thus the formation of stoichiometric $AgSbSe_2$ NCs. Likewise, the absence of OLA resulted in a polydisperse mixture of $AgSbSe_2$ and Ag_2Se (Figures 2.3 and 2.4).

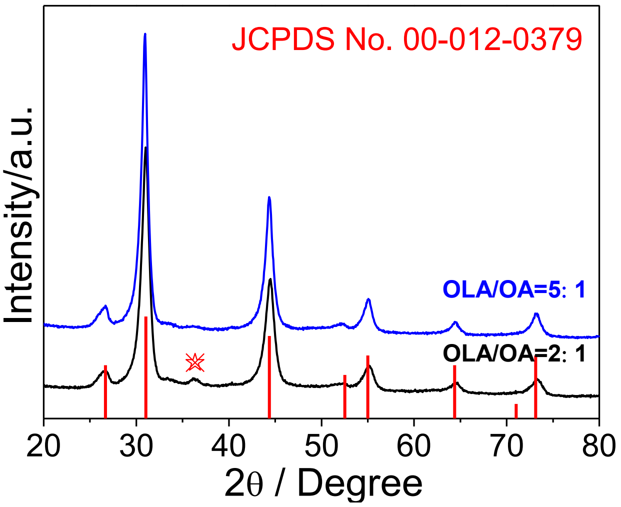

Figure 2.3. XRD patterns of $AgSbSe_2$ NCs prepared with non-optimum OLA/OA volume ratios. An additional peak (red star marker) corresponding to Ag_2Se appears at low OLA concentrations.

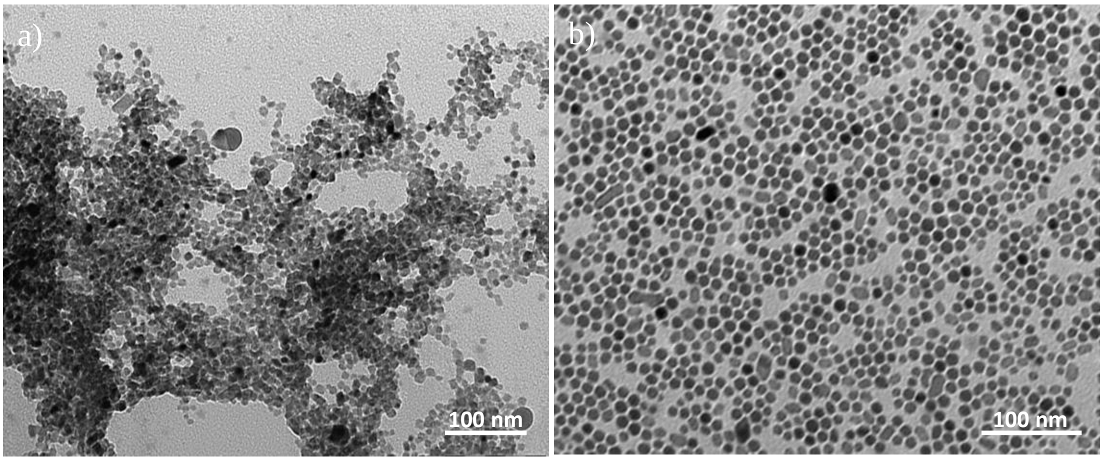

Figure 2.4. TEM images of $AgSbSe_2$ NCs prepared with non-optimum OLA/OA volume ratios. Left: OLA: OA=2: 1; right: OLA: OA=5:1.

Although the reaction mixture already turned dark brown upon injection of the selenium precursor, relatively long reaction times were necessary to produce monodisperse NCs (Figures 2.5 and 2.6). Within the first 15 min, NCs with a bimodal size distribution were obtained. This bimodal distribution possibly originates from an extended nucleation time due to a relatively low reactivity of the precursor complexes, which translates into a slow NC growth that prevents a rapid monomer reduction in the supersaturation.[40] A focusing of the size distribution, most probably mediated by an Ostwald ripening process, was observed up to 30 min reaction time, when the narrowest size distribution was obtained. Larger reaction times resulted in a non-uniform growth of the NCs, increasing the size distribution width.

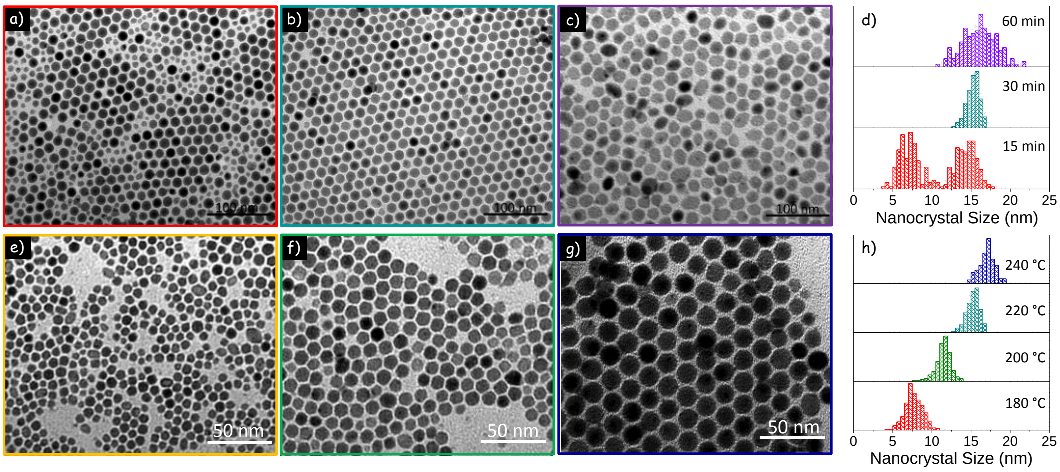

Figure 2.5. a-c) TEM micrographs of $AgSbSe_2$ NCs prepared at a fixed temperature, 220 °C, and different reaction times: a) 15 min; b) 30 min; c) 60 min. d) Histogram of the particle size distribution for NCs produced at increasing reaction times. e-f) TEM micrographs of $AgSbSe_2$ NCs prepared at different reaction temperatures and a fixed reaction time, 30 min: e) 180 °C; f) 200 °C; g) 240 °C (5 min). h) Histogram of the measured particle size distribution for NCs produced at increasing reaction temperatures.

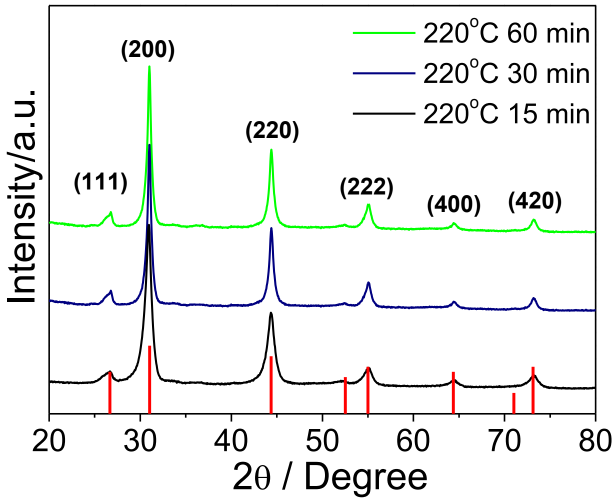

Figure 2.6. XRD patterns of $AgSbSe_2$ NCs with varying reaction time.

Consistent with this growth mechanism, an increase of the injection and reaction temperature and thus of the monomer reactivity resulted in larger NCs. Therefore, fixing the reaction time, $AgSbSe_2$ NC size could be easily tailored in the range from 7±1 nm to around 17±2 nm by just adjusting the reaction temperature in the range from 180 to 240 °C (Figures 2.5 and 2.7). Reaction temperatures below 180 °C did not allow the growth of $AgSbSe_2$ NCs. Higher reaction temperatures resulted in highly polydisperse NCs.

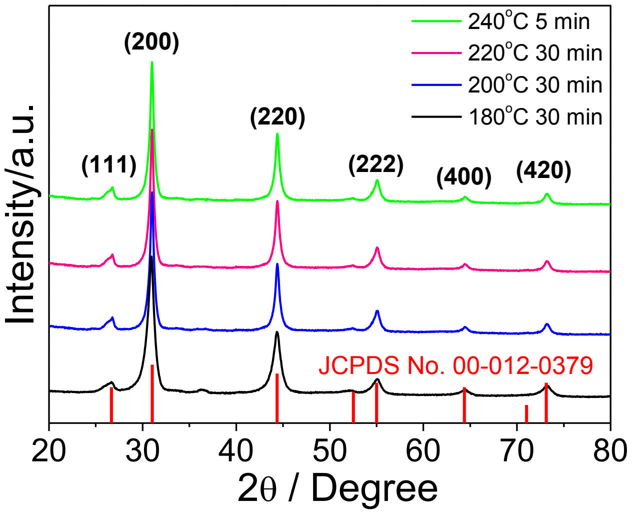

Figure 2.7. XRD patterns of $AgSbSe_2$ NCs prepared at different reaction temperature; from down to top:180 °C (30 min), 200 °C (30 min), 220 °C (30 min), and 240 °C (5 min), respectively.

In the ^1H nuclear magnetic resonance (NMR) spectrum of the resulting NC dispersion in deuteroform, slightly broadened resonances are observed which correspond to an oleyl chain (Figure 2.8a). Since the integrations from the alkene resonance (5) and the CH_3 resonance (6) fit the expected 2:3 ratio we conclude that fully saturated molecules are not present. However, it is difficult to distinguish OA from OLA since the characteristic CH_2 resonances (1 and 2) next to the functional group are not detected, presumably due to the interaction of the ligand with the NC surface. The nuclear Overhauser effect spectroscopy (NOESY) spectrum (Figure 2.8b) indeed confirms that the oleyl species are interacting with the surface since negative (black) nOe cross peaks are observed.[41] The total ligand concentration was determined to be 4.5 mM (based on resonance 6) and with the NC concentration and NC size, a rather low ligand density of 1.2 nm^{-2} was calculated. The diffusion ordered NMR spectrum (DOSY, Figure 2.8c) features two sets of resonances (apart from acetone), with a different diffusion coefficient, D. This indicates that two species are present which are diffusing with a different speed.

However, none of the two species diffuses slow enough to correspond to a 15 nm nanocrystal plus a tightly bound ligand shell, which would yield a solvodynamic diameter, d_s = 19 nm. We thus infer that the ligands are not tightly bound but are in a dynamic exchange regime between a free and a boundstate. Therefore, the ligand density that was calculated earlier is a maximum value and, in reality, the ligands only spend part of their time on the surface. A low bond strength of the ligands to the NC surface and the observed ligand dynamic exchange are consistent with the NC growth not being limited by the surfactant concentration, but by the growth kinetics.

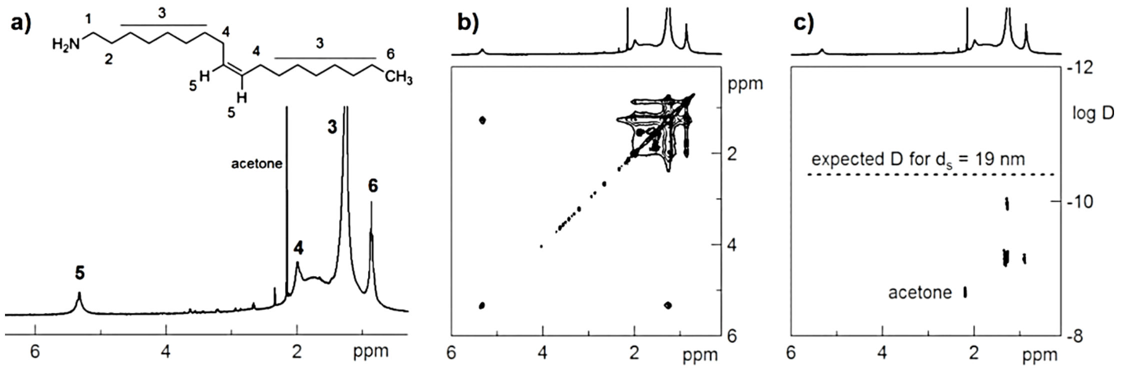

Figure 2.8. (a) ^{1}H NMR spectrum of $AgSbSe_2$ 15±2 nm NCs (4 µM) and the corresponding (b) NOESY and (c) DOSY spectrum.

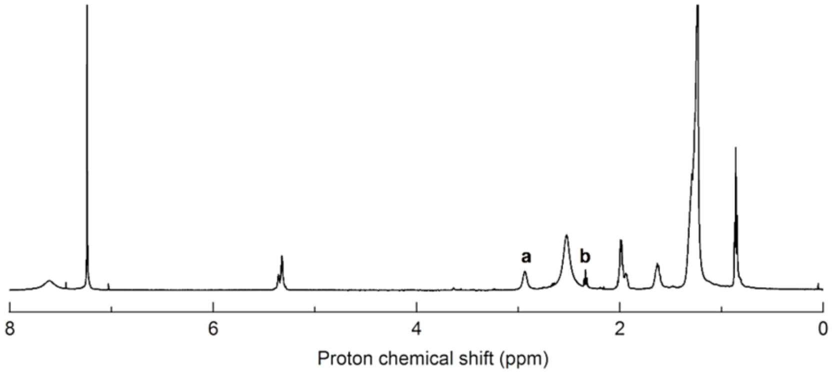

Figure 2.9. Supernatant after addition of TFA to a $AgSbSe_2$ NCs dispersion and centrifugation to remove the NCs. Both the alpha CH_2 resonances of oleylamine (a) and acid acid (b) are recognized. Integration after baseline correction leads to a ratio of 4.6:1 and corresponds to 82 % of oleylamine and 18 % of oleic acid.

To elucidate the nature of the two species in DOSY, we stripped the ligands from the NC surface by the addition of TFA. After removal of the NCs by centrifugation, the supernatant was again measured in NMR (Figure 2.9) and the characteristic resonances of both OA and OLA were observed with a relative abundance of 18 % and 82 % respectively.

Controlled amounts of bismuth were incorporated within the $AgSbSe_2$ NCs by replacing a small amount of $SbCl_3$ by an equivalent amount of $Bi(CH_3COO)_3$ in the precursor solution. At relatively low Bi concentrations, [Bi] < 5%, EDX analysis showed the final Bi composition in the NCs to match, within the experimental error, the nominal concentration of introduced $Bi(CH_3COO)_3$. The incorporation of Bi ions within the $AgSbSe_2$ lattice was confirmed by a slight peak shift toward lower angles in the XRD pattern (Figure 2.10b), pointing towards an increase of the lattice parameters. Bi-doping had also an evident influence on the size and shape distribution of the produced NCs (Figure 2.10a).

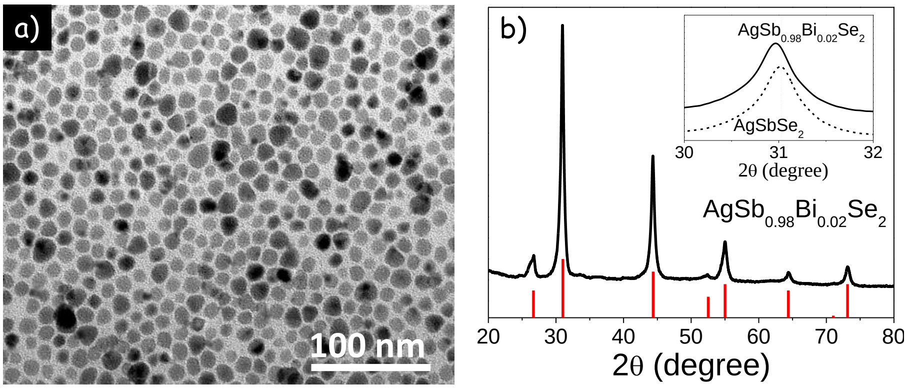

Figure 2.10. a) TEM micrograph of $AgSb_{0.98}Bi_{0.02}Se_2$ NCs and b) their XRD pattern including reference JCPDS 00-012-0379. Inset shows detail of (200) peak.

To use $AgSbSe_2$ NCs in solid-state devices that require efficient transport of charge carriers, original insulating organic ligands have to be removed. Among the different ligand displacement agents tested, $NaNH_2$ was the most effective one, as characterized by Fourier-transform infrared spectroscopy (FTIR). After ligand removal with a 0.02 M $NaNH_2$ solution, $AgSbSe_2$ could not be re-dispersed in non-polar solvents and the strong C-H vibration modes (2850–3000 cm^{-1}) and the bands corresponding to C-C, C-N and NH_2 (700-1650 cm^{-1}) had completely disappeared from the FTIR spectrum (Figure 2.11), proving the effective removal of OLA and OA from the NC surface.

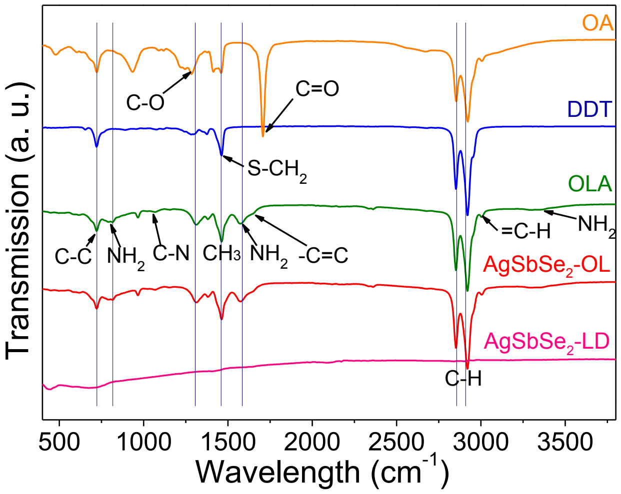

Figure 2.11. From top to down, FTIR spectra of pure OA, DDT, OLA, as-produced $AgSbSe_2$ NCs ($AgSbSe_2$–OL) and $AgSbSe_2$ NC after ligand removal with $NaNH_2$ ($AgSbSe_2$–LD).

After ligand displacement, dried 15 nm $AgSbSe_2$ NCs were hot-pressed into 10 mm in diameter and 1.5 mm thick pellets at 350 °C and 70 MPa of pressure for 30 min. All pellets produced had a metallic lustre, were mechanically robust and had relative densities above 93% as measured by the Archimedes' method. No secondary phases or changes in composition of the $AgSbSe_2$ and $AgSb_{0.98}Bi_{0.02}Se_2$ materials during the hot press process were detected by EDX and XRD (Figures 2.12 and 2.13). SEM and TEM characterization showed a very low porosity and large grains, up to several hundred nanometers, during the thermal processes (Figures 2.14a and 2.14c). However, HRTEM characterization allowed discerning crystallographic order domains in the nanometer size regime (Figure 2.14b).

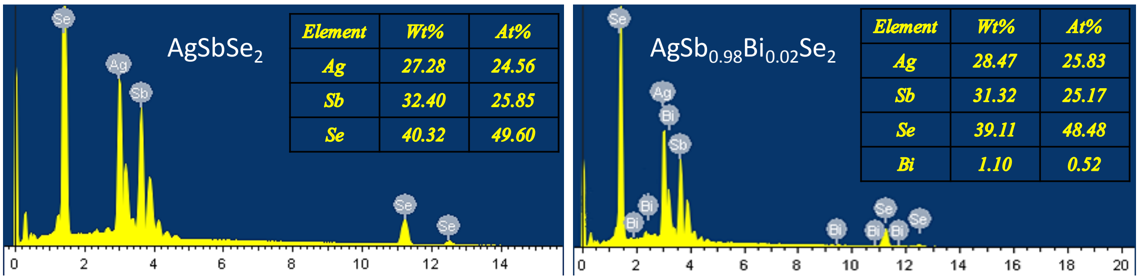

Element	Wt%	At%
Ag	27.28	24.56
Sb	32.40	25.85
Se	40.32	49.60

Element	Wt%	At%
Ag	28.47	25.83
Sb	31.32	25.17
Se	39.11	48.48
Bi	1.10	0.52

Figure 2.12. EDX spectra of $AgSbSe_2$ and $AgSb_{0.98}Bi_{0.02}Se_2$ pellets after hot-press.

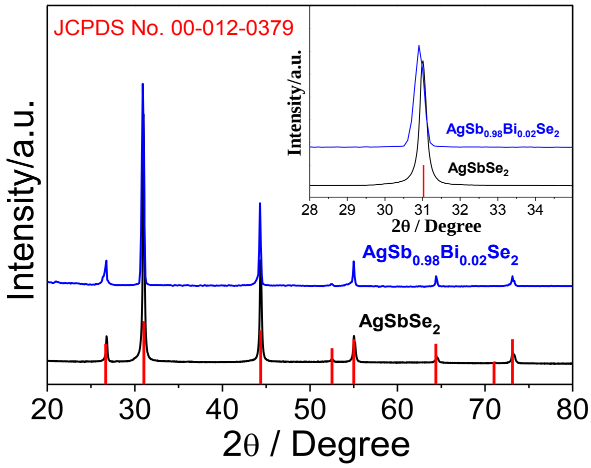

Figure 2.13. XRD of the AgSbSe$_2$ and AgSb$_{0.98}$Bi$_{0.02}$Se$_2$ pellets after hot-press. Inset shows detail of (200) peak.

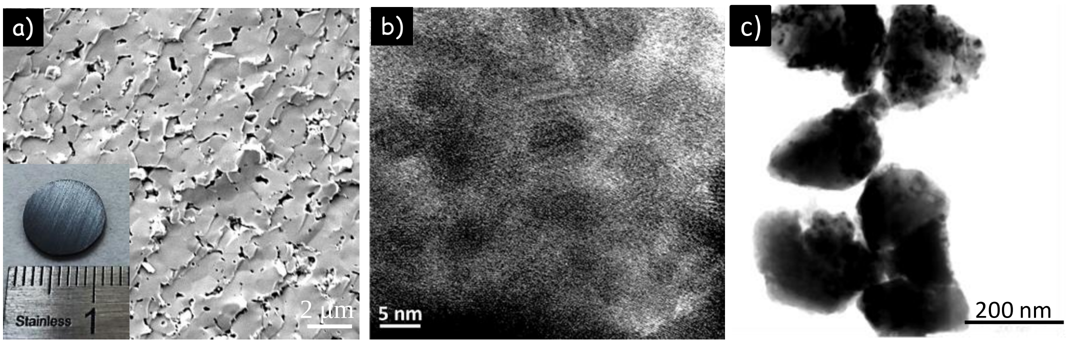

Figure 2.14. a) SEM micrograph of the fractured surface of a AgSbSe$_2$ pellet (inset); b) HRTEM micrograph of the same AgSbSe$_2$ pellet showing several crystal nanodomains; c) Representative TEM micrograph of the nanopowder obtained after grinding a AgSbSe$_2$ pellet after annealing and thermoelectric measurements. Crystal size domains of ~200 nm with nanoinclusions can be observed.

Figures 2.15-18 shows the electrical conductivity (σ), Seebeck coefficient (S), power factor (PF), thermal conductivity (κ), and thermoelectric figure of merit ($ZT=\sigma S^2T/\kappa$) of AgSbSe$_2$ and AgSb$_{0.98}$Bi$_{0.02}$Se$_2$ pellets. Both materials showed a p-type electronic character. AgSbSe$_2$ was characterized by a relatively low σ, which increased from 1380 Sm^{-1} at ambient temperature up to 1700 Sm^{-1} at 600 K. It showed high Seebeck coefficients reaching up to 462 μV/K at 695 K, which relates with its flat valence band maximum and multipeak valence band structure.[16] The introduction of an atomic 0.5% of Bi significantly enhanced the electrical conductivity, which increased from 4520 Sm^{-1} at room temperature to 5970 Sm^{-1} at 618 K in $AgSb_{0.98}Bi_{0.02}Se_2$. These values are slightly above those previously reported for bulk $AgSb_{0.98}Bi_{0.02}Se_2$ produced by solid state methods.[16] With the Bi doping, the Seebeck coefficient decreased to values below 360 µV/K, which is consistent with an increase of carrier concentration. Overall, the $AgSb_{0.98}Bi_{0.02}Se_2$ power factor (PF) was higher than that of $AgSbSe_2$, up to ~0.74 mWm^{-1}K^{-2} at 580 K (Figure 2.15c), and slightly higher than previously reported for bulk $AgSb_{0.98}Bi_{0.02}Se_2$ (Figure 2.15f).[16]

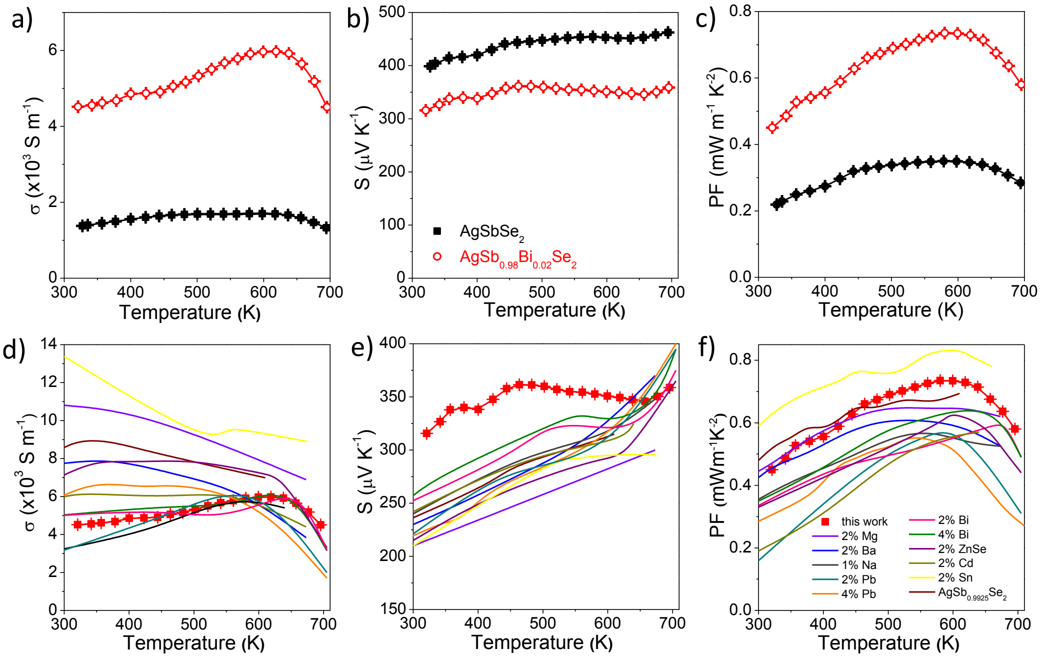

Figure 2.15. Temperature dependence of: a) electric conductivity (σ); b) Seebeck coefficient (S); c) power factor (PF) of $AgSbSe_2$ and $AgSb_{0.98}Bi_{0.02}Se_2$, respectively. d)-f) Comparison of the electrical conductivity (σ), Seebeck coefficient (S) and power factor (PF) of the $AgSb_{0.98}Bi_{0.02}Se_2$ sample measured in the present work with results reported in the literature: Bi^{3+},[16] Pb^{2+},[16] Zn^{2+},[23] Sn^{2+},[42] Cd^{2+},[26] Mg^{2+},[27] Ba^{2+},[27] Na^{+},[28] $AgSb_{0.9925}Se_2$.[25]

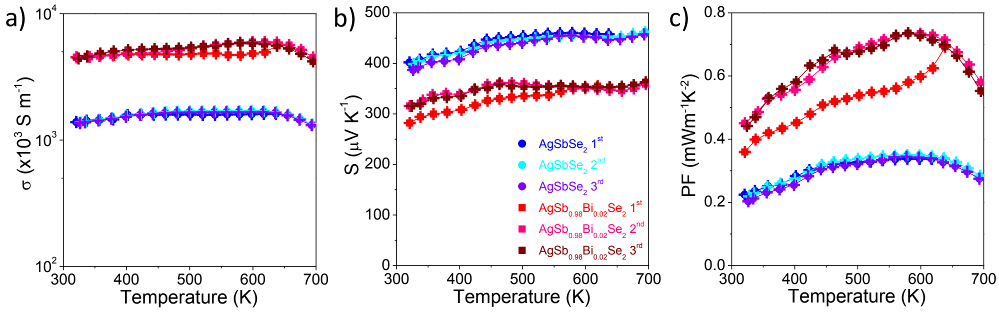

Figure 2.16. Temperature dependence of the electrical conductivity (σ), Seebeck coefficient (S)

and power factor (PF) of $AgSbSe_2$ and $AgSb_{0.98}Bi_{0.02}Se_2$ measured 3 consecutive times during heating up to around 700 K. No pre-stabilization treatment was carried out before the first measurement.

Room temperature Hall measurements provided hole concentrations $p = 4 \pm 2 \times 10^{19}$ cm^{-3} in $AgSbSe_2$ and 5–fold higher for $AgSb_{0.98}Bi_{0.02}Se_2$, $p = 2 \pm 1 \times 10^{20}$ cm^{-3}. As in related Cu_2SbSe_3[43, 44] and $AgSbTe_2$[45-48] compounds, the origin of the p-type conductivity in $AgSbSe_2$ is found in its defect structure and non-stoichiometry, and it is generally associated to Ag vacancies. The introduction of a small amount of an impurity may perturb the $AgSbSe_2$ lattice and modify this defect concentration. In the particular case of substituting Sb^{3+} ions by the larger Bi^{3+} ions a compressive strain is introduced, which we hypothesize can be in part alleviated by a larger density of Ag vacancies and thus an increase of the hole concentration. The confirmation of this hypothesis needs in all cases a careful analysis of the defect formation energies within this compound in the presence of Bi, which is out of the scope of the present work. Besides, the relatively low Hall mobilities measured, 2.5 $cm^2V^{-1}s^{-1}$ and 1.9 $cm^2V^{-1}s^{-1}$ for $AgSbSe_2$ and $AgSb_{0.98}Bi_{0.02}Se_2$, respectively, are consistent with the large degree of disorder, the nanoscale precipitates and the intrinsically large effective mass of holes in this system. The mobility decrease with the introduction of Bi ions is also consistent with the presence of additional point defects scattering charge carriers.

Very low thermal conductivities ($\kappa = \lambda C_p \rho < 0.5$ $Wm^{-1}K^{-1}$) were measured for both $AgSbSe_2$ and $AgSb_{0.98}Bi_{0.02}Se_2$ compounds in the whole studied temperature range of 300 to 700 K (Figure 2.17c). These low thermal conductivities can be explained by an efficient multi-level phonon scattering; that is by nanometer scale precipitates, by the highly disordered lattice and by the strong phonon–phonon interactions from the high degree of anharmonicity of the Sb - Se bonds in this material.[18] In spite of the higher density of defects associated to the Bi presence, thermal conductivities were slightly higher for $AgSb_{0.98}Bi_{0.02}Se_2$ due to the larger contribution from the electronic thermal conductivity κ_e (Figure 2.17d).

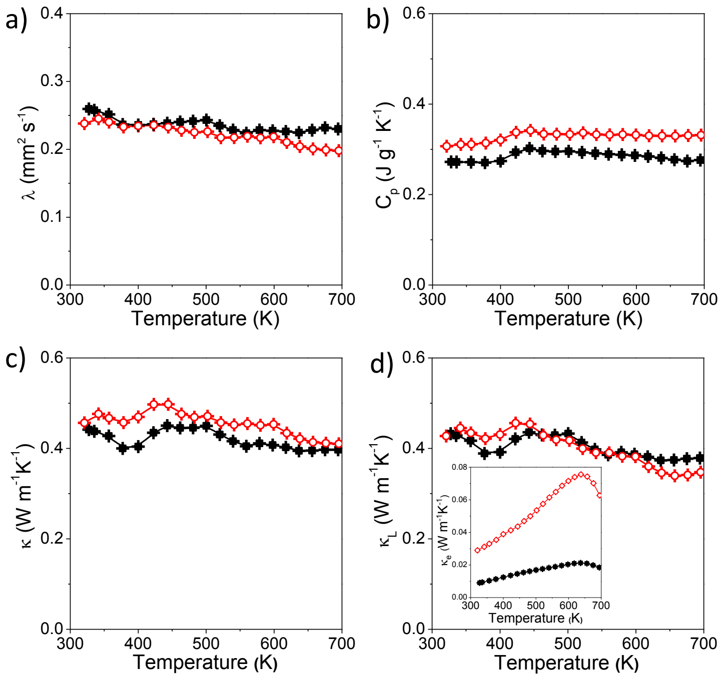

Figure 2.17. Temperature dependence of: a) thermal diffusivity (λ); b) pecific heat capacity (C_p); c) thermal conductivity (κ) and d) thermal conductivity (κ_L) including electronic thermal conductivity (κ_e) in the inset of $AgSbSe_2$ and $AgSb_{0.98}Bi_{0.02}Se_2$, respectively.

As a result, ZT values up to 1.1 at 640 K were obtained for the $AgSb_{0.98}Bi_{0.02}Se_2$ (Figure 2.18), which represents a two-fold increase over pristine $AgSbSe_2$ and is among the best values obtained for a Pb- and Te-free material at this temperature (Table 2.1).

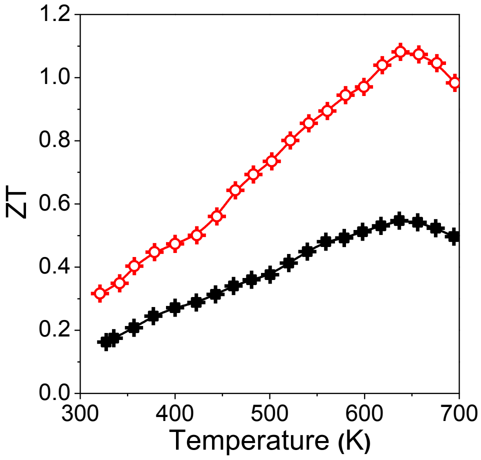

Figure 2.18. Temperature dependence of thermoelectric figure of merit (ZT) of $AgSbSe_2$ and $AgSb_{0.98}Bi_{0.02}Se_2$.

Table 2.1. State-of-art thermoelectric performance values for Te-free Cu- and Ag-based ternary and quaternary chalcogenides and some other Pb- and Te- free compounds at 640 K (except when otherwise specified).

Material	**σ x10^3 Sm^{-1}**	**S µV/K**	**PF mWm^{-1}K^{-2}**	**κ Wm^{-1}K^{-1}**	**ZT**	**Ref.**
$CuFeS_2$	0.33	816	0.23	0.43	0.26 (500 K)	49
$Cu_{0.975}BiSeO$	2.8	228	0.15	0.50	0.19	50
Cu_2GeSe_3	5.2	150	0.12	0.33	0.22	51
Cu_2SnSe_3	6.3	210	0.27	0.68	0.25	34
Cu_2SnSe_3	12	299	1.07	1.91	0.34 (598 K)	52
$Cu_{2.15}Zn_{0.85}GeSe_{3.9}$	30	90	0.24	0.41	0.37	53
$Cu_{2.15}Cd_{0.85}SnSe_{3.9}$	8.2	150	0.19	0.31	0.40	53
$Cu_2Sn_{0.90}In_{0.10}Se_3$	52	140	1.02	1.50	0.44	54
$AgBiSe_{1.98}Cl_{0.02}$	19	-150	0.45	0.46	0.48	55
$Cu_2CdSnSe_4$	27	157	0.66	0.89	0.48	56
$Cu_{2.1}Cd_{0.9}SnSe_4$	21	150	0.47	0.60	0.50	57
$Cu_3Sb_{0.98}Sn_{0.02}Se_4$	24	200	0.96	1.10	0.50 (575 K)	58
$Cu_3Sb_{0.97}Al_{0.03}Se_4$	20	230	1.05	1.08	0.58 (600 K)	59
$Cu_3Sb_{0.975}Sn_{0.025}Se_4$	22	228	1.20	1.22	0.63	60
$CuBi_{0.875}Ba_{0.125}SeO$	27	144	0.56	0.53	0.68	61
$Ag_{0.96}Nb_{0.04}BiSe_2$	15	-200	0.61	0.56	0.70	62
$Cu_3Sb_{0.98}Bi_{0.02}Se_4$	10	325	1.10	0.90	0.70 (600 K)	63
β-Cu_2Se	26	200	1.05	0.90	0.75	64
$AgSb_{0.96}Pb_{0.04}Se_2$	3.5	325	0.37	0.30	0.79	16
β-Zn_4Sb_3	33	183	1.09	0.75	0.80 (550 K)	65
$Cu_3Sb_{0.97}Ge_{0.03}Se_{2.8}S_{1.2}$	23	230	1.22	0.93	0.84	66
$CuAgSe$	10	202	0.41	0.28	0.90 (623 K)	67
$Mm_{0.9}Fe_{3.1}Co_{0.9}Sb_{12}$	75	195	2.85	1.83	0.99	68
$Cu_{11}MnSb_4S_{13}$	28	145	0.58	0.29	1.13 (575 K)	69
$Cu_3Sb_{0.98}Sn_{0.02}Se_4$	32	220	1.54	1.15	0.86	70
$AgSb_{0.99}Na_{0.01}Se_2$	4.8	330	0.52	0.38	0.88	28
$AgBiSe_2$	2.3	400	0.37	0.26	0.90	71
$AgSb_{0.98}Ba_{0.02}Se_2$	4.8	340	0.55	0.37	0.95	27

$AgSb_{0.98}Cd_{0.02}Se_2$	5.4	325	0.57	0.36	0.95	[26]
$AgSb_{0.98}Mg_{0.02}Se_2$	7.4	295	0.64	0.42	0.98	[27]
$AgSb_{0.98}Bi_{0.02}Se_2$	5.6	323	0.58	0.35	1.05	[16]
$AgBi_{0.5}Sb_{0.5}Se_2$	3.3	275	0.25	0.13	1.07 (550 K)	[72]
$AgSbSe_2$–ZnSe	7.0	295	0.61	0.36	1.08	[73]
$AgSb_{0.98}Bi_{0.02}Se_2$	6.0	347	0.72	0.42	1.10	This work
$AgSb_{0.99}Sn_{0.01}Se_2$	9.5	290	0.80	0.45	1.12	[42]
$In_{0.2}Co_4Sb_{12}$	63	-245	3.77	1.95	1.20 (620 K)	[74]
$In_{0.2}Ce_{0.05}Yb_{0.1}Co_4Sb_{12}$	44	-252	2.81	1.45	1.20 (620 K)	[74]
$In_{0.25}Co_4Sb_{12}$	62	-270	4.53	2.17	1.20 (575 K)	[75]
$In_{0.2}Ce_{0.15}Co_4Sb_{12}$	63	-240	3.65	1.63	1.40 (625 K)	[74]
$(Zr_{0.5}Hf_{0.5})_{0.5}Ti_{0.5}NiSn_{0.998}Sb_{0.002}$	67	-300	6.00	2.75	1.40	[76]
$Ti_{0.5}(Zr_{0.5}Hf_{0.5})_{0.5}NiSn_{0.998}Sb_{0.002}$	84	-280	6.56	3.00	1.40	[77]
SnSe	30	280	2.35	0.75	2.0	[78]

2.5 Conclusions

In summary, a scalable colloidal synthesis of monodisperse $AgSbSe_2$ NCs and Bi-doped $AgSb_{1-x}Bi_xSe_2$ NCs was developed. We showed OLA and OA to be present in dynamic exchange at the surface of the NCs, rendering them soluble in non-polar solvents while allowing a kinetic control of their growth. After displacing these surfactants, NCs were used as building blocks to produce 93% relative density nanomaterials. A preliminary optimization of the doping level resulted in $AgSb_{0.98}Bi_{0.02}Se_2$ nanomaterials reaching ZT=1.1 at 640 K. This figure of merit is among the largest values reported for a tellurium-free material in the middle temperature range, with the additional advantage of the low-cost and convenient solution processability of the materials and related devices.

2.6 References

1. Abdelghany, A.; Elsayed, S.; Abdelwahab, D.; El Ela, A. A.; Mousa, N. *Materials chemistry and physics* **1996,** 44, (3), 277-280.
2. Patel, A.; Lakshminarayana, D.; Rao, K. *Thin Solid Films* **1982,** 94, (1), 51-57.
3. Patel, A.; Lakshminarayana, D. *Thin Solid Films* **1982,** 98, (1), 59-63.
4. Wang, K.; Steimer, C.; Wuttig, M. *Journal of optoelectronics and advanced materials* **2007,** 9, (7), 2008.
5. Soliman, H.; Abdel-Hady, D.; Ibrahim, E. *Journal of Physics: Condensed Matter* **1998,** 10, (4), 847.
6. Wang, K.; Steimer, C.; Detemple, R.; Wamwangi, D.; Wuttig, M. *Applied Physics A* **2005,** 81, (8), 1601-1605.
7. Wojciechowski, K.; Schmidt, M. *Physical Review B* **2009,** 79, (18), 184202.
8. Geller, S.; Wernick, J. *Acta Crystallographica* **1959,** 12, (1), 46-54.
9. Wernick, J.; Benson, K. *Journal of Physics and Chemistry of Solids* **1957,** 3, (1), 157- 159.
10. Wolfe, R.; Wernick, J.; Haszko, S. *Journal of Applied Physics* **1960,** 31, (11), 1959-1964.
11. Aggarwal, L.; Sekhon, J. S.; Guin, S. N.; Arora, A.; Negi, D. S.; Datta, R.; Biswas, K.; Sheet, G. *Applied Physics Letters* **2014,** 105, (11), 113903.
12. Quarez, E.; Hsu, K.-F.; Pcionek, R.; Frangis, N.; Polychroniadis, E.; Kanatzidis, M. G. *Journal of the American Chemical Society* **2005,** 127, (25), 9177-9190.
13. Hoang, K.; Mahanti, S.; Salvador, J. R.; Kanatzidis, M. G. *Physical Review Letters* **2007,** 99, (15), 156403.
14. Salimi, M.; Hashemifar, S. J. *Journal of Alloys and Compounds* **2015,** 650, 143-148.
15. Wojciechowski, K.; Tobola, J.; Schmidt, M.; Zybala, R. *Journal of Physics and Chemistry of Solids* **2008,** 69, (11), 2748-2755.
16. Guin, S. N.; Chatterjee, A.; Negi, D. S.; Datta, R.; Biswas, K. *Energy & Environmental Science* **2013,** 6, (9), 2603-2608.
17. Garza, J.; Shaji, S.; Rodriguez, A.; Roy, T. D.; Krishnan, B. *Applied Surface Science* **2011,** 257, (24), 10834-10838.
18. Asokan, T. N.; Urmila, K.; Jacob, R.; Philip, R. R.; Okram, G.; Ganesan, V.; Pradeep, B. *Journal of Semiconductors* **2014,** 35, (5), 052001.
19. González, J.; Shaji, S.; Avellaneda, D.; Castillo, A.; Roy, T. D.; Krishnan, B. *Materials Research Bulletin* **2013,** 48, (5), 1939-1945.
20. Bindu, K.; Nair, M.; Roy, T. D.; Nair, P. *Electrochemical and Solid-State Letters* **2006,** 9, (6), G195-G199.
21. Bindu, K.; Campos, J.; Nair, M.; Sanchez, A.; Nair, P. *Semiconductor Science and*

Technology **2005,** 20, (6), 496.

22. Wojciechowski, K.; Schmidt, M.; Tobola, J.; Koza, M.; Olech, A.; Zybała, R. *Journal of Electronic Materials* **2010,** 39, (9), 2053-2058.
23. Guin, S. N.; Negi, D. S.; Datta, R.; Biswas, K. *Journal of Materials Chemistry A* **2014,** 2, (12), 4324-4331.
24. Kim, H. S.; Liu, W.; Chen, G.; Chu, C.-W.; Ren, Z. *Proceedings of the National Academy of Sciences* **2015,** 112, (27), 8205-8210.
25. Guin, S. N.; Biswas, K. *Journal of Materials Chemistry C* **2015,** 3, (40), 10415-10421.
26. Guin, S. N.; Chatterjee, A.; Biswas, K. *RSC Advances* **2014,** 4, (23), 11811-11815.
27. Liu, Z.; Shuai, J.; Geng, H.; Mao, J.; Feng, Y.; Zhao, X.; Meng, X.; He, R.; Cai, W.; Sui, J. *ACS applied materials & interfaces* **2015,** 7, (41), 23047-23055.
28. Cai, S.; Liu, Z.; Sun, J.; Li, R.; Fei, W.; Sui, J. *Dalton Transactions* **2015,** 44, (3), 1046-1051.
29. Cook, B. A.; Kramer, M. J.; Harringa, J. L.; Han, M. K.; Chung, D. Y.; Kanatzidis, M. G. *Advanced Functional Materials* **2009,** 19, (8), 1254-1259.
30. Levin, E.; Bud'Ko, S.; Schmidt‐Rohr, K. *Advanced Functional Materials* **2012,** 22, (13), 2766-2774.
31. Talapin, D. V.; Lee, J.-S.; Kovalenko, M. V.; Shevchenko, E. V. *Chemical reviews* **2009,** 110, (1), 389-458.
32. Kovalenko, M. V.; Manna, L.; Cabot, A.; Hens, Z.; Talapin, D. V.; Kagan, C. R.; Klimov, V. I.; Rogach, A. L.; Reiss, P.; Milliron, D. J. *ACS nano* **2015,** 9, (2), 1012-1057.
33. Ibáñez, M.; Zamani, R.; Gorsse, S.; Fan, J.; Ortega, S.; Cadavid, D.; Morante, J. R.; Arbiol, J.; Cabot, A. *ACS nano* **2013,** 7, (3), 2573-2586.
34. Ibáñez, M.; Cadavid, D.; Anselmi-Tamburini, U.; Zamani, R.; Gorsse, S.; Li, W.; López, A. M.; Morante, J. R.; Arbiol, J.; Cabot, A. *Journal of Materials Chemistry A* **2013,** 1, (4), 1421-1426.
35. Ibáñez, M.; Korkosz, R. J.; Luo, Z.; Riba, P.; Cadavid, D.; Ortega, S.; Cabot, A.; Kanatzidis, M. G. *Journal of the American Chemical Society* **2015,** 137, (12), 4046-4049.
36. Cadavid, D.; Ibáñez, M.; Shavel, A.; Durá, O. J.; de la Torre, M. L.; Cabot, A. *Journal of Materials Chemistry A* **2013,** 1, (15), 4864-4870.
37. Connell, M. A.; Bowyer, P. J.; Bone, P. A.; Davis, A. L.; Swanson, A. G.; Nilsson, M.; Morris, G. A. *Journal of Magnetic Resonance* **2009,** 198, (1), 121-131.
38. Sinnaeve, D. *Concepts in Magnetic Resonance Part A* **2012,** 40, (2), 39-65.
39. Zhou, B.; Li, M.; Wu, Y.; Yang, C.; Zhang, W. H.; Li, C. *Chemistry–A European Journal* **2015,** 21, (31), 11143-11151.

40. Owen, J. *Science* **2015,** 347, (6222), 615-616.
41. Hens, Z.; Martins, J. C. *Chemistry of Materials* **2013,** 25, (8), 1211-1221.
42. Li, D.; Qin, X.; Zou, T.; Zhang, J.; Ren, B.; Song, C.; Liu, Y.; Wang, L.; Xin, H.; Li, J. *Journal of Alloys and Compounds* **2015,** 635, 87-91.
43. Li, X.; Li, D.; Xin, H.; Zhang, J.; Song, C.; Qin, X. *Journal of Alloys and Compounds* **2013,** 561, 105-108.
44. Zhang, Y.; Xi, L.; Wang, Y.; Zhang, J.; Zhang, P.; Zhang, W. *Computational Materials Science* **2015,** 108, 239-249.
45. Ye, L.-H.; Hoang, K.; Freeman, A.; Mahanti, S.; He, J.; Tritt, T. M.; Kanatzidis, M. *Physical Review B* **2008,** 77, (24), 245203.
46. Du, B.; Li, H.; Tang, X. *Journal of Alloys and Compounds* **2011,** 509, (5), 2039-2043.
47. Jovovic, V.; Heremans, J. *Physical Review B* **2008,** 77, (24), 245204.
48. Mohanraman, R.; Sankar, R.; Chou, F.-C.; Lee, C.-H.; Iizuka, Y.; Muthuselvam, I. P.; Chen, Y.-Y. *APL Materials* **2014,** 2, (9), 096114.
49. Liang, D.; Ma, R.; Jiao, S.; Pang, G.; Feng, S. *Nanoscale* **2012,** 4, (20), 6265-6268.
50. Liu, Y.; Zhao, L.-D.; Liu, Y.; Lan, J.; Xu, W.; Li, F.; Zhang, B.-P.; Berardan, D.; Dragoe, N.; Lin, Y.-H. *Journal of the American Chemical Society* **2011,** 133, (50), 20112-20115.
51. Ibáñez, M.; Zamani, R.; Li, W.; Cadavid, D.; Gorsse, S. p.; Katcho, N. A.; Shavel, A.; López, A. M.; Morante, J. R.; Arbiol, J. *Chemistry of Materials* **2012,** 24, (23), 4615-4622.
52. Song, J.-M.; Liu, Y.; Niu, H.-L.; Mao, C.-J.; Cheng, L.-J.; Zhang, S.-Y.; Shen, Y.-H. *Journal of Alloys and Compounds* **2013,** 581, 646-652.
53. Ibáñez, M.; Zamani, R.; LaLonde, A.; Cadavid, D.; Li, W.; Shavel, A.; Arbiol, J.; Morante, J. R.; Gorsse, S.; Snyder, G. J. *Journal of the American Chemical Society* **2012,** 134, (9), 4060-4063.
54. Shi, X.; Xi, L.; Fan, J.; Zhang, W.; Chen, L. *Chemistry of Materials* **2010,** 22, (22), 6029-6031.
55. Guin, S. N.; Srihari, V.; Biswas, K. *Journal of Materials Chemistry A* **2015,** 3, (2), 648-655.
56. Fan, F.-J.; Yu, B.; Wang, Y.-X.; Zhu, Y.-L.; Liu, X.-J.; Yu, S.-H.; Ren, Z. *Journal of the American Chemical Society* **2011,** 133, (40), 15910-15913.
57. Liu, M. L.; Chen, I. W.; Huang, F. Q.; Chen, L. D. *Advanced Materials* **2009,** 21, (37), 3808-3812.
58. Wu, Y.; Qiao, X.; Fan, X.; Zhang, X.; Cui, S.; Wan, J. *Journal of Nanoparticle Research* **2015,** 17, (7), 285.
59. Li, Y.; Qin, X.; Li, D.; Li, X.; Liu, Y.; Zhang, J.; Song, C.; Xin, H. *Rsc Advances*

2015, 5, (40), 31399-31403.

60. Yang, C.; Huang, F.; Wu, L.; Xu, K. *Journal of Physics D: Applied Physics* **2011,** 44, (29), 295404.
61. Li, J.; Sui, J.; Pei, Y.; Barreteau, C.; Berardan, D.; Dragoe, N.; Cai, W.; He, J.; Zhao, L.-D. *Energy & Environmental Science* **2012,** 5, (9), 8543-8547.
62. Pan, L.; Bérardan, D.; Dragoe, N. *Journal of the American Chemical Society* **2013,** 135, (13), 4914-4917.
63. Li, X.; Li, D.; Xin, H.; Zhang, J.; Song, C.; Qin, X. *Journal of Alloys and Compounds* **2013,** 561, 105-108.
64. Liu, H.; Shi, X.; Xu, F.; Zhang, L.; Zhang, W.; Chen, L.; Li, Q.; Uher, C.; Day, T.; Snyder, G. J. *Nature materials* **2012,** 11, (5), 422.
65. Toberer, E. S.; Rauwel, P.; Gariel, S.; Taftø, J.; Snyder, G. J. *Journal of materials chemistry* **2010,** 20, (44), 9877-9885.
66. Skoug, E. J.; Cain, J. D.; Morelli, D. T. *Applied Physics Letters* **2011,** 98, (26), 261911.
67. Han, C.; Sun, Q.; Cheng, Z. X.; Wang, J. L.; Li, Z.; Lu, G. Q.; Dou, S. X. *Journal of the American Chemical Society* **2014,** 136, (50), 17626-17633.
68. Dahal, T.; Gahlawat, S.; Jie, Q.; Dahal, K.; Lan, Y.; White, K.; Ren, Z. *Journal of Applied Physics* **2015,** 117, (5), 055101.
69. Heo, J.; Laurita, G.; Muir, S.; Subramanian, M. A.; Keszler, D. A. *Chemistry of Materials* **2014,** 26, (6), 2047-2051.
70. Li, D.; Li, R.; Qin, X.-Y.; Song, C.-J.; Xin, H.-X.; Wang, L.; Zhang, J.; Guo, G.-l.; Zou, T.-H.; Liu, Y.-F. *Dalton Transactions* **2014,** 43, (4), 1888-1896.
71. Xiao, C.; Qin, X.; Zhang, J.; An, R.; Xu, J.; Li, K.; Cao, B.; Yang, J.; Ye, B.; Xie, Y. *Journal of the American Chemical Society* **2012,** 134, (44), 18460-18466.
72. Xiao, C.; Xu, J.; Cao, B.; Li, K.; Kong, M.; Xie, Y. *Journal of the American Chemical Society* **2012,** 134, (18), 7971-7977.
73. Mohanraman, R.; Sankar, R.; Boopathi, K. M.; Chou, F.-C.; Chu, C.-W.; Lee, C.-H.; Chen, Y.-Y. *Journal of Materials Chemistry A* **2014,** 2, (8), 2839-2844.
74. Biswas, K.; Good, M. S.; Roberts, K. C.; Subramanian, M.; Hendricks, T. J. *Journal of Materials Research* **2011,** 26, (15), 1827-1835.
75. He, T.; Chen, J.; Rosenfeld, H. D.; Subramanian, M. *Chemistry of materials* **2006,** 18, (3), 759-762.
76. Sakurada, S.; Shutoh, N. *Applied Physics Letters* **2005,** 86, (8), 082105.
77. Shutoh, N.; Sakurada, S. *Journal of alloys and compounds* **2005,** 389, (1-2), 204-208.
78. Zhao, L.-D.; Tan, G.; Hao, S.; He, J.; Pei, Y.; Chi, H.; Wang, H.; Gong, S.; Xu, H.; Dravid, V. P. *Science* **2015**, 3749.

Chapter 3

Solution-Based Synthesis and Processing of Sn- and Bi-Doped Cu_3SbSe_4 Nanocrystals, Nanomaterials and Ring-Shaped Thermoelectric Generators

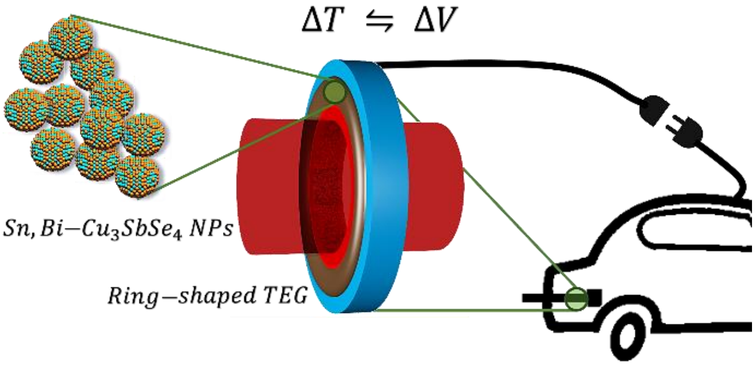

“*Thermoelectric devices with a ring architecture, made of an efficient and environmentally-friendly nanomaterial, Sn- and Bi-doped* Cu_3SbSe_4*, for energy recovery from exhaust pipes*”

3.1 Abstract

Copper-based chalcogenides that comprise abundant, low-cost, and environmental friendly elements are excellent materials for a number of energy conversion applications, including photovoltaics, photocatalysis, and thermoelectrics (TE). In such applications, the use of solution-processed nanocrystal (NC) to produce thin films or bulk nanomaterials has associated several potential advantages, such as high material yield and throughput, and composition control with unmatched spatial resolution and cost. Here we report on the production of Cu_3SbSe_4 (CASe) NCs with tuned amounts of Sn and Bi dopants. After proper ligand removal, as monitored by nuclear magnetic resonance and infrared spectroscopies, these NCs were used to produce dense CASe bulk nanomaterials

for solid state TE energy conversion. By adjusting the amount of extrinsic dopants, dimensionless TE figures of merit (ZT) up to 1.26 at 673 K were reached. Such high ZT values are related to an optimized carrier concentration by Sn doping, a minimized lattice thermal conductivity due to efficient phonon scattering at point defects and grain boundaries, and to an increase of the Seebeck coefficient obtained by a modification of the electronic band structure with the Bi doping. Nanomaterials were further employed to fabricate ring-shaped TE generators to be coupled to hot pipes and which provided 20 mV and 1 mW per TE element when exposed to a 160 °C temperature gradient. The simple design and good thermal contact associated with the ring geometry and the potential low cost of the material solution processing may allow the fabrication of TE generators with short payback times.

3.2 Introduction

Tetrahedrally coordinated copper-based chalcogenides have emerged as realistic alternative materials for a number of energy conversion applications, including photovoltaics, photocatalysis and thermoelectricity.[1-7] Beyond the best studied ternary and quaternary Cu-Ga-In,[8-10] Cu-Zn-Sn,[11-15] Cu-Zn-Ge[16, 17] compounds, some I−V−VI tetrahedrally coordinated semiconductors also offer excellent functional properties, but remain largely underexplored. In particular, Cu_3SbSe_4 (CASe) is a semiconductor with a relatively small direct band gap of 0.3 eV and a defect-related carrier density on the order of 10^{18} cm^{-3} at ambient temperature.[18] It crystallizes in a zinc blende-type tetragonal superstructure that can be viewed as a three-dimensional Cu-Se framework of distorted [$CuSe_4$] tetrahedra with inserted one dimensional array of [$SbSe_4$] tetrahedra. It features two Cu sites with different Cu-Se bond lengths. The valence band maximum (VBM) is mainly formed by a hybridization of Cu-3d and Se-4p states, while the conduction band minimum (CBM) has a strong contribution from the Sb-5s and Se-4p hybridization. In such structure, the Cu-Se framework provides avenues for hole transport with relatively high mobility, up to 135 $cm^2V^{-1}s^{-1}$ for undoped and

49 $cm^2V^{-1}s^{-1}$ for highly doped materials.[19-21] Furthermore, such a complex lattice structure is not effective for phonon propagation, resulting in low thermal conductivities. The high hole mobility and the low phonon mean free path, combined with proper electronic band structure (including a large degeneracy at the VBM)[19, 20] render CASe an excellent thermoelectric (TE) material. However, to maximize its TE performance, it is strictly necessary to optimize its charge carrier concentration either by adjusting the density of intrinsic defects that control hole concentration or by introducing an extrinsic p-type dopant, preferably in the non-conducting sub-lattice, i.e. by substituting Sb, to minimize the adverse effects on the hole mobility.

Nanoparticle-based bottom-up strategies offer several advantages to produce thin films and bulk nanostructured materials for a wide range of applications. From an engineering viewpoint, the unmatched compositional and interfacial control makes this route very robust and versatile, allowing to establish structure-property relationships and subsequently enabling the rational design of superior materials. From a commercial viewpoint, facile and inexpensive solution synthesis and processing allows for a low-cost and high throughput production with high material yields.[22-27] However, two major challenges in this technology are the incorporation of controlled amounts of electronic dopants and the removal of organics. Both of them are critical to optimize transport properties within such nanomaterials.[26]

Thus far, colloidal Cu_3SbS_4[28-30] and $Cu_{12}Sb_4S_{13}$[29-31] nanocrystals (NCs) have been primarily used for photoelectrochemical studies. Few reports have also detailed the production of bulk nanostructured CASe.[32-34] However bottom-up strategies to cost-effectively produce efficient CASe NCs, nanomaterials and CASe-based devices remain to be demonstrated. Here, we report a solution-based scalable synthesis approach to produce several grams of monodisperse CASe NCs doped with controlled amounts of Sn and Bi. We demonstrate their bottom-up processing into bulk nanostructured materials with high relative density and excellent TE performances. We further use this material to fabricate ring-shaped TE devices, which provide improved thermal contact for heat recovery from pipes.

3.3 Experimental Section

Chemicals and solvents: Copper (I) chloride (CuCl, ≥99%), antimony (III) chloride ($SbCl_3$, 99%), bismuth (III) acetate ($Bi(CH_3CO_2)_3$, 99.99%), selenium powder (Se, 99.5%), ammonium thiocyanate (NH_4SCN, ≥99%), dodecanethiol (DDT, 98%), 1-octadecene (ODE, technical grade 90%), oleic acid (OA, technical grade 99%), decanoic acid (DAc, ≥98%), and oleylamine (OLA, technical grade 70%) were purchased from Sigma Aldrich. Tin (II) chloride ($SnCl_2$, 98%) was purchased from Strem. Analytical grade methanol, ethanol and chloroform were obtained from various sources. All chemicals were used as received without further purification.

Se precursor solution: Se powder (23.69 g, 300 mmol) was dissolved in 300 ml OLA and 300 ml DDT at room temperature, cycled between vacuum and Ar to remove oxygen, and then stirred under Ar atmosphere until Se powder was completely dissolved.

Synthesis of Cu_3SbSe_4 NCs: In a typical synthesis, 10.0 mmol CuCl, 4.0 mmol $SbCl_3$, 15 ml OLA, 10 ml OA and 100 ml ODE were mixed in a 500 ml three-neck flask and stirred for 20 min at room temperature. The solution was kept at 130 °C under vacuum and vigorous stirring for 30 min, and then heated to 180 °C. The colour of the solution changed from light green to yellowish-brown at ~170 °C. At 180 °C, 50 ml of the Se precursor solution was swiftly injected and the color of the solution changed immediately from brown to dark green, indicating the nucleation and subsequent growth of CASe NCs. After injection, the temperature of the reaction mixture dropped to around 165 °C, but it was allowed to recover to 180 °C. The overall reaction time after recovering to 180 °C was 30 min. Then the sample was rapidly cooled to room temperature using a water bath. NCs were collected by precipitation with ethanol. The final product could be dispersed in relatively non-polar solvents such as toluene or chloroform, forming a stable, dark-green dispersion (inset of Figure 3.2b). For subsequent chemical, structural and functional characterization, NCs were purified by multiple precipitation (6000 rpm for 5 min) and redispersion steps using chloroform as solvent and ethanol as non-solvent. The resulting powder was re-suspended in chloroform and stored for subsequent characterization and use. This synthesis protocol was optimized to produce more than 2.0 g of NCs per batch (Figure 3.2a), which was the amount required for a complete characterization of the material at the laboratory scale, including the fabrication of a ring-shaped prototype device.

Synthesis of $Cu_3Sb_{1-x}Sn_xSe_4$, $Cu_3Sb_{1-x}Bi_xSe_4$ and $Cu_3Sb_{1-x-y}Sn_xBi_ySe_4$ NCs: $Cu_3Sb_{1-x}Sn_xSe_4$, $Cu_3Sb_{1-x}Bi_xSe_4$ and $Cu_3Sb_{1-x-y}Sn_xBi_ySe_4$ NCs were produced following the above procedure but replacing the desired amount of $SbCl_3$ by $SnCl_2$ and/or $Bi(CH_3CO_2)_3$.

Ligand displacement: Cu_3SbSe_4, $Cu_3Sb_{1-x}Sn_xSe_4$, $Cu_3Sb_{1-x}Bi_xSe_4$ and $Cu_3Sb_{1-x-y}Sn_xBi_ySe_4$ NCs produced in one batch were divided into 6 centrifuge tubes. In each of the tubes, containing ~350 mg in 10 ml of chloroform, 2 ml of a 50 mM NH_4SCN solution in acetone was added. Then the solution was shacked during 1 − 2 min to displace the organic ligands attached to the NC surface, followed by precipitation of the NCs by centrifugation. This process was repeated several times, adding chloroform and NH_4SCN in each step. Finally, NCs were precipitated and dried under vacuum to obtain a fine powder.

Bulk nanomaterial consolidation: The dried NCs were loaded into a graphite die and compacted into pellets (Ø10 mm × ~1.5 mm). The process was carried out in Ar atmosphere, using a custom-made hot press to simultaneously apply a pressure of 70 MPa and a temperature of 370 − 380 °C during 30 min. In this system, the heat was provided by an induction coil operated at 30 − 80 KHz and it was applied directly to a graphite die acting as a susceptor. Fast heating ramps of 20 °C s^{-1} were reached by this method with a 25 kW induction heater. The relative densities of all the pressed pellets were measured by the Archimedes' method and found to be ~90% of the theoretical values.

Ring thermoelectric generators: TE rings with an overall internal diameter of 28 mm and an external diameter of 39 mm were fabricated by placing the dried NCs between two concentric copper rings with 2 mm in thickness and hot-pressing the material at a temperature of 370-380 °C during 30 min and 20 MPa of pressure using a custom-made die.

Structural and chemical characterization: Crystallographic phases were characterized by X-ray diffraction (XRD, 2θ angle: 20° to 80°; scanning rate: 1°/min) on a Bruker AXS D8 ADVANCE X-ray diffractometer with Cu–Kα radiation (λ= 0.15406 Å). X-ray photoelectron spectroscopy (XPS) was performed on a VG ESCA scientific theta probe spectrometer in constant analyser energy mode with a pass energy of 28 eV and Al K α (1486.6 eV) radiation as the excitation source. Size and shape of initial NCs were examined by transmission electron microscopy (TEM) using a ZEISS LIBRA 120, operating at 120 kV. In depth TEM analyses were performed in a FEI Tecnai F20 microscope operated at 200 keV with a point to point resolution of 0.19 nm. High-resolution TEM (HRTEM) analyses were combined with high angle annular dark field (HAADF) scanning TEM (STEM). We also examined elemental composition using spectroscopy analyses with nanometer resolution by means of electron energy loss spectroscopy (EELS) and energy dispersive X-ray spectroscopy (EDX) with a Gatan Quantum EELS and an Oxford EDX detector, respectively, both coupled to the FEI TEM. The grain size and morphology of the hot-pressed materials was characterized using field-emission scanning electron microscopy (SEM, Auriga Zeiss) at 5.0 kV. The overall material composition was analyzed by an Oxford energy dispersive X-ray spectrometer (EDX) attached to the Zeiss Auriga SEM and by optical emission spectroscopy by means of inductively coupled plasma (ICP) on a Perkin Elmer Optima 3200 RL system. Fourier-transform infrared spectroscopy (FTIR) were acquired by using an Alpha Bruker FTIR spectrometer with the platinum attenuated total reflectance (ATR) single reflection module.

Nuclear Magnetic Resonance (NMR): NMR measurements were recorded on a Bruker Avance III Spectrometer operating at a ^{1}H frequency of 500.13 MHz and equipped with a BBI-Z probe. The sample temperature was set to 298.2 K. One dimensional (1D) 1H and 2D NOESY (Nuclear Overhauser Effect Spectroscopy) spectra were acquired using standard pulse sequences from the Bruker library; zg and noesygpphpp respectively. For the quantitative 1D ^{1}H measurements, 64k data points were sampled with the spectral width set to 16 ppm and a relaxation delay of 30 sec. The NOESY mixing time was set to 300 ms, with 2048 data points sampled in the direct dimension for 512 data points in the indirect dimension, with the spectral width set to 11.5 ppm. For 2D processing, the spectra were zero filled to a 4096 × 2048 real data matrix, followed by multiplication with squared cosine bell function in both dimensions prior to Fourier transformation. The 1D spectra were apodized with an exponential window function. Concentrations were obtained using the Digital ERETIC method. Diffusion measurements (2D DOSY) were performed using a double stimulated echo sequence (dstegp2s)[35] for convection compensation and with monopolar gradient pulses.[35] Smoothed rectangle gradient pulse shapes were used throughout. The gradient strength was varied linearly from 2-95% of the probe's maximum value (calibrated at 50.2 G/cm) in 64 steps, with the gradient pulse duration and diffusion delay optimized to ensure a final attenuation of the signal in the final increment of less than 10% relative to the first increment. The diffusion coefficients were obtained by fitting the Stejskal-Tanner (ST) equation to the signal intensity decay. For the pulse sequence at hand, the appropriate ST equation is: [36]

$$I = I_0 e^{-(\gamma \delta g \xi)^2 D(\Delta - 0.6\delta)} \tag{1}$$

with the gyromagnetic ratio of the observed 1H nucleus γ, the gradient pulse length δ, the gradient strength g, the diffusion time Δ and the diffusion coefficient D. The shape factor ξ depends on the gradient shape but this is usually already corrected for in the gradient strength value by the Bruker software, TOPSPIN. The ST equation for other pulse programs is only slightly different and the impact on the diffusion coefficient is very small in the case of long diffusion times (Δ>250 ms). In a real DOSY experiment, values of Δ and δ are set while varying g to derive the decay curve.[36]

Thermoelectric property measurements: Seebeck coefficients were measured using a static DC method. Electrical resistivity data was obtained by a standard four-probe method. Both the Seebeck coefficient and the electrical resistivity were measured simultaneously in a LSR-3 LINSEIS system in the temperature range between room temperature and 673 K, under helium atmosphere. At each temperature 3 measurements were generally taken. Taking into account the system accuracy and the measurement precision, we estimate an error of ca. 4 % in the measurement of the electrical conductivity and Seebeck coefficient. The thermal conductivity was calculated by $\kappa = \lambda C_p\rho$, where λ is the thermal diffusivity, C_p is the heat capacity, and ρ is the mass density of the specimen. A XFA 600 Xenon Flash apparatus from Linseis was used to determine the thermal diffusivities of the samples with an estimated error of 5%. The specific heat (C_p) was measured by means of the differential scanning calorimeter method (DSC model T2000 TA Instruments) with an associated error of ca. 2 %. The density (ρ) values used here were calculated using the Archimedes' method with a measurement error of ca. 2 %.

Hall measurement: Hall carrier concentrations and mobilities at room temperature were measured using a magnetic field of 2 T with a PPMS-9T (Quantum Design Inc., USA). Values reported correspond to the average of 5 consecutive measurements, from which an error of ca. 10 % was estimated.

Device test: TE rings were tested in a custom-made test station. Temperature was monitored by two thermocouples attached at the copper electrodes and the open circuit voltage was measured by a Keithley 2400. A heating cartridge within a cylindrical metal block was used to raise the temperature of the internal part of the ring, while the external part of the ring was kept at lower temperature by means of TE coolers. The maximum temperature reached at the hot side was 250 °C. At this point the temperature at the cold side was 90 °C, what provided a maximum temperature gradient of 160 °C.

Density Functional Theory (DFT): It is well known that common DFT methods fail to correctly predict the bandgap.[37, 38] Unfortunately, accurate methods such as screened hybrid functional or quasi particle energy calculations are extremely time-consuming and computationally expensive.[37] D. Do *et al.* carried out electronic structure calculations for Cu_3SbSe_4 using GGA, GGA+U, m-BJ exchange potential and HSE06 exchange-correlation potential.[39-41] Only bandgap values calculated by using HSE06 and GGA+U were in agreement with experimental values (0.1 − 0.4 eV),[42, 43] and a large effective value of U (U_{eff} = 15 eV) was necessary to get an accurate bandgap. Based on these results and to minimize computational cost, total energy calculations were carried out using the GGA+U approach. The PBE exchange correlation functional,[44] along to the formalism proposed by Dudared *et al.* were applied.[45] We use U_{eff} = 15 eV for the Cu-*3d* states. Total energy calculations were carried out with the plane-wave based Vienna *ab initio* simulation package (VASP),[46, 47] along to projector augmented wave (PAW) potentials to represent the inert core electrons.[48, 49] We used a plane-wave energy cutoff of 400 eV, an energy convergence criterion of 10^{-4} eV, and a Methfessel-Paxton first-order scheme with 0.1 eV of smearing to extract the occupations of Kohn-Sham eigenvalues.[50] For the Brillouin zone integration, we used a 12 × 12 × 12 Monkhorst-Pack scheme k-point mesh.[51] All the calculations were performed with the experimental lattice parameters of the native compound. The model system Cu_3SbSe_4 was studied through a tetragonal unit cell with 64 atoms ($Cu_{24}Sb_8Se_{32}$). Structures derived from Cu_3SbSe_4 due to the substitution with Bi or Sn were obtained by replacing one Sb atom by one Bi or Sn atom. In this way, the doping concentration was equal to x = 0.125, which is similar to the largest values experimentally produced and measured (x = 0.10). The transport properties were calculated using a semi-classical solution based on Boltzmann's transport theory within the constant scattering time and the rigid band approximations using the BoltzTraP code.[52]

Influence of the minority carriers on the Seebeck coefficient: The measurement of the TE parameters from DFT calculations did not take into account the effect of the minority carriers. This effect becomes important as the temperature increases and more carriers of each type are thermally generated, eventually reaching densities comparable to that of the doping level.

To qualitatively determine the influence of the thermally generated charge carriers on the Seebeck coefficient, we calculated the Seebeck coefficient for holes and electrons using the expressions:

$$S_e = -\frac{8\pi^2\kappa_B^2}{3eh^2}\left(\frac{\pi}{3n}\right)^{2/3} m_e^* T \tag{2}$$

$$S_e = -\frac{8\pi^2\kappa_B^2}{3eh^2}\left(\frac{\pi}{3p}\right)^{2/3} m_h^* T \tag{3}$$

where K_B is the Boltzmann constant, e is the electron charge, h is the Plank constant and n, p and m_e^* are the charge carrier concentration and effective masses for electrons and holes.

We considered the following charge carrier concentrations:

$$\mathrm{n} = n_i = \sqrt{M_c M_v} e^{-E_g/2K_BT} \tag{4}$$

$$p = p_o + p_i = p_o + n_i \tag{5}$$

where n_i and p_i are the thermally generated charge carrier concentations, is the hole concentration associated to the doping (which we consider independent of temperature) that we could approximate to the value measured at ambient temperature by Hall effect, E_g is the semiconductor band gap and M_c and M_v are the densities of states at the CBM and VBM, respectively. We approximate the values of M_c and M_v to:

$$M_c = 2\,(\frac{2\pi m_e^* K_B T}{h^2})^{3/2} \tag{6}$$

$$M_v = 2\,(\frac{2\pi m_h^* K_B T}{h^2})^{3/2} \tag{7}$$

Then we calculate the Seebeck coefficient using:

$$\mathrm{S} = \frac{S_n\sigma_n + S_p\sigma_p}{\sigma_n + \sigma_p} \tag{8}$$

with

$$\sigma_n = en\mu_n \tag{9}$$

$$\sigma_p = ep\mu_p \tag{10}$$

In our calculations, we took: $\mu_n = 2\mu_p$ and used the values of E_g, m_e^* and m_h^* obtained from DFT calculations. Overall this calculation cannot be used to obtain a quantitative fitting to the experimental data due to the many approximations used. However, we believe it gives a useful qualitative view of the influence of the thermally generated carriers on the Seebeck coefficient.

3.4 Results and discussion

CASe NCs were produced from copper chloride, antimony chloride and selenium powder dissolved in OLA and DDT, as detailed in the experimental part. This synthesis protocol enabled a high batch-to-batch reproducibility and a 94% material yield. Figure 3.1 shows representative TEM and HRTEM micrographs with the respective indexed power spectrum of the 18 ± 2 nm CASe NCs produced following this procedure. From HRTEM analysis, the NC crystallographic phase was identified as tetragonal CASe (space group I$\bar{4}$ 2m (121), Table 3.1) with lattice constants a=b=0.566 nm and c=1.128 nm, which is in agreement with XRD data (Figure 3.3a, JCPDS card No. 85-0003). No secondary phases were detected by HRTEM and XRD analysis.

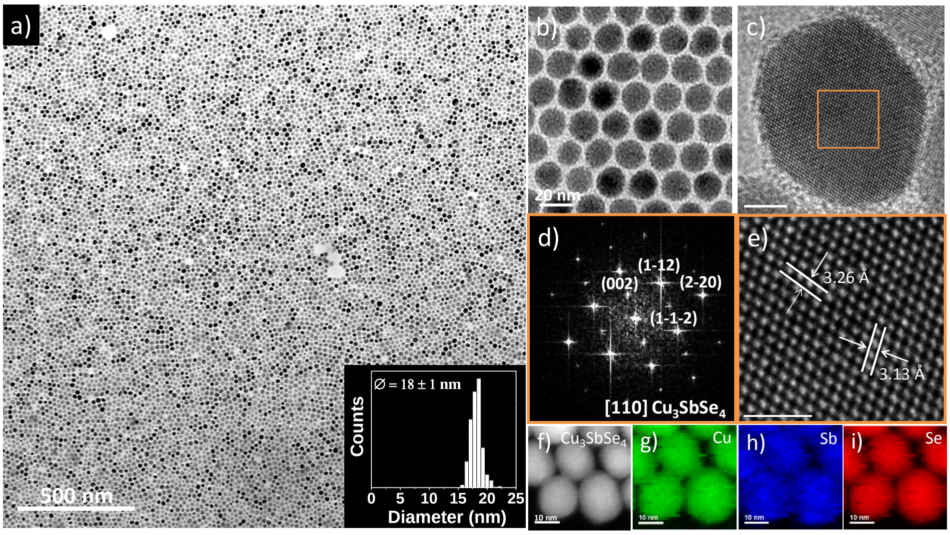

Figure 3.1. (a) Representative TEM micrograph of CASe NCs. The inset shows the histogram for the measured particle size distribution (18 ± 2 nm). (b) Higher-magnification TEM micrograph; (c) HRTEM image of a single CASe NC. (d) Its respective power spectrum fitting with CASe tetragonal phase. (e) Detail of the squared regions of the single CASe NCs. (f) Annular dark field scanning TEM (ADF-STEM) image of some CASe NCs and (g)-(i) areal density of each of the elements extracted from the EELS spectrum image.

Within its experimental error, SEM-EDX and ICP analysis showed the metal and chalcogen ratios to match those of stoichiometric CASe (Cu_3SbSe_4, Figures 3.4e and 3.4f). Electron Energy Loss Spectroscopy (EELS) was used for compositional analysis within each particle using Sb $M_{4,5}$, Cu $L_{2,3}$ and Se $L_{2,3}$ edges Figures 1f-i, 3.4a-d). In the central region of the NC, elemental quantification (in at %) showed the presence of around 12% Sb, 30% Cu and 48% Se, which is compatible with the CASe stoichiometry. In the outer part of the NCs, the relative composition of Sb and Cu were found to be slightly higher than in the core and that of Se was slightly lower: 17 % Sb, 40% Cu and 43% Se (Figures 3.4a-d).

Table 3.1. Summary of the peaks simulated for tetragonal CASe. (Crystal data: JCPDS No. 85-0003, Formula CASe, Crystal system Tetragonal, Space group $I\bar{4}2m$ (No. 121), Unit cell dimensions a = b = 5.6609 Å and c =11.280 Å).

hkl	*d-spacing/ Å*	*2θ/deg*	*hkl*	*d-spacing/ Å*	*2θ/deg*
101	5.0595	17.514	**204**	1.9977	45.360
110	4.0028	22.190	**312**	1.7062	53.675
112	3.2642	27.299	**116**	1.7016	53.831
103	3.1320	28.475	**400**	1.4152	65.953
202	2.5297	35.456	**008**	1.4100	66.229
211	2.4701	36.340	**332**	1.2984	72.775
114	2.3053	39.040	**316**	1.2964	72.908
105	2.0957	43.130	**424**	1.1548	83.677
220	2.0014	45.272	**228**	1.1526	83.867

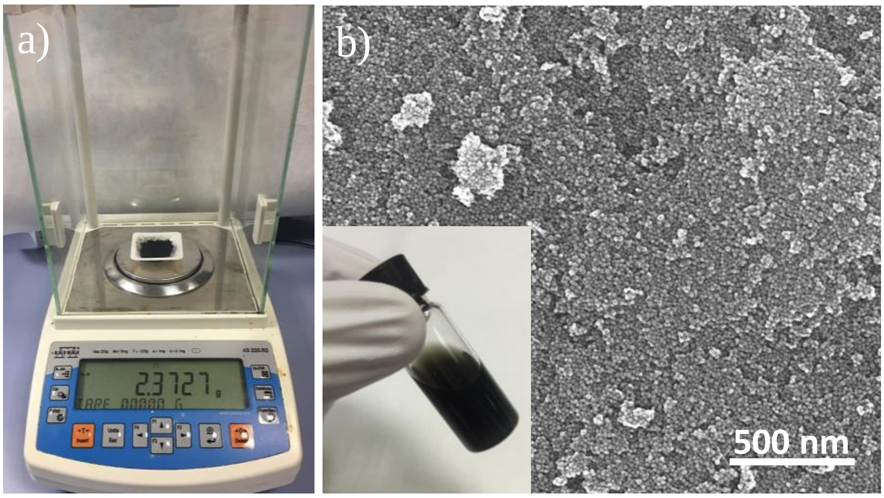

Figure 3.2. (a) Usual yield of CASe NCs obtained from one large-scale synthesis. (b) SEM image of CASe NCs after ligand exchange. Inset shows the stable, dark-green dispersion in chloroform formed by the NCs before ligand exchange.

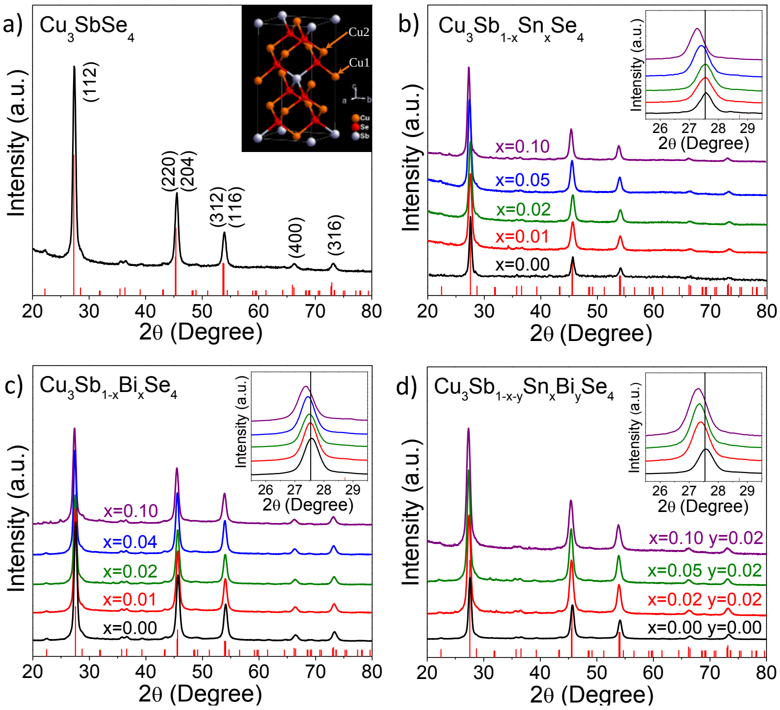

Figure 3.3. (a) XRD pattern of CASe NCs including the JCPDS 85-0003 reference. The inset shows a unit cell of tetragonal CASe. (b) XRD patterns of $Cu_3Sb_{1-x}Sn_xSe_4$ (x=0.00, 0.01, 0.02, 0.05, 0.10) NCs. (c) XRD patterns of $Cu_3Sb_{1-x}Bi_xSe_4$ (x=0.00, 0.01, 0.02, 0.04, 0.10) NCs. (d) XRD patterns of $Cu_3Sb_{1-x-y}Sn_xBi_ySe_4$ (x=0.02, 0.05, 0.10 and y=0.02) NCs. Insets in graphs (b)-(c) show a detail of the (112) peak, at around 2θ =27.5°.

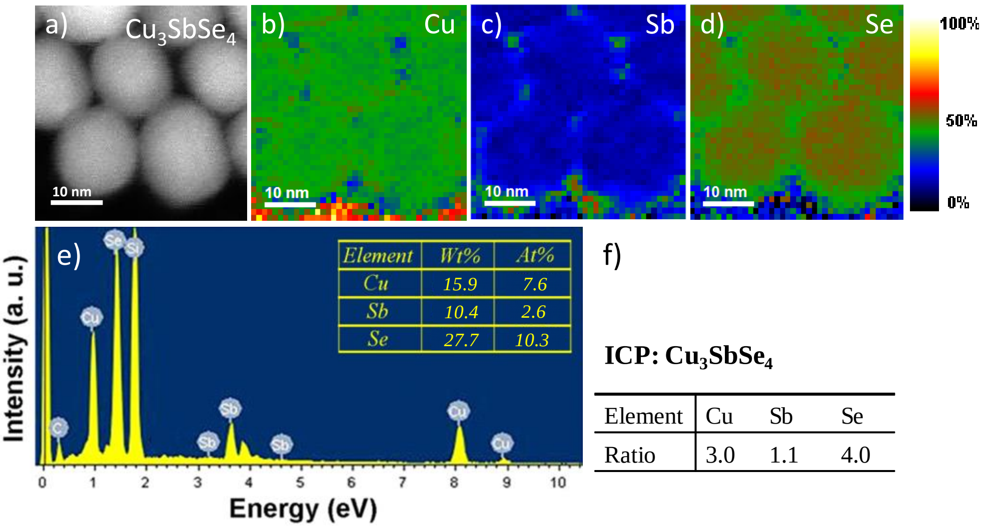

Element	Wt%	At%
Cu	15.9	7.6
Sb	10.4	2.6
Se	27.7	10.3

ICP: Cu_3SbSe_4

Element	Cu	Sb	Se
Ratio	3.0	1.1	4.0

Figure 3.4. (a) HAADF-STEM image of CASe NCs. (b-d) relative atomic composition of Sb, Cu and Se. (e) EDX spectrum of CASe NCs and quantitative analysis of the as-synthesized CASe NCs showing a composition consistent with stoichiometric Cu_3SbSe_4. (f) Results of the ICP analysis of CASe NCs showing a composition of $Cu_{3.0}Sb_{1.1}Se_{4.0}$.

$Cu_3Sb_{1-x}Sn_xSe_4$ (Figure 3.5), $Cu_3Sb_{1-x}Bi_xSe_4$ (Figure 3.6) and $Cu_3Sb_{1-x-y}Sn_xBi_ySe_4$ (Figure 3.7) NCs showed quasi-spherical morphologies with an average size of around 18 nm. Increasingly broader size and shape distributions were obtained as the amount of doping was augmented (Figures 3.5 and 3.6). Doped CASe NCs were characterized by larger a and c lattice parameters, as evidenced by a slight peak shift toward lower angles in the XRD patterns (Figure 3b, c and d). The lattice expansion is attributed to the substitution of Sb^{5+} (0.6 Å) by larger Sn^{4+} (0.69 Å) or Bi^{3+}/Bi^{5+} (≥ 0.76 Å) cations.[53, 54] TEM-EDX analysis evidenced the presence of Sn and Bi in all Sn- and Bi-doped NCs, respectively. However, Sn and Bi signals were too weak to quantify (Figure 3.8). The overall NCs composition was studied by ICP (Table 3.2). The composition of the consolidated materials used for TE characterization (see below) was also analyzed by SEM-EDX (Tables 3.3 and 3.4). Within their experimental errors, both ICP and SEM-EDX results matched the nominal Bi and Sn concentrations.

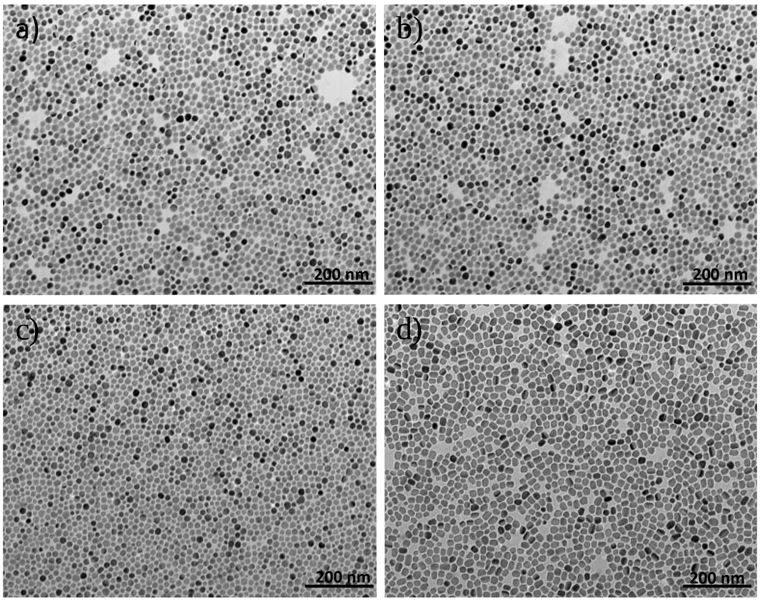

Figure 3.5. Representative TEM images of $Cu_3Sb_{1-x}Sn_xSe_4$ NCs with (a) x=0.01, (b) x=0.02, (c) x=0.05 and (d) x=0.10. Scale bars correspond to 200 nm.

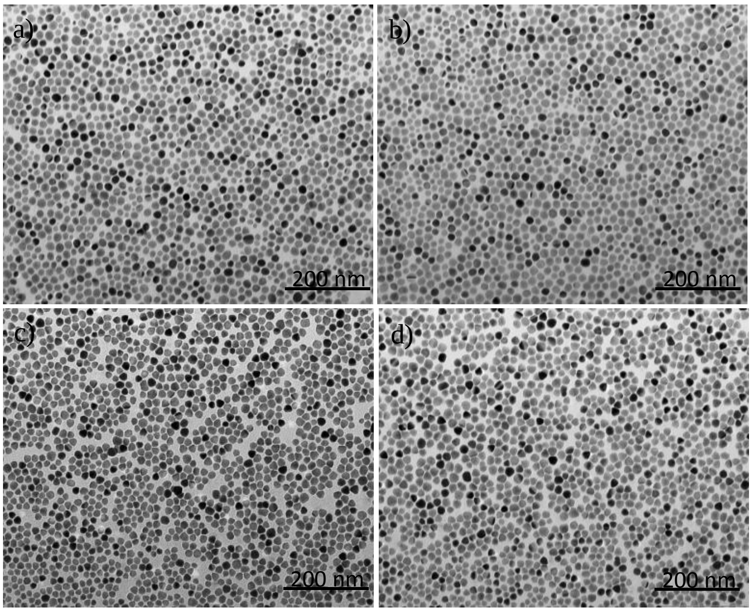

Figure 3.6. Representative TEM images of $Cu_3Sb_{1-x}Bi_xSe_4$ NCs with (a) x=0.01, (b) x=0.02, (c) x=0.04 and (d) x=0.10. Scale bars correspond to 200 nm.

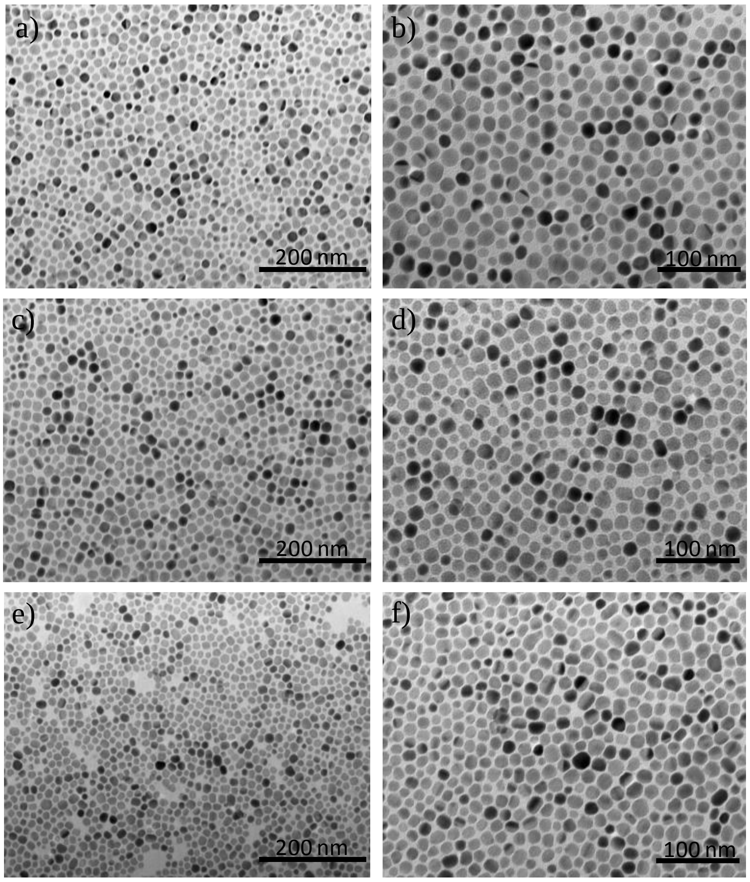

Figure 3.7. Representative TEM images of $Cu_3Sb_{0.98-x}Sn_xBi_{0.02}Se_4$ NCs with (a),(b) x=0.02, (c),(d) x=0.05 and (e),(f) x=0.10. Scale bars correspond to 200 nm.

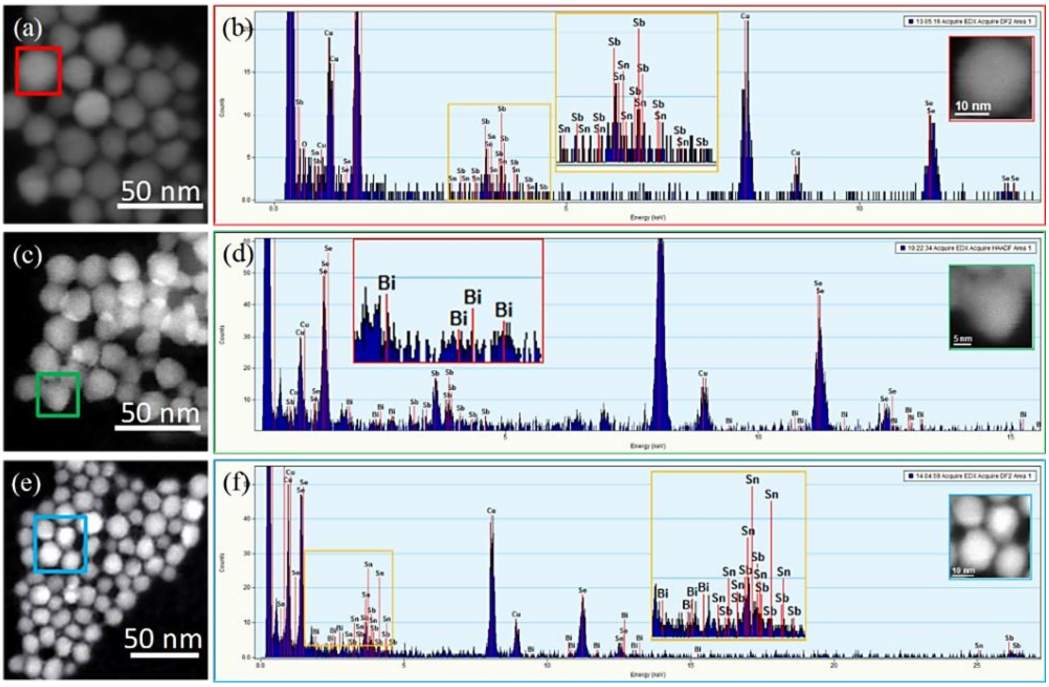

Figure 3.8. Left: ADF-STEM images of $Cu_3Sb_{0.98}Sn_{0.02}Se_4$ (a), $Cu_3Sb_{0.98}Bi_{0.02}Se_4$ (b) and $Cu_3Sb_{0.88}Sn_{0.10}Bi_{0.02}Se_4$ (c) NCs. Right: (d-f) EDX spectrum from single or few particles (inset), as indicated in the squared regions on the left. As observed, Sn and Sb peaks appear almost overlapped and the Sn signal was generally so weak that it was just on the detection threshold. Thus, although the analysis confirmed the presence of Sn, quantification was not possible. Similarly, the Bi signal could be observed in Bi-doped CASe, but it was quite weak, in the detection threshold, preventing quantification from single particle analysis.

Table 3.2. Composition of $Cu_3Sb_{1-x}Sn_xSe_4$ and $Cu_3Sb_{1-x}Bi_xSe_4$ NCs obtained from ICP analysis.

Element	x=0	x=0.01	x=0.02	x=0.05	x=0.10	Element	x=0	x=0.02
Cu	3	3	3	3	3	Cu	3	3
Sb	1.1	1.1	1.2	1.2	1.1	Sb	1.1	1.1
Sn	0	0.01	0.02	0.06	0.11	Bi	0	0.02

Table 3.3. Composition of $Cu_3Sb_{1-x}Sn_xSe_4$ and $Cu_3Sb_{1-x}Bi_xSe_4$ after consolidation obtained from SEM-EDX analysis.

Element	x=0.01	x=0.02	x=0.05	x=0.10	Element	x=0.01	x=0.02	x=0.04	x=0.10
Cu	3.0	3.0	3.0	3.0	Cu	3.0	3.0	3.0	3.0
Sb	1.1	1.1	1.1	0.9	Sb	1.1	1.1	1.0	1.0
Sn	0.01	0.02	0.05	0.11	Bi	0.01	0.02	0.04	0.11
Se	3.8	4.1	4.0	3.9	Se	3.9	4.1	3.7	4.0

Table 3.4. Composition of $Cu_3Sb_{1-x-y}Sn_xBi_ySe_4$ after consolidation obtained from SEM-EDX analysis.

Element	x=0.02, y=0.02	x=0.05, y=0.02	x=0.010, y=0.02
Cu	3.0	3.0	3.0
Sb	1.0	0.9	0.9
Sn	0.02	0.05	0.10
Bi	0.02	0.02	0.02
Se	3.8	3.9	3.9

XPS analysis was performed to investigate the chemical state of elements within CASe NCs. The survey scan is shown in Figure 3.9a. High-resolution spectra of Cu 2p, Sb 3d, and Se 3d are shown in Figure 3.9b, c, and d, respectively. All spectra were shifted to locate the C1s peak at 284.6 eV, correcting in this way potential charging effects. The narrow doublet peaks in the Cu 2p spectrum appear at 932.1 eV ($2p_{3/2}$) and 951.9 eV ($2p_{1/2}$), consistent with the standard separation of 19.8 eV and indicative of Cu (I) (Figure 3.9b).[55, 56] In addition, we exclude the presence of Cu^{2+} because the Cu $2p_{3/2}$ satellite peak of Cu (II) (936 eV and 942 eV) did not appear in the spectrum.[57]

Figure 3.9c displays peaks corresponding to Sb 3d. There has been debate on the specific valence number of Sb in CASe, both Sb^{5+} and Sb^{3+} have been suggested. [19, 58, 59] In this compound, the Sb 5s bands are quite narrow ~0.5 eV and located approximately at -9.4 eV between 529.5 eV ($3d_{5/2}$) and 538.9 eV ($3d_{3/2}$), while the Sb p bands are above the Fermi level.[58] Figure 9d shows the Se $3d_{5/2}$ peak at 54.75 eV, indicating Se with a valence of Se^{2-}. From the inset of Figure 3.9d, the Se 3p core located at 161.1 eV ($3p_{3/2}$) and 166.8 eV ($3p_{1/2}$) with a peak separation of 5.7 eV, which are in good agreement with values reported previously for Se $3p_{3/2}$ and $3p_{1/2}$, respectively. [55, 60]

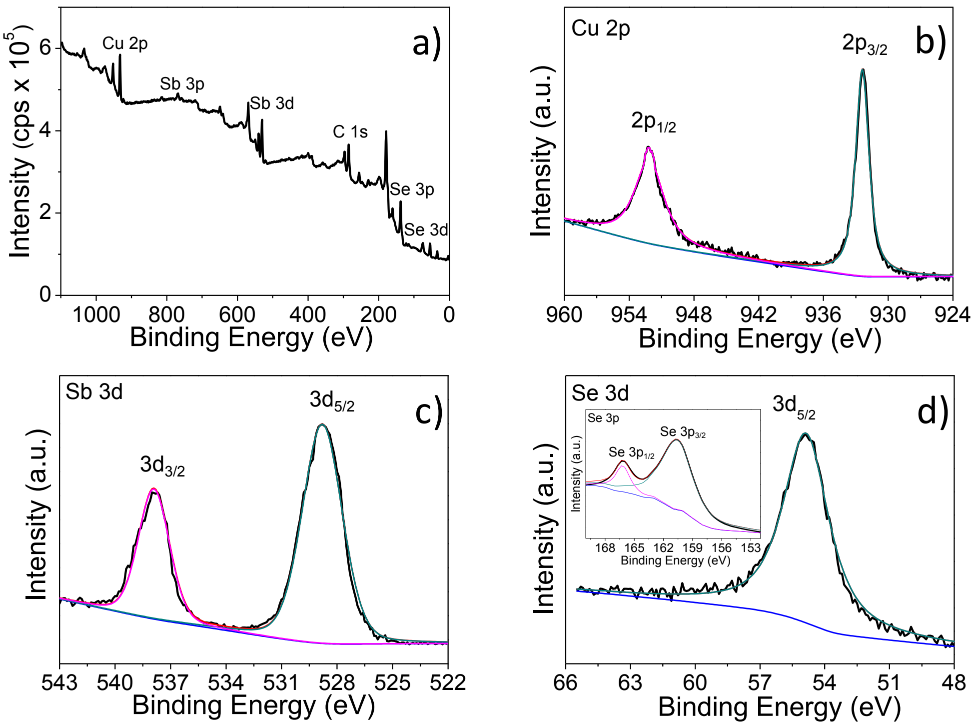

Figure 3.9. XPS spectrum of the obtained CASe NCs: (a) survey spectrum of CASe, and high resolution spectrum of (b) Cu 2p, (c) Sb 3d, and (d) Se 3d.

Figure 3.10 shows the XPS spectra of $Cu_3Sb_{0.90}Bi_{0.10}Se_4$ NCs. Figure 3.10e shows the high-resolution spectrum of the Bi 4f region (Figure 3.10e). Most interesting, the Bi $4f_{5/2}$ and $4f_{7/2}$ peaks exist at binding energies of 166.2 eV and 161.0 eV, respectively. These values are clearly above those generally reported for Bi^{3+} compounds such as Bi_2Se_3[61-63] and Bi_2O_3.[64] However, Bi^{5+} is a very strong oxidizer with a very high reduction potential (Bi^{3+}/Bi^{5+} E = 2V), which makes it extremely improvable to be found within CASe, especially taking into account Bi was introduced as Bi^{3+}.

The high resolution XPS spectrum of the Bi 4f region obtained from the $Cu_3Sb_{0.88}Sn_{0.10}Bi_{0.02}Se_4$ sample is shown on Figure 10f. The Bi $4f_{5/2}$ and $4f_{7/2}$ peaks were found at binding energies of 165.9 eV and 160.4 eV, respectively. These binding energies are again slightly above those that would correspond to a Bi^{3+} state, indicating that the chemical environment seen by Bi 4f electrons when Bi replaces a Sb, resembles that of Bi^{5+}.

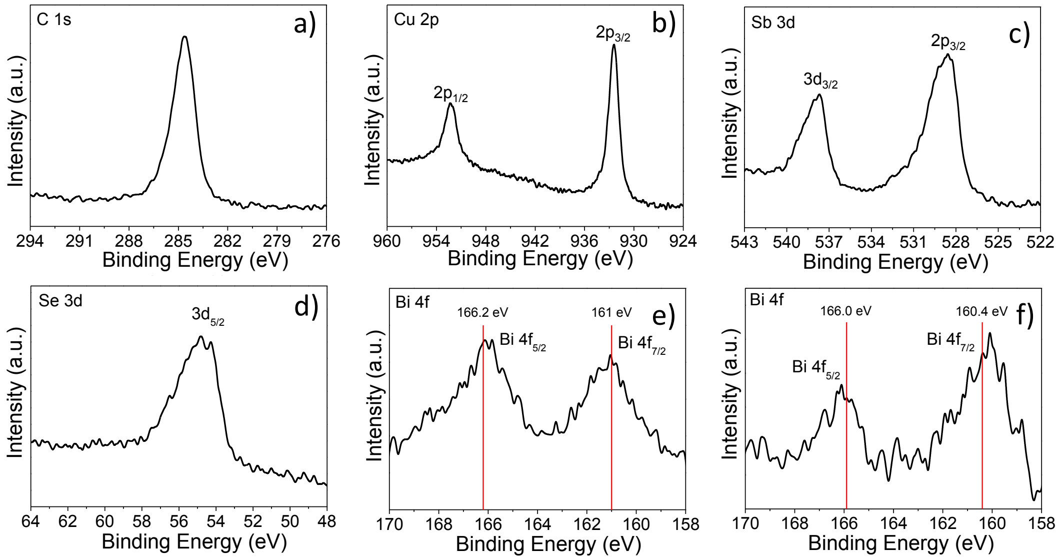

Figure 3.10. High resolution XPS spectrum of $Cu_3Sb_{0.90}Bi_{0.10}Se_4$ NCs and $Cu_3Sb_{0.88}Sn_{0.10}Bi_{0.02}Se_4$ NCs. a)-e) C 1s, Cu 2p, Sb 3d, Se 3d and Bi 4f spectra of $Cu_3Sb_{0.90}Bi_{0.10}Se_4$ NCs. f) Bi 4f spectra of $Cu_3Sb_{0.88}Sn_{0.10}Bi_{0.02}Se_4$ NCs.

CASe NCs were synthesized in the presence of OLA, OA and DDT. In order to identify which surfactants were finally present on the NC surface and establish their bonding nature, NMR analysis was performed. Figure 3.11a shows a ^{1}H NMR spectrum of the as synthesized NCs (unpurified) and the 1H NMR spectrum of NCs purified four times by precipitation/ redispersion with acetonitrile as non-solvent and toluene as solvent. In the spectrum of unpurified NCs we observe the characteristic resonances of a terminal alkene at 5.0 and 5.8 ppm, associated to ODE. The resonance around 5.5 ppm is associated with an internal alkene, from OLA and/or OA. The ODE resonances possess fine structure, indicating the unbound nature of ODE. In contrast, the alkene resonance is a superposition of sharp and broad resonances, associated with free and bound ligands respectively.[65] After purification, the ODE features disappear completely together with the majority of the sharp resonance corresponding to the free molecules OLA or OA, indicating a successful purification of the NCs solution. Further purification to remove the remaining free ligands in solution, render the NCs completely insoluble in any solvent. The NOESY spectrum (Figure 3.11c) contains negative (black) nOe cross peaks confirming the interaction of OLA/OA with the surface.[65] To discriminate whether OLA or OA (or both) is stabilizing the NC surface, we reproduced the exact same synthesis described above but instead of OA we used DAc. Although DAc and OA are both fatty acids and are expected to interact identically with NC surfaces, DAc has no alkene group and this allows us to distinguish OLA from OA. Figure 3.11b shows the NMR spectra of CASe NCs synthesized with DAc. Since the ^{1}H NMR spectra are almost identical to spectra of the dispersions prepared with OA and because OLA is now the only molecule with an alkene resonance, we identify OLA as a ligand. Additionally, the intensity of the alkene resonance and CH_3 resonance features a 2:3 ratio. This excludes any other (fully saturated) ligands such as DDT or DAc, proving that OLA is the only ligand present. Since OLA is an L-type ligand and the NCs were found to be stoichiometric (vide supra), this NC system belongs to the earlier established class of binding motifs; NCs (L).[66] To assess the dynamics of interaction, DOSY experiments were performed. A good fitting of the CH_3 signal decay was only obtained with two exponentials, indicating two populations (Figure 3.11d). The small fraction with a high diffusion coefficient (552 $\mu m^2/s$) is attributed to free OLA while the fraction with a low diffusion coefficient (45 $\mu m^2/s$) is associated with bound OLA. Using the Stokes-Einstein equation, a solvodynamic diameter of 16.5 nm is calculated from the diffusion coefficient. Since this is close to the diameter from TEM (16 − 20 nm), we conclude that OLA is firmly attached to the NC surface and diffuses together with the NC. Considering the L-type nature of OLA,[66] it is usually involved in a more dynamic stabilization of the NC surface.[67] However, it was repeatedly reported that Cu-based NCs typically have tightly bound amines bound to the surface.[13, 68] It should however be noted that OLA is quite easily desorbed during purification suggesting only a moderate binding affinity for the NC surface, in line with L-type ligand behavior.

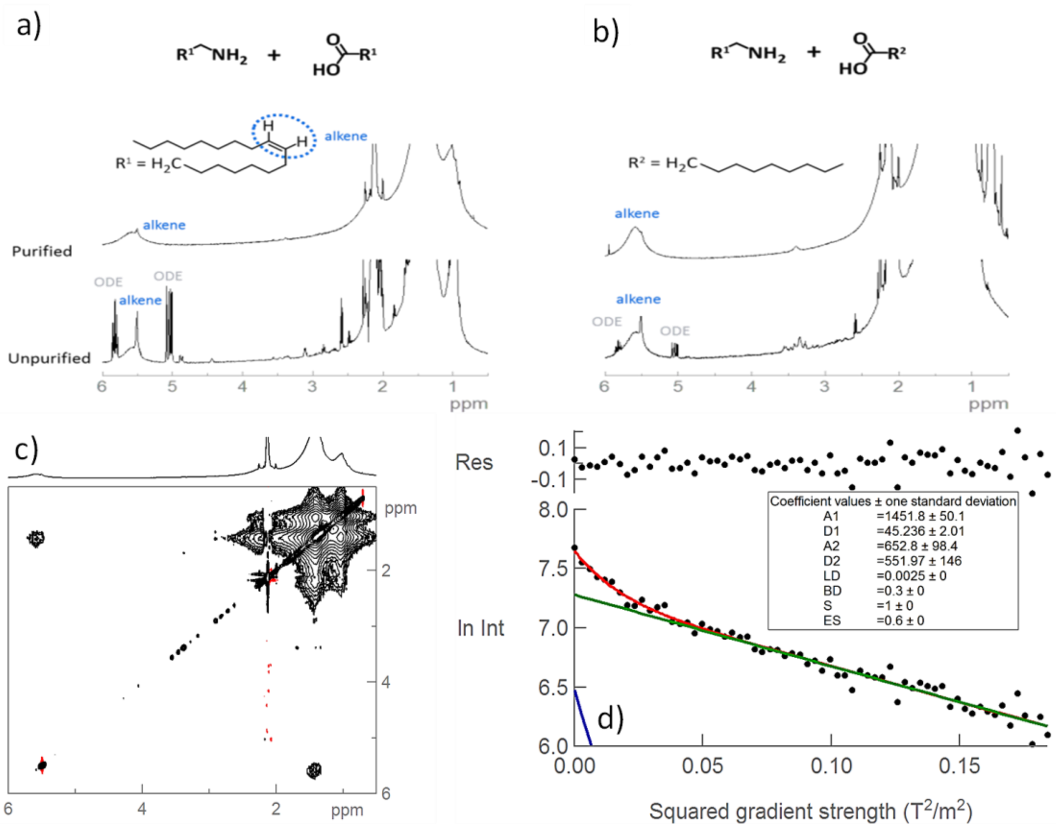

Figure 3.11. ^{1}H NMR spectrum of CASe 18 ± 2 nm NCs synthesized with (a) OA and (b) DAc shown before (bottom) and after (top) purification. (c) NOESY spectrum of CASe synthetized with OA. (d) Fitting the signal intensity decay with the Stejskal-Tanner equation of CASe NCs synthetized with OA (further information on the experimental section). Bi exponential fitting with two different diffusion coefficients D1 and D2 (slow: 45 µm²/s => 16 nm; fast: 652 µm²/s).

To facilitate charge transport/transfer, CASe NCs were thoroughly purified by multiple precipitation/re-dispersion steps and subsequently treated with NH_4SCN, which could efficiently displace remaining OLA. Figure 3.12 shows FTIR spectra of dried CASe NCs before (CASe–OL) and after (CASe–LD) organic ligand displacement with a 50 mM NH_4SCN solution. CASe–OL spectrum showed the characteristic features of OLA: C–H vibration modes have a strong band in the high-frequency region (2850–3000 cm^{-1}) and various peaks in the lower frequency region, between 700 cm^{-1} and 1650 cm^{-1}. These features completely disappeared from the CASe–LD spectrum, proving the effective organic ligand displacement.

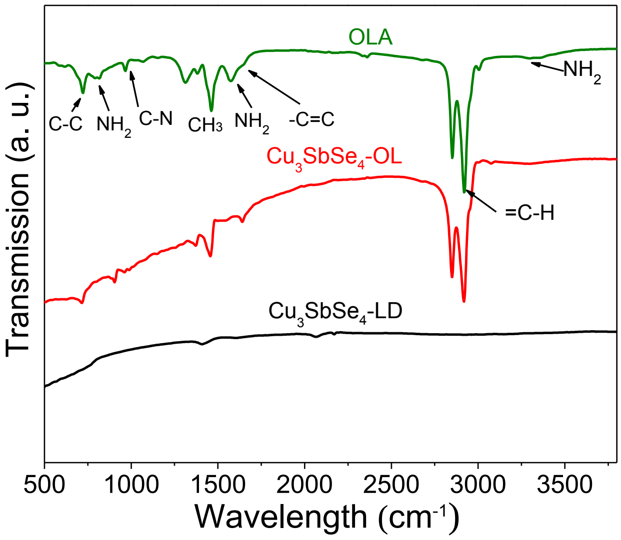

Figure 3.12. FTIR spectra of pure OLA, Cu_3SbSe_4–OL and Cu_3SbSe_4–LD NCs.

Nanocrystalline disk-shaped CASe pellets (Ø10 mm×~1.5 mm) were prepared under Ar atmosphere by hot-pressing ~700 mg of ligand-displaced NCs at ~380 °C, 70 MPa and for 30 min. The pellets had a metallic luster and were mechanically robust enough to endure polishing. Relative densities ~90% of the theoretical value were measured for all samples. XRD analysis of the CASe pellets showed no crystallographic or related compositional change after the hot-press process except for a minor peak at 2θ ~34° in the XRD pattern, which could correspond to Cu_3SbSe_3 (JCPDS card No. 1-86-1751, Figures 3.13 and 3.14). However, during this process, CASe NCs coalesced to form larger crystalline domains with sizes ranging from tens to few hundred nanometers (Figure 3.15).

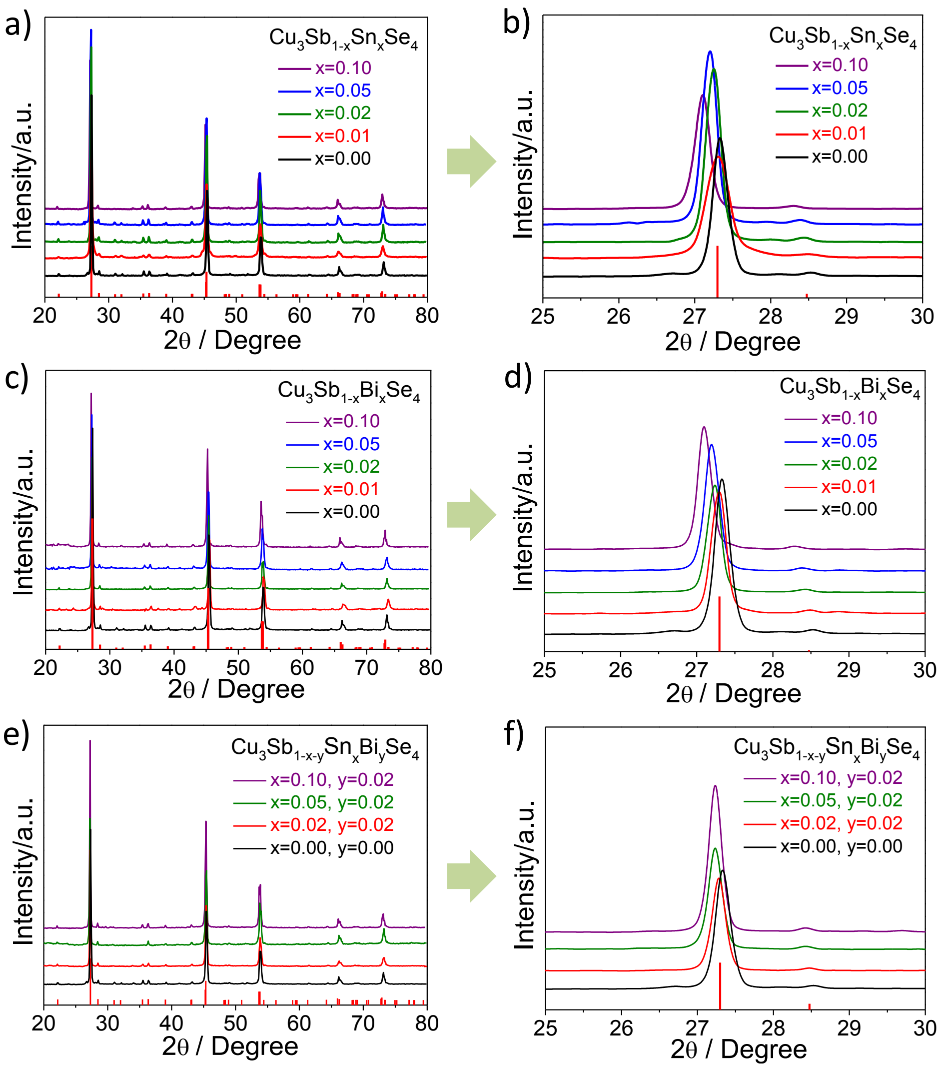

Figure 3.13. XRD patterns (a, c, e) and detail of the (112) peaks around 27.2° 2*θ* values (b, d, f) of a) $Cu_3Sb_{1-x}Sn_xSe_4$ (x=0.00, 0.01, 0.02, 0.05, 0.10), b) $Cu_3Sb_{1-x}Bi_xSe_4$ (x=0.00, 0.01, 0.02, 0.04, 0.10) and c) $Cu_3Sb_{1-x-y}Sn_xBi_ySe_4$ (x=0.02, 0.05, 0.10 and y=0.02) pellets. Red vertical lines correspond to the reference literature data for CASe, JCPDS NO. 85-0003.

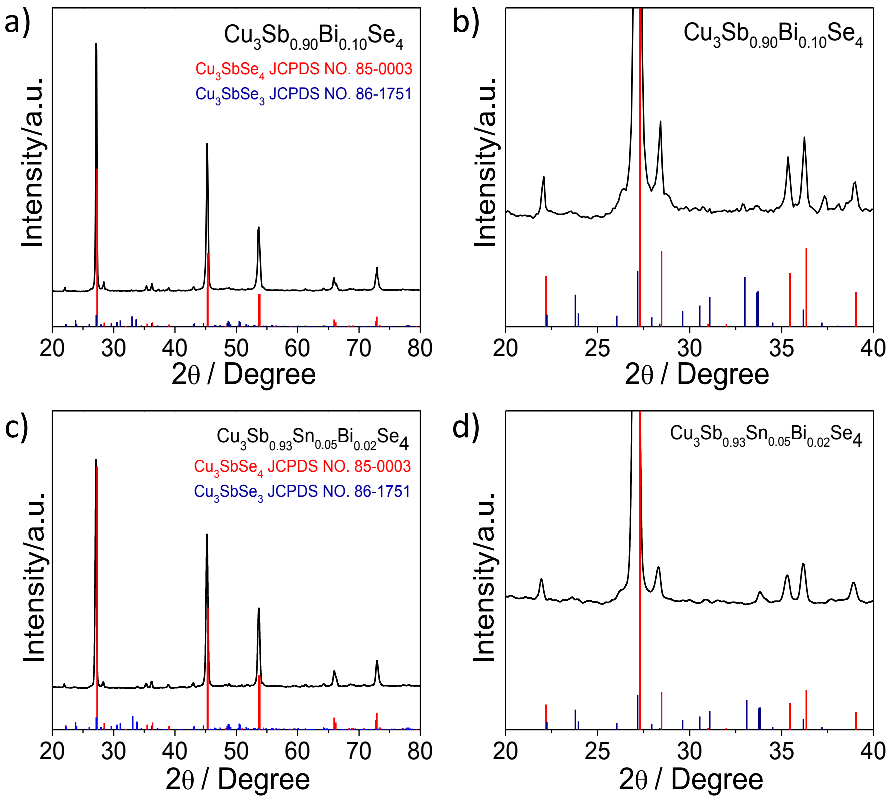

Figure 3.14. XRD patterns (a,c) and detail of the (112) peaks between 20º and 40º 2θ values (b,d) of $Cu_3Sb_{0.90}Bi_{0.10}Se_4$ (a,b) and $Cu_3Sb_{0.93}Sn_{0.05}Bi_{0.02}Se_4$ (c,d) pellets. Red vertical lines correspond to the reference literature data for Cu_3SbSe_4, JCPDS NO. 85-0003. Blue vertical lines correspond to Cu_3SbSe_3, JCPDS NO. 1-86-1751.

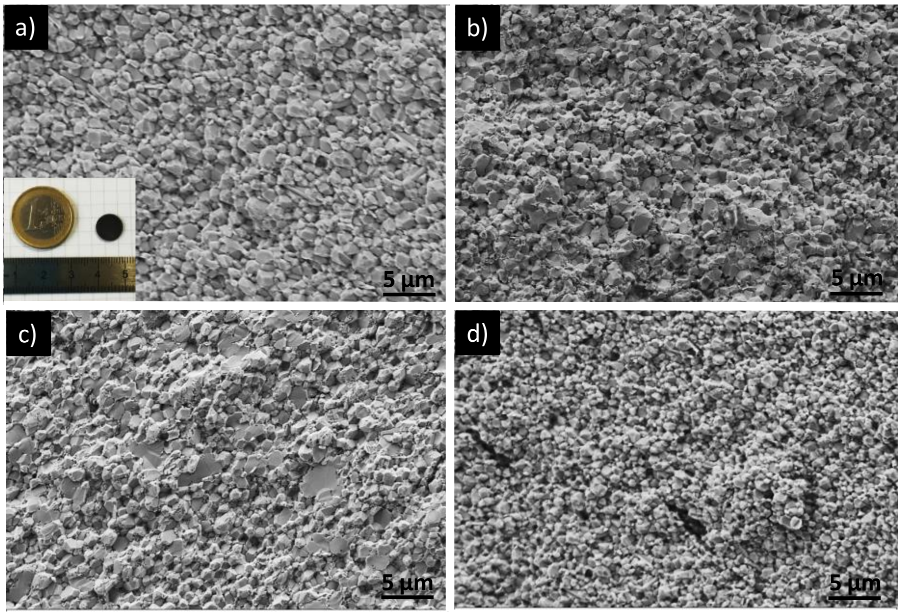

Figure 3.15. Representative SEM images of the fracture surfaces of bulk materials compacted from (a) Cu_3SbSe_4; (b) $Cu_3Sb_{0.98}Sn_{0.02}Se_4$; (c) $Cu_3Sb_{0.98}Bi_{0.02}Se_4$ and (d) $Cu_3Sb_{0.88}Sn_{0.10}Bi_{0.02}Se_4$ NCs. Inset of (a) shows one of the pellets measured.

The electrical conductivity (σ), Seebeck coefficient (S), thermal conductivity (κ), and the dimensionless TE figure or merit (ZT=σS^2T/κ) of undoped and Sn- and Bi-doped CASe pellets are displayed in Figures 3.16 and 3.18. Undoped CASe nanomaterials were characterized by relatively low σ, which increased with temperature up to 6.2×10^3 Sm^{-1}, and positive S in the whole temperature range measured. Significantly higher σ, up to 9.0×10^4 Sm^{-1} at room temperature, were obtained for Sn-CASe (Figure 3.16a), which showed a degenerated semiconductor behavior with a decrease of σ with temperature. On the contrary, S decreased with the Sn introduction (Figure 3.16b). The observed increase of σ and decrease of S with the amount of Sn indicated Sn ions to act as a p-type dopant within CASe. This electronic role was confirmed by a one order of magnitude increase in the Hall charge carrier concentration with the Sn introduction, from p=5×10^{18} cm^{-3} in CASe to p=9×10^{19} cm^{-3} in $Cu_3Sb_{0.98}Sn_{0.02}Se_4$ (Table 3.5). Overall, higher power factors (PF=σ S^2) were obtained for the Sn-doped samples, with a maximum PF of 1.14 $mWm^{-1}K^{-2}$ at 673 K for the sample containing a 2% replacement of Sb by Sn, $Cu_3Sb_{0.98}Sn_{0.02}Se_4$ (Figure 3.16c).

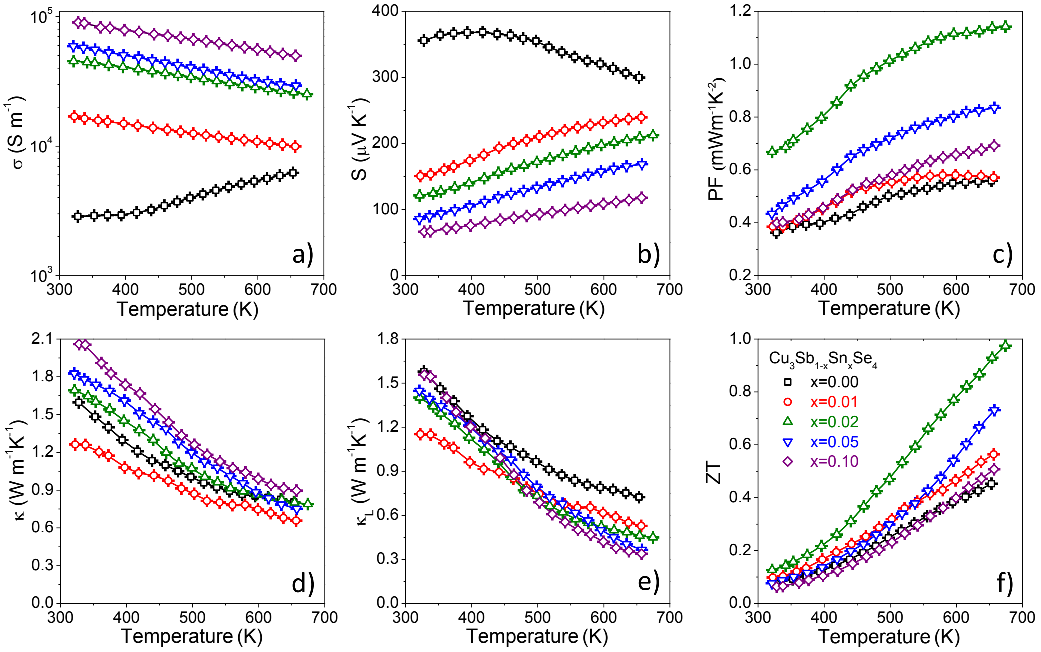

Figure 3.16. Temperature dependence of (a) electric conductivity (σ), (b) Seebeck coefficient (S), (c) power factor (PF), (d) thermal conductivity (κ), (e) lattice thermal

conductivity (κ_L) and (d) TE figure of merit (ZT) of $Cu_3Sb_{1-x}Sn_xSe_4$ (x=0.01, 0.02, 0.05 and 0.10).

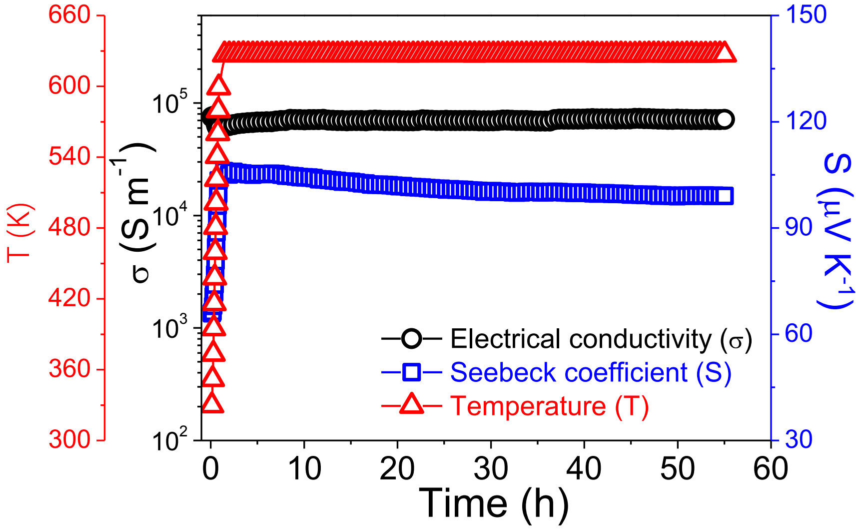

Figure 3.17. Time evolution of the electrical conductivity (σ), Seebeck coefficient (S) and temperature (T) of $Cu_3Sb_{0.9}Sn_{0.1}Se_4$ during a 55 h test.

Relatively low thermal conductivities, which as expected decreased with temperature, were obtained for all the analyzed materials. For undoped CASe, κ dropped from 1.60 $Wm^{-1}K^{-1}$ to 0.81 $Wm^{-1}K^{-1}$ (Figure 3.16d) in the temperature range from 327 K to 653 K. These are lower κ values than those previously reported for bulk CASe,[19, 20, 53, 69] but slightly higher than those reported for nanostructured CASe produced by co-precipitation,[32] and much higher than the estimated minimum κ of this material (0.26 $Wm^{-1}K^{-1}$).[70, 71] Lower lattice thermal conductivities (κ_L) were obtained with the incorporation of Sn due to the introduced lattice distortion and the increased density of point defects (Figure 3.16e). However, the associated increase of the electronic contribution to the thermal conductivity (κ_e) resulted in an overall increase of κ for most of the Sn-CASe pellets. Overall, ZT significantly increased with the introduction of relatively small amounts of Sn, reaching ZT=0.97 at 673 K for $Cu_3Sb_{0.98}Sn_{0.02}Se_4$, which represents more than a 2-fold increase over undoped CASe (Figure 3.16f).

Nanocrystalline CASe showed good stability even when maintained at relatively high temperatures for long periods of time. Figure 3.25 shows the results obtained from 5 consecutive heating-cooling cycles. Minor differences were observed from cycle to cycle and mainly from the first cycle to the following ones. To account for the minor variations obtained from the first to the following cycles, all samples were measured at least 3 consecutive times and results from the first cycle were discarded. Figure 3.17 shows the results obtained from $Cu_3Sb_{0.9}Sn_{0.1}Se_4$ during a 55 h test involving the heating of the sample from 323 to 626 K at a rate of 10 K/min and then maintaining the sample at 656 K for 54 h. During this time, the electrical conductivity and Seebeck coefficient changed by around 1% and 3%, respectively.

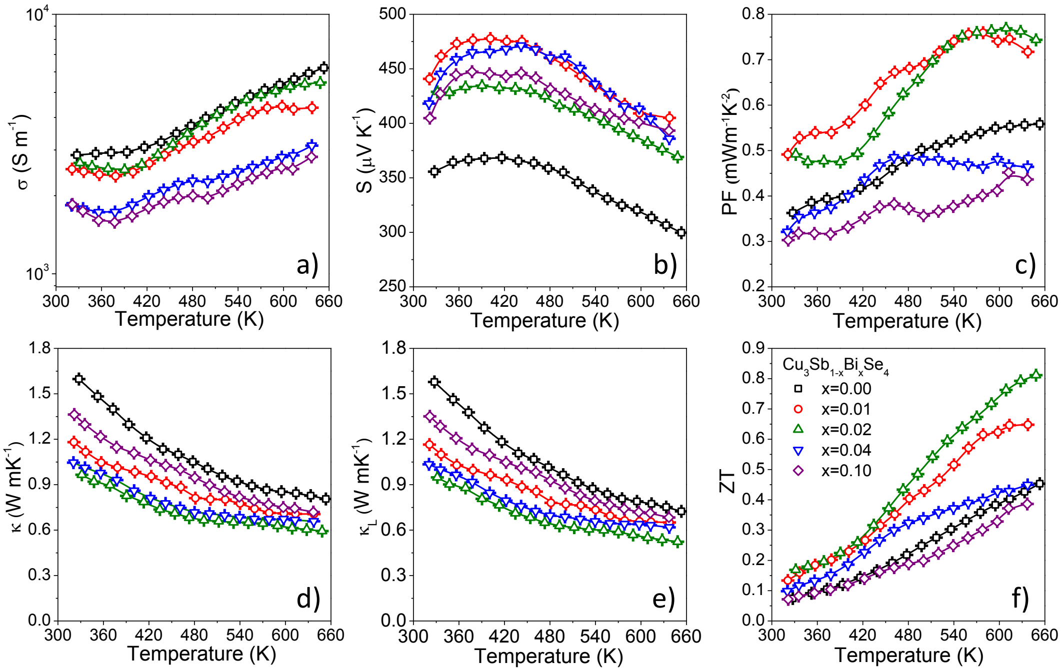

Figure 3.18. Temperature dependence of (a) electric conductivity (σ), (b) Seebeck coefficient (S), (c) power factor (PF), (d) thermal conductivity (κ), (e) lattice thermal conductivity (κ_L) and (d) TE figure of merit (ZT) of $Cu_3Sb_{1-x}Bi_xSe_4$ (x=0.01, 0.02, 0.04 and 0.10).

When replacing part of Sb by Bi, slightly lower σ were obtained (Figure 3.18a), which correlated with a small decrease in the Hall hole concentrations (p = $2x10^{18}$ cm^{-3}, Table 3.5). This was a surprising experimental evidence if assuming Sb^{5+} to be replaced by Bi^{3+} as it has to be the case taking into account the very high energy required to oxidize Bi^{3+} to Bi^{5+}. As no increase of the hole concentration was observed, the difference in oxidation state between Sb and Bi is probably compensated with the creation of an equivalent amount of Se^{2-} vacancies. The slight decrease in the measured charge carrier concentration could be further associated to an indirect diminution of the concentration of intrinsic defects acting as p-type dopants, e.g. the presence of Cu^{1+} at Sb^{5+} sites or Cu or Sb vacancies.

Significantly larger S values were measured for all Bi-CASe samples (Figure 3.18b) when compared with CASe, which did not correlate well with the small decrease in electrical conductivity when just taking into account a slight modification of the charge carrier concentration (Table 3.5).

Combining σ with S, the highest PF values for Bi-CASe were obtained with a composition $Cu_3Sb_{0.98}Bi_{0.02}Se_4$ (~0.77 $mWm^{-1}K^{-2}$ at 608 K, Figure 18c). Additionally, Bi-doped CASe was characterized by lower κ than CASe due to slightly lower κ_e and κ_L contributions (Figures 3.18d and 3.18e). Overall, higher ZT values, up to 0.81 for $Cu_3Sb_{0.98}Bi_{0.02}Se_4$ at 648 K, were obtained for Bi-CASe when compared with CASe (Figure 3.18f).

To further determine the influence of Sn and Bi in the electronic band structure of CASe, DFT calculations were carried out. Figure 3.6 shows the band structure of pure CASe, $Cu_3Sb_{0.875}Sn_{0.125}Se_4$ and $Cu_3Sb_{0.875}Bi_{0.125}Se_4$. Results indicate that pure CASe is a semiconductor with a direct band gap of 0.27 eV measured at Γ point, which is consistent with experimental values (0.1 − 0.4 eV).[38, 42, 72] The calculated bandgap was also in agreement with theoretical results from Do *et al.*[73] using the non-local exchange HS06 model (0.26 eV). As expected, the VBM in CASe is mainly composed of Cu-3d and Se-4p states and the CBM is mainly formed by Sb-5s and Se-4p states (Figure 3.19a).

Figure 3.20 shows the temperature dependence of the DFT-derived S for different concentrations of the majority charge carrier. For pure CASe, at moderate p levels ($p < 5\times10^{19}$ cm^{-3}) the Seebeck coefficient increases with temperature up to a maximum and then rapidly decreases. At higher hole concentrations ($p > 5\times10^{19}$ cm^{-3}), S monotonously increases with temperature in the analysed range ($T \leq 700$

K). Calculated values matched relatively well experimental results and qualitatively predicted the measured temperature evolution.

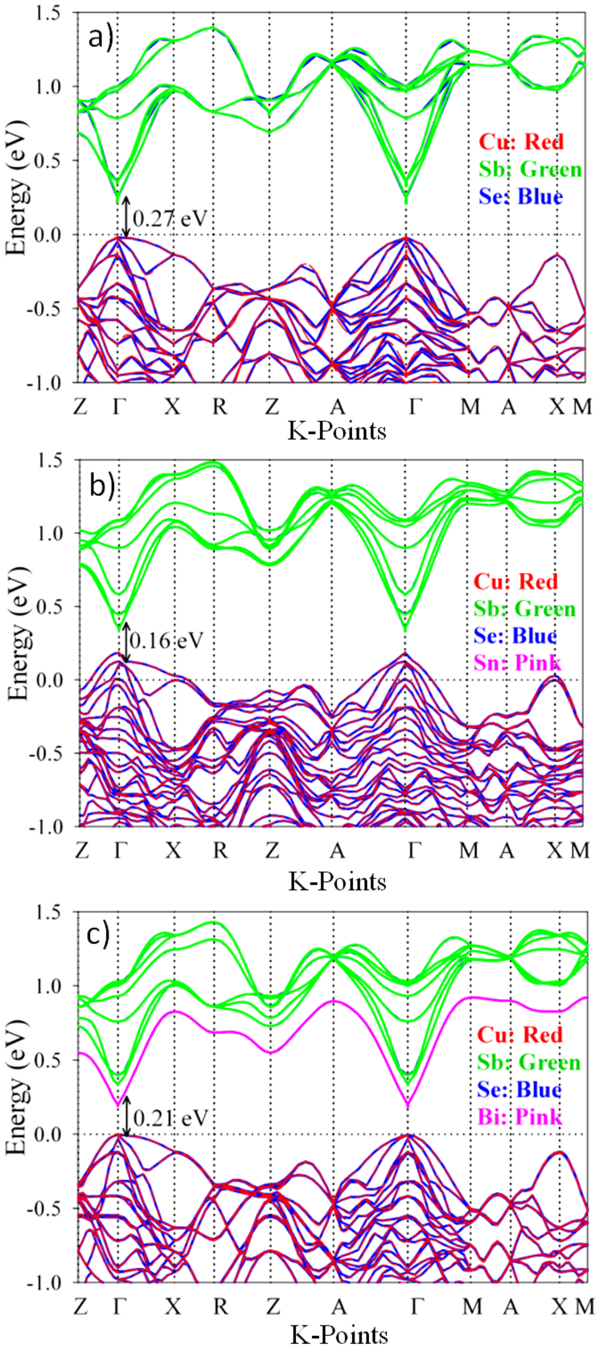

Figure 3.19. Electronic band structure of (a) CASe, (b) $Cu_3Sb_{0.875}Sn_{0.125}Se_4$ and (c) $Cu_3Sb_{0.875}Bi_{0.125}Se_4$. The symbols stand for the main atomic contributions of the bands. Band energies were plotted with respect to the Fermi level.

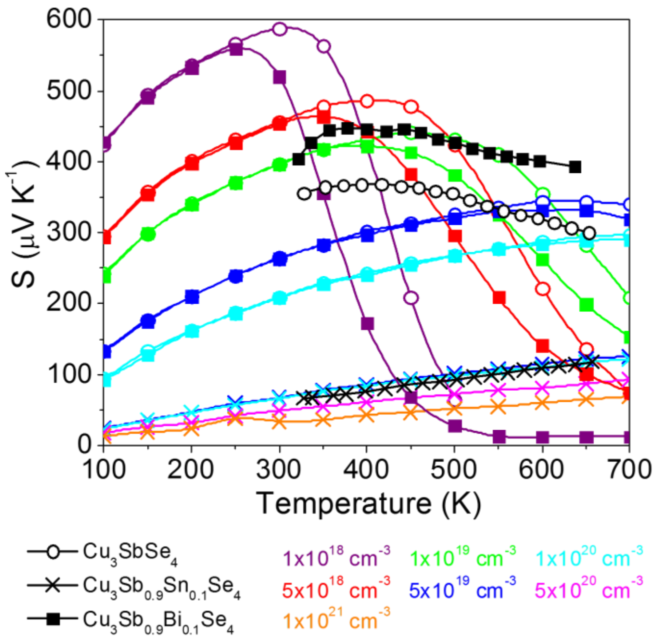

Figure 3.20. Temperature dependence of DFT-calculated Seebeck coefficients (S) of pure CASe, $Cu_3Sb_{0.875}Bi_{0.125}Se_4$ and $Cu_3Sb_{0.875}Sn_{0.125}Se_4$ at different hole concentrations (colored lines and symbols). Experimental values for pure CASe, $Cu_3Sb_{0.9}Bi_{0.1}Se_4$ and $Cu_3Sb_{0.9}Sn_{0.1}Se_4$ are also plotted (in black).

The introduction of small amounts of Sn at the Sb sites significantly reduced the band gap, to 0.16 eV, and shifted the Fermi level to within the valence band due to the p-type doping character of Sn^{4+} ions (Figure 3.19b). Thus, only Seebeck coefficients for relatively high carrier concentrations $p > 5\times10^{19}$ cm^{-3} were reliably calculated. In agreement with experimental measurements, such large charge carrier concentrations resulted in an important diminution of S. A hole carrier concentration $p \approx 1x10^{20}$ cm^{-3} was needed to match the experimental S values, which is consistent with the Hall charge carrier concentrations measured for the Sn-doped materials.

The partial substitution of Sb by Bi had little effect on the band structure at the VBM, but it significantly affected the CBM, decreasing the band gap and resulting in a divergence of the multi-valleys (Figure 3.19c). Taking into account only the contribution of majority carriers, the DFT-derived S just slightly changed with the Bi introduction (Figure 3.20) mainly due to the bandgap reduction. However, the perturbation of the CBM associated with the Bi presence certainly had a strong influence on the contribution of the conduction electrons to the transport properties. In this regard, the splitting of the degenerated multi-valleys at the CBM should translate in a reduction of a bipolar effect on S, thus resulting in overall higher S values. In this direction, our DFT analysis clearly showed a significant diminution of the effective mass of electrons with the introduction of Bi (Table 3.6, Figure 3.21). While the calculation of this effect is beyond the present work, we qualitatively analyzed the bipolar impact to S by calculating the contribution of thermally generated charge carriers (Figures 3.22 and 3.23).[74] Results obtained clearly showed that in spite of the lower bandgap of Bi-CASe, and thus the higher charge carrier concentrations associated to thermal generation, the reduced effective mass for electrons in this compound should translate in a lower contribution of the minority carriers to S and thus to an overall higher Seebeck coefficient. A bipolar contribution could also explain the differences in the temperature dependence of κ_L between Bi-CASe and pure CASe, but this point is to be confirmed.[75]

The introduction of Sn also translated into large differences in the effective masses of holes and electrons which in spite of the strong band gap decrease in this material, also resulted in higher S values at moderate doping levels. However, the modification of the electronic band structure by means of sufficient amounts of Sn injected very large amounts of charge carrier, which inevitably resulted in overall lower S. Thus, the introduction of both dopants, a small amount of Sn to control charge carrier concentration and Bi to modify the band structure was necessary to optimize performance.

Table 3.5. Room temperature carrier concentration (p), electrical conductivity (σ), carrier mobility (μ) and effective mass (m*) of pristine Cu_3SbSe_4, $Cu_3Sb_{0.98}Sn_{0.02}Se_4$, $Cu_3Sb_{0.98}Bi_{0.02}Se_4$ and $Cu_3Sb_{0.88}Sn_{0.10}Bi_{0.02}Se_4$ samples.

Sample	p (cm^{-3})	σ (S cm^{-1})	μ (cm^2 V^{-1} s^{-1})
Cu_3SbSe_4	5×10^{18}	29	36
$Cu_3Sb_{0.98}Sn_{0.02}Se_4$	9×10^{19}	454	32
$Cu_3Sb_{0.98}Bi_{0.02}Se_4$	2×10^{18}	26	58
$Cu_3Sb_{0.88}Sn_{0.10}Bi_{0.02}Se_4$	1×10^{20}	1309	80

Table 3.6. Effective masses of studied compounds for holes (m^+) and electrons (m^-) along different directions of the Brillouin Zone. Effective masses are in unit of the mass electron (m_e).

		Γ-Z	**Γ-X**	**Γ-A**	**Γ-M**
CASe	m^-/m_e	0.06	0.17	0.19	0.18
	m^+/m_e	0.10	0.30	0.17	0.14
Bi-CASe	m^-/m_e	0.06	0.11	0.11	0.10
	m^+/m_e	0.10	0.32	0.20	0.15
Sn-CASe	m^-/m_e	0.07	0.13	0.14	0.13
	m^+/m_e	0.14	0.38	0.65	0.45

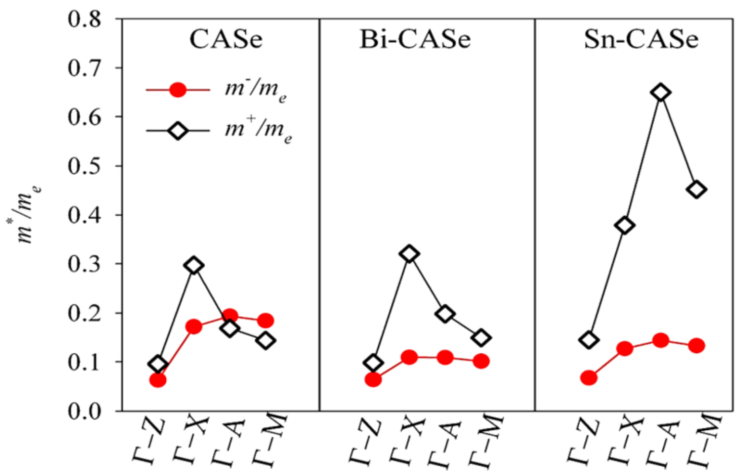

Figure 3.21. Effective masses for electrons (m^-) and holes (m^+) calculated from DFT for CASe, Bi-CASe and Sn-CASe

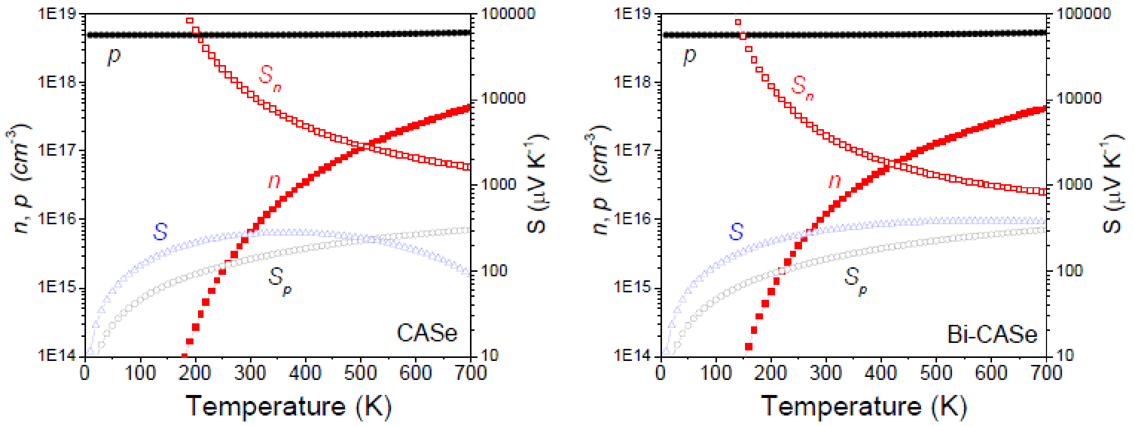

Figure 3.22. Temperature dependence of the charge carrier concentrations (n, p) and Seebeck

coefficients (S_n, S_p, S) of Cu_3SbSe_4 (left) and $Cu_3Sb_{0.875}Bi_{0.125}Se_4$ (right) calculated using equations 2-8 and considering $p_0 = 5\times10^{18}$.

Notice how in spite of the lower bandgap of Bi-CASe, and thus the higher charge carrier concentrations associated to thermal generation, the reduced m_e^* in this compound translates in a lower S_n and thus an overall higher Seebeck coefficient. It should be noticed that the introduction of Sn also translates into larger differences in the effective masses of holes and electrons and that in spite of the strong band gap decrease in this material, the calculated Seebeck coefficients at moderate doping concentrations are higher than those of CASe and even Bi-CASe. However, the introduction of sufficient amounts of Sn to modify the band structure has associated the injection of very large amounts of charge carrier, which inevitably results in overall lower Seebeck coefficients. Thus, the introduction of both dopants, Sn to control charge carrier concentration and Bi to modify the band structure is necessary to optimize performance in this material.

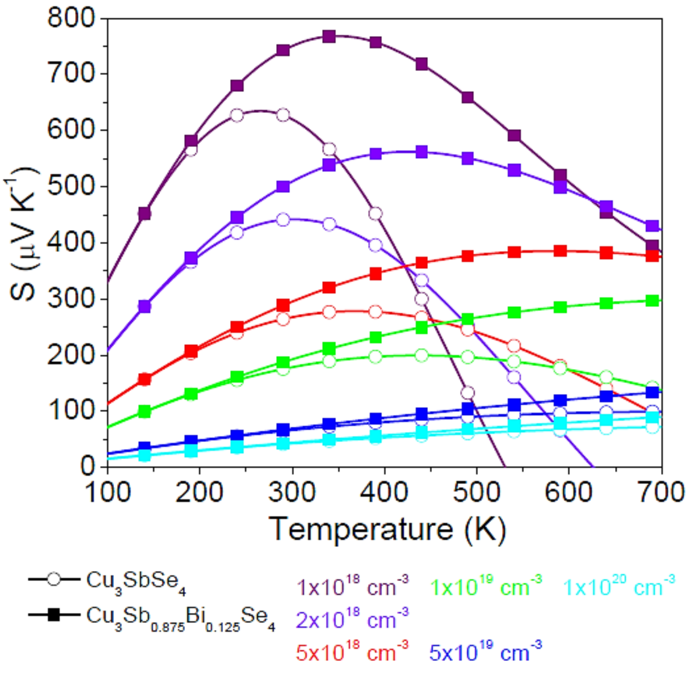

Figure 3.23. Temperature dependence of the Seebeck coefficient (S) of Cu3SbSe4 and $Cu_3Sb_{0.875}Bi_{0.125}Se_4$ calculated using equation 1-9 for different doping levels as indicated by the different colors.

To take advantage of the carrier concentration control provided by Sn doping and the relative increase of S with the inclusion of Bi, we prepared a series of Sn,Bi-doped CASe samples. Figure 3.24 shows the temperature dependence of the electrical and thermal transport properties of $Cu_3Sb_{0.98-x}Sn_xBi_{0.02}Se_4$. These samples showed a degenerated electrical conductivity behavior, associated to a large level of doping. σ increased with the Sn content as in the Sn-CASe series. Surprisingly, σ of co-doped Sn,Bi-CASe was systematically larger than that of Sn-CASe samples with the same amount of Sn. Hall measurements showed the presence of high charge carrier concentrations, up to $p=1x10^{20}$ cm^{-3} for $Cu_3Sb_{0.88}Sn_{0.10}Bi_{0.02}Se_4$ (Table 3.5). On the other hand, S decreased for all Sn,Bi-CASe samples when compared with plain CASe due to the large increase of charge carrier concentration. However, S values of co-doped materials slightly increased when compared with Sn-CASe with equivalent electrical conductivities, proving the positive effect of the Bi addition.

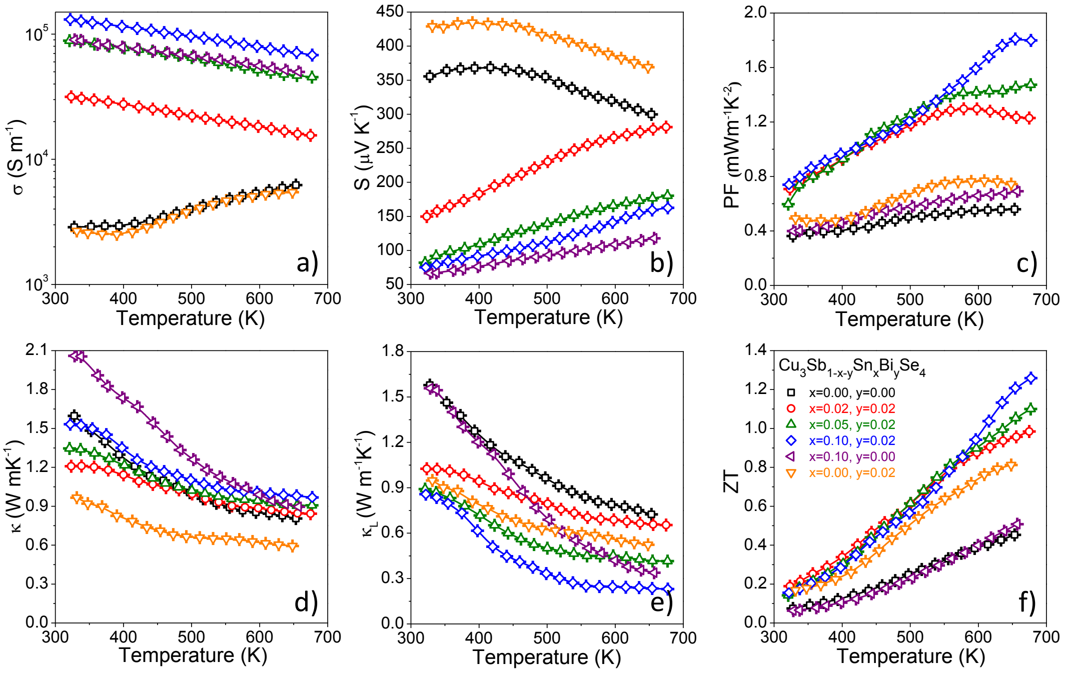

Figure 3.24. Temperature dependence of (a) electric conductivity (σ), (b) Seebeck coefficient (S), (c) power factor (PF), (d) thermal conductivity (κ), (e) lattice thermal conductivity (κ_L) and (d) TE figure of merit (ZT) of $Cu_3Sb_{0.98-x}Sn_xBi_{0.02}Se_4$.

Overall, the PFs of co-doped Sn,Bi-CASe were significantly higher than those of Sn- or Bi-CASe, and reached up to around 1.81 $mWm^{-1}K^{-2}$ at 654 K for $Cu_3Sb_{0.88}Sn_{0.10}Bi_{0.02}Se_4$ (Figure 3.24a). Like in the case of Sn-CASe, in Sn,Bi-CASe the dependence of κ with the dopant concentration showed a competition between the decrease of κ_L associated with the introduction of lattice defects and the increase of κ_e associated to the much higher carrier concentrations (Figures 3.24d and 3.24e). Overall, ZT values up to 1.26 at 673 K were obtained for $Cu_3Sb_{0.88}Sn_{0.10}Bi_{0.02}Se_4$, which is among the best ZT values obtained with a Pb- and Te-free material in this middle temperature range (Figure 3.24f, Table 3.7).

These materials were further employed to fabricate simple TE generator prototypes with ring geometry (Figure 3.26). When compared with conventional flat devices, the ring design optimizes the thermal contact between the TE generator and the walls of a hot or cold pipe, and at the same time minimizes the module form factor and provides improved mechanical stability. In a ring-based module, rings with n and p type materials could be placed thermally in parallel and electrically in series to harvest radial heat fluxes (Figure 3.26a). Alternatively, multiple n and p elements could be integrated within each ring (Figure 3.26d). The module, containing multiple n- and p-type rings or several multi-element rings, makes use of thin thermal and electrical insulators between rings to alternatively contact the outer and inner rings as shown in Figure 3.26a.

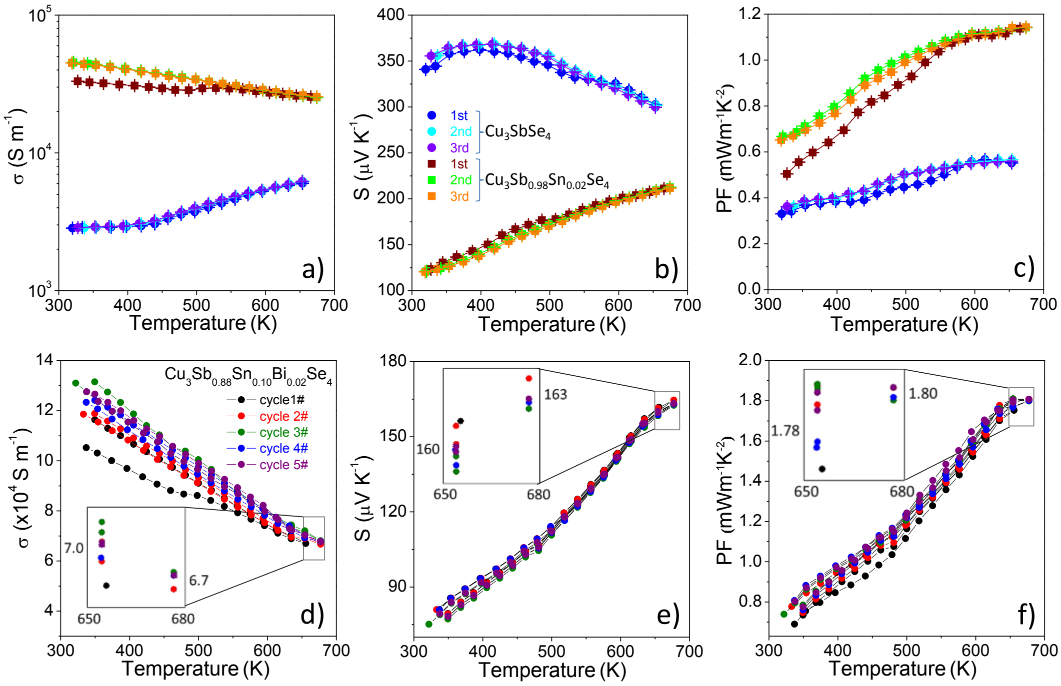

Figure 3.25. (a-c) Temperature dependence of the electrical conductivity (σ), Seebeck coefficient (S) and power factor (PF) of Cu_3SbSe_4 and $Cu_3Sb_{0.98}Sn_{0.02}Se_4$ measured 3 consecutive times during heating up to around 673 K. No pre-stabilization treatment was carried out before the first measurement. (d-f) display the thermoelectric properties of $Cu_3Sb_{0.88}Sn_{0.10}Bi_{0.02}Se_4$ pellet measured for 5 consecutive up-down cycles between room temperature and up to 673K. From here we can find that these up-down cycles measurements obtained during the first temperature ramp are slightly different from the ones obtained in posterior cycles, especially at low temperatures. We also observed a slight increase in electrical conductivity with the cycle number and no appreciable variation of the Seebeck coefficient in the low temperature range of the measurement.

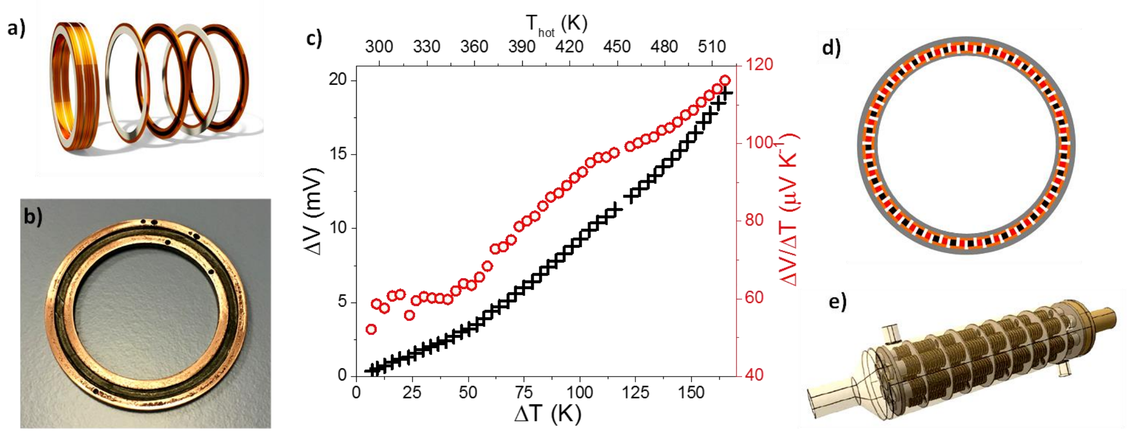

Figure 3.26. a) Scheme of a basic ring-based TE module, b) $Cu_3Sb_{0.88}Sn_{0.10}Bi_{0.02}Se_4$-based ring, c) Voltage obtained from a single $Cu_3Sb_{0.88}Sn_{0.10}Bi_{0.02}Se_4$ ring as a function of the temperature gradient when increasing the temperature at the hot side (top axis). Red open circles display the effective Seebeck coefficient of the ring. d) Scheme of a ring with

multiple p and n type elements (in black and red). e) Scheme of a multi-ring system to be coupled to a hot pipe including a jacket for the circulation of cooling fluid.

Single p-type $Cu_3Sb_{0.88}Sn_{0.10}Bi_{0.02}Se_4$ rings, with inner and outer diameter of 28 mm and 39 mm, respectively, and with copper ring thicknesses of 2 mm and thus a CASe thickness of 1.5 mm were assembled and tested in a custom made set-up as detailed in the experimental part (Figure 3.26b). The inner ring temperature was raised up to 250 °C using a heat cartridge within a cylindrical metal block, while maintaining the outside ring at lower temperature using a metal block cooled using commercial thermoelectric devices. Figure 9c shows the voltage obtained from a single p-type ring as a function of the temperature gradient. Open circuit voltages close to 20 mV were obtained for a single TE element exposed to a temperature gradient of 160 °C. Being the electrical resistance of the ring $< 0.4\ \Omega$, this voltage translates into a > 1 mW of generated electric power for each single TE element. The combination of several TE p-n pairs in each ring (Figure 9d) and of several rings into a module (Figures 3.26e) could provide electric powers on the order of 100 W for $200 - 300$ °C temperature gradients as those available among other in exhaust gas pipes of vehicles with combustion engines. Such power could suffice to supply all the electric energy spent by the vehicle, allowing the alternator replacement and thus improving the vehicle fuel efficiency.

Table 3.7. State-of-art thermoelectric performance values for Pb- and Te-free Cu- and Ag-based chalcogenides and some other Pb- and Te- free compounds at 673 K (excepted when otherwise specified).

Material	σx10^3 Sm^{-1}	S, µV/K	PF, mWm^{-1}K^{-2}	κ, Wm^{-1}K^{-1}	ZT	Ref.
$Cu_{0.975}BiSeO$	3.2	230	0.17	0.50	0.23	76
Cu_2GeSe_3	5.2	160	0.13	0.39	0.23	77
$CuFeS_2$	0.33	816	0.23	0.43	0.26 (500 K)	78
Cu_2SnSe_3	6.0	215	0.28	0.68	0.27	79
Cu_2SnSe_3	12	299	1.07	1.91	0.34 (598 K)	80
$Cu_{2.15}Zn_{0.85}GeSe_{3.9}$	25	100	0.25	0.41	0.41	81

$Cu_2Sn_{0.90}In_{0.10}Se_3$	49	150	1.10	1.52	0.49	82
$Cu_3Sb_{0.98}Sn_{0.02}Se_4$	24	200	0.96	1.10	0.50 (575 K)	33
$Cu_2CdSnSe_4$	24	170	0.70	0.85	0.55	83
$AgBiSe_{1.98}Cl_{0.02}$	21	-150	0.47	0.56	0.56	84
$Cu_3Sb_{0.97}Al_{0.03}Se_4$	20	230	1.05	1.08	0.58 (600 K)	69
$Cu_{2.15}Cd_{0.85}SnSe_{3.9}$	7.9	165	0.22	0.25	0.59	85
$Cu_{2.1}Cd_{0.9}SnSe_4$	20	155	0.48	0.55	0.59	86
$Cu_{1.85}Ag_{0.15}Sn_{0.85}In_{0.15}Se_3$	46	140	0.90	1.01	0.60	87
$Cu_2Sn_{0.90}In_{0.10}Se_3$	50	150	1.13	1.12	0.68	88
$CuBi_{0.875}Ba_{0.125}SeO$	24	152	0.56	0.55	0.69	89
$Cu_3Sb_{0.98}Bi_{0.02}Se_4$	10	325	1.10	0.90	0.70 (600 K)	53
$AgSb_{0.96}Pb_{0.04}Se_2$	2.3	375	0.32	0.30	0.70	90
$Cu_3Sb_{0.975}Sn_{0.025}Se_4$	23	235	1.30	1.17	0.75	20
$Ag_{0.96}Nb_{0.04}BiSe_2$	19	-200	0.76	0.64	0.80	91
β-Cu_2Se	24	210	1.07	0.90	0.80	92
β-Zn_4Sb_3	33	183	1.09	0.75	0.80 (550 K)	93
$Cu_3Sb_{0.97}Ge_{0.03}Se_{2.8}S_{1.2}$	22	235	1.20	0.91	0.89 (650 K)	94
CuAgSe	10	202	0.41	0.28	0.90 (623 K)	95
$Cu_{1.97}S$	16	210	0.70	0.52	0.91	96
$AgSb_{0.99}Na_{0.01}Se_2$	4.4	340	0.51	0.37	0.92	97
$Cu_3Sb_{0.98}Sn_{0.02}Se_4$	29	230	1.55	1.10	0.95	32
$AgSb_{0.98}Ba_{0.02}Se_2$	4.2	350	0.51	0.35	0.98	98
$AgSb_{0.98}Cd_{0.02}Se_2$	5.4	325	0.57	0.37	0.98 (640 K)	99
$Ag_2Se_{1.08}$	20	-125	0.32	1.30	0.99 (400 K)	100
$AgSb_{0.98}Mg_{0.02}Se_2$	6.7	300	0.60	0.40	1.00	98
$AgSbSe_2$–ZnSe	5.0	348	0.60	0.40	1.00	101
$Mm_{0.9}Fe_{3.1}Co_{0.9}Sb_{12}$	75	202	3.06	1.96	1.05	102
$AgBi_{0.5}Sb_{0.5}Se_2$	3.3	275	0.25	0.13	1.07 (550 K)	103
$YbCd_{1.9}Mg_{0.1}Sb_2$	32	230	1.70	1.03	1.08 (650K)	104
$AgSb_{0.98}Bi_{0.02}Se_2$	5.3	330	0.58	0.35	1.10	90
$In_{0.27}Co_4Sb_{11.9}$	80	-225	4.06	2.5	1.13	105
$Cu_{11}MnSb_4S_{13}$	28	145	0.58	0.29	1.13 (575 K)	106

$In_{0.2}Co_4Sb_{12}$	63	-245	3.77	1.95	1.20 (620 K)	[107]
$In_{0.2}Ce_{0.05}Yb_{0.1}Co_4Sb_{12}$	44	-252	2.81	1.45	1.20 (620 K)	[107]
$In_{0.25}Co_4Sb_{12}$	62	-270	4.53	2.17	1.20 (575 K)	[108]
$AgSb_{0.99}Sn_{0.01}Se_2$	9.2	295	0.80	0.44	1.21 (660 K)	[109]
$AgBiSe_2$	2.3	450	0.47	0.25	1.25	[110]
$Cu_3Sb_{0.88}Sn_{0.10}Bi_{0.02}Se_4$	68	163	1.80	0.97	1.26	This work
$In_{0.2}Ce_{0.15}Co_4Sb_{12}$	63	-240	3.65	1.63	1.40 (625 K)	[107]
$(Zr_{0.5}Hf_{0.5})_{0.5}Ti_{0.5}NiSn_{0.998}Sb_{0.002}$	68	-300	6.14	2.85	1.45	[111]
$Ti_{0.5}(Zr_{0.5}Hf_{0.5})_{0.5}NiSn_{0.998}Sb_{0.002}$	65	-310	6.25	2.90	1.45	[112]
SnSe	30	280	2.35	0.75	2.0	[113]

3.5 Conclusions

In summary, a novel solution-based strategy to produce monodisperse CASe NCs and Sn- and Bi-doped CASe NCs at the gram scale was presented in this chapter. The effect of Sn- and Bi-doping on the TE performance of CASe nanomaterials obtained via hot press was discussed. Sn was demonstrated to be a p-type dopant which effectively helped to control charge carrier concentration. On the other hand, the introduction of Bi conveniently modified the electronic band structure of the compound resulting in higher S values. We tentatively associated the Bi effect to a reduction of the negative contribution of conduction electrons on the Seebeck coefficient, but further theoretical calculations and detailed experimental results are required to clarify the exact Bi role in such a complex system. Besides, the introduction of these impurities helped to reduce the material lattice thermal conductivity. By optimizing the amount of Sn in a Bi-doped material, ZT values up to 1.26 at 673 K were obtained for $Cu_3Sb_{0.88}Sn_{0.10}Bi_{0.02}Se_4$, which is among the best ZT values obtained with a Pb- and Te-free material in this middle temperature range, with the additional advantage of the high versatility and low cost associated to solution processing technologies. Taking advantage of this processability, we fabricated innovative ring-shaped TE generators, which provided 1 mW of electric power per TE element with a 160 °C temperature gradient.

3.6 References

1. Yuan, M.; Mitzi, D. B.; Liu, W.; Kellock, A. J.; Chey, S. J.; Deline, V. R. *Chemistry of Materials* **2009,** 22, (2), 285-287.
2. Zhao, Y.; Burda, C. *Energy & Environmental Science* **2012,** 5, (2), 5564-5576.
3. Aldakov, D.; Lefrançois, A.; Reiss, P. *Journal of Materials Chemistry C* **2013,** 1, (24), 3756-3776.
4. Fan, F.-J.; Wu, L.; Yu, S.-H. *Energy & Environmental Science* **2014,** 7, (1), 190-208.
5. Singh, A.; Singh, A.; Ciston, J.; Bustillo, K.; Nordlund, D.; Milliron, D. J. *J. Am. Chem. Soc.* **2015,** 137, (20), 6464-6467.
6. Van Der Stam, W.; Berends, A. C.; de Mello Donega, C. *ChemPhysChem* **2016**, 17, (5), 559-581.
7. Ibáñez, M.; Cadavid, D.; Zamani, R.; García-Castelló, N.; Izquierdo-Roca, V.; Li, W.; Fairbrother, A.; Prades, J. D.; Shavel, A.; Arbiol, J. *Chemistry of Materials* **2012,** 24, (3), 562-570.
8. Shi, J.; Li, Z.; Zhang, D.; Liu, Q.; Sun, Z.; Huang, S. *Progress in Photovoltaics: Research and Applications* **2011,** 19, (2), 160-164.
9. Yu, X.; An, X.; Shavel, A.; Ibanez, M.; Cabot, A. *Journal of Materials Chemistry A* **2014,** 2, (31), 12317-12322.
10. Chirilă, A.; Buecheler, S.; Pianezzi, F.; Bloesch, P.; Gretener, C.; Uhl, A. R.; Fella, C.; Kranz, L.; Perrenoud, J.; Seyrling, S. *Nature materials* **2011,** 10, (11), 857-861.
11. Shavel, A.; Cadavid, D.; Ibanez, M.; Carrete, A.; Cabot, A. *Journal of the American Chemical Society* **2012,** 134, (3), 1438-1441.
12. Carrete, A.; Shavel, A.; Fontané, X.; Montserrat, J.; Fan, J.; Ibáñez, M.; Saucedo, E.; Pérez-Rodríguez, A.; Cabot, A. *Journal of the American Chemical Society* **2013,** 135, (43), 15982-15985.
13. Shavel, A.; Ibáñez, M.; Luo, Z.; De Roo, J.; Carrete, A.; Dimitrievska, M.; Genç, A.; Meyns, M.; Pérez-Rodríguez, A.; Kovalenko, M. V. *Chemistry of Materials* **2016,** 28, (3), 720-726.
14. Yu, X.; Shavel, A.; An, X.; Luo, Z.; Ibanez, M.; Cabot, A. *Journal of the American Chemical Society* **2014,** 136, (26), 9236-9239.
15. Lesnyak, V.; George, C.; Genovese, A.; Prato, M.; Casu, A.; Ayyappan, S.; Scarpellini, A.; Manna, L. *ACS nano* **2014,** 8, (8), 8407-8418.
16. Shi, L.; Yin, P.; Zhu, H.; Li, Q. *Langmuir* **2013,** 29, (27), 8713-8717.
17. Ibáñez, M.; Zamani, R.; LaLonde, A.; Cadavid, D.; Li, W.; Shavel, A.; Arbiol, J.; Morante, J. R.; Gorsse, S.; Snyder, G. J. *Journal of the American Chemical Society* **2012,** 134, (9), 4060-4063.
18. Berger, L. I., Springer Science & Business Media: 2012.

19. Wei, T.-R.; Wang, H.; Gibbs, Z. M.; Wu, C.-F.; Snyder, G. J.; Li, J.-F. *Journal of Materials Chemistry A* **2014,** 2, (33), 13527-13533.
20. Yang, C.; Huang, F.; Wu, L.; Xu, K. *Journal of Physics D: Applied Physics* **2011,** 44, (29), 295404.
21. L. I. Berger; V. D. Prochukhan. Ternary Diamond-Like Semiconductors **1969,** 111-118.
22. Pang, X.; Zhao, L.; Han, W.; Xin, X.; Lin, Z. *Nature nanotechnology* **2013,** 8, (6), 426-431.
23. Chang, J.; Waclawik, E. R. *RSC Advances* **2014,** 4, (45), 23505-23527.
24. van Embden, J.; Chesman, A. S.; Jasieniak, J. J. *Chemistry of Materials* **2015,** 27, (7), 2246-2285.
25. Talapin, D. V.; Lee, J.-S.; Kovalenko, M. V.; Shevchenko, E. V. *Chemical reviews* **2009,** 110, (1), 389-458.
26. Ibáñez, M.; Zamani, R.; Gorsse, S.; Fan, J.; Ortega, S.; Cadavid, D.; Morante, J. R.; Arbiol, J.; Cabot, A. *ACS nano* **2013,** 7, (3), 2573-2586.
27. Ibáñez, M.; Luo, Z.; Genç, A.; Piveteau, L.; Ortega, S.; Cadavid, D.; Dobrozhan, O.; Liu, Y.; Nachtegaal, M.; Zebarjadi, M.; Arbiol, J.; Kovalenko, M.V.; Cabot, A. *Nature communications* **2016**, 7, 10766.
28. van Embden, J.; Tachibana, Y. *J. Mater. Chem.* **2012,** 22, (23), 11466-11469.
29. van Embden, J.; Latham, K.; Duffy, N. W.; Tachibana, Y. *Journal of the American Chemical Society* **2013,** 135, (31), 11562-11571.
30. Ramasamy, K.; Sims, H.; Butler, W. H.; Gupta, A. *Chemistry of Materials* **2014,** 26, (9), 2891-2899.
31. Chen, K.; Zhou, J.; Chen, W.; Zhou, P.; He, F.; Liu, Y. *Particle & Particle Systems Characterization* **2015,** 32, (11), 999-1005.
32. Li, D.; Li, R.; Qin, X.-Y.; Song, C.-J.; Xin, H.-X.; Wang, L.; Zhang, J.; Guo, G.-l.; Zou, T.-H.; Liu, Y.-F. *Dalton Transactions* **2014,** 43, (4), 1888-1896.
33. Wu, Y.; Qiao, X.; Fan, X.; Zhang, X.; Cui, S.; Wan, J. *Journal of Nanoparticle Research* **2015,** 17, (7), 1-7.
34. Balow, R. B.; Tomlinson, E. P.; Abu-Omar, M. M.; Boudouris, B. W.; Agrawal, R. *Journal of Materials Chemistry A* **2016,** 4, (6), 2198-2204.
35. Connell, M. A.; Bowyer, P. J.; Bone, P. A.; Davis, A. L.; Swanson, A. G.; Nilsson, M.; Morris, G. A. *Journal of Magnetic Resonance* **2009,** 198, (1), 121-131.
36. Sinnaeve, D. *Concepts in Magnetic Resonance Part A* **2012,** 40, (2), 39-65.
37. Chan, M.; Ceder, G. *Physical Review Letters* **2010,** 105, (19), 196403.
38. Zhang, Y.; Xi, L.; Wang, Y.; Zhang, J.; Zhang, P.; Zhang, W. *Computational Materials Science* **2015,** 108, 239-249.
39. Do, D.; Ozolins, V.; Mahanti, S. D.; Lee, M.-S.; Zhang, Y.; Wolverton, C. *Journal of*

Physics: Condensed Matter **2012,** 24, (41), 415502.

40. Do, D. T.; Mahanti, S. D. *Journal of Physics and Chemistry of Solids* **2014,** 75, (4), 477-485.
41. Do, D. T.; Mahanti, S. *Journal of Alloys and Compounds* **2015,** 625, 346-354.
42. Skoug, E. J.; Cain, J. D.; Majsztrik, P.; Kirkham, M.; Lara-Curzio, E.; Morelli, D. T. *Sci. Adv. Mater.* **2011,** 3, (4), 602-606.
43. Nakanishi, H.; Endo, S.; Irie, T. *Japanese Journal of Applied Physics***1969,** 8, (4), 443.
44. Perdew, J. P.; Burke, K.; Ernzerhof, M. *Physical Review Letters* **1996,** 77, (18), 3865.
45. Dudarev, S.; Botton, G.; Savrasov, S.; Humphreys, C.; Sutton, A. *Physical Review B* **1998,** 57, (3), 1505.
46. Kresse, G.; Hafner, J. *Physical Review B* **1993,** 47, (1), 558.
47. Kresse, G.; Furthmüller, J. *Physical Review B* **1996,** 54, (16), 11169.
48. Blöchl, P. E. *Physical Review B* **1994,** 50, (24), 17953.
49. Kresse, G.; Joubert, D. *Physical Review B* **1999,** 59, (3), 1758.
50. Methfessel, M.; Paxton, A. *Physical Review B* **1989,** 40, (6), 3616.
51. Monkhorst, H. J.; Pack, J. D. *Physical Review B* **1976,** 13, (12), 5188.
52. Madsen, G. K.; Singh, D. J. Computer Physics Communications **2006,** 175, (1), 67-71.
53. Li, X.; Li, D.; Xin, H.; Zhang, J.; Song, C.; Qin, X. *Journal of Alloys and Compounds* **2013,** 561, 105-108.
54. Shannon, R. t. *Acta Crystallographica Section A: Crystal Physics, Diffraction, Theoretical and General Crystallography* **1976,** 32, (5), 751-767.
55. Li, S.; Zhao, Z.; Liu, Q.; Huang, L.; Wang, G.; Pan, D.; Zhang, H.; He, X. *Inorganic Chemistry* **2011,** 50, (23), 11958-11964.
56. NIST-XPS database, v., http://srdata.nist.gov/xps/, accessed Nov 30, 2011.
57. Partain, L.; Schneider, R.; Donaghey, L.; Mcleod, P. *Journal of Applied Physics* **1985,** 57, (11), 5056-5065.
58. Do, D.; Ozolins, V.; Mahanti, S. D.; Lee, M. S.; Zhang, Y.; Wolverton, C. *Journal of physics. Condensed matter : an Institute of Physics journal* **2012,** 24, (41), 415502.
59. Skoug, E. J.; Morelli, D. T. *Physical Review Letters* **2011,** 107, (23), 235901.
60. Chiang, M.-Y.; Chang, S.-H.; Chen, C.-Y.; Yuan, F.-W.; Tuan, H.-Y. *The Journal of Physical Chemistry C* **2011,** 115, (5), 1592-1599.
61. Politano, A.; Caputo, M.; Nappini, S.; Bondino, F.; Magnano, E.; Aliev, Z.; Babanly, M.; Goldoni, A.; Chiarello, G.; Chulkov, E. *The Journal of Physical Chemistry C* **2014,** 118, (37), 21517-21522.
62. Nascimento, V.; De Carvalho, V.; Paniago, R.; Soares, E.; Ladeira, L.; Pfannes, H.

Journal of Electron Spectroscopy and Related Phenomena **1999,** 104, (1), 99-107.

63. Song, L.; Zhang, S.; Chen, C.; Hu, X.; Wei, Q. *Chemical Engineering Journal* **2011,** 171, (3), 1454-1457.
64. Moulder, J. F.; Stickle, W. F.; Sobol, P. E.; Bomben, K. D., *Physical Electronics Division, Perkin-Elmer Corporation:* 1992.
65. Hens, Z.; Martins, J. C. *Chemistry of Materials* **2013,** 25, (8), 1211-1221.
66. De Roo, J.; De Keukeleere, K.; Hens, Z.; Van Driessche, I. *Dalton Transactions* **2016**.
67. Fritzinger, B.; Moreels, I.; Lommens, P.; Koole, R.; Hens, Z.; Martins, J. C. *Journal of the American Chemical Society* **2009,** 131, (8), 3024-3032.
68. Dierick, R.; Van den Broeck, F.; De Nolf, K.; Zhao, Q.; Vantomme, A.; Martins, J. C.; Hens, Z. *Chemistry of Materials* **2014,** 26, (20), 5950-5957.
69. Li, Y.; Qin, X.; Li, D.; Li, X.; Liu, Y.; Zhang, J.; Song, C.; Xin, H. *Rsc Advances* **2015,** 5, (40), 31399-31403.
70. L. I. Berger, S. M., CRC Press, Boca Raton, FL, **1997**, 267.
71. A. Pfitzner, Z. K. **1995,** 209, 685–685.
72. Hisayuki Nakanishi and Saburo Endo and Taizo, I. *Japanese Journal of Applied Physics* **1969,** 8, (4), 443.
73. Dat Do and Vidvuds Ozolins and, S. D. M. a. M.-S. L. a. Y. Z. a. C. W. *Journal of Physics: Condensed Matter* **2012,** 24, (41), 415502.
74. Gong, J.; Hong, A.; Shuai, J.; Li, L.; Yan, Z.; Ren, Z.; Liu, J.-M. *Physical Chemistry Chemical Physics* **2016,** 18, 16566-16574.
75. Wang, S.; Yang, J.; Toll, T.; Yang, J.; Zhang, W.; Tang, X. Scientific Reports **2015,** 5, 10136.
76. Liu, Y.; Zhao, L.-D.; Liu, Y.; Lan, J.; Xu, W.; Li, F.; Zhang, B.-P.; Berardan, D.; Dragoe, N.; Lin, Y.-H. *Journal of the American Chemical Society* **2011,** 133, (50), 20112-20115.
77. Ibáñez, M.; Zamani, R.; Li, W.; Cadavid, D.; Gorsse, S. p.; Katcho, N. A.; Shavel, A.; López, A. M.; Morante, J. R.; Arbiol, J.; Cabot, A. *Chemistry of Materials* **2012,** 24, (23), 4615-4622.
78. Liang, D.; Ma, R.; Jiao, S.; Pang, G.; Feng, S. *Nanoscale* **2012,** 4, (20), 6265-6268.
79. Ibáñez, M.; Cadavid, D.; Anselmi-Tamburini, U.; Zamani, R.; Gorsse, S.; Li, W.; López, A. M.; Morante, J. R.; Arbiol, J.; Cabot, A. *Journal of Materials Chemistry A* **2013,** 1, (4), 1421-1426.
80. Song, J.-M.; Liu, Y.; Niu, H.-L.; Mao, C.-J.; Cheng, L.-J.; Zhang, S.-Y.; Shen, Y.-H. *Journal of Alloys and Compounds* **2013,** 581, 646-652.
81. Ibáñez, M.; Zamani, R.; LaLonde, A.; Cadavid, D.; Li, W.; Shavel, A.; Arbiol, J.; Morante, J. R.; Gorsse, S.; Snyder, G. J.; Cabot, A. *Journal of the American*

Chemical Society **2012,** 134, (9), 4060-4063.

82. Shi, X.; Xi, L.; Fan, J.; Zhang, W.; Chen, L. *Chemistry of Materials* **2010,** 22, (22), 6029- 6031.
83. Fan, F.-J.; Yu, B.; Wang, Y.-X.; Zhu, Y.-L.; Liu, X.-J.; Yu, S.-H.; Ren, Z. *Journal of the American Chemical Society* **2011,** 133, (40), 15910-15913.
84. Guin, S. N.; Srihari, V.; Biswas, K. *Journal of Materials Chemistry A* **2015,** 3, (2), 648-655.
85. Ibáñez, M.; Cadavid, D.; Zamani, R.; García-Castelló, N.; Izquierdo-Roca, V.; Li, W.; Fairbrother, A.; Prades, J. D.; Shavel, A.; Arbiol, J.; Pérez-Rodríguez, A.; Morante, J. R.; Cabot, A. *Chemistry of Materials* **2012,** 24, (3), 562-570.
86. Liu, M. L.; Chen, I. W.; Huang, F. Q.; Chen, L. D. *Advanced Materials* **2009,** 21, (37), 3808-3812.
87. Li, Y.; Liu, G.; Cao, T.; Liu, L.; Li, J.; Chen, K.; Li, L.; Han, Y.; Zhou, M. *Advanced Functional Materials* **2016**.
88. Li, Y.; Liu, G.; Li, J.; Chen, K.; Li, L.; Han, Y.; Zhou, M.; Xia, M.; Jiang, X.; Lin, Z. *New Journal of Chemistry* **2016**.
89. Li, J.; Sui, J.; Pei, Y.; Barreteau, C.; Berardan, D.; Dragoe, N.; Cai, W.; He, J.; Zhao, L.-D. *Energy & Environmental Science* **2012,** 5, (9), 8543-8547.
90. Guin, S. N.; Chatterjee, A.; Negi, D. S.; Datta, R.; Biswas, K. *Energy & Environmental Science* **2013,** 6, (9), 2603-2608.
91. Pan, L.; Bérardan, D.; Dragoe, N. *Journal of the American Chemical Society* **2013,** 135, (13), 4914-4917.
92. Liu, H.; Shi, X.; Xu, F.; Zhang, L.; Zhang, W.; Chen, L.; Li, Q.; Uher, C.; Day, T.; Snyder, G. J. *Nature materials* **2012,** 11, (5), 422.
93. Toberer, E. S.; Rauwel, P.; Gariel, S.; Taftø, J.; Snyder, G. J. *Journal of materials chemistry* **2010,** 20, (44), 9877-9885.
94. Skoug, E. J.; Cain, J. D.; Morelli, D. T. *Applied Physics Letters* **2011,** 98, (26), 261911.
95. Han, C.; Sun, Q.; Cheng, Z. X.; Wang, J. L.; Li, Z.; Lu, G. Q.; Dou, S. X. *Journal of the American Chemical Society* **2014,** 136, (50), 17626-17633.
96. Coronado, H.; Peña, J. P.; Muñoz, R. E.; Ortega, E.; Flórez, J. *Revista Agropecuaria y Agroindustrial La Angostura* **2014,** 1, (1).
97. Cai, S.; Liu, Z.; Sun, J.; Li, R.; Fei, W.; Sui, J. *Dalton Transactions* **2015,** 44, (3), 1046-1051.
98. Liu, Z.; Shuai, J.; Geng, H.; Mao, J.; Feng, Y.; Zhao, X.; Meng, X.; He, R.; Cai, W.; Sui, J. *ACS Applied Materials & Interface* **2015,** 7, (41), 23047-23055.
99. Guin, S. N.; Chatterjee, A.; Biswas, K. *RSC Advances* **2014,** 4, (23), 11811-11815.
100. Mi, W.; Qiu, P.; Zhang, T.; Lv, Y.; Shi, X.; Chen, L. *Applied Physics Letters* **2014,**

104, (13), 133903.

101. Guin, S. N.; Negi, D. S.; Datta, R.; Biswas, K. *Journal of Materials Chemistry A* **2014,** 2, (12), 4324-4331.
102. Dahal, T.; Gahlawat, S.; Jie, Q.; Dahal, K.; Lan, Y.; White, K.; Ren, Z. *Journal of Applied Physics* **2015,** 117, (5), 055101.
103. Xiao, C.; Xu, J.; Cao, B.; Li, K.; Kong, M.; Xie, Y. *Journal of the American Chemical Society* **2012,** 134, (18), 7971-7977.
104. Cao, Q.; Zheng, J.; Zhang, K.; Ma, G. *Journal of Alloys and Compounds* **2016,** 680, 278-282.
105. Tang, Y.; Qiu, Y.; Xi, L.; Shi, X.; Zhang, W.; Chen, L.; Tseng, S.-M.; Chen, S.-w.; Snyder, G. J. *Energy & Environmental Science* **2014,** 7, (2), 812-819.
106. Heo, J.; Laurita, G.; Muir, S.; Subramanian, M. A.; Keszler, D. A. *Chemistry of Materials* **2014,** 26, (6), 2047-2051.
107. Biswas, K.; Good, M. S.; Roberts, K. C.; Subramanian, M.; Hendricks, T. J. *Journal of Materials Research* **2011,** 26, (15), 1827-1835.
108. He, T.; Chen, J.; Rosenfeld, H. D.; Subramanian, M. *Chemistry of materials* **2006,** 18, (3), 759-762.
109. Li, D.; Qin, X.; Zou, T.; Zhang, J.; Ren, B.; Song, C.; Liu, Y.; Wang, L.; Xin, H.; Li, J. *Journal of Alloys and Compounds* **2015,** 635, 87-91.
110. Xiao, C.; Qin, X.; Zhang, J.; An, R.; Xu, J.; Li, K.; Cao, B.; Yang, J.; Ye, B.; Xie, Y. *Journal of the American Chemical Society* **2012,** 134, (44), 18460-18466.
111. Sakurada, S.; Shutoh, N. *Applied Physics Letters* **2005,** 86, (8), 082105.
112. Shutoh, N.; Sakurada, S. *Journal of Alloys and Compounds* **2005,** 389, (1), 204-208.
113. Zhao, L.-D.; Tan, G.; Hao, S.; He, J.; Pei, Y.; Chi, H.; Wang, H.; Gong, S.; Xu, H.; Dravid, V. P. *Science* **2016,** 351, (6269), 141-144.

Chapter 4

Thermoelectric Properties of Semiconductor-Metal Composites Produced by Particle Blending

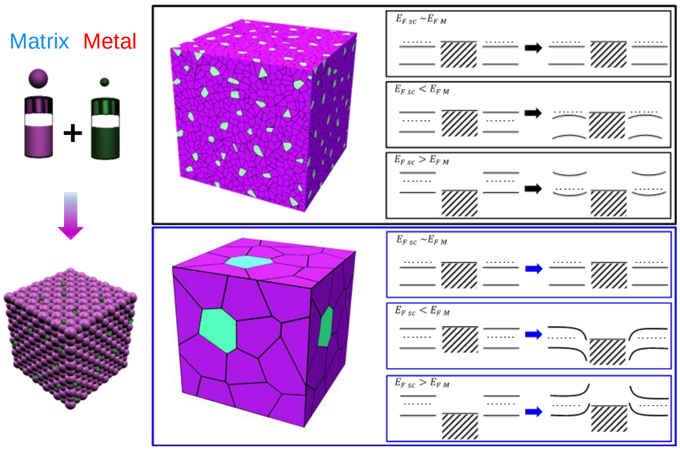

4.1 Abstract

In the quest for more efficient thermoelectric material able to convert thermal to electrical energy and vice versa, composites that combine a semiconductor host with a large Seebeck coefficient and metal nanodomains that provide phonon scattering and free charge carriers are particularly appealing. Here, we present our experimental results on the thermal and electrical transport properties of PbS-metal composites produced by a versatile particle blending procedure, and where the metal is able to inject electrons to the intrinsic PbS host. We compare the thermoelectric performance of microcrystalline composites with those of nanocrystalline composites. The electrical conductivity of the microcrystalline host can be increased several orders of magnitude with the metal inclusion, while relatively high Seebeck coefficient can be simultaneously conserved. On the other hand, a nanostructured host is not able to maintain a band bending at its interface

with the metal and thus it is flooded with electrons, which translates into even higher electrical conductivities that the microcrystalline material, but much lower Seebeck coefficients.

4.2 Introduction

The cost-effective use of solid state thermoelectric devices to directly convert heat to electricity and vice versa requires designing and engineering more efficient materials. In this direction, composite materials offer several advantages.[1-8] The thermal conductivity of composite materials can be strongly reduced with respect to their components by effective phonon scattering at the interfaces of two dissimilar materials. Additionally, high charge carrier concentrations can be reached by modulation doping, that is by introducing electronic doping in just one of the phases, thus minimizing the influence of ionized doping impurities on charge carrier transport when this takes place through the other phase.[9] Furthermore, higher Seebeck coefficients can be obtained by selectively scattering low energy charge carriers at interfaces.[10] Or alternatively, by properly selecting the constituent materials and engineering the composite, the minority phase can be made invisible to charge carriers.[11-13] Besides, in particular cases, inclusions can even improve charge carrier mobility by reducing intergrain potential barriers in the matrix material, as recently observed in semiconductor-metal nanocomposites.[14]

This last type of composite, obtained from combining a semiconductor host having a large Seebeck coefficient with metal inclusions, is particularly interesting. A potentially strong acoustic impedance mismatch between the semiconductor and the metal provides a very efficient interface phonon scattering. Besides, the very high density of free carriers in metals represents a convenient charge pool to adjust the composite charge carrier concentration if a proper band alignment for charge spillover exist.[14, 15] Additionally, Schottky metal-semiconductor interfaces may effectively and preferentially scatter low energy carriers.[10, 16] Such is the interest of this type of material, that in the last decade a wide spectrum of experimental results, in some cases not obviously consistent between each other, has been reported from numerous semiconductor-metal combinations (Table

4.1).

Table 4.1 *(single column)***.** Effect of the metal on semiconductor-metal composites as reported in the literature. Red: worsens; green: improves; yellow: unchanged; blue: no data.[14,15,17–36] κ is thermal conductivity, S the Seebeck coefficient, σ the electrical conductivity and, n and p are the carrier density according to the type of the semiconductor N or P.

Semiconductor	***Metal***	***κ***	***S***	***σ***	***n/p***	***μ***	***Ref***
PbS (N)	Ag	🟥	🟥	🟩	🟩	🟩	14
PbTe (P)	Pb	🟦	🟩	🟩	🟩	🟥	17
Bi_2Te_3 (N)	Au	🟩	🟥	🟩	🟩	🟥	18
Bi_2Te_3 (N)	Cu	🟩	🟩	🟥	🟥	🟩	19
Bi_2Te_3 (N)	Ag	🟩	🟩	🟩	🟩	🟥	20
Bi_2Te_3 (N)	Bi	🟩	🟥	🟩	🟩	🟥	21
Sb_2Te_3 (P)	Ag	🟦	🟥	🟩	🟥	🟩	22
Sb_2Te_3 (P)	Pt	🟦	🟩	🟥	🟩	🟥	23
$Bi_{0.5}Sb_{1.5}Te_3$ (N)	Cu	🟩	🟥	🟩	🟩	🟥	24
$Bi_{0.5}Sb_{1.5}Te_3$ (P)	Ag	🟩	🟥	🟩	🟩	🟥	25
$Bi_{0.5}Sb_{1.5}Te_3$ (P)	Cu	🟩	🟥	🟩	🟩	🟥	25
$Bi_2Te_{2.7}Se_{0.3}$ (N)	Pt	🟩	🟩	🟩	🟩	🟥	26
$Bi_2(Te_{0.9}Se_{0.1})_3$ (P)	Cu	🟩	🟥	🟩	🟩	🟥	27
$Bi_2(Te_{0.9}Se_{0.1})_3$ (P)	Zn	🟥	🟥	🟩	🟩	🟥	27
GaAs (N)	Bi	🟩	🟩	🟥	🟥	🟦	28
GaAs (N)	In	🟩	🟩	🟥	🟥	🟦	29
$FeSb_2$ (N)	Cu	🟩	🟥	🟩	🟩	🟩	15
$FeSb_2$ (N)	AgSb	🟩	🟥	🟩	🟩	🟦	30
$Ba_{0.3}Co_4Sb_{12}$ (N)	Ag	🟩	🟩	🟩	🟨	🟩	31
Na_xCoO_2 (P)	Au	🟦	🟥	🟩	🟦	🟦	32
$Bi_2Sr_2Co_2O_y$ (P)	Ag	🟥	🟨	🟩	🟦	🟦	33
$Ca_3Co_4O_{9+\delta}$ (P)	Ag	🟩	🟩	🟩	🟦	🟦	34
$Ca_3Co_4O_9$ (P)	Ag	🟥	🟥	🟩	🟦	🟦	35
$Na_xCo_2O_4$ (P)	Ag	🟥	🟩	🟩	🟦	🟦	36

The proper design and engineering of a semiconductor-metal composite requires not only to select materials with a suitable band alignment, but also to use production approaches that allow distributing them appropriately while controlling their composition. In this regard, the blending of metal and semiconductor particles in a controlled atmosphere represents an extremely simple methodology to produce composites with a huge compositional versatility and an excellent control over a number of parameters, such as distribution and composition of the phases. Within this approach, the particle sizes of both metal and semiconductor are key parameters as they determine the final metal and semiconductor domain size in the composite and the metal domain density. These parameters not only determine the extent of phonon scattering, charge spillover or potential energy filtering, but also the extent that the metal influences the host semiconductor Fermi level, especially when employing intrinsic semiconductors as those required to take full advantage of the modulation doping strategy.

We recently demonstrated that low work function metals such as Ag are able to inject electrons to a quasi-intrinsic and nanostructured PbS host.[14] We also observed that the presence of Ag at the interfaces allowed reducing the energy barriers for charge transport between PbS grains, thus not only minimizing the influence over mobility, as in a conventional modulation-doping scenario, but actually improving it. In the present work, we demonstrate combinations of intrinsic PbS with low work function non-noble metals, such as copper and tin, can also provide higher thermoelectric performances. Besides, we compare here the results obtained from a nanocrystalline host which Fermi level should be pinned to the metal's, with those of a microcrystalline host able to support the band bending at the metal-semiconductor interface. We demonstrate that while higher electrical conductivities can be reached with a more extensive distribution of metal within the host semiconductor, larger Seebeck coefficients can be maintained with the microcrystalline host.

4.3 Experimental Section

Chemicals and solvents: Lead (II) oxide (99.9%), elemental sulfur (99.98 %), copper (I) acetate (CuOAc, 97%), lithium bis(trimethylsilyl)amide ($LiN(SiMe_3)_2$, 97%), lead (II) sulfide (99.9%), copper (99.999%), platinum acetylacetonate ($Pt(acac)_2$, 97%), manganese(0) carbonyl ($Mn_2(CO)_{10}$, 98%), oleic acid (OA, tech. 90%), 1-octadecene (ODE, 90%), oleylamine (OLA, tech. 70%), benzyl ether (98%), trioctylamine and lithium triethylborohydride (superhydride, $Li(Et_3BH)$, 1.0 M solution in THF) were purchased from Sigma Aldrich. Tin (II) chloride ($SnCl_2$, 98%) was purchased from Strem. Tri-n-octylamine (TOA, 97%) was purchased from Across. Tetradecylphosphonic acid

(TDPA, 97%) was purchased from Plasma Chem. Anhydrous hexane, chloroform, toluene and methanol were obtained from various sources. All chemicals, except OLA were used as received without further purification. OLA was distillated to remove impurities. All the syntheses were carried out using standard airless techniques: a vacuum/dry argon gas Schlenk line was used for the synthesis and argon glove-box for storing and handling air and moisture sensitive chemicals.

PbS nanocrystals (NCs): Cubic PbS NCs with a mean edge size of ~10 nm were prepared following our previously reported procedure.[37] In a typical synthesis, A 1.0 M sulfur stock solution was prepared by dissolving sulfur powder (0.64 g, 20 mmol) in 20 ml distilled OLA at room temperature, and then sonicated until sulfur powder was completely dissolved. PbO (4.64 g, 20 mmol) and OA (50 ml, 158 mmol) were mixed with 100 ml of ODE (312 mmol). This mixture was degassed at room temperature for 30 min, then heated to 100 °C for 60 min and after that kept at 130 °C for another 30 min each to form the Pb-OA complex. Then the solution was flushed with argon, and the temperature was raised to 210 °C. At this temperature, the sulfur precursor was rapidly injected. The reaction mixture was maintained between 195 °C and 210 °C for 5 min and then quickly cooled down to room temperature using a water bath. PbS NCs were thoroughly washed by multiple precipitation/re-dispersion steps using acetone as a non-solvent and chloroform as solvent. Purified NCs were dried out under vacuum and stored for further use.

Cu NCs: Cu NCs with an average diameter of ~5 nm were prepared following the approach developed by Yang et al.[38] In a typical synthesis, TOA (50 ml, 0.114 mol) was heated in a 100 ml three-neck flask to 130 °C for 30 min under Ar atmosphere. After cooling to RT, 5 mmol CuOAc and 2.5 mmol TDPA were added to the flask. The mixture was heated to 180 °C and maintained at this temperature for 30 min. Then, the reaction temperature was rapidly increased to 270 °C and held for additional 30 min, and then and then quickly cooled down to room temperature using a water bath. Cu NCs are highly air sensitive and easily oxidized. To avoid any possible oxidation, the NCs were purified in an argon filled glove box. The colloidal solution was mixed with acetone and the particles were precipitated through centrifugation at 7000 rpm for 5 min. The precipitate was redispersed in chloroform for further use.

Sn NCs: Sn NCs with an average diameter of ~13 nm were prepared using the method developed by Kovalenko et al.[39] In a typical synthesis of 14 nm Sn NCs, 50 ml OLA was loaded into the three-neck flask and dried under vacuum at 140 °C for 60 min under constant stirring. After cooling of OLA down to 50°C, the flask was briefly opened to add 1.0 mmol anhydrous SnCl2 and again dried under vacuum at 140°C for 30 min. In parallel, $LiN(SiMe_3)_2$ (7.2 mmol, 1.202 g) was solved in 4 ml toluene in glovebox. Then the temperature of $SnCl_2$/OLA mixture was increased to 180 °C under argon, followed by the injection of $LiN(SiMe_3)_2$/toluene solution, and, in 10s, 1.2 mL of 1M DIBAH solution in THF. The solution immediately turned dark brown upon injection of DIBAH. In 10 min, the reaction solution was quickly cooled to room temperature using water bath. After cooling, to avoid any possible oxidation, the NCs were purified in an argon filled glove box. Sn NCs were mixed with acetone and then were precipitated through centrifugation at 7000 rpm for 5 min. The precipitate was re-dispersed in chloroform for further use.

Nanocrystal blends: The blending of NCs was performed by wetting 750 mg of dried PbS NCs with different amounts of a solution of metal NCs in anhydrous chloroform. Subsequently, the solvent was allowed to evaporate under argon atmosphere.

Microcrystal blends: Proper amounts of commercial PbS and Cu powders were mixed inside an argon-filled glove-box by manually grinding them with an agate mortar.

Composites: PbS-metal blends were annealed at 450 °C for 60 min under an Ar flow inside a tube furnace. Then, the annealed powders were loaded into a graphite die and compacted into pellets (Ø10 mm×1.5 mm) in an Ar atmosphere using a custom-made hot press for 5 min at 420 °C and under 70 MPa pressure. The relative density of the obtained pellets was higher than 85% of the theoretical value in all cases.

Structural and chemical characterization: X-ray diffraction (XRD) patters were obtained on a Bruker AXS D8 ADVANCE X-ray diffractometer with Cu–Kα radiation ($\lambda = 0.15406$ Å). Transmission electron microscopy (TEM) characterization was carried out on a Zeiss Libra 120, operating at 120 kV. High resolution TEM (HRTEM) images were obtained using a Jeol 2010F field-emission gun microscope at 200 keV. Field-emission scanning electron microscopy (SEM) micrographs were obtained on Zeiss Auriga at 5.0 kV. Composition was analyzed by means of an Oxford energy dispersive X-ray spectrometer (EDX) coupled to the SEM.

Thermoelectric properties: Both the Seebeck coefficient and the electrical resistivity were measured simultaneously in a LSR-3 LINSEIS system under helium atmosphere. XFA 600 Xenon Flash Apparatus was used to determine the thermal diffusivities of the samples. The carrier concentration and mobility were measured using the Hall measurement system (PPMS-9T, Quantum Design Inc., USA) at room temperature under a magnetic field of 2 T. The thermal conductivity was calculated by $\kappa = \lambda C_p \rho$, where λ is the thermal diffusivity, C_p is the heat capacity, and ρ is the mass density of the specimen. The specific heat (C_P) was calculated by the Dulong-Petit approximation, and the density (ρ) values used were obtained using the Archimedes' method. Error bars were estimated from the repeatability of the experimental result obtained, calculated after measuring 3 times each parameter.

4.4 Results and discussion

Figures 4.1a-1d display representative TEM micrographs and the corresponding particle size histograms of the 10 nm cubic PbS, the 5 nm spherical Cu and the 13 nm spherical Sn NCs obtained following the above procedures and used to produce semiconductor-metal nanocomposites. Figure 4.2a shows the NCs XRD patterns. Importantly, no secondary phases, including the corresponding oxides, were detected when carefully producing, manipulating and purifying the NCs in air-free conditions.

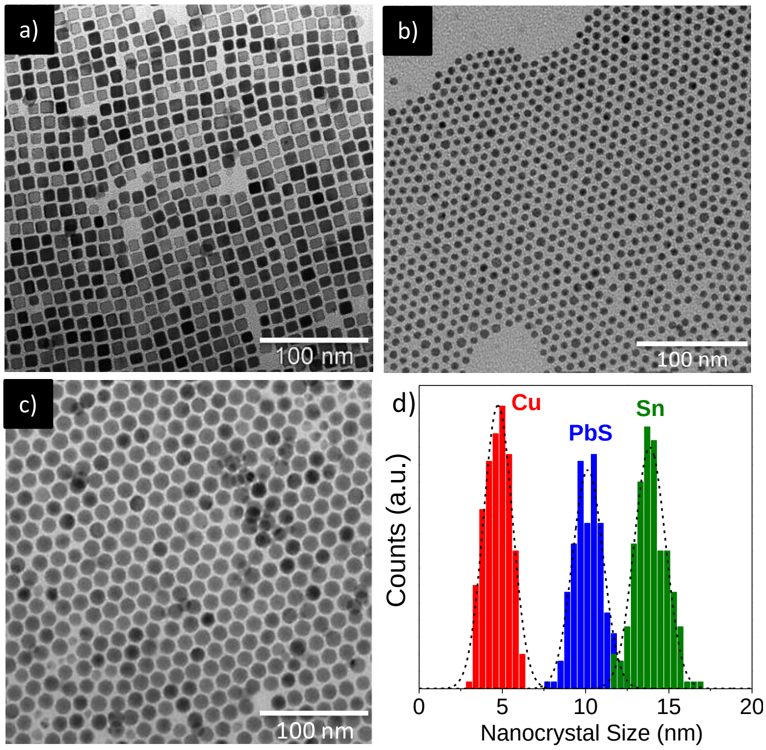

Figure 4.1. TEM micrographs of PbS (a), Cu (b) and Sn (c) NCs and the corresponding size histograms (d).

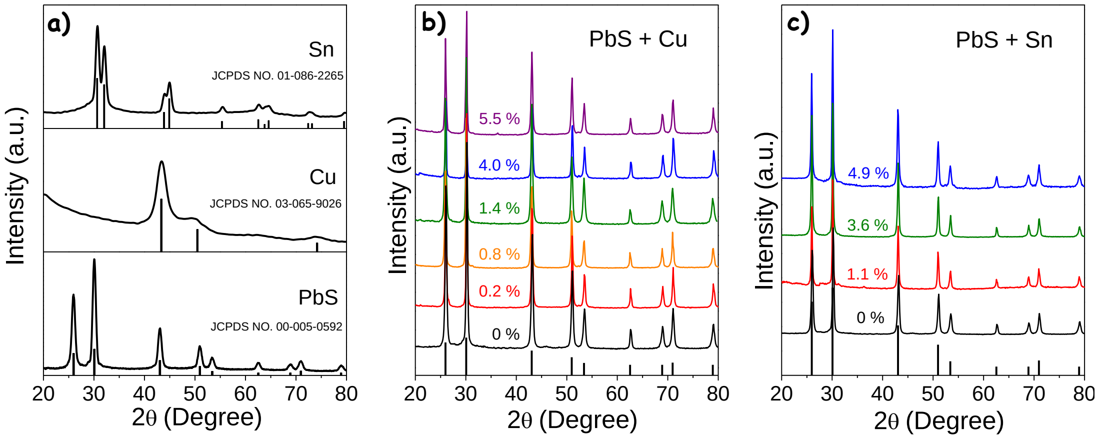

Figure 4.2. a) XRD patterns of PbS, Cu and Sn NCs. The respective reference patterns are also plotted. b) XRD patterns of the PbS-Cu nanocomposite pellets. c) XRD patterns of the PbS-Sn nanocomposite pellets. The reference pattern of PbS (JCPDS 00-005-0592) is also shown.

PbS-Cu and PbS-Sn nanocomposites with adjusted metal concentrations were produced by combining purified PbS NCs with different amounts of a suspension of colloidal Cu or Sn NCs, respectively. To remove residual organic compounds and chemically and structurally stabilize the material, nanocomposites were annealed at 450 °C for 60 min under an Ar flow. Subsequently, the annealed powders were consolidated into disk-shaped pellets using a hot-press. EDX analysis showed the amount of Cu and Sn in the final nanocomposite to be consistent, within the experimental error, with the nominal composition of the nanocomposites prepared (Tables 4.1 and 4.2). This result was to be expected as no additional purification process was performed after the nanocrystal combination, and processing temperatures were not high enough for metal evaporation.

Table 4.1. SEM-EDX Composition of the PbS-Cu pellets after consolidation.

Element	Sample 1	Sample 2	Sample 3	Sample 4	Sample 5	Sample 6
Pb	49.39	48.90	49.56	49.13	48.69	48.80
S	50.61	50.99	50.04	50.15	49.28	48.45
Cu	0	0.11	0.40	0.72	2.03	2.75
Total	PbS	PbS-0.2%Cu	PbS-0.8%Cu	PbS-1.4%Cu	PbS-4.0%Cu	PbS-5.5%Cu

Table 4.2. SEM-EDX Composition of the PbS-Sn pellets after consolidation.

Element	Sample 1	Sample 2	Sample 3	Sample 4
Pb	49.39	49.45	48.69	48.14
S	50.61	50.01	49.46	49.38
Sn	0	0.54	1.85	2.48
total	PbS	PbS-1.1%Sn	PbS-3.6%Sn	PbS-4.9%Sn

Figures 4.2b and 4.2c show the XRD patterns of PbS-Cu and PbS-Sn nanocomposite pellets, respectively. Because of the low amount of metal introduced and the coincidence of the main x-ray diffraction peaks of the metal with those of PbS, the presence of metallic Cu and Sn phases was not detected by XRD. During the annealing processes, PbS grains were observed to grow from the initial 10 nm to around 100-200 nm (Figure 4.3a). However, careful HRTEM analysis showed the grains to be highly polycrystalline, with crystal domain sizes in the range 10-20 nm (Figures 4.3b). The coincidence of interplanar

spacings did not allow obtaining evidences of the presence of metallic Cu or Sn crystals from HRTEM and electron diffraction.

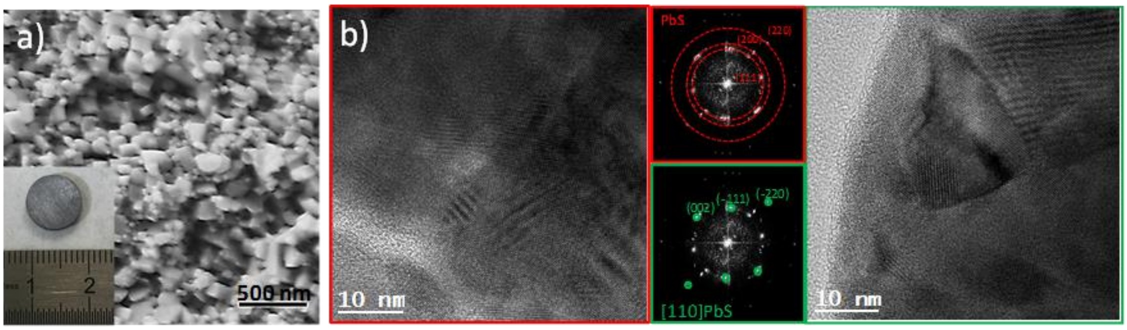

Figure 4.3. a) Representative SEM micrograph of a PbS-Sn nanocomposite showing 100-200 nm grains. Inset shows an image of the actual pellet. b) HRTEM micrograph and power spectra of the PbS-Sn nanocomposite showing the material polycristallinity with crystal domain sizes in the range between 10 and 20 nm.

The electrical conductivities (σ), Seebeck coefficients (S), thermal conductivities (κ), and the dimensionless thermoelectric figure of merit $ZT=\sigma S^2T/$□ of a series of PbS-Cu and PbS-Sn nanocomposites with metal concentrations up to 5 mol% are displayed in Figures 4.4 and 4.5. The pristine PbS material was characterized by low electrical conductivity at ambient temperature, which, as it corresponds to an intrinsic or poorly-doped semiconductor, strongly increased with temperature. Consistently, relatively high Seebeck coefficients were measured for PbS at ambient temperature. Besides, a sign inversion was observed at around 450 K, corresponding to a change from p-type to n-type conductivity. PbS–Cu and PbS–Sn nanocomposites showed significantly higher electrical conductivities, which increased with the metal content. For the nanocomposites with the highest metal contents, electrical conductivities decreased with temperature (Figures 4.4 and 4.5a), as it corresponds to a degenerated semiconductor. This result demonstrates the important electronic role that Cu and Sn play on the final material. Over the entire temperature range measured, both PbS–Cu and PbS–Sn nanocomposites exhibited negative Seebeck coefficients (Figures 4.4b and 4.5b), which absolute value increased with temperature. This n-type behavior points towards an injection of electrons from the metal to the host semicondutor. Consistently with the higher electrical conductivities measured, lower Seebeck coefficients were generally obtained for the nanocomposites when compared with the pristine PbS.

Hall charge carrier concentration measurements provided further evidence of the charge carrier increase, of up to 3 orders of magnitude, obtained with the introduction of metal NCs. The Hall charge carrier concentrations at room temperature for PbS, PbS-Cu 4 mol%, and PbS-Sn 3.6 mol% were $p = 2 \times 10^{16}$ cm^{-3}, $n = 3 \times 10^{19}$ cm^{-3}, and $n = 1 \times 10^{19}$ cm^{-3}, respectively. The majority carrier mobilities directly calculated from the measured electrical conductivities were $\mu_p = 14$ cm^2·V^{-1}·s^{-1}, $\mu_n = 130$ cm^2·V^{-1}·s^{-1}, and $\mu_n = 130$ cm^2·V^{-1}·s^{-1}, for PbS, PbS–Cu 4 mol%, and PbS–Sn 3.6 mol%, respectively.

With the metal addition, higher thermal conductivities, which increased with the metal content, were obtained in the whole temperature range. This increase is associated with the higher electronic component of the thermal conductivity. Nevertheless, all nanocomposites displayed significantly higher power factors ($PF=\sigma S^2$) and figures of merit than pristine PbS (Figures 4.4c and 4.5c). Maximum ZT values were obtained for PbS–Cu 4.0 mol% and PbS–Sn 3.6 mol% nanocomposites, which reached ZT values up to 0.86 and 0.88 at 855 K (Figures 4.4f and 4.5f), respectively, that is a two-fold increase over pristine PbS. Higher metal concentrations provided either a too large reduction in the Seebeck coefficient or a too large incrase on thermal conductivity, thus decreasing the overal thermoelectric figure of merit. To estimate measurement accuracy and have a first assessment of the sample stability (Figure 4.6), all measurements were repeated at least three times for each sample, observing minimal variations.

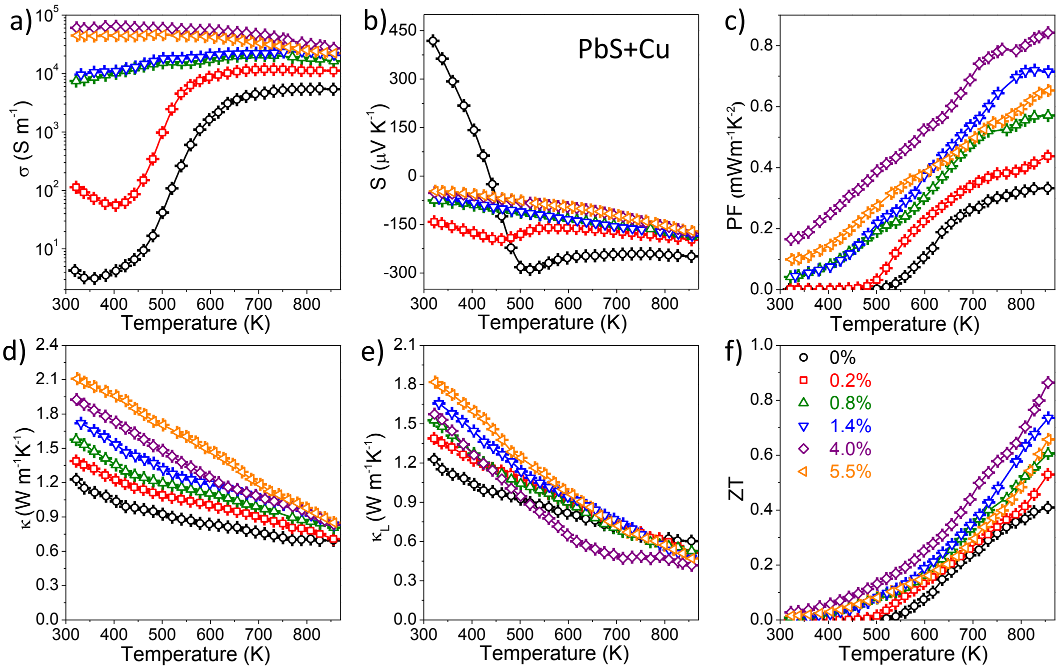

Figure 4.4. Thermoelectric characterization of PbS–Cu nanocomposites. Temperature dependence of the (a) electrical conductivity, σ; (b) Seebeck coefficient, S; (c) power factor, PF; (d) thermal conductivity, κ; (e) lattice thermal conductivity, κ_L; and (f) thermoelectric figure of merit (ZT). Error bars were estimated from the repeatability of the experimental result obtained, calculated after measuring 3 times each parameter.

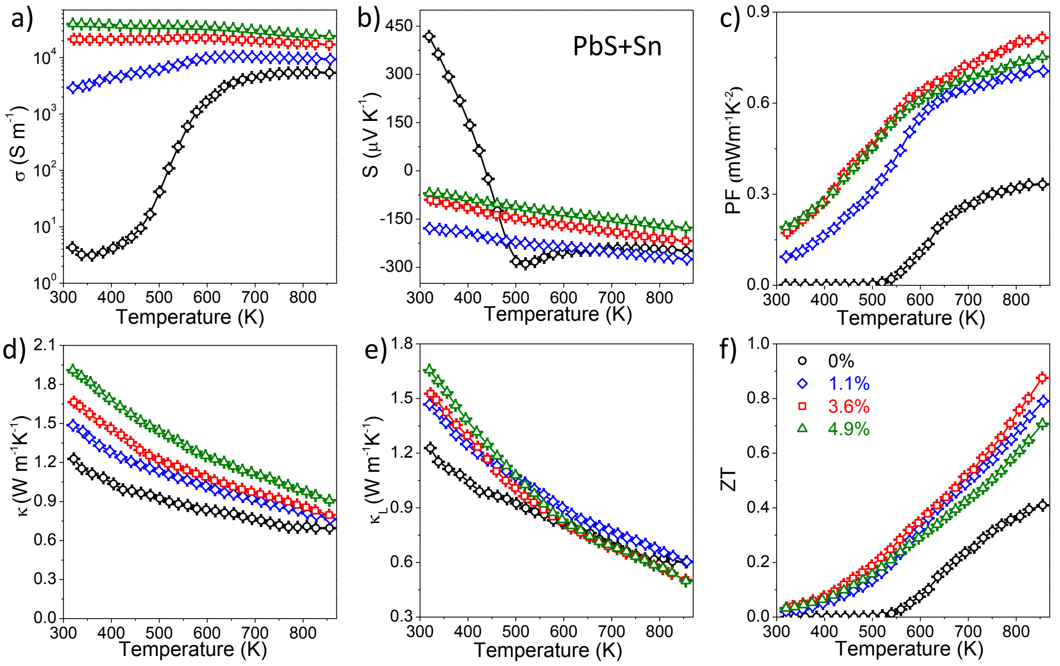

Figure 4.5. Thermoelectric characterization of PbS–Sn nanocomposites. Temperature dependence of the (a) electrical conductivity, σ; (b) Seebeck coefficient, S; (c) power factor, PF; (d) thermal conductivity, κ; (e) lattice thermal conductivity, κ_L; and (f) thermoelectric figure of merit (ZT). Error bars were estimated from the repeatability of the experimental result obtained,

calculated after measuring 3 times each parameter.

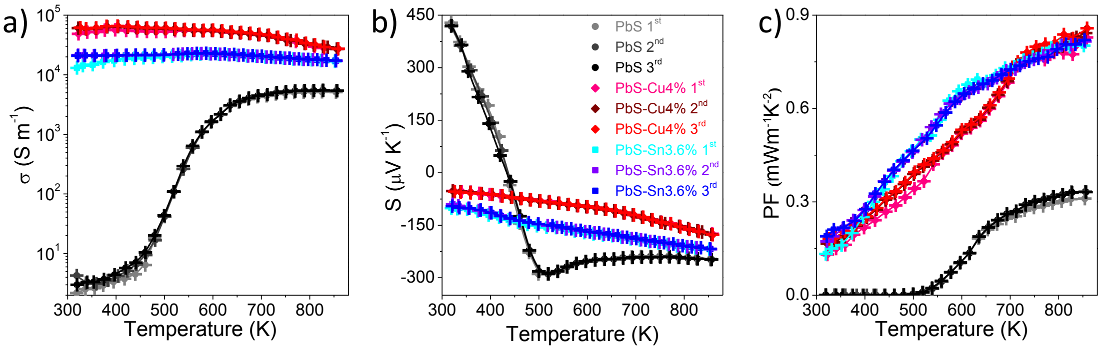

Figure 4.6. (a)-(c) The typical temperature dependence of the electrical conductivity (σ), Seebeck coefficient (S) and power factor (PF) of pristine PbS, PbS–Cu mol 4% and PbS–Sn 3.6 mol% nanocomposites measured 3 consecutive times during heating up to around 855 K, respectively. No pre-stabilization treatment was carried out before the first measurement.

Figure 4.7 displays the results obtained from the thermoelectric characterization of PbS–Cu 4.0 mol% composites produced from commercial powders. Results are compared with those obtained from the PbS–Cu 4.0 mol% nanocomposite produced from colloidal NCs. Electrical conductivities of the pristine microcrystalline PbS were low, similar to those of the PbS nanomaterial, as both are intrinsic. In the high temperature range, higher electrical conductivities where obtained for the nanocrystalline PbS, which we associate to a higher density of surface defects, susceptible to be ionized in the high temperature range and thus providing higher carrier concentrations. With the Cu introduction, the electrical conductivities of the microcrystalline composite increased several orders of magnitude, up to 10^4 S m^{-1}, but remained a factor 4 lower than those of the PbS–Cu nanocomposite.

On the other hand, the Seebeck coefficients of the pristine PbS microcrystalline material showed a similar temperature evolution as the nanocrystalline PbS, but reached higher values in the high temperature range, which is consistent with the relatively lower electrical conductivities measured in this temperature range for the microcrystalline material. In the presence of copper, negative Seebeck coefficients were measured in the whole temperature range, which, together with the large increase of electrical conductivity, points toward a spillover of electrons from the metal to the host semiconductor, as in the case of the PbS–Cu nanocomposite. In the microcrystalline composite however, much higher Seebeck coefficients than in the nanocomposite were obtained, even when comparing with nanocomposites having lower Cu loads and similar electrical conductivities. We associate the relatively lower Seebeck coefficients obtained in the nanocrystalline material to their charge flooding, not being able to sustain a sufficient band bending due to their small size and low electronic doping. In the microcrystalline compound, the injection of charge from copper to PbS introduces a band bending in the semiconductor, but still most of the PbS crystal remains quasi-intrinsic thus overall providing much larger Seebeck coefficients (Figure 4.8).

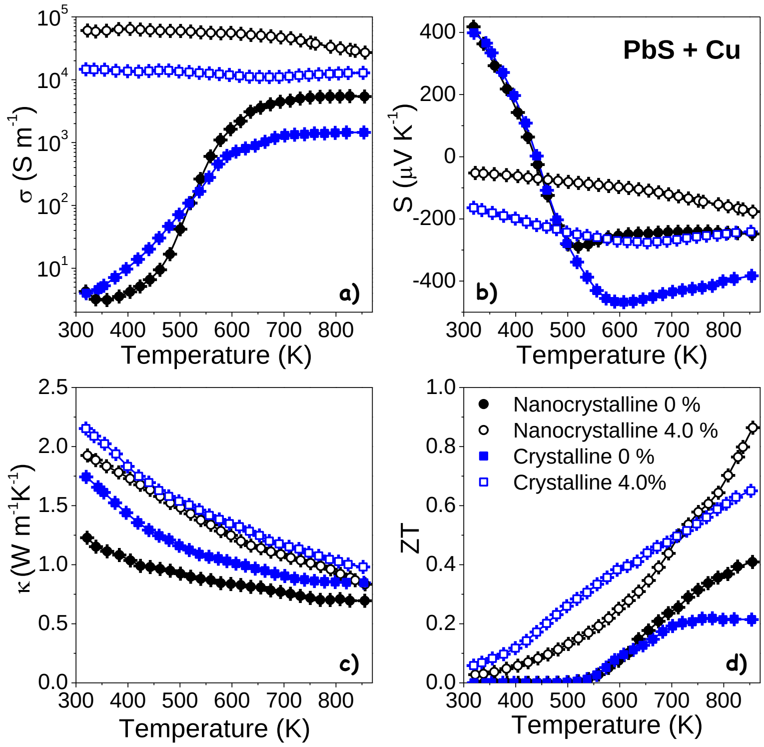

Figure 4.7. a-d) Temperature dependence of the (a) electrical conductivity; (b) Seebeck coefficient; (c) thermal conductivity; and (d) thermoelectric figure of merit for microcrystalline PbS–Cu composites (blue squares) and PbS-Cu nanocomposites (black circles).

In microcrystalline PbS, the measured Hall charge carrier concentration at room temperature was $p = 9\times10^{15}$ cm^{-3}, just slightly lower than for nanocrystalline PbS. The related charge carrier mobility was $\mu_p = 28$ cm$^2\cdot$V$^{-1}\cdot$s^{-1}, twofold higher than in nanocrystalline PbS. When introducing a 4 mol% of Cu, the microcrystalline PbS–Cu 4 mol% composite displayed a charge carrier concentration of n = 2×10^{18} cm^{-3}, which was one order of magnitude lower than when blending the same amount of Cu with nanocrystalline PbS. From this carrier concentration value, the calculated mobility in the microcrystalline composite was 3–fold larger than that of the nanocomposite, which is consistent with the higher crystallinity of the former.

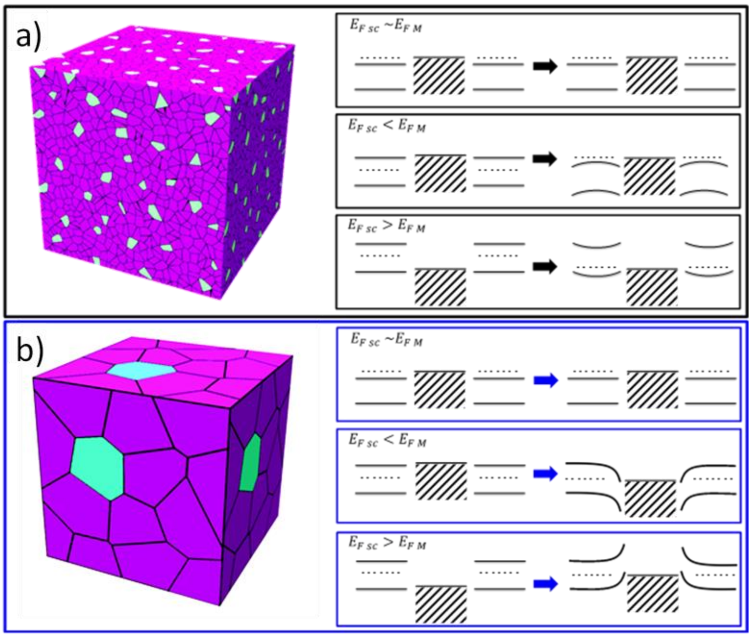

Figure 4.8. a) and b) Scheme of a semiconductor-metal nanocomposite and a microcomposite and the band alignments in three scenarios depending on the relative position of the semiconductor and metal Fermi levels.

As expected, the thermal conductivities of the microcrystalline PbS and the PbS–Cu composite were larger than those of the nanocrystalline PbS and PbS–Cu. Overall, while larger ZT values were obtained for the microcrystalline compound in the low temperature range measured, due to the much higher Seebeck coefficients provided, in the high temperature range, the nanocomposite was characterized by higher ZT values related to the lower lattice thermal conductivity due to more efficient phonon scattering and the higher electrical conductivities associated to a more efficient charge carrierinjection from the metal to the semiconductor.

4.5 Conclusions

PbS–Cu and PbS–Sn composites were prepared by a facile and extremely versatile approach consisting on blending the proper amount of particles of each components and subsequently hot-pressing the resulting mixture. Compared with pristine PbS, PbS–metal composites exhibited much higher electrical conductivities and negative Seebeck coefficients in the whole temperature range, consistent with a spillover of electrons from the low work function metal to the semiconductor. Due to the strong contribution of the electronic thermal conductivity, the metal addition had associated an increase of the thermal conductivity. When comparing the thermoelectric properties of PbS–Cu composites with crystal domain sizes in the micrometer scale with those of nanocomposites with dimensions of both components in the nanometer size regime, we observed that with the same metal loading, higher electrical conductivities were reached in the nanocomposite, but higher Seebeck coefficients were maintained in the microcomposite. Both results were associated to a more efficient charge transfer from the metal to the semiconductor in the nanocrystalline materials. As expected, lower thermal conductivities were also measured in the nanocomposite. Overall, higher ZT values were measured on the microcomposite in the low temperature range, but higher ZT values were measured from the nanocomposites in the higher temperature range. Both in microcomposites and nanocomposites, a 2–fold increase of ZT was obtained over pristine PbS.

4.6 References

1. Zhao, L.-D.; Dravid, V. P.; Kanatzidis, M. G. *Energy & Environmental Science* **2014,** 7, (1), 251-268.
2. He, J.; Kanatzidis, M. G.; Dravid, V. P. *Materials Today* **2013,** 16, (5), 166-176.
3. Lan, Y.; Minnich, A. J.; Chen, G.; Ren, Z. *Advanced Functional Materials* **2010,** 20, (3), 357-376.
4. Zhang, Y.; Stucky, G. D. *Chemistry of Materials* **2013,** 26, (1), 837-848.
5. Sootsman, J. R.; Chung, D. Y.; Kanatzidis, M. G. *Angewandte Chemie International Edition* **2009,** 48, (46), 8616-8639.
6. Ibáñez, M.; Zamani, R.; Gorsse, S.; Fan, J.; Ortega, S.; Cadavid, D.; Morante, J. R.; Arbiol, J.; Cabot, A. *ACS nano* **2013,** 7, (3), 2573-2586.
7. Vineis, C. J.; Shakouri, A.; Majumdar, A.; Kanatzidis, M. G. *Advanced Materials* **2010,** 22, (36), 3970-3980.
8. Dehkordi, A. M.; Zebarjadi, M.; He, J.; Tritt, T. M. *Materials Science and Engineering: R: Reports* **2015,** 97, 1-22.
9. Zebarjadi, M.; Joshi, G.; Zhu, G.; Yu, B.; Minnich, A.; Lan, Y.; Wang, X.; Dresselhaus, M.; Ren, Z.; Chen, G. *Nano letters* **2011,** 11, (6), 2225-2230.
10. Faleev, S. V.; Léonard, F. *Phys. Rev. B* **2008,** 77, (21), 214304.
11. Zebarjadi, M.; Liao, B.; Esfarjani, K.; Dresselhaus, M.; Chen, G. *Advanced Materials* **2013,** 25, (11), 1577-1582.
12. Shen, W.; Tian, T.; Liao, B.; Zebarjadi, M. *Physical Review B* **2014,** 90, (7), 075301.
13. Lee, J. Y.; Lee, R.-K. *Physical Review B* **2014,** 89, (15), 155425.
14. Ibáñez, M.; Luo, Z.; Genç, A.; Piveteau, L.; Ortega, S.; Cadavid, D.; Dobrozhan, O.; Liu, Y.; Nachtegaal, M.; Zebarjadi, M. *Nature communications* **2016,** 7.
15. Koirala, M.; Zhao, H.; Pokharel, M.; Chen, S.; Dahal, T.; Opeil, C.; Chen, G.; Ren, Z. *Applied Physics Letters* **2013,** 102, (21), 213111.
16. Zide, J.; Bahk, J.-H.; Singh, R.; Zebarjadi, M.; Zeng, G.; Lu, H.; Feser, J.; Xu, D.; Singer, S.; Bian, Z. *Journal of Applied Physics* **2010,** 108, (12), 123702.
17. Heremans, J. P.; Thrush, C. M.; Morelli, D. T. *Journal of Applied Physics* **2005,** 98, (6), 063703.
18. Lee, E.; Ko, J.; Kim, J.-Y.; Seo, W.-S.; Choi, S.-M.; Lee, K. H.; Shim, W.; Lee, W. *Journal of Materials Chemistry C* **2016**.
19. Sie, F.; Kuo, C.; Hwang, C.; Chou, Y.; Yeh, C.; Lin, Y.; Huang, J. *Journal of Electronic Materials* **2016**, 1-8.
20. Zhang, Q.; Ai, X.; Wang, L.; Chang, Y.; Luo, W.; Jiang, W.; Chen, L. *Advanced Functional Materials* **2015,** 25, (6), 966-976.
21. Sumithra, S.; Takas, N. J.; Misra, D. K.; Nolting, W. M.; Poudeu, P.; Stokes, K. L. *Advanced Energy Materials* **2011,** 1, (6), 1141-1147.

22. Zhang, Y.; Snedaker, M. L.; Birkel, C. S.; Mubeen, S.; Ji, X.; Shi, Y.; Liu, D.; Liu, X.; Moskovits, M.; Stucky, G. D. *Nano letters* **2012,** 12, (2), 1075-1080.
23. Ko, D.-K.; Kang, Y.; Murray, C. B. *Nano letters* **2011,** 11, (7), 2841-2844.
24. Kim, I.-H.; Choi, S.-M.; Seo, W.-S.; Cheong, D.-I. *Nanoscale research letters* **2012,** 7, (1), 1-6.
25. Lee, K.-H.; Kim, H.-S.; Kim, S.-I.; Lee, E.-S.; Lee, S.-M.; Rhyee, J.-S.; Jung, J.-Y.; Kim, I.-H.; Wang, Y.; Koumoto, K. *Journal of electronic materials* **2012,** 41, (6), 1165-1169.
26. Sun, T.; Samani, M. K.; Khosravian, N.; Ang, K. M.; Yan, Q.; Tay, B. K.; Hng, H. H. *Nano Energy* **2014,** 8, 223-230.
27. Wang, S.; Li, H.; Lu, R.; Zheng, G.; Tang, X. *Nanotechnology* **2013,** 24, (28), 285702.
28. Warren, M.; Canniff, J.; Chi, H.; Naab, F.; Stoica, V.; Clarke, R.; Uher, C.; Goldman, R. *Journal of Applied Physics* **2015,** 117, (6), 065101.
29. Warren, M. V.; Canniff, J. C.; Chi, H.; Morag, E.; Naab, F.; Stoica, V. A.; Clarke, R.; Uher, C.; Goldman, R. S. *Journal of Applied Physics* **2013,** 114, (4), 043704.
30. Zhao, H.; Pokharel, M.; Chen, S.; Liao, B.; Lukas, K.; Opeil, C.; Chen, G.; Ren, Z. *Nanotechnology* **2012,** 23, (50), 505402.
31. Zhou, X.; Wang, G.; Zhang, L.; Chi, H.; Su, X.; Sakamoto, J.; Uher, C. *Journal of Materials Chemistry* **2012,** 22, (7), 2958-2964.
32. Zhao, X.; Wang, H.; Wang, S.; Elhadj, D.; Wang, J.; Fu, G. *RSC Advances* **2014,** 4, (100), 57148-57152.
33. Wang, S.; Bai, Z.; Wang, H.; Lü, Q.; Wang, J.; Fu, G. *Journal of Alloys and Compounds* **2013,** 554, 254-257.
34. Nong, N.; Pryds, N.; Linderoth, S.; Ohtaki, M. *Advanced Materials* **2011,** 23, (21), 2484-2484.
35. Wang, Y.; Sui, Y.; Cheng, J.; Wang, X.; Su, W. *Journal of Alloys and Compounds* **2009,** 477, (1), 817-821.
36. Ito, M.; Furumoto, D. *Scripta materialia* **2006,** 55, (6), 533-536.
37. Ibáñez, M.; Korkosz, R. J.; Luo, Z.; Riba, P.; Cadavid, D.; Ortega, S.; Cabot, A.; Kanatzidis, M. G. *Journal of the American Chemical Society* **2015,** 137, (12), 4046-4049.
38. Hung, L. I.; Tsung, C. K.; Huang, W.; Yang, P. *Advanced Materials* **2010,** 22, (17), 1910-1914.
39. Kravchyk, K.; Protesescu, L.; Bodnarchuk, M. I.; Krumeich, F.; Yarema, M.; Walter, M.; Guntlin, C.; Kovalenko, M. V. *Journal of the American Chemical Society* **2013,** 135, (11), 4199-4202.

Chapter 5

Crystallographically Textured Nanomaterials Produced from the Liquid Phase Sintering of $Bi_xSb_{2-x}Te_3$ Nanocrystal Building Blocks

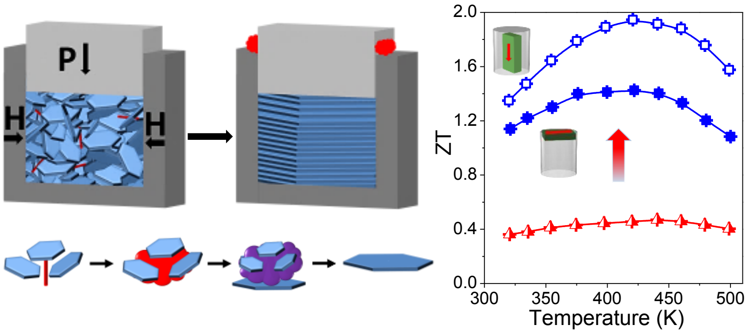

5.1 Abstract

Bottom-up approaches for producing bulk nanomaterials have traditionally lacked control over the crystallographic alignment of nanograins. This limitation has prevented nanocrystal-based nanomaterials from achieving optimized performances in numerous applications. Here we demonstrate the production of nanostructured $Bi_xSb_{2-x}Te_3$ alloys with controlled stoichiometry and crystallographic texture through proper selection of the starting building blocks and the adjustment of the nanocrystal-to-nanomaterial consolidation process. In particular, we hot pressed disk-shaped $Bi_xSb_{2-x}Te_3$ nanocrystals (NCs) and tellurium nanowires as building blocks using multiple pressure and release steps at a temperature above the tellurium melting point. We explain the formation of the textured nanomaterials though a solution-reprecipitation mechanism under a uniaxial pressure. Additionally, we further demonstrate these alloys to reach unprecedented thermoelectric figures of merit, up to ZT = 1.96 at 420 K, with an average value of ZT_{ave}

= 1.77 for the record material in the temperature range 320 − 500 K, thus potentially allowing up to 60 % higher energy conversion efficiencies than commercial materials.

5.2 Introduction

Nanostructured materials hold the key to the cost-effective use of thermoelectric devices in a broad range of applications. Nanomaterials are characterized by reduced thermal conductivities attributed to phonon scattering at grain boundaries;[1, 2] the potential to simultaneously combine high charge carrier concentrations with large charge carrier mobilities through modulation doping;[3-5] and the possibility to maximize the Seebeck coefficient by modifying the electronic band structure or through electron energy filtering at interphases.[6, 7] However, to optimize all these properties, an exquisite control over nanomaterial parameters in three dimensions is necessary. Such level of control cannot be reached by current high throughput bulk nanomaterial fabrication technologies, such as mechanical grinding. Alternative vacuum-based thin film technologies are able to produce compositionally tuned films, but with limited thickness and at expenses of high production costs and low throughputs.

Bottom-up assembly strategies that use NCs as starting building blocks allow producing bulk nanomaterials with parameters tuned at the nanometer-scale and in a cost-effective manner. This approach has been successful to produce a plethora of nanocrystalline materials with exceptional thermoelectric properties.[2, 3, 8-10] However, this methodology faces limitations in the production of highly anisotropic materials with proper crystallographic alignment, as required in numerous application fields, including thermoelectrics.[2]

In particular, n-type $Bi_2Te_{3-x}Se_x$ and p-type $Bi_xSb_{2-x}Te_3$ alloys, the most ubiquitous thermoelectric materials operated at ambient temperature, have layered structures consisting of stacks of covalently bonded quintuple atomic layers, Te-Bi/Sb-Te-Bi/Sb-Te, that are held together by weak van der Waals interactions (Figure 5.1). Such layered materials are characterized by strongly anisotropic transport properties. In single crystals, the electrical conductivities in the *ab* plane are higher than in the *c* direction, up to factors 4.38 and 2.65 for $Bi_2Te_{2.6}Se_{0.4}$ and $Bi_{0.5}Sb_{1.5}Te_3$ respectively.[11, 12] Similarly, two-fold higher thermal conductivities are measured within the *ab* plane. Even though the Seebeck coefficient is nearly isotropic, overall, higher thermoelectric figures of merit, up to factors 2.17 and 1.42 for $Bi_2Te_{2.6}Se_{0.4}$ and $Bi_{0.5}Sb_{1.5}Te_3$, are measured in the *ab* plane when compared with the *c* direction. Such strong anisotropy requires producing crystallographically textured $Bi_2Te_{3-x}Se_x$ and $Bi_xSb_{2-x}Te_3$ nanomaterials to optimize their thermoelectric properties.

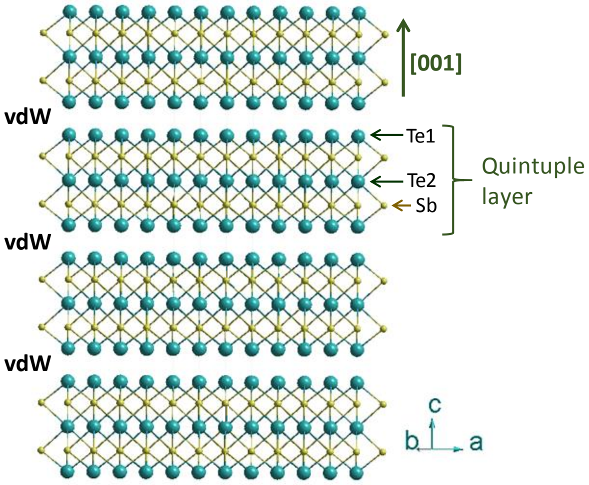

Figure 5.1. Crystal structure of Sb_2Te_3.

To generate crystallographically textured polycrystalline materials, severe plastic deformation approaches, such as particular extrusion strategies[13, 14] and high pressure torsion[15] have been used with some success. More conventional processes, such as hot press and spark plasma sintering, have been also effective in producing $Bi_2Te_{3-x}Se_x$ and $Bi_xSb_{2-x}Te_3$ polycrystalline materials with significant degrees of crystallographic alignment.[16-18] Combining these methodologies with micropowders produced by ball milling, polycrystalline pellets with relatively thick layered structures, ca. 0.5-1 μm, have been obtained. To optimize such consolidation processes, most parameters have been investigated, but some controversy has arisen. As an example, it is generally assumed that anisotropy is stimulated by severe pressures and temperatures, but in some cases, less orientation at higher processing temperatures have been reported.[17] In other works the size of the die was considered as the main parameter determining the degree of crystallographic texture.[16] Overall, three main conclusions have been generally accepted: i) crystallographically aligned $Bi_2Te_{3-x}Se_x$ and $Bi_xSb_{2-x}Te_3$ alloys are produced with the *c* direction oriented along the pressing direction; ii) in such materials, improved thermoelectric properties are measured or assumed within the *ab* plane when compared with the *c* direction; and iii) much room is left for improvement through optimizing these processes.

Here, we detail a liquid phase sintering strategy to systematically produce crystallographically textured $Bi_xSb_{2-x}Te_3$ materials with thin layered structures. We further prove that these nanomaterials are characterized by record thermoelectric figures of merit, although not in the *ab* plane, but in the *c* direction.

5.3 Experimental Section

Chemicals and solvents: Bismuth (III) nitrate pentahydrate ($Bi(NO_3)_3 \cdot 5H_2O$, ≥99.99%), bismuth (III) chloride ($BiCl_3$, ≥99%). antimony (III) chloride ($SbCl_3$, 99%), potassium hydroxide (KOH, ≥98%), Polyvinylpyrrolidone ($(C_6H_9NO)_n$, average mol wt ~55,000), tellurium dioxide (TeO_2, ≥99%), hydrazine monohydrate ($NH_2NH_2 \cdot H_2O$, 64~65%) and diethylene glycol ($(HOCH_2CH_2)_2O$, DEG, ≥99%) were purchased from Sigma Aldrich. Sodium tellurite (Na_2TeO_3, 99.5%) and ethylene glycol ($HOCH_2CH_2OH$, EG, 99%) were purchased from Fisher. Analytical grade acetone and ethanol were obtained from various sources. All chemicals were used as received, without further purification.

Synthesis of $Bi_xSb_{2-x}Te_3$ nanoplatelets: To produce around 5 g of $Bi_xSb_{2-x}Te_3$ (x= 0, 0.4, 0.5 and 0.6) nanoplatelets with a nominal 25% mol excess tellurium, 7.2x mmol of $Bi(NO_3)_3 \cdot 5H_2O$, [7.2·(2-x)] mmol of $SbCl_3$, 27 mmol Na_2TeO_3, 72 mmol KOH and 1.44 g PVP as stabilizing agent were dissolved in 280 mL DEG in a 500 mL three-neck flask. The mixture was stirred under argon atmosphere at room temperature for 20 min. Then the solution was heated to 190 °C, and during the heating up, at 110 °C, 10.8 mL hydrazine monohydrate was swiftly injected. Upon hydrazine injection, the color of the solution immediately changed from slightly brown to dark. The mixture was kept at 190 °C for 4 h and then it was naturally cooled to room temperature by removing the heating mantle. The solid product was collected by adding acetone to the solution and centrifuging it. In a second step, ethanol was used to redisperse the particles and acetone ($V_{ethanol}/V_{acetone}=1:2$) to precipitate them again. In a third step, deionized water was added to solubilize remaining impurities and NCs were precipitated by slow centrifugation. This procedure was repeated twice. In a last step, particles were redispersed with ethanol and precipitated with acetone, like in step two. Finally, particles were dried under vacuum at room temperature. This synthesis protocol was optimized to produce more than 5 g of nanoplatelets per batch, which was the amount required for a complete characterization of the material at the laboratory scale.

Synthesis of tellurium and Bi_2Te_3 nanowires: Tellurium and Bi_2Te_3 nanowires were prepared following the approach developed by Yue Wu et al.[19] In a typical synthesis of tellurium nanowires, 5.6 mmol of TeO_2, 37 mmol of KOH, 1.5 g of PVP, and 56 mL of EG were added into a 250 mL three-neck flask. The mixture was stirred and heated to 140 °C. At this temperature, 0.87 mL of a 64~65% $N_2H_4 \cdot H_2O$ solution was injected into the flask. The reaction mixture was maintained at 140 °C for 1 h to allow all tellurium to be reduced.

Bi_2Te_3 nanowires were produced by adding bismuth to the just formed tellurium nanowires produced as described in the previous paragraph. Briefly, after 1 h of reaction at 140 ºC to form the tellurium nanowires, the temperature of the solution was raised to 160 °C. At this point, a hot $BiCl_3$/EG solution was injected into the flask. This $BiCl_3$/EG solution was produced by adding 3.6 mmol of $BiCl_3$ into 15 mL of EG in a glass vial that was heated to 100−120 °C. The $BiCl_3$/EG solution was allowed to react with the tellurium nanowires for 1 h at 160 °C. Then, the solution was naturally cooled to room temperature. Both, tellurium and Bi_2Te_3 nanowires were purified using the same procedure as described above for $Bi_xSb_{2-x}Te_3$ NCs.

Bulk nanomaterial consolidation: Dried $Bi_xSb_{2-x}Te_3$ (x=0.4, 0.5 and 0.5) nanoplatelets were annealed at 350 °C for 60 min under an argon flow inside a tube furnace. The annealed particles, in the form of a powder, were loaded into a graphite die and compacted into cylinders (Ø 10 mm×10 mm) in an argon atmosphere using a custom-made hot press. The hot press temperature was set at 480 ºC and pressure to 80 MPa and the amount of time that the material was kept in these conditions was 210 s. From these cylinders, rectangular bars of about 8 × 6 × 1 mm^3 were cut in two directions, along the press axis and within the plane normal to this axis. The relative densities of the compacted pellets were measured by the Archimedes' method and found to be above 90% of the theoretical value, when materials with an excess of tellurium where hot pressed in these conditions.

Structural and chemical characterization: X-ray diffraction (XRD, 2θ: 20° to 80°; scanning rate: 5 °/min) analyses were carried out on a Bruker AXS D8 ADVANCE X-ray diffractometer with Cu–Kα radiation (λ= 1.5406 Å). Size and morphology of the initial NCs and the consolidated materials were examined by transmission electron microscopy (TEM) using a ZEISS LIBRA 120, operating at 120 kV and field-emission scanning electron microscopy (SEM) using a Zeiss Auriga at 5.0 kV. High resolution TEM (HRTEM) micrographs were obtained using a Tecnai F20 field-emission gun microscope with a 0.19 nm point-to-point resolution at 200 keV with an embedded Gatan QUANTUM image filter for EELS analyses. Compositions were analyzed using an Oxford energy dispersive X-ray spectrometer (EDX) attached to the Zeiss Auriga SEM at 20.0 kV. TGA-DSC was done using the NETZSCH STA 409 C/CD Instrument in the temperature range from 40°C to 900°C with a heating rate of 3.0 K/min under argon atmosphere.

Thermoelectric property measurements: Seebeck coefficients were measured using a static DC method. Electrical resistivity data was obtained by a standard four-probe method. Both the Seebeck coefficient and the electrical resistivity were measured simultaneously in a LSR-3 LINSEIS system in the temperature range between room temperature and 498 K under helium atmosphere. All samples were measured at least 3 consecutive times during heating up to around 498 K. Taking into account the system accuracy and the measurement precision, an error of ca. 4 % in the measurement of the electrical conductivity and Seebeck coefficient was estimated. Thermal conductivities (κ) were calculated from the thermal diffusivity (λ), the heat capacity (C_p) and the mass density of the material (ρ), using $\kappa = \lambda C_p \rho$. A Xenon Flash Apparatus XFA600 was used to determine the thermal diffusivities of the samples with an estimated error of ca. 5 %. The constant pressure heat capacity was estimated from empirical formulas by the Dulong–Petit limit (3R law). The density values were calculated using the Archimedes' method. To avoid cluttering the plots, error bars were not included in the figures. The Hall carrier concentration (n) and mobility (μ) at room temperature (298 K) were measured with a Physical Property Measurement System (PPMS-9T, 10 % error, Quantum Design Inc., USA) using a magnetic field of 2 T. Values provided correspond to the average of 5 consecutive measurements.

5.4 Results and discussion

$Bi_xSb_{2-x}Te_3$ NCs with controlled composition were used as precursor building blocks to produce bulk nanocrystalline pellets. Figure 5.2a shows a representative SEM micrograph of the disk-shaped $Bi_xSb_{2-x}Te_3$ NCs produced in diethylene glycol from bismuth (III) nitrate, antimony (III) chloride and sodium tellurite in the presence of hydrazine and PVP at 190 °C. Over 5 g of NCs per batch were produced using this synthetic protocol (Figure 5.3a). Composition could be easily tuned around its optimum value for thermoelectric applications (x=0.5) by adjusting the initial ratios of the bismuth and antimony precursors (Figure 5.2b and Table 5.1). In all samples, excess amounts of tellurium, nominally Te/(Bi+Sb) =1.875, were introduced in the reaction mixture. The produced nanocrystal ensemble systematically conserved the nominal Bi/Sb ratios and an excess of tellurium: Te/(Bi+Sb)~1.7. Excess tellurium was found in the form of thin tellurium nanorods, segregated from $Bi_xSb_{2-x}Te_3$ nanodisks, as pointed out by red arrows in Figure 5.2a.

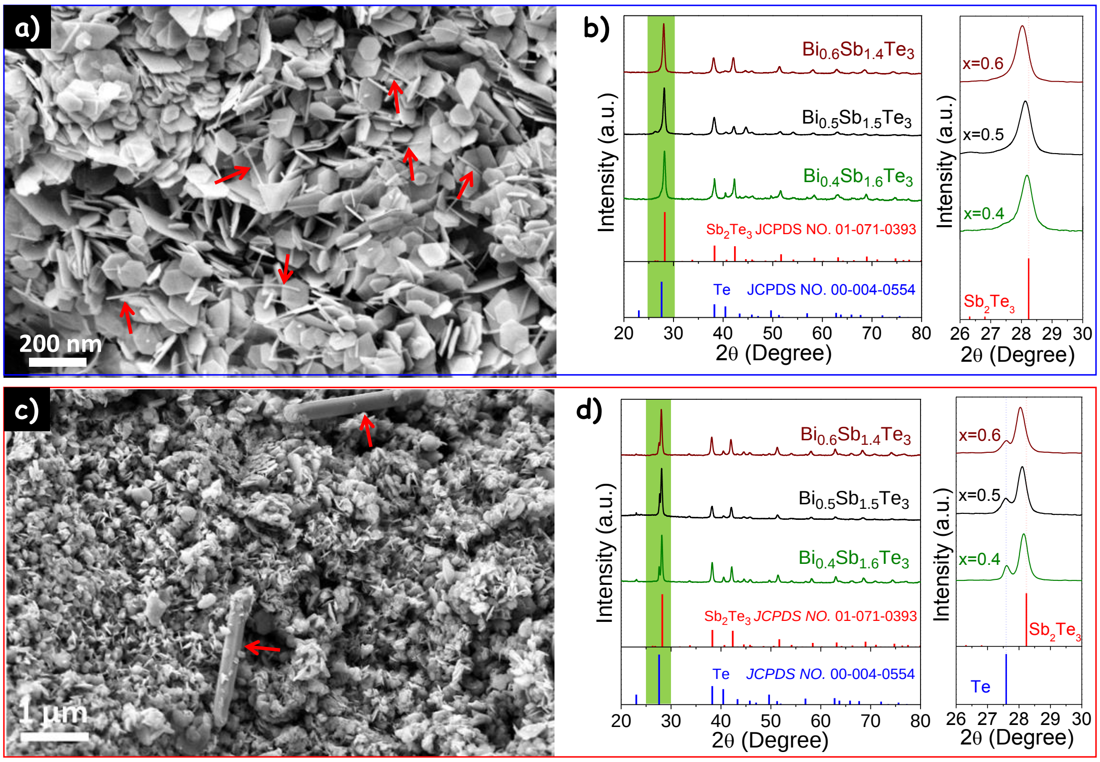

Figure 5.2. Representative SEM micrographs (a,c) and XRD patterns (b,d) of the $Bi_xSb_{2-x}Te_3$ disk-shaped NCs used in this work, before (a,b) and after (c,d) annealing. Tellurium nanorods were present in samples prepared with a nominal excess of tellurium and are pointed out by arrows in the SEM images of the sample before and after annealing. The presence of large tellurium nanorods in the annealed sample is also evidenced from the XRD peak at 2θ=27.6°.

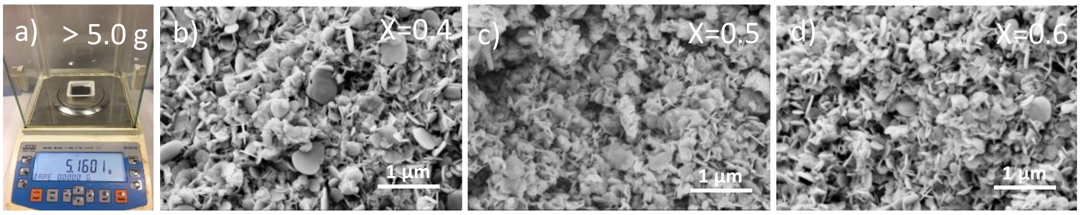

Figure 5.3. a) NCs produced per batch. b-d) SEM images of $Bi_xSb_{2-x}Te_3$ (x=0.4, 0.5 and 0.6) nanoplatelets with 25% excess tellurium after annealing at 350 ºC for 1 h.

$Bi_xSb_{2-x}Te_3$ NCs were purified by multiple precipitation and redispersion steps. Subsequently, they were dried and annealed at 350 °C for 60 min under argon flow inside a tube furnace to remove remaining organics. The annealed nanopowders still consisted of disk-shaped $Bi_xSb_{2-x}Te_3$ NCs (Figure 5.2c and Figure 5.3b-d) and contained large tellurium nanorods grown during the annealing step from the excess amounts of this element in the original sample, as observed by SEM (Figure 5.2c) and x-ray diffraction

(XRD, Figure 5.2d).

Table 5.1. SEM-EDX composition of $Bi_xSb_{2-x}Te_3$ (x=0.4, 0.5 and 0.6) NCs, annealed nanopowders and consolidated pellets. Data was obtained from averaging 5 analyses, resulting in an estimated error of ca. 3 %.

Nominal / **Material**	***x = 0.4***			***x = 0.5***			***x = 0.6***		
	Bi	***Sb***	***Te***	***Bi***	***Sb***	***Te***	***Bi***	***Sb***	***Te***
NCs	0.43	1.57	3.42	0.52	1.48	3.26	0.61	1.39	3.38
Nanopowder	0.42	1.54	3.39	0.52	1.48	3.25	0.60	1.39	3.33
Pellet	0.41	1.57	3.03	0.53	1.47	2.96	0.61	1.38	297

The annealed nanopowders were hot-pressed for 210 s within an inert atmosphere into cylindrical pellets (10 mm in diameter and 10 mm length) using 80 MPa of pressure. The whole procedure, lasting less than 5 minutes and requiring no vacuum and moderate processing temperatures, resulted in $Bi_xSb_{2-x}Te_3$ cylinders with relative densities ca. 90% of the theoretical value, as measured by the Archimedes' method. From these cylinders, rectangular bars of about 8×6×1 mm^3 were cut in two directions, along the press axis, i.e. the cylinder length, and within the plane normal to this axis, i.e. the cylinder disk plane (Figure 5.4).

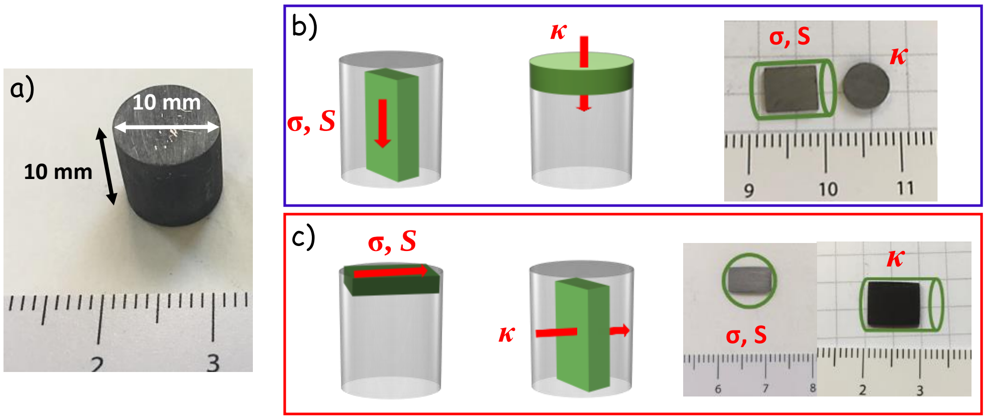

Figure 5.4. a) Photograph of one of the cylindrical pellet produced by hot pressing and to measure the thermoelectric properties of the materials in the two directions. b-c) Schematic illustrations and photographs of the samples obtained from the cylindrical pellets and used to measure thermoelectric properties in both direction, parallel (b) and normal (c) to the press direction.

Electrical conductivities and Seebeck coefficients were always measured using rectangular samples. Thermal conductivities were measured from disk-shaped samples in the direction of the press axis and from rectangular samples in the direction normal to the press axis.

The uniaxial hot press of the materials at temperatures below 400 °C resulted in relatively isotropic pellets containing small nanograins with random orientations (Figure 5.5f, g). On the other hand, when hot pressing the annealed nanopowders at temperatures above 450 °C, pellets with strong crystallographic texture, with the [001] crystallographic direction oriented along the press axis, were produced (Figures 5.5a-d). Figures 5.5a-5c show top-view and cross-section SEM micrographs of a pellet produced from hot pressing $Bi_xSb_{2-x}Te_3$ nanodisks at 480 °C. A laminar structure, with layer thicknesses of around 40 nm and extending several tens and even hundreds of microns in the disk plane, was systematically observed in all the samples produced at this temperature.

These layers displayed a homogeneous distribution of Bi and Sb and contained numerous stacking faults as observed from STEM-EELS and HRTEM characterization of a pellet cross-section (Figures 5.6 and 5.7). In order to study the crystal structure of the pellets, we obtained cross-sectional samples by using conventional mechanical thinning and ion milling. HRTEM analyses such as those shown in Figures 5.6 and 5.7 show the layered structure of a $Bi_{0.5}Sb_{1.5}Te_3$ pellet. The material was found to crystallize in the monoclinic C12-M phase with lattice constants a=15.705 Å, b = 4.305 Å, c = 9.395 Å, $\alpha = \gamma = 90.00^o$ and $\beta = 90.05^o$,[20] presenting a layered pattern along the c-axis as commonly found in Bi_2Te_3[21] or other $Bi_xSb_{2-x}Te_3$ composites.[22] Notice that in the later cases, the structure tends to crystallize in the trigonal R3-M structure instead of the monoclinic C12-M found here. Nevertheless, both structures show clear layered patterns along the c-axis. Compositional analyses were performed with STEM-EELS. Bi, Te and Sb were found to be homogeneously distributed through the pellet.

Figures 5.5d and 5.8 display the XRD patterns measured in two perpendicular orientations of the cylinder, along and normal to the press axis. The XRD pattern of the pellet held with the press axis normal to the support, showed a clear increase of the diffraction peaks corresponding to the [001] crystallographic directions with respect to the pattern obtained from the cylinder held planar (Figure 5.5d).

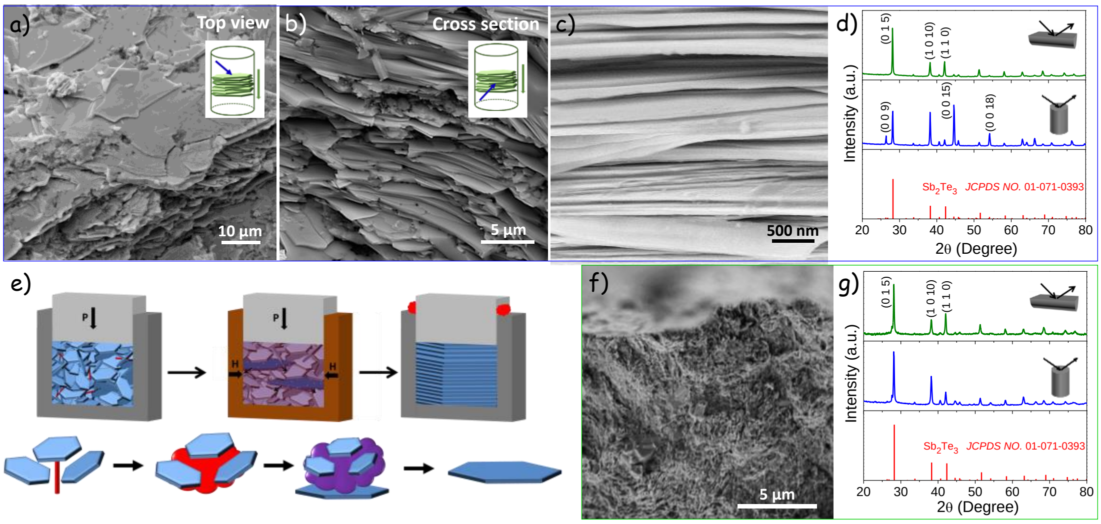

Figure 5.5. a) Top-view SEM micrograph of a $Bi_xSb_{2-x}Te_3$ pellet produced at 480 °C. b) Cross-section SEM micrograph of the same pellet. c) Detail of the cross-section SEM micrograph. d) XRD patterns of the pellet placed to have the press axis within the diffraction plane (green) and normal to it (blue). e) Cartoon of the liquid-assisted sintering of the NCs under uniaxial pressure. f) Cross-section SEM micrograph of a pellet hot-pressed at 300 °C. g) XRD patterns of the pellet hot-pressed at 300 °C placed to have the press axis within the diffraction plane (green) and normal to it (blue).

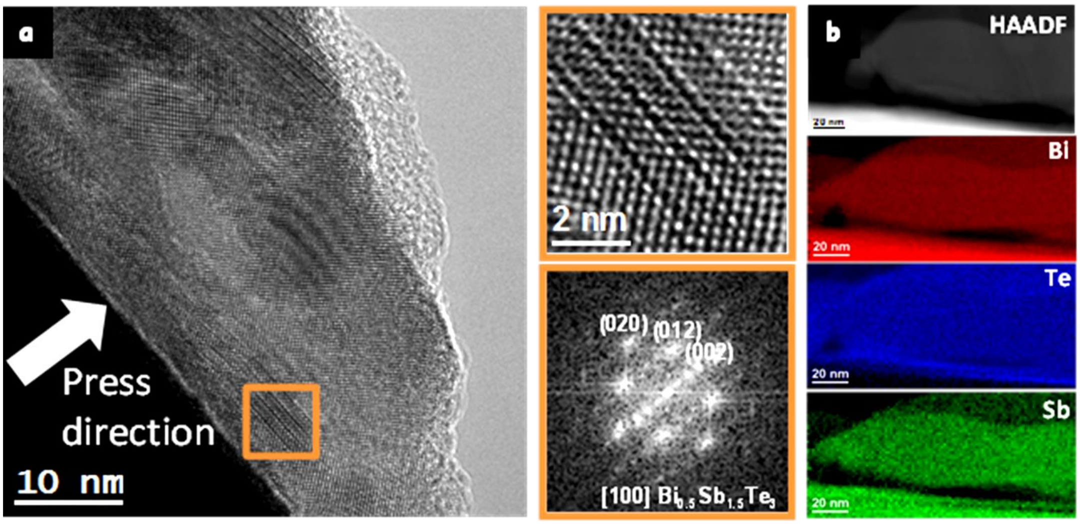

Figure 5.6. a) HRTEM micrograph obtained on a region of the pellet showing the multiple layered structure of the $Bi_{0.5}Sb_{1.5}Te_3$ along its [100] zone axis. The region observed presents several crystalline domains oriented along the basal planes. Details of the squared area and the corresponding indexed power spectrum are also shown. Notice that the structure present stacking faults. b) Areal density of Bi, Te and Sb obtained through STEM-EELS signal integration after background removal using Bi (N-edge), Te (M-edge) and Sb (M-edge), respectively.

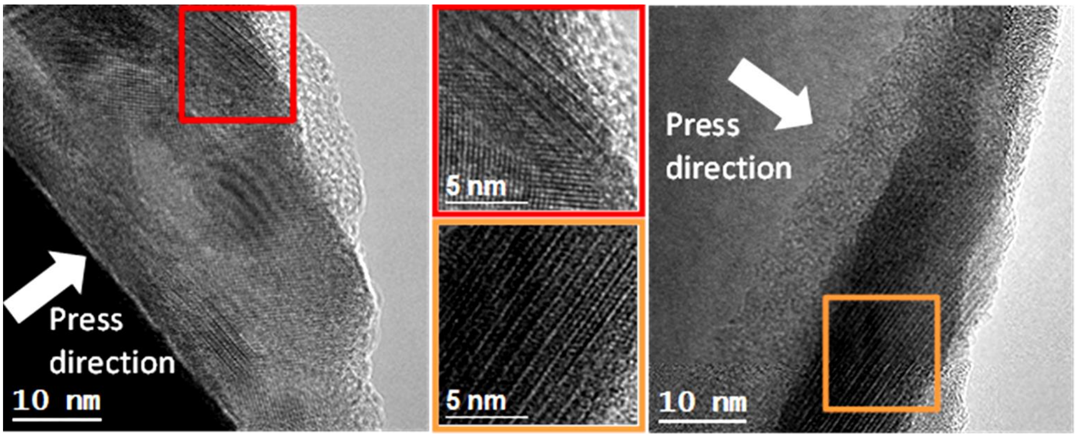

Figure 5.7. HRTEM micrographs of two areas within the pellet cross section showing the layered monoclinic structure of $Bi_{0.5}Sb_{1.5}Te_3$ along its [100] zone axis.

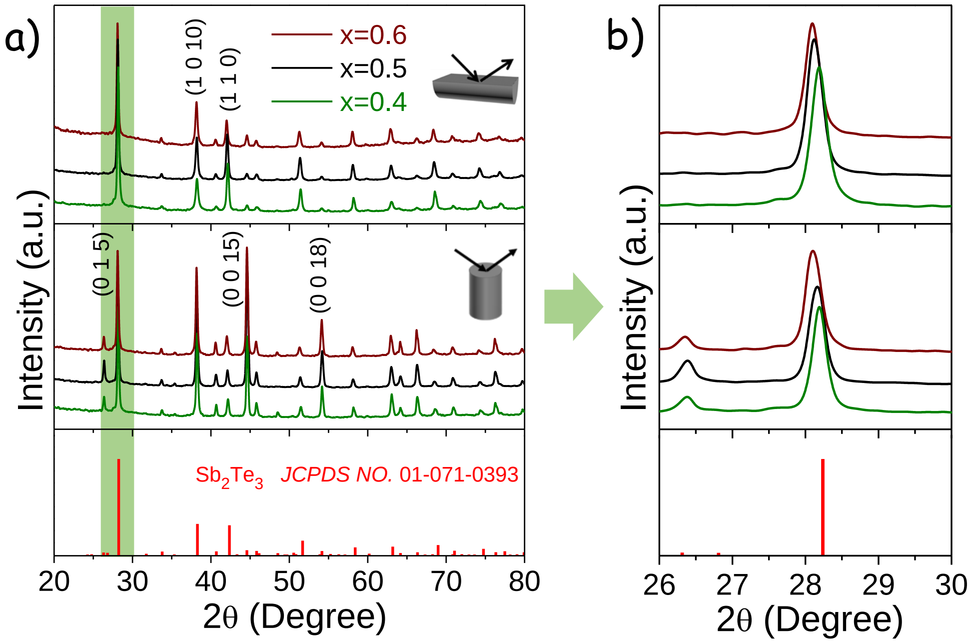

Figure 5.8. a) XRD patterns of consolidated $Bi_xSb_{2-x}Te_3$ (x=0.4, 0.5 and 0.6) pellets measured in the two directions, parallel and normal to the press direction. b) Detail of the same XRD patterns showing the systematic shift of the (0 1 5) peak with the bismuth composition (x).

The excess of tellurium in the initial nanopowder was essential to produce highly crystallographically textured nanomaterials (Figure 5.9). During the hot press process at 480 ºC, the excess of tellurium, ca. 8% in volume, liquefied (tellurium melting point is 449.5 °C), creating a solid-liquid interface with two main potential consequences.

The liquid interface reduced the interparticle friction, potentially facilitating the reaccommodation of the solid NCs. In a pure nanocrystal rearrangement scenario, the final pellet would consist of disk-shaped NCs identical to those observed in the precursor nanopowders, but all aligned in one preferential direction dictated by the press axis. However, this was not the observed pellet nanostructure (Figures 5.5a-c).

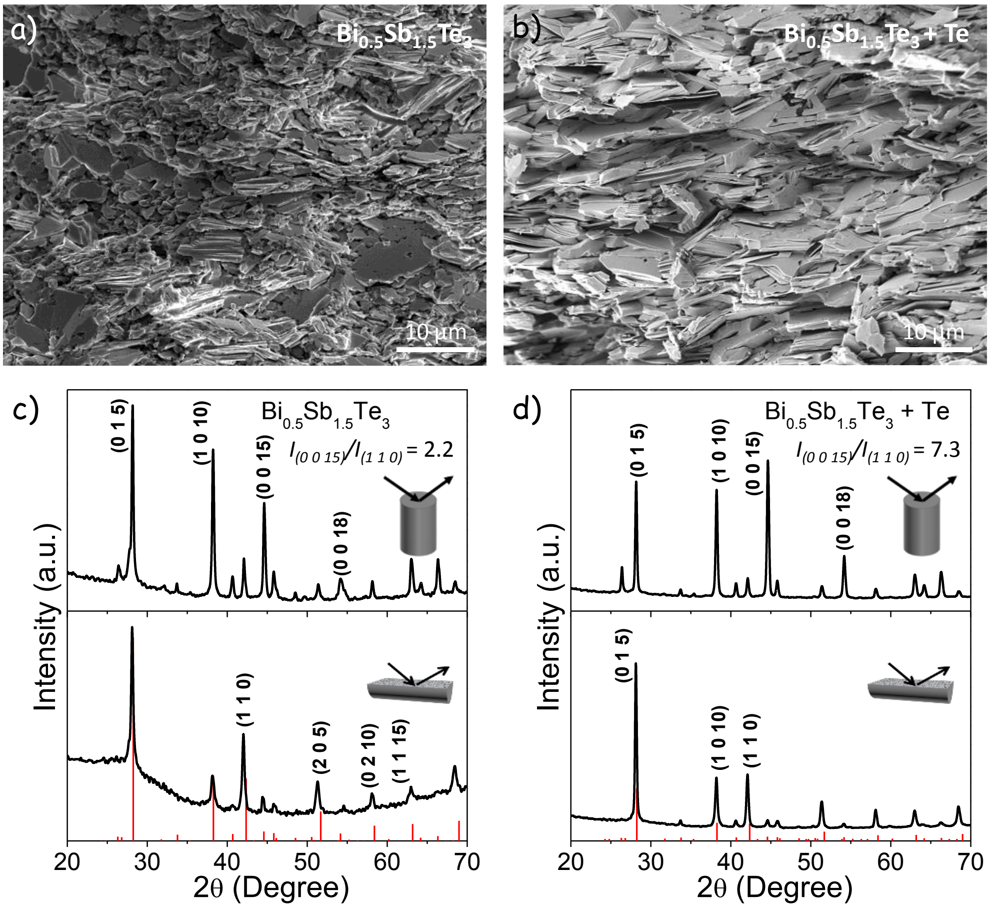

Figure 5.9. a-b) Cross-section SEM micrographs of the $Bi_{0.5}Sb_{1.5}Te_3$ pellets produced without (a) and with (b) an excess of tellurium in the initial nanoplatelets. c) and d) XRD pattern of the $Bi_{0.5}Sb_{1.5}Te_3$ pellet produced without and with an excess of tellurium, respectively. Red vertical lines correspond to the reference literature data for Sb_2Te_3, JCPDS NO. 01-071-0393.

The tellurium liquid phase could also dissolve the randomly oriented $Bi_xSb_{2-x}Te_3$ NCs, allow a fast-atomic diffusion of the alloy elements, and feed, when oversaturated, the nucleation and growth of new $Bi_xSb_{2-x}Te_3$ crystals oriented in a preferential direction dictated by the press axis. In the liquid phase sintering literature, this sintering mechanism is known as the solution-reprecipitation stage.[23] Indeed, at 480 °C, liquid tellurium can dissolve around 15% of Sb and 25% of Bi. Actually, both the Sb-Te and Bi-Te systems have eutectic points: at 422 °C for Sb-Te with a 7.4% of Sb and at 413 °C with 10% of Bi in the Bi-Te system.[24, 25] The dissolution of the solid in the liquid phase varies inversely with the crystal size, thus smaller grains and higher energy surfaces preferentially dissolve, contributing to the formation of larger grains. In this Ostwald ripening scenario, randomly oriented small disk-shaped NCs are rapidly dissolved and larger and crystallographically oriented structures are produced, strongly reducing the material porosity.[23, 26] Such nanostructure matched well with the results obtained.

The presence of a uniaxial hydrostatic pressure during the liquid phase sintering decisively influenced the orientation of the growing crystals. During the solution and reprecipitation step, the preferred orientation of the precipitating crystals is the one that minimizes chemical potential required for equilibrium across the plane normal to the pressure axis.[27] Such orientation depends on the elasticity of the material in each crystallographic direction, in such a way that in rather elastically anisotropic materials, such as $Bi_xSb_{2-x}Te_3$, crystals align with the weakest crystallographic plane normal to the pressure axis. The layered structure of $Bi_xSb_{2-x}Te_3$ crystals, with a strong bonding between atoms inside the *ab* plane and weak bonding between the layers in the *c* direction, results in a rather strong anisotropy of the elastic constants.[28] In particular, the Young modulus of Bi_2Te_3 crystals in the *a* and *b* axes are close to 30% larger than in the *c* axis.[29, 30] Thus, during the liquid phase sintering under a uniaxial pressure, reprecipitated crystals would be oriented with the *c* direction parallel to the press axis, as we observed experimentally.

The presence of a uniaxial pressure during the liquid phase sintering may not only introduce a preferential orientation of the reprecipitated crystals, but it may also influence their geometry.[27, 28] In the presence of a liquid phase able to partially dissolve and reprecipitate the crystals, the uniaxial pressure promotes growth in its normal directions and aids the dissolution of the crystal in the directions parallel to this axis.[27, 28] In the particular case of $Bi_xSb_{2-x}Te_3$, already in solution, at moderate temperatures and in the absence of a uniaxial pressure, NCs grow faster in the *ab* plane than in the *c*-axis, thus acquiring flat, disk-shaped, morphologies. During the hot press process, the relative growth in the *ab* plane is much more accentuated and plates with much higher aspect ratios are finally obtained.

The initial shape of the pressed NCs could influence the direction and even existence of a predominant orientation of the crystal domains in the final material.[31] Actually, in a previous work, no significant crystallographic texture was observed in pellets obtained from the hot press of ball milled $Bi_xSb_{2-x}Te_3$ containing an excess of tellurium, even when using processing temperatures above the tellurium melting point.[32] To determine the role of the geometry of the precursor nanocrystal, we hot-pressed Bi_2Te_3 nanorods with the same excess of tellurium, Te/Bi~1.7, and following the exact same steps as in the case of $Bi_xSb_{2-x}Te_3$ nanodisks (Figure 5.10).[33] The polycrystalline material produced had a significant crystallographic texture ($I_{(00\underline{15})}/I_{(110)}=5.6$, Figures 5.11 and 5.12), but lower than that obtained with the $Bi_xSb_{2-x}Te_3$ nanodisks ($I_{(00\underline{15})}/I_{(110)}=7.3$, Figure 5d). We also produced pellets by hot pressing a powder obtained from the ball milling of a commercial ingot and adding an excess of elemental tellurium to it. These pellets also showed some crystallographic alignment ($I_{(00\underline{15})}/I_{(110)}=3.1$, Figures 5.13 and 5.14), but also lower than the pellets produced from nanodisks (Figure 5.5d).

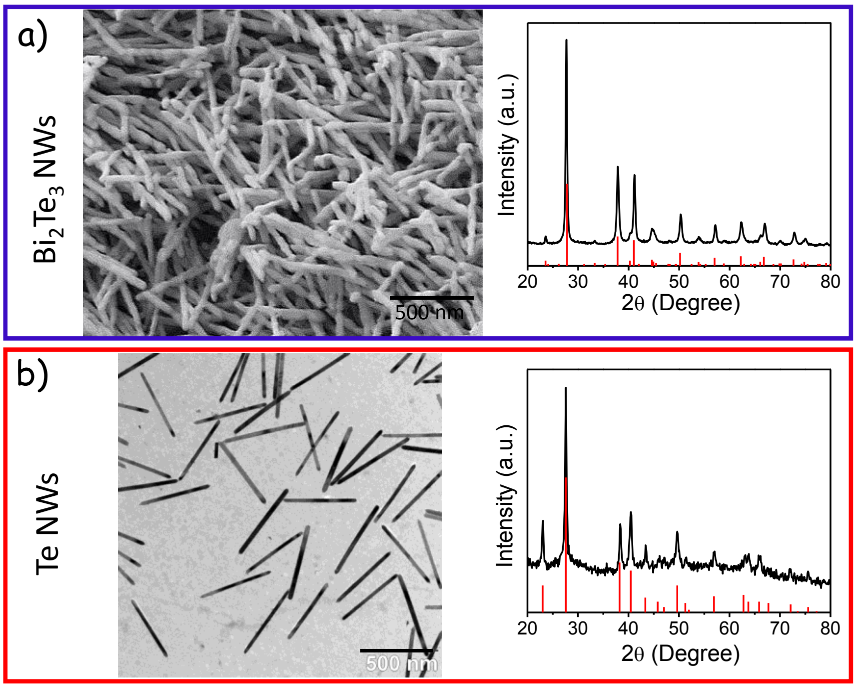

Figure 5.10. a) Representative SEM micrograph of Bi_2Te_3 nanowires and the corresponding XRD pattern including a Bi_2Te_3 reference (JCPDS NO. 01-089-2009). b) TEM micrograph of tellurium nanowires and the corresponding XRD pattern, including a tellurium reference (JCPDS NO. 00-004-0555).

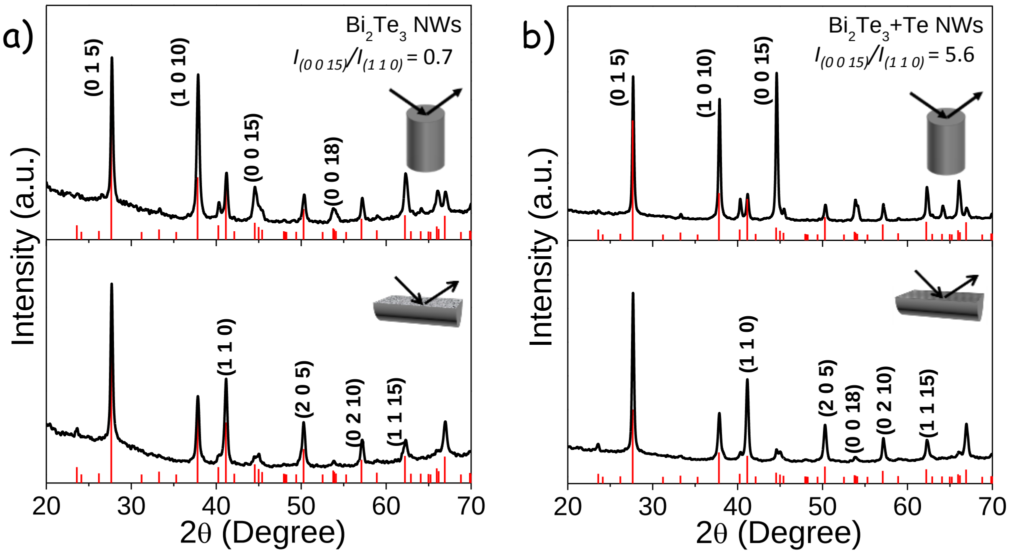

Figure 5.11. XRD patterns of the Bi_2Te_3 (a) and Bi_2Te_3+Te (b) pellets placed to have the x-ray diffraction plane in two perpendicular directions as marked within the graph. Pellets were consolidated by hot pressing the nanowires at 480 °C for 210 s. Red vertical lines correspond to the reference literature data for Bi_2Te_3, JCPDS NO. 01-089-2009.

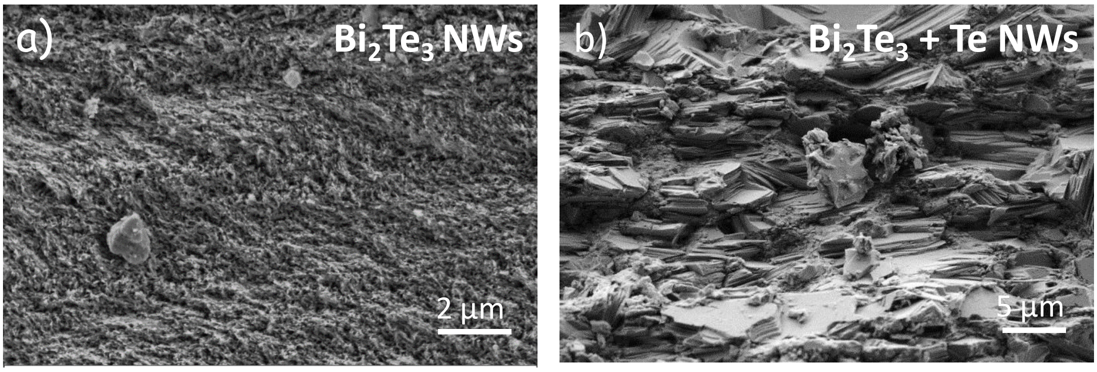

Figure 5.12. Cross-section SEM micrographs of Bi_2Te_3 (a) and Bi_2Te_3+Te (b) nanowires hot-pressed at 480 °C.

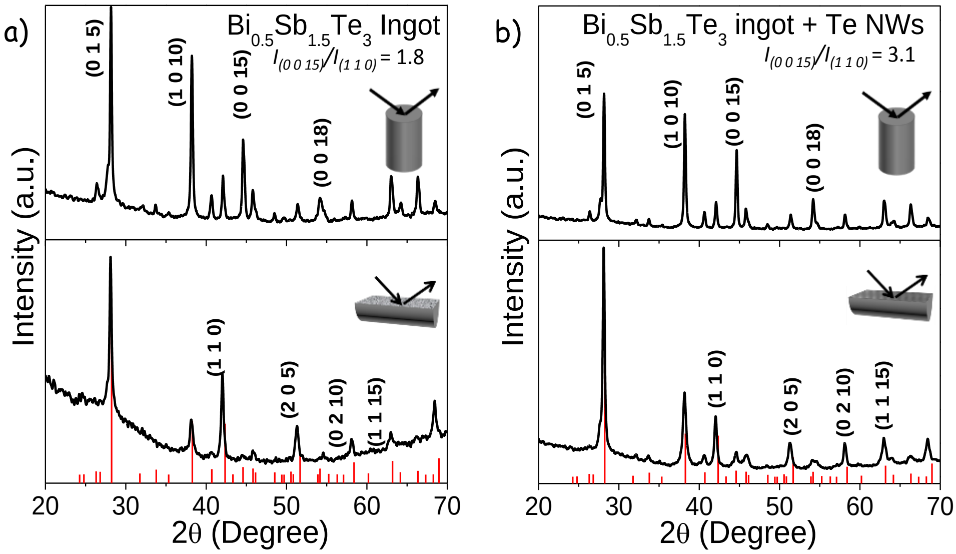

Figure 5.13. XRD patterns of a ball milled and later consolidated (hot press at 480 ºC during 210 s) commercial ingot. a) Pellet produced from the consolidation of a $Bi_{0.5}Sb_{1.5}Te_3$ nanopowder obtained by ball milling a commercial ingot. b) Pellet produced from the consolidation of a $Bi_{0.5}Sb_{1.5}Te_3$+Te nanopowder obtained by ball milling a commercial ingot and adding tellurium nanowires to it. Red vertical lines correspond to the reference literature data for Sb_2Te_3, JCPDS NO. 01-071-0393.

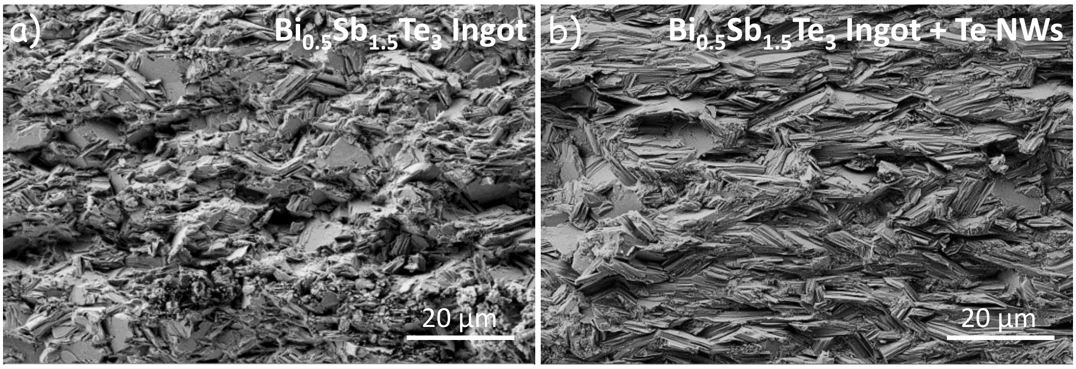

Figure 5.14. Cross-section SEM micrographs of a ball milled and later consolidated (hot press at 480 ºC during 210 s) commercial ingot. a) Pellet produced from the consolidation of a $Bi_{0.5}Sb_{1.5}Te_3$ nanopowder obtained by ball milling a commercial ingot. b) Pellet produced from the consolidation of a $Bi_{0.5}Sb_{1.5}Te_3$+Te nanopowder obtained by ball milling a commercial ingot and adding tellurium nanowires to it.

To produce consolidated nanomaterials with stoichiometric composition and having the finest crystallographic texture and optimum thermoelectric properties, it was essential to completely remove the excess amount of tellurium. Conveniently, during the hot press, while the temperature was above the tellurium melting point, the excess of this element was expelled through the plunger rod (Figure 5.15). However, in just one pressure and release step, the tellurium excess was not completely removed from the sample, probably due to the blocking of the escape paths within the layered structure or the plunger rod (Figures 5.16-5.18). Only upon multiple pressure and release steps the excess of tellurium could be totally ejected. Specifically, we used 5 pressure and release steps during the 210 s that the temperature was set at 480 °C to completely get rid of the tellurium excess. A similar cycling uniaxial pressure was previously reported to improve crystal alignment in spark plasma sintered $Bi_xSb_{2-x}Te_3$, having no tellurium excess.[18] No inside of the involved mechanism was reported in this previous work.

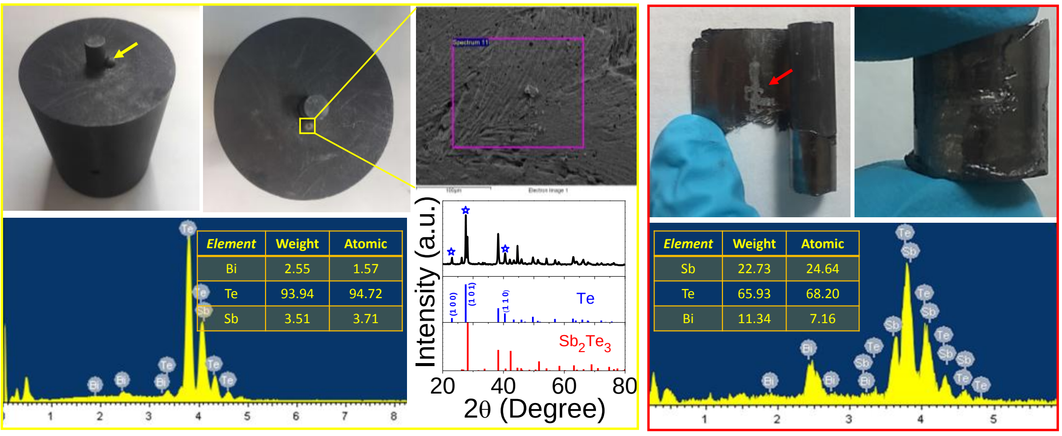

Element	Weight	Atomic
Bi	2.55	1.57
Te	93.94	94.72
Sb	3.51	3.71

Element	Weight	Atomic
Sb	22.73	24.64
Te	65.93	68.20
Bi	11.34	7.16

Figure 5.15. Photographs of the graphite dies and the carbon rod covered with a graphite foil after hot press. As indicated by the yellow and red arrows, some material was expelled out from the graphite die during the hot press. XRD and EDX analysis of the material spilled out confirming that between 70-90% of this material is tellurium.

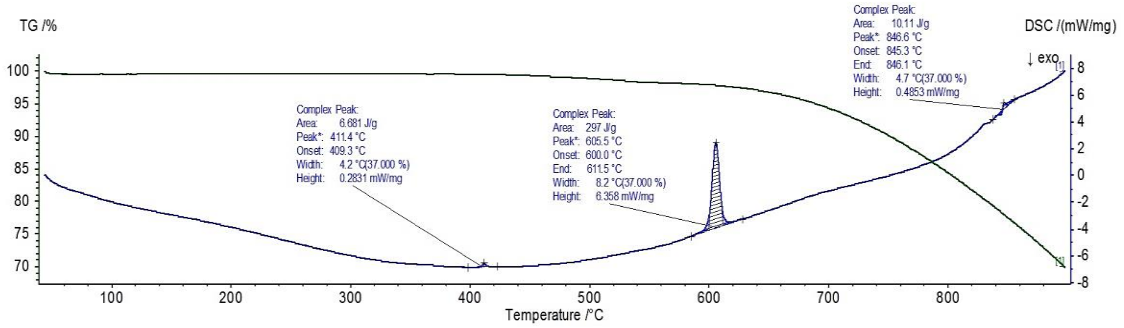

Figure 5.16. TGA-DSC of a $Bi_{0.5}Sb_{2.5}Te_3$+Te pellet hot pressed at 480 ºC for 210 s using just one pressure and release step. Besides the large exothermic peak at 605 ºC associated to the melting of the $Bi_{0.5}Sb_{2.5}Te_3$ alloy, a weak exothermic peak at ~411 ºC associated to a tellurium-rich phase is observed.

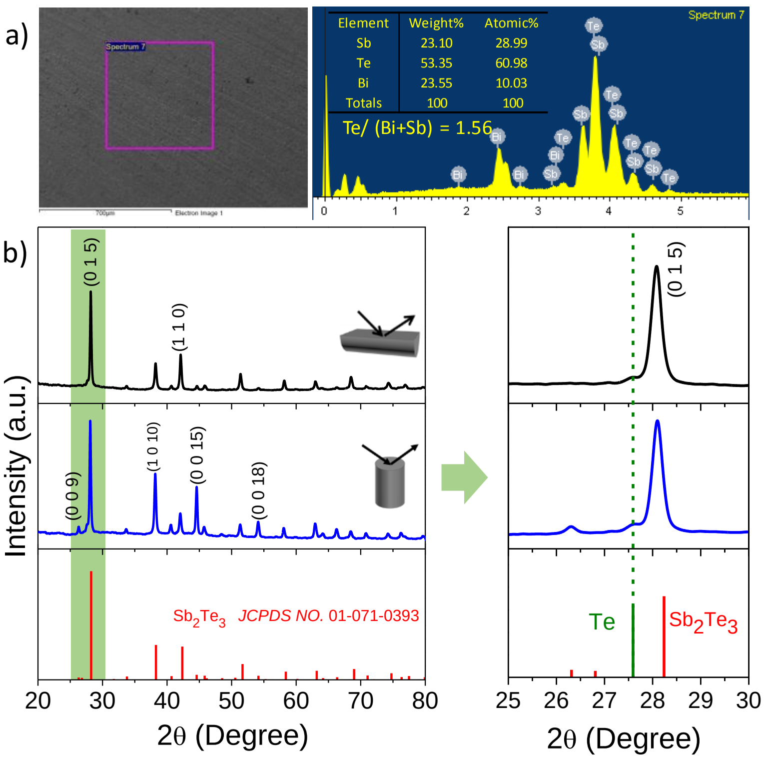

Element	Weight%	Atomic%
Sb	23.10	28.99
Te	53.35	60.98
Bi	23.55	10.03
Totals	100	100

Te/ (Bi+Sb) = 1.56

Figure 5.17. a) SEM micrograph and SEM-EDX composition of a $Bi_{0.5}Sb_{2.5}Te_3$+Te pellet hot pressed at 480 ºC for 210 s using just one pressure and release step. b) XRD patterns of the same pellet showing the presence of a weak tellurium peak at 27.5º, according to the tellurium reference pattern JCPDS NO. 00-004-0554.

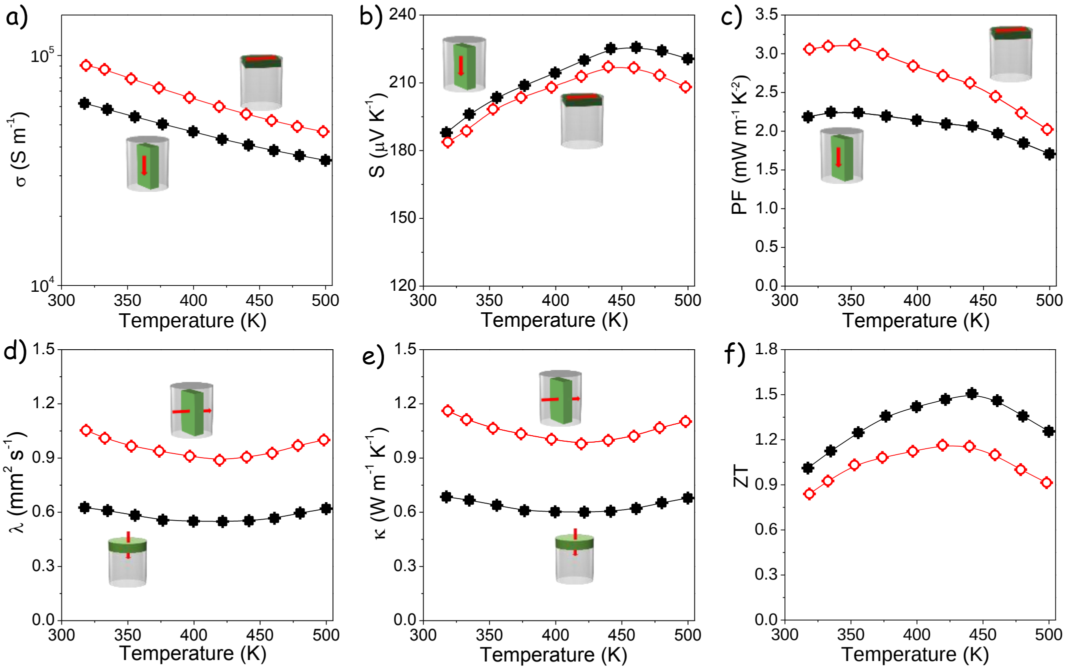

Figure 5.18. Temperature dependence of electric conductivity, σ (a); Seebeck coefficient, S (b); power factor, PF (c); thermal diffusivity, λ (d); thermal conductivity, κ (e); and thermoelectric figure of merit, ZT (f) of the $Bi_{0.5}Sb_{2.5}Te_3$+Te pellet hot pressed at 480 ºC for 210 s using just one

pressure and release step.

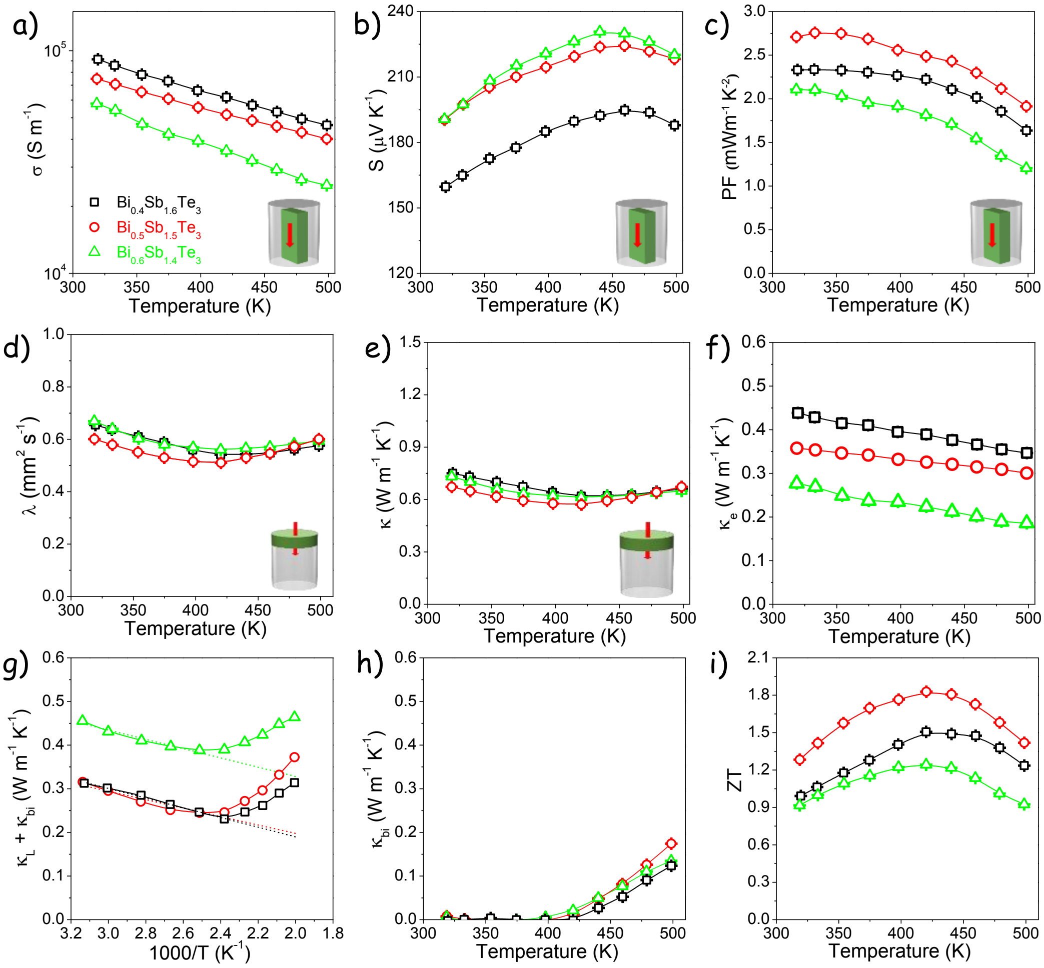

Figure 5.19. Temperature dependence of electric conductivity, σ (a); Seebeck coefficient, S (b); power factor, PF (c); thermal diffusivity, λ (d); thermal conductivity, κ (e); electrical thermal conductivity, κ_e (f); lattice and bipolar thermal conductivities, $\kappa_L+\kappa_{bi}$ (g); bipolar component to the thermal conductivity, κ_{bi}, estimated as the difference between κ- κ_e and a linear fitting of $\kappa-\kappa_e$ as a function of 1/T in the low temperature range (h) and thermoelectric figure of merit, ZT (i) of $Bi_xSb_{2-x}Te_3$ (x=0.4, 0.5 and 0.6) samples measured in the direction parallel to the press axis. The plotted data values were obtained by averaging the experimental data measured from five samples having approximately the same composition.

Among the different compositions tested, $Bi_{0.5}Sb_{1.5}Te_3$ provided the highest thermoelectric figures of merit (Figures 5.19 and 5.20). We associated this experimental fact to a more optimum charge carrier concentration in this sample. This result is consistent with previous reports and with the use of this composition in commercial devices. Figure 5.21 shows the electrical conductivity, σ; Seebeck coefficient, S; power factor, PF; thermal conductivity, κ; lattice and bipolar thermal conductivity, $\kappa_L + \kappa_{bi} = \kappa$

− κ_e, and overall thermoelectric figure of merit, $ZT=S^2\sigma T/\kappa$, of the $Bi_{0.5}Sb_{1.5}Te_3$ nanomaterial hot pressed at 480 °C and measured in two directions, parallel and normal to the press axis (Figure 5.4). Displayed results were obtained from averaging experimental data from five different pellets (Figure 5.25). These results are compared in Figure 5.21 with those obtained from a pellet produced with the exact same material, but hot pressed at a lower temperature, 300 °C, and a commercial ingot measured in the cleavage plane (*ab*) and its normal direction (*c*).

The nanomaterials hot pressed at 300 °C showed relatively low electrical conductivities (Figure 5.21a). Such low electrical conductivities were associated to a strong scattering of charge carriers at the ubiquitous grain interfaces of these materials. Additionally, these materials had lower relative densities than materials hot pressed at higher temperatures and contained an excess amount of tellurium which had not been expelled during the hot-press step.

On the other hand, nanomaterials hot-pressed at 480 °C showed very high electrical conductivities, comparable to those of the commercial sample. As expected, the electrical conductivities measured in the disk plane where higher than those obtained in the press direction ($\sigma_{ab}/\sigma_c = 1.6$ at 320 K). Such high electrical conductivities have been previously measured in samples processed in an excess of tellurium and were related to two main factors:[31, 34] i) an increase (over materials with similar Bi/Sb ratios) of the hole concentration associated to a modification of the antisite and vacancy defects due to the tellurium excess;[33] ii) formation during the liquid phase sintering of semicoherent grain boundaries having a minimal effect on hole scattering.[31]

Hall measurements of a series of five hot-pressed $Bi_{0.5}Sb_{1.5}Te_3$ nanomaterials measured three times showed the average charge carrier concentrations to be $p = 5 \pm 3$ x10^{19} cm^{-3}, i.e. sensibly higher than that of the commercial material $p = 1.0 \pm 0.5$ x10^{19} cm^{-3}. The mobilities measured in the plane normal to the press axis were on average a factor 1.6 higher than those measured in the press axis direction.

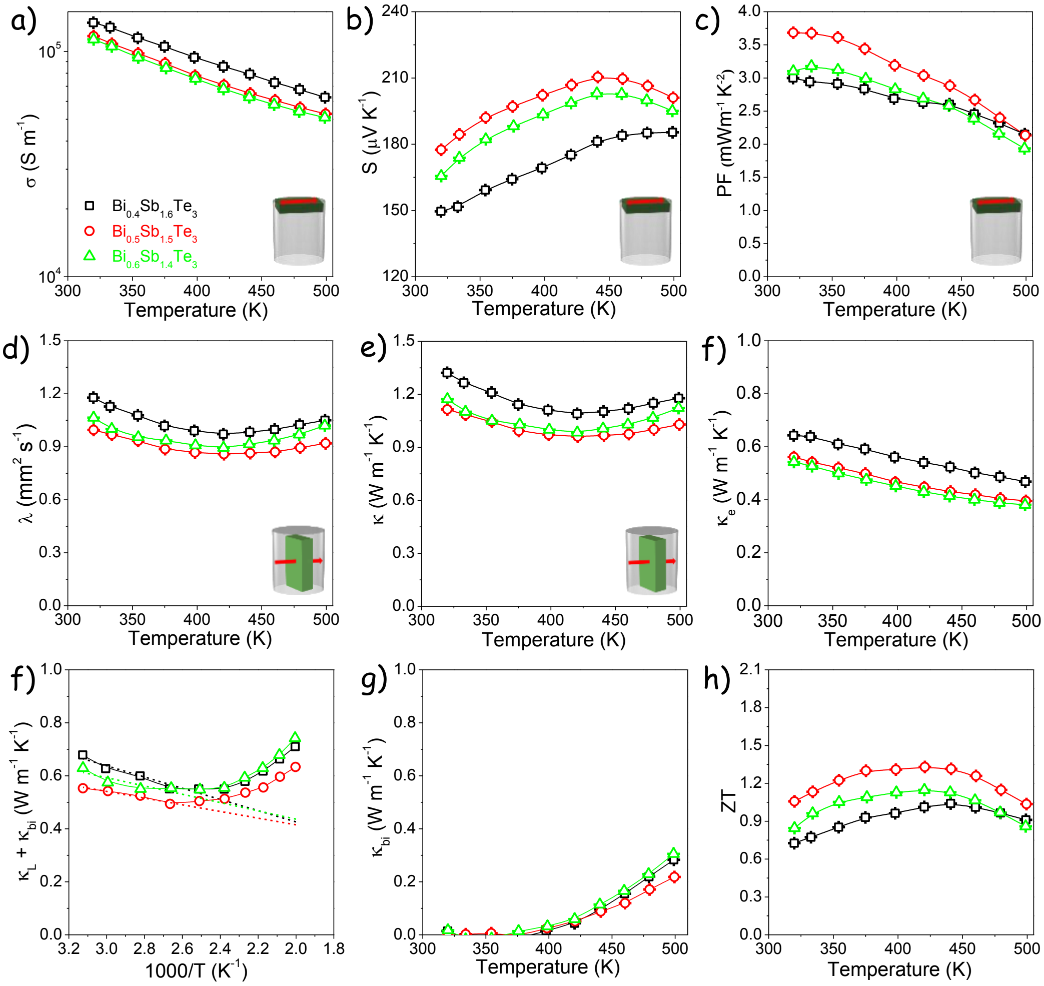

Figure 5.20 Temperature dependence of electric conductivity, σ (a); Seebeck coefficient, S (b); power factor, PF (c); thermal diffusivity, λ (d); thermal conductivity, κ (e); electrical thermal conductivity, κ_e (f); lattice and bipolar thermal conductivities, κ_L+κ_{bi} (g); bipolar component to the thermal conductivity, κ_{bi}, estimated as the difference between κ- κ_e and a linear fitting of κ-κ_e as a function of 1/T in the low temperature range (h) and thermoelectric figure of merit, ZT (i) of $Bi_xSb_{2-x}Te_3$ (x=0.4, 0.5 and 0.6) samples measured in the plane normal to the press axis. The plotted data values were obtained by averaging the experimental data measured from five samples having approximately the same composition.

The Seebeck coefficients of the bottom-up assembled nanomaterials were significantly lower than those of the commercial sample, especially for the nanomaterial hot pressed at 480 °C (Figure 5.21b). These lower Seebeck coefficients were associated to the higher charge carrier concentrations present in the bottom-up nanomaterials. The higher charge carrier concentrations also explained that the Seebeck coefficients started to decrease at a higher temperature in the nanomaterial hot-pressed at 480 °C when compared with the commercial sample. On top of this retard of the bipolar effect associated to the higher charge carrier concentration, the excess of tellurium during the consolidation step could also reduce the density of tellurium vacancies, an n-type defect, thus additionally decreasing the extent of the bipolar effect and shifting to even higher temperature the ZT maximum.

Seebeck coefficients measured in each of the two directions were very similar (S_c/S_{ab} = 1.07 at 320 K), as expected from the reduced anisotropy of this parameter already reported for single crystals (S_c/S_{ab} = 1.02).[11] Nevertheless, the coefficients measured in the press axis direction were slightly higher, which could point at some extend of selective scattering of the minority carriers at the crystal interfaces in the *c* direction.

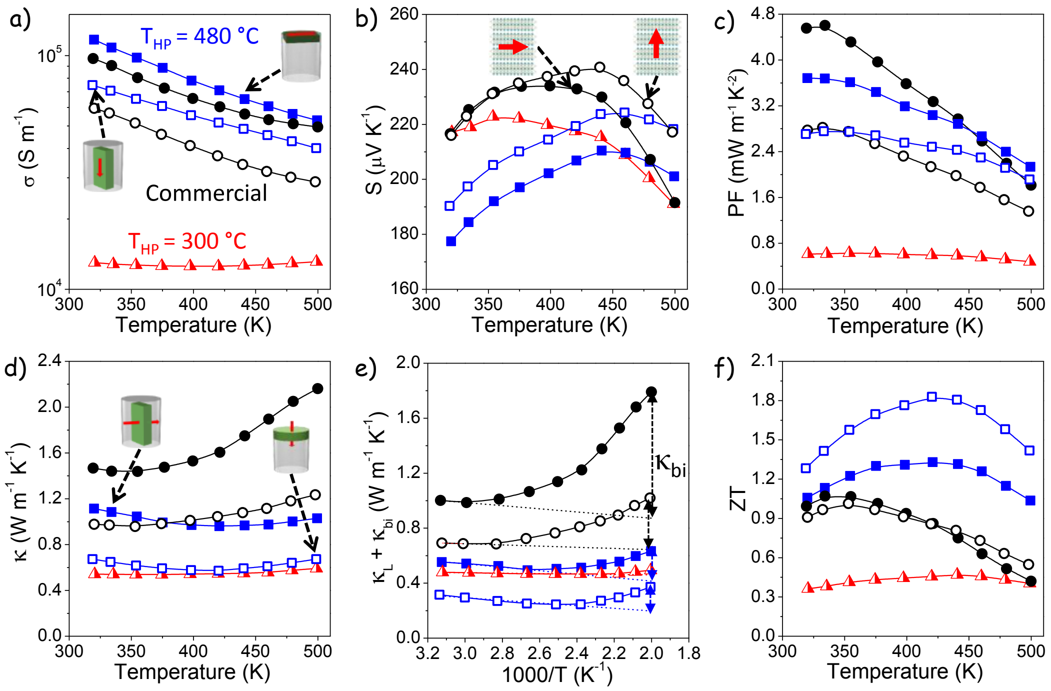

Figure 5.21. Thermoelectric properties of $Bi_{0.5}Sb_{1.5}Te_3$ nanomaterial hot pressed at 480 °C (blue squares) measured in two directions, parallel (open squares) and normal (solid squares) to the press axis (data were obtained from averaging the data values experimentally measured from 5 samples); $Bi_{0.5}Sb_{1.5}Te_3$ nanomaterial hot pressed at 300 °C (red triangles); and a commercial ingot (black circles) measured in two directions, parallel (solid circles) and normal (open circles) to the cleavage direction. a) Electrical conductivity, σ; b) Seebeck coefficient, S; c) power factor, PF, d) thermal conductivity, κ; e) lattice and bipolar thermal conductivity, $\kappa_L + \kappa_{bi} = \kappa - \kappa_e$; and f) thermoelectric figure of merit, ZT.

As expected, the thermal conductivities of the nanomaterials were significantly lower than those of the commercial sample, due to effective scattering at grain boundaries and crystal defects such as stacking faults (Figure 5.21d). For the nanomaterial hot pressed at 480 °C, the thermal conductivity was particularly low in the direction of the press axis ($\kappa_{ab}/\kappa_c = 1.64$ at 320 K), where a higher density of interfaces and stacking faults existed. In this direction, the thermal conductivity of this nanomaterial became comparable to that measured on the pellet hot pressed at 300 °C containing a random distribution of very small crystals. When taking into account the correction for the 10% porosity measured, i.e.a factor 1.33, the lowest lattice thermal conductivities that we measured at room temperature (0.43 $Wm^{-1} K^{-1}$) were slightly above the amorphous limit for Bi_2Te_3 (0.31 $Wm^{-1} K^{-1}$),[35] and clearly above those estimated for highly defective Bi_2Te_3 (ca. 0.17 $Wm^{-1}K^{-1}$),[36] or for very small Bi_2Te_3 nanograins (0.12 $Wm^{-1}K^{-1}$) [37] and those measured for stacked Bi_2Te_3 2D films at room temperature (0.1 $Wm^{-1}K^{-1}$).[37]

Thermal conductivities decreased with increasing temperature in the low temperature range and stabilized or increased in the high temperature range, when the bipolar contribution became significant (Figures 5.21e). Consistently with previous observations,[38] the bipolar contribution to the thermal conductivity was lower in the nanomaterial than in the commercial sample, which was attributed to a combination of the higher majority carrier concentration, the suppression of a source of minority carriers, such as tellurium vacancies, and the scattering of minority carriers at crystal interfaces or planar defects such as stacking faults.

Overall, the thermoelectric figures of merit of the nanomaterial hot pressed at 480 °C were significantly higher than those of the commercial sample (Figure 5.21f). In particular, in the direction of the press axis, i.e. *c*, the combination of a high electrical conductivity, a notable Seebeck coefficient and a very low thermal conductivity resulted in thermoelectric figures of merit up to ZT = 1.96 at 420 K for the record material and ZT = 1.83 when averaged for 5 pellets. Dispersion of results provided from a dispersion of the charge carrier concentration in the samples. These values are the highest thermoelectric figure of merit reported in the ambient temperature range (Figure 5.22). Importantly, these high thermoelectric figures of merit were sustained in an extended temperature range. The average ZT, calculated over 180 K, from 320 K to 500 K, was ZT_{ave}=1.77 for the record material and ZT_{ave}=1.65 when averaging for 5 pellets. These values translated in potential energy conversion efficiencies up to 60% higher than those of commercial materials as shown in the following[39, 40]

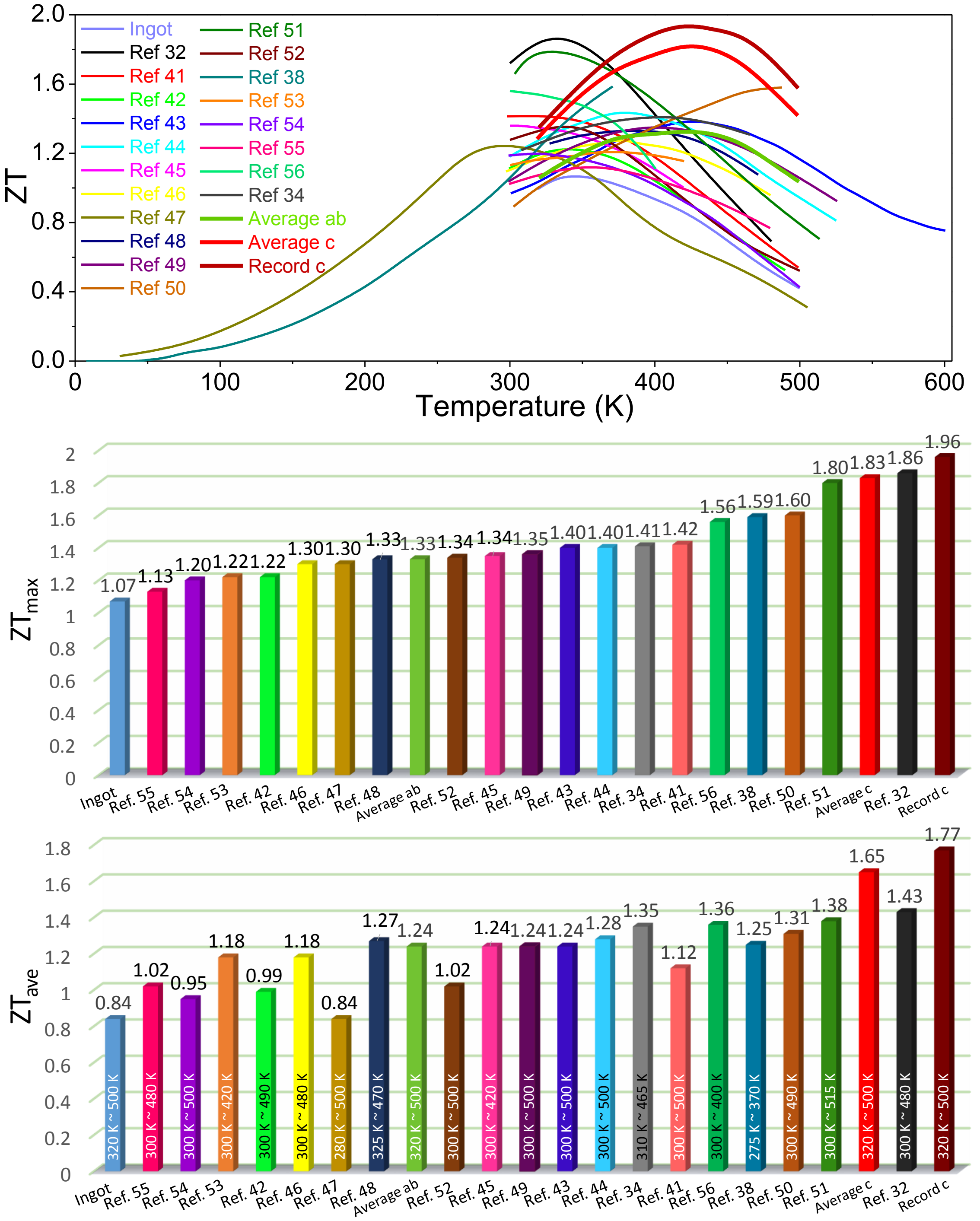

Figure 5.22. State-of-the-art ZT values and average ZT values for p-type Bi_2Te_3-based alloys.[32, 34, 38, 41-56] Our data is named as "average ab", "average c" and "record c", corresponding to the values obtained from averaging the experimental data measured from five different samples in the two directions (perpendicular (ab) and parallel (c) to the press axis), and to the record materials (among the five samples) measured in the direction parallel to the press axis, respectively.

Notice that the figures of merit measured from the nanomaterial in the *ab* plane were systematically lower than those in the *c* direction (Figure 5.21f). This was somehow unexpected, since higher ZT values have been generally measured or assumed in the *ab* plane for single crystals and partially oriented polycrystalline materials.[11, 15] The general assumption that the figures of merit in the *ab* plane must be higher than those in the *c* direction explain that in several previous works only the thermoelectric properties in the ab plane were measured, when possibly higher figures of merit would have been obtained in the normal direction.[38, 57]

Finally, we want to highlight that the nanocrystalline $Bi_xSb_{2-x}Te_3$ materials presented here showed good stability even when heated up to relatively high temperature (500 K) and during prolonged periods of time, as can be seen in Figures 5.23 and 5.24.

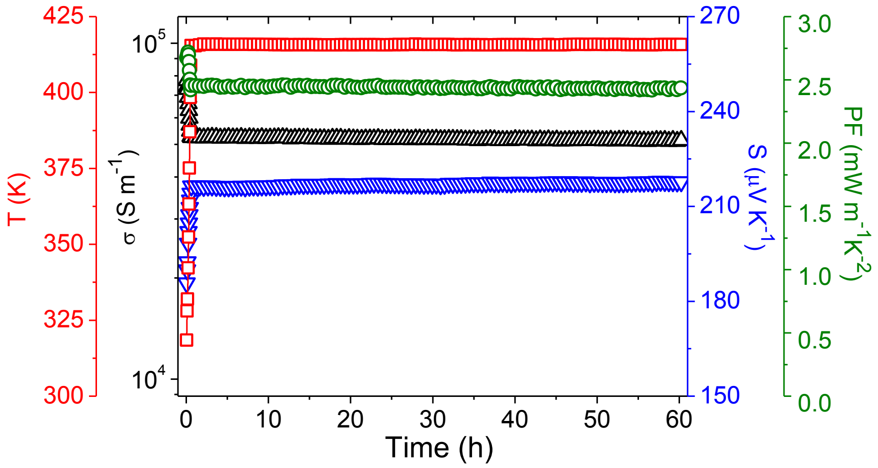

Figure 5.23. Time evolution of the electric conductivity (σ), Seebeck coefficient (S), power factor (PF) and temperature (T) of $Bi_{0.5}Sb_{1.5}Te_3$ during a 60 h test.

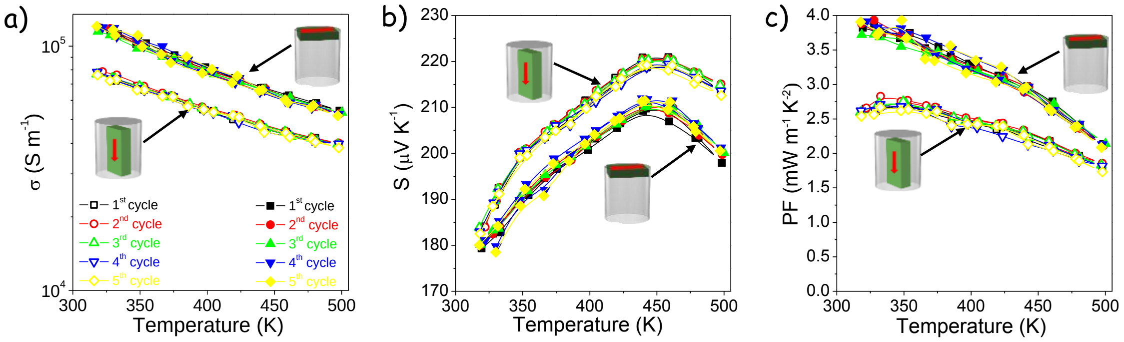

Figure 5.24. Temperature dependence of the electrical conductivity, σ (a), Seebeck coefficient, S (b), and power factor, PF (c) of $Bi_{0.5}Sb_{1.5}Te_3$ pellets measured in 5 consecutive up-down cycles during the heating up from room temperature to 498 K. No pre-stabilization treatment was carried out before the first measurement.

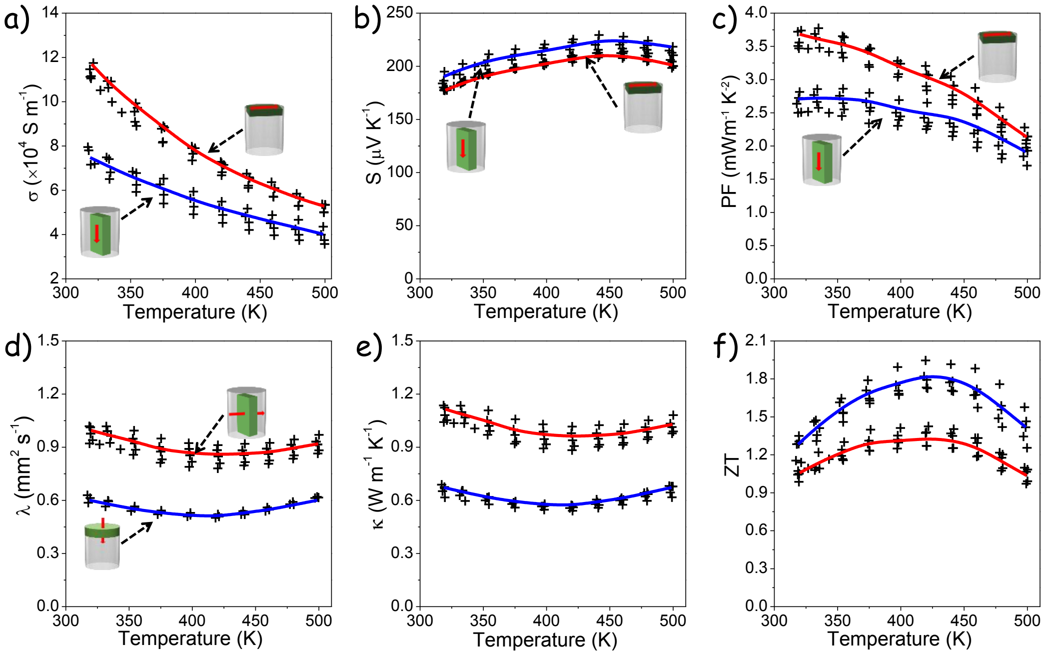

Figure 5.25. Temperature dependence of electric conductivity, σ (a); Seebeck coefficient, S (b); thermal conductivity, κ (c); and TE figure of merit, ZT (d) of five $Bi_{0.5}Sb_{1.5}Te_3$ pellets measured in the direction parallel and normal to the pressing direction. Data from the 5 samples is plotted with black crosses, and red and blue color lines display the average values.

In this work, average ZT values were calculated in the range from 320 K to 500 K by integrating the ZT values curve interpolated with a spline function and dividing the obtained area by the temperature difference (180 K). For this calculated we used the mean values from the experimental data measured from five samples having approximately the same composition.

$$ZT_{ave} = \frac{\int_{T_0}^{T_f} ZTdT}{\Delta T}$$

From this calculation, the average ZT obtained in the *c* direction from the bottom-up nanomaterial was:

$$ZT_{ave}=1.65.$$

The average ZT obtained from the commercial sample was:

$$ZT_{ave}=0.84$$

The maximum efficiency based on cumulative temperature-dependent properties was calculated from:[39, 40]

$$\eta_{max} = \eta_c \frac{\sqrt{1 + ZT_{eng}\left(\alpha/\eta_c - 1/2\right)} - 1}{\alpha\left(\sqrt{1 + ZT_{eng}\left(\alpha/\eta_c - 1/2\right)} + 1\right) - \eta_c}$$

with

$$\mathrm{ZT}_{eng} = \frac{\left(\int_{T_c}^{T_h} S(T)dT\right)^2}{\int_{T_c}^{T_h} \rho(T)dT \int_{T_c}^{T_h} \kappa(T)dT} \Delta T$$

$$\eta_c = \frac{T_h - T_c}{T_h}$$

$$\alpha = \frac{S(T_h)\Delta T}{\int_{T_c}^{T_h} S(T)dT}$$

From these equations, the maximum efficiency obtained in the *c* direction from the bottom-up nanomaterial considering T_h=500 K and T_c=320 K was:

$$\eta_{max} = 10.4\ \%.$$

The maximum efficiency from the commercial sample considering T_h=500 K and T_c=320 K was:

$$\eta_{max} = 7.1\%$$

5.5 Conclusions

In this chapter, we demonstrated the production of crystallographically textured $Bi_xSb_{2-x}Te_3$ bulk nanomaterials with record thermoelectric figures of merit: ZT = 1.96 for the record sample and ZT = 1.83 when averaged over five materials at 420 K. These high ZT values also extended over a larger temperature range, resulting in ZT values averaged over 180 K as high as: $ZT_{ave} = 1.77$ for the record material and $ZT_{ave} = 1.65$ as the mean value from 5 samples. These unprecedented figures of merit were obtained in the *c* direction, in contrast with most previous works measuring or assuming better thermoelectric performances in the *ab* plane. Our procedure was based on several key parameters: i) the use of p-type $Bi_xSb_{2-x}Te_3$ disk-shaped NCs having controlled composition; b) the uniaxial hot press of the NCs containing an excess of tellurium homogeneously distributed across the material; and c) the use of a proper hot press temperature and processing steps to ensure a proper liquid-assisted sintering and the complete removal of the tellurium excess.

5.6 References

1. Zhu, T.; Hu, L.; Zhao, X.; He, J. *Advanced Science* **2016,** 3, (7), 1600004.
2. Ortega, S.; Ibáñez, M.; Liu, Y.; Zhang, Y.; Kovalenko, M. V.; Cadavid, D.; Cabot, A. *Chemical Society Reviews* **2017**, 46, 3510-3528.
3. Ibáñez, M.; Luo, Z.; Genç, A.; Piveteau, L.; Ortega, S.; Cadavid, D.; Dobrozhan, O.; Liu, Y.; Nachtegaal, M.; Zebarjadi, M.; Arbiol, J.; Kovalenko, M.V.; Cabot, A. *Nature communications* **2016,** 7, 10766.
4. Liu, Y.; Cadavid, D.; Ibáñez, M.; Ortega, S.; Martí-Sánchez, S.; Dobrozhan, O.; Kovalenko, M. V.; Arbiol, J.; Cabot, A. *APL Materials* **2016,** 4, (10), 104813.
5. Zebarjadi, M.; Joshi, G.; Zhu, G.; Yu, B.; Minnich, A.; Lan, Y.; Wang, X.; Dresselhaus, M.; Ren, Z.; Chen, G. *Nano letters* **2011,** 11, (6), 2225-2230.
6. Ko, D.-K.; Kang, Y.; Murray, C. B. *Nano letters* **2011,** 11, (7), 2841-2844.
7. Zhang, Q.; Ai, X.; Wang, L.; Chang, Y.; Luo, W.; Jiang, W.; Chen, L. *Advanced Functional Materials* **2015,** 25, (6), 966-976.
8. Ibáñez, M.; Zamani, R.; Gorsse, S.; Fan, J.; Ortega, S.; Cadavid, D.; Morante, J. R.; Arbiol, J.; Cabot, A. *ACS nano* **2013,** 7, (3), 2573-2586.
9. Ibáñez, M.; Korkosz, R. J.; Luo, Z.; Riba, P.; Cadavid, D.; Ortega, S.; Cabot, A.; Kanatzidis, M. G. *Journal of the American Chemical Society* **2015,** 137, (12), 4046-4049.
10. Liu, Y.; García, G.; Ortega, S.; Cadavid, D.; Palacios, P.; Lu, J.; Ibáñez, M.; Xi, L.; De Roo, J.; López, A. M. *Journal of Materials Chemistry A* **2017,** 5, (6), 2592-2602.
11. Caillat, T.; Carle, M.; Pierrat, P.; Scherrer, H.; Scherrer, S. *Journal of Physics and Chemistry of Solids* **1992,** 53, (8), 1121-1129.
12. Carle, M.; Pierrat, P.; Lahalle-Gravier, C.; Scherrer, S.; Scherrer, H. *Journal of Physics and Chemistry of Solids* **1995,** 56, (2), 201-209.
13. Kim, S.; Yamamoto, S.; Aizawa, T. *Journal of alloys and compounds* **2004,** 375, (1), 107-113.
14. Fan, X.; Yang, J.; Zhu, W.; Bao, S.; Duan, X.; Xiao, C.; Li, K. *Journal of Alloys and Compounds* **2008,** 461, (1), 9-13.
15. Santamaría, J. A.; Alkorta, J.; Sevillano, J. G. *Journal of Materials Research* **2015,** 30, (17), 2593-2604.
16. Yan, X.; Poudel, B.; Ma, Y.; Liu, W.; Joshi, G.; Wang, H.; Lan, Y.; Wang, D.; Chen, G.; Ren, Z. *Nano letters* **2010,** 10, (9), 3373-3378.
17. Han, L.; Spangsdorf, S. H.; Nong, N.; Hung, L.; Zhang, Y.; Pham, H. N.; Chen, Y.; Roch, A.; Stepien, L.; Pryds, N. *RSC Advances* **2016,** 6, (64), 59565-59573.
18. Kitagawa, H.; Takimura, K.; Ido, S.; Morito, S.; Kikuchi, K. *Journal of Alloys and Compounds* **2017,** 692, 388-394.

19. Zhang, G.; Kirk, B.; Jauregui, L. A.; Yang, H.; Xu, X.; Chen, Y. P.; Wu, Y. *Nano letters* **2011**, 12, (1), 56-60.
20. Serebryanaya, N.; Tatyanin, E.; Buga, S.; Kruglov, I.; Lvova, N.; Blank, V. *physica status solidi (b)* **2015,** 252, (2), 267-273.
21. Zhao, Y.; de la Mata, M.; Qiu, R. L.; Zhang, J.; Wen, X.; Magen, C.; Gao, X. P.; Arbiol, J.; Xiong, Q. *Nano Research* **2014,** 7, (9), 1243-1253.
22. Chen, C.; Zhang, B.; Liu, D.; Ge, Z. *Intermetallics* **2012,** 25, 131-135.
23. German, R. M., *Liquid phase sintering*. Springer Science & Business Media: 2013.
24. Ghosh, G. *Journal of phase equilibria* **1994,** 15, (3), 349-360.
25. H. O. L. E. Tanner, Phase Diagram, ASM, 1986.
26. Randall, M. G.; Pavan, S.; Seong, J. *J. Mater. Sci* **2009,** 44, 1-39.
27. Kamb, W. B. *The Journal of Geology* **1959,** 67, (2), 153-170.
28. Abdullaev, N. *Physics of the Solid State* **2006,** 48, (4), 663-669.
29. Feng, S.; Li, S.; Fu, H. *Computational Materials Science* **2014,** 82, 45-49.
30. Jenkins, J.; Rayne, J.; Ure Jr, R. *Physical Review B* **1972,** 5, (8), 3171.
31. Paterson, M. *Reviews of Geophysics* **1973,** 11, (2), 355-389.
32. Kim, S. I.; Lee, K. H.; Mun, H. A.; Kim, H. S.; Hwang, S. W.; Roh, J. W.; Yang, D. J.; Shin, W. H.; Li, X. S.; Lee, Y. H. *Science* **2015,** 348, (6230), 109-114.
33. Zhang, G.; Kirk, B.; Jauregui, L. A.; Yang, H.; Xu, X.; Chen, Y. P.; Wu, Y. *Nano letters* **2011,** 12, (1), 56-60.
34. Kim, Y. M.; Lydia, R.; Kim, J.-H.; Lin, C.-C.; Ahn, K.; Rhyee, J.-S. *Acta Materialia* **2017,** 135, 297-303.
35. Chiritescu, C.; Mortensen, C.; Cahill, D. G.; Johnson, D.; Zschack, P. *Journal of Applied Physics* **2009,** 106, (7), 073503.
36. Termentzidis, K.; Pokropyvnyy, O.; Woda, M.; Xiong, S.; Chumakov, Y.; Cortona, P.; Volz, S. *Journal of Applied Physics* **2013,** 113, (1), 013506.
37. Teweldebrhan, D.; Goyal, V.; Balandin, A. A. *Nano letters* **2010,** 10, (4), 1209-1218.
38. Zhang, C.; de la Mata, M.; Li, Z.; Belarre, F. J.; Arbiol, J.; Khor, K. A.; Poletti, D.; Zhu, B.; Yan, Q.; Xiong, Q. *Nano Energy* **2016,** 30, 630-638.
39. Kim, H. S.; Liu, W.; Chen, G.; Chu, C.-W.; Ren, Z. *Proceedings of the National Academy of Sciences* **2015,** 112, (27), 8205-8210.
40. Kim, H. S.; Liu, W.; Ren, Z. *Energy & Environmental Science* **2017,** 10, (1), 69-85.
41. Yu, Y.; He, D.-S.; Zhang, S.; Cojocaru-Mirédin, O.; Schwarz, T.; Stoffers, A.; Wang, X.-Y.; Zheng, S.; Zhu, B.; Scheu, C. *Nano Energy* **2017,** 37, 203-213.
42. Zheng, Y.; Zhang, Q.; Su, X.; Xie, H.; Shu, S.; Chen, T.; Tan, G.; Yan, Y.; Tang, X.; Uher, C. *Advanced Energy Materials* **2015,** 5, (5), 1401391.
43. Hao, F.; Qiu, P.; Song, Q.; Chen, H.; Lu, P.; Ren, D.; Shi, X.; Chen, L. *Materials* **2017,** 10, (3), 251.

44. Poudel, B.; Hao, Q.; Ma, Y.; Lan, Y.; Minnich, A.; Yu, B.; Yan, X.; Wang, D.; Muto, A.; Vashaee, D. *Science* **2008,** 320, (5876), 634-638.
45. Tang, X.; Xie, W.; Li, H.; Zhao, W.; Zhang, Q.; Niino, M. *Applied physics letters* **2007,** 90, (1), 012102.
46. Hu, L.-P.; Zhu, T.-J.; Wang, Y.-G.; Xie, H.-H.; Xu, Z.-J.; Zhao, X.-B. *NPG Asia Materials* **2014,** 6, (2), 88.
47. Zhu, T.; Xu, Z.; He, J.; Shen, J.; Zhu, S.; Hu, L.; Tritt, T. M.; Zhao, X. *Journal of Materials Chemistry A* **2013,** 1, (38), 11589-11594.
48. Li, J.; Tan, Q.; Li, J. F.; Liu, D. W.; Li, F.; Li, Z. Y.; Zou, M.; Wang, K. *Advanced Functional Materials* **2013,** 23, (35), 4317-4323.
49. Xu, Z.; Hu, L.; Ying, P.; Zhao, X.; Zhu, T. *Acta Materialia* **2015,** 84, 385-392.
50. Li, Y.; Qin, X.; Li, D.; Zhang, J.; Li, C.; Liu, Y.; Song, C.; Xin, H.; Guo, H. *Applied Physics Letters* **2016,** 108, (6), 062104.
51. Fan, S.; Zhao, J.; Guo, J.; Yan, Q.; Ma, J.; Hng, H. H. *Applied Physics Letters* **2010,** 96, (18), 182104.
52. Madavali, B.; Kim, H.; Lee, K.; Hong, S. *Journal of Applied Physics* **2017,** 121, (22), 225104.
53. Mehta, R. J.; Zhang, Y.; Karthik, C.; Singh, B.; Siegel, R. W.; Borca-Tasciuc, T.; Ramanath, G. *Nature materials* **2012,** 11, (3), 233-240.
54. Hong, M.; Chen, Z. G.; Yang, L.; Zou, J. *Nano Energy* **2016,** 20, 144-155.
55. Suh, D.; Lee, S.; Mun, H.; Park, S.-H.; Lee, K. H.; Kim, S. W.; Choi, J.-Y.; Baik, S. *Nano Energy* **2015,** 13, 67-76.
56. Xie, W.; Tang, X.; Yan, Y.; Zhang, Q.; Tritt, T. M. *Applied Physics Letters* **2009,** 94, (10), 102111.
57. Park, K.; Ahn, K.; Cha, J.; Lee, S.; Chae, S. I.; Cho, S.-P.; Ryee, S.; Im, J.; Lee, J.; Park, S.-D. *Journal of the American Chemical Society* **2016,** 138, (43), 14458-14468.

Chapter 6

High Thermoelectric Performance in Crystallographically Textured n-type $Bi_2Te_{3-x}Se_x$ Produced from Asymmetric Colloidal Nanocrystals

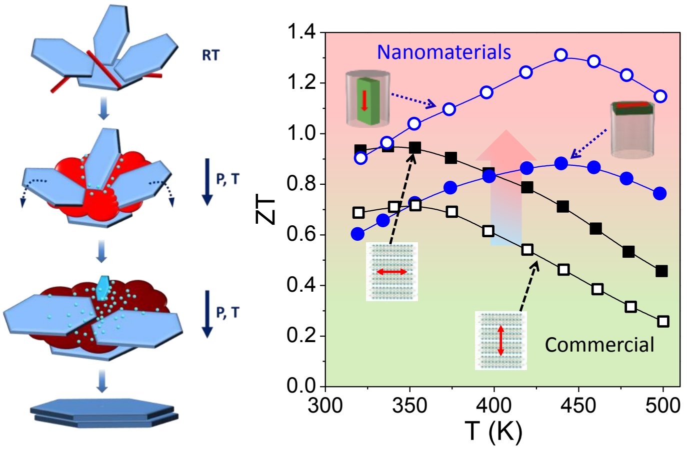

6.1 Abstract

In this chapter, we demonstrate n-type $Bi_2Te_{3-x}Se_x$ alloys with record thermoelectric (TE) figures of merit by consolidating disk-shaped $Bi_2Te_{3-x}Se_x$ colloidal nanocrystals (NCs) with controlled composition into crystallographically textured nanomaterials. Crystallographic texture was achieved by hot pressing the asymmetric NCs in the presence of an excess of tellurium which acted both as lubricant to facilitate rotation of NCs lying mostly normal to the pressure axis and as solvent that habilitate the dissolution and reprecipitation of the NCs aligned in the pressing direction. NC-based $Bi_2Te_{3-x}Se_x$ nanomaterials showed very high electrical conductivities associated to large charge carrier concentrations, *n*. Such large *n* resulted from the presence of an excess of tellurium during processing, which introduced a high density of donor Ti_{Bi} anitistes. Additionally,

the presence of traces in between grains of elemental Te, a narrow band gap semiconductor with a work function well below $Bi_2Te_{3-x}Se_x$, might further contribute to increase *n*, though spillover over of electrons, while at the same time blocking phonon propagation and hole transport through the nanomaterial. NC-based $Bi_2Te_{3-x}Se_x$ nanomaterials were also characterized by very low thermal conductivities in the pressing direction, which resulted in ZT values up to 1.31 at 438 K in this direction. This corresponds to a ca. 40 % enhancement in ZT compared to commercial ingots. Additionally, high ZT values were extended over larger temperature ranges due to reduced bipolar contribution to the Seebeck coefficient and the thermal conductivity. Thus, ZT values of up to 1.15 when averaged over a wide temperature range, 320 k to 500 K, were measured, what represents a 50 % increase over commercial materials in the same temperature range. Contrary to most previous works, higher ZT values were obtained in the pressing direction, corresponding to the c crystallographic axis, due to the predominance of the thermal conductivity reduction over the electrical conductivity difference when comparing the two crystal directions.

6.2 Introduction

The recovery of the huge amounts of energy wasted in the form of heat in transportation and in all industrial and domestic processes is an extremely appealing pursuit both from economic and environmental points of view.[1, 2] This goal requires the use of a distributed network of modular and cost-effective systems that convert temperature gradients into electricity. With the steam turbines being not suitable for small scale and portable generation, solid state thermoelectric (TE) devices become a worthwhile alternative. TE devices contain n-type and p-type semiconductors connected thermally in parallel and electrically in series. They can be manufactured with virtually any size, are highly durable and can be adapted to harvest energy from any temperature gradient.[1, 3] However, their widespread implementation requires improving their cost-effectiveness by increasing energy conversion efficiency and/or reducing manufacturing costs.

The energy conversion efficiency of a TE device can be analytically expressed in terms of the temperature at the hot and cold sides and a unique dimensionless TE figure of merit, $ZT=\sigma S^2T/\kappa$, where T is the absolute temperature, σ - the electrical conductivity, S - the Seebeck coefficient and κ-the thermal conductivity.[2, 4-6] Nanostructured materials have been proven successful in meeting the very demanding set of interrelated properties that maximize this figure of merit, i.e. high σ and S, and low κ. An additional advantage of nanomaterials is their superior mechanical robustness as compared to fragile single crystals.[7, 8]

NC-based bottom-up strategies allow combining a delicate control over material parameters with high production throughputs suitable for cost-effective bulk manufacturing.[4, 9-12] In this regard, they might offer certain advantages over current nanomaterial fabrication methods, which lack sufficient control over material parameters (e.g. ball milling)[13] and/or are eventually too costly for industrial manufacturing (e.g. vacuum-based thin film technologies).[14]

Bi_2Te_3-based alloys are the most widely used TE materials for operation at ambient temperatures, being commercialized for refrigeration and used in radioisotope TE generation systems since several decades ago.[15, 16] In recent years, great progress has been made in improving the figure of merit of the p-type Bi_2Te_3-based alloy,[3, 13, 17-21] reaching record ZT values up to 1.96 at 420 K and of 1.77 when averaged over a wide temperature range 320 – 500 K.[17] On the other hand, the performance of n-type Bi_2Te_3-based materials lags substantially behind, with ZT values just above 1.[22-26]

Structurally, Bi_2Te_3 crystallizes in a rhombohedral crystal phase ($R\overline{3}m$ space group) and can be viewed as a layered material consisting of stacked quintuple layers Te-Bi-Te-Bi-Te along the c-axis.[27] Quintuple layers are bonded together by weak van der Waals interactions. Such structure is characterized by highly anisotropic transport properties. In n-type $Bi_2Te_{2.6}Se_{0.4}$ single crystals, the electrical and thermal conductivities in the ab plane are ~4.38 times and over 2 times higher than along the c axis, respectively.[28]

The strong anisotropy of its transport properties requires producing $Bi_2Te_{3-x}Se_x$

nanomaterials with proper crystallographic texture. Such textured $Bi_2Te_{3-x}Se_x$ samples have been produced using a variety of strategies, [24, 29-33] but without significantly increasing the material figure of merit over un-textured samples, probably due to a lack of the simultaneous optimization of the microstructure, composition and point defects.

In this chapter, we demonstrate that using asymmetric colloidal $Bi_2Te_{3-x}Se_x$ NCs with controlled composition (x = 0, 0.2, 0.3, 0.4, 0.5 and 0.7) and a proper consolidation process, highly textured nanomaterials with high relative densities and record TE figures of merit can be produced.

6.3 Experimental Section

Chemicals and solvents: Bismuth (III) nitrate pentahydrate (Bi $(NO_3)_3 \cdot 5H_2O$, ≥99.99%), sodium selenite (Na_2SeO_3, ≥98%), potassium hydroxide (KOH, ≥98%), and polyvinylpyrrolidone (PVP, $(C_6H_9NO)_n$, average mol wt ~55,000) were purchased from Sigma Aldrich. Sodium tellurite (Na_2TeO_3, 99.5%) and ethylene glycol (EG, $HOCH_2CH_2OH$, 99%) were purchased from Fisher. Analytical grade acetone and ethanol were obtained from various sources. All chemicals were used as received without further purification. Syntheses were carried out using a standard vacuum/dry argon Schlenk line.

Synthesis of $Bi_2Te_{3-x}Se_x$ NCs with Te excess: In a typical synthesis of 5 mmol of $Bi_2Te_{3-x}Se_x$ (x=0, 0.2, 0.3, 0.4, 0.5) NCs with a 25 mol% excess of Te, 10 mmol $Bi(NO_3)_3 \cdot 5H_2O$, 5x mmol of Na_2SeO_3, [5×(3-x)×(1+0.25)] mmol of Na_2TeO_3, 50 mmol of KOH and 0.5 g of PVP were dissolved in 200 ml of EG within a 500 ml three-neck flask by stirring under argon atmosphere at room temperature for 20 min. Then the solution was heated to 185 ºC. During this process, above 150 ºC, the color of the solution gradually changed from slightly brown to black. Finally, the reaction mixture was kept at 185 °C for 3 h. After this time, the solution was naturally cooled to room temperature by removing the heating mantle. NCs were purified in a multi-step process using various solvents to remove the different impurities. Notice that a proper NC purification was essential to produce nanomaterials with optimized TE properties. In a first step, the solid product was collected by adding acetone to the solution and centrifuging it. In a second step, ethanol was used to redisperse the NCs and acetone ($V_{ethanol}/V_{acetone}=1:2$) to precipitate them again. In a third step, deionized water was added to solubilize remaining impurities and NCs were precipitated by slow centrifugation. This 3rd step was repeated twice. In a last step, NCs were redispersed with ethanol and precipitated with acetone, like in step two. Finally, NCs were dried under vacuum at room temperature. This synthesis protocol was optimized to produce almost 4 g of NCs per batch, which was the amount required for a complete characterization of their TE properties at the laboratory scale.

Bulk nanomaterial consolidation: Dried $Bi_2Te_{3-x}Se_x$ (x=0, 0.2, 0.3, 0.4, 0.5 and 0.7) NCs were annealed at 350 °C for 60 min under an Ar flow inside a tube furnace. The annealed NC, in the form of a powder, were loaded into a graphite die and compacted into cylinders (Ø 10 mm×10 mm) using a custom-made hot press. This process was carried out within a glove box having an argon atmosphere. The hot press temperature was set at 480 ºC and pressure was increased up to 70 MPa and released for 5 times during the 210 s that the material was kept at 480 ºC. This pressure cycling was found fundamental to remove the excess of tellurium from the sample and to reach proper crystal texture. When materials with an excess of tellurium were hot pressed in these conditions, the relative densities of the compacted pellets were measured by the Archimedes' method and found to be around 92 % of the theoretical value. From these cylinders, rectangular bars of about $8 \times 6 \times 1$ mm^3 were cut in two normal directions, along the pressing direction and within the cylinder plane.

Structural and chemical characterization: X-ray diffraction (XRD, 2θ angle: 20° to 80°; scanning rate: 5 °/min) analyses were carried out on a Bruker AXS D8 ADVANCE X-ray diffractometer with Cu–Kα radiation (λ= 1.5406 Å). Size and morphology of initial NCs were examined by transmission electron microscopy (TEM) using a ZEISS LIBRA 120, operating at 120 kV, and field-emission scanning electron microscopy (SEM) on an Auriga Zeiss operated at 5.0 kV. Electron energy loss spectroscopy (EELS) analysis were carried out using a Tecnai F20 field-emission gun microscope at 200 keV with an embedded Gatan QUANTUM image filter. The material composition was analyzed using an Oxford energy dispersive X-ray spectrometer (EDX) attached to a Zeiss Auriga SEM at 20.0 kV.

Thermoelectric property measurement: Seebeck coefficients were measured by using a static DC method. Electrical resistivity data was obtained by a standard four-probe method. Both the Seebeck coefficient and the electrical resistivity were measured simultaneously in a LSR-3 LINSEIS system in the temperature range between room temperature and 498 K, under helium atmosphere. At each temperature, 3 measurements were taken. Taking into account the system accuracy and the measurement precision, an error of ca. 4 % in the measurement of the electrical conductivity and Seebeck coefficient was estimated. The thermal conductivity was calculated by $\kappa= \lambda C_p\rho$, where λ is the thermal diffusivity, C_p is the heat capacity, and ρ is the mass density of the specimen. A XFA 600 Xenon Flash Apparatus was used to determine the thermal diffusivities (λ) of the samples with an estimated error of ca. 5 %. The constant pressure heat capacity (C_p) was estimated from empirical formulas by the Dulong–Petit limit (3R law), and the density (ρ) values used here were calculated using the Archimedes' method. To avoid cluttering the plots, error bars were not included in the figures. Hall charge carrier concentrations (n_H) and mobilities (μ_H) at room temperature (300 K) were measured with a Physical Property Measurement System (PPMS-9T, 10 % error, Quantum Design Inc., USA) using a magnetic field of 2 T. Values provided correspond to the average of 5 consecutive measurements.

6.4 Results and discussion

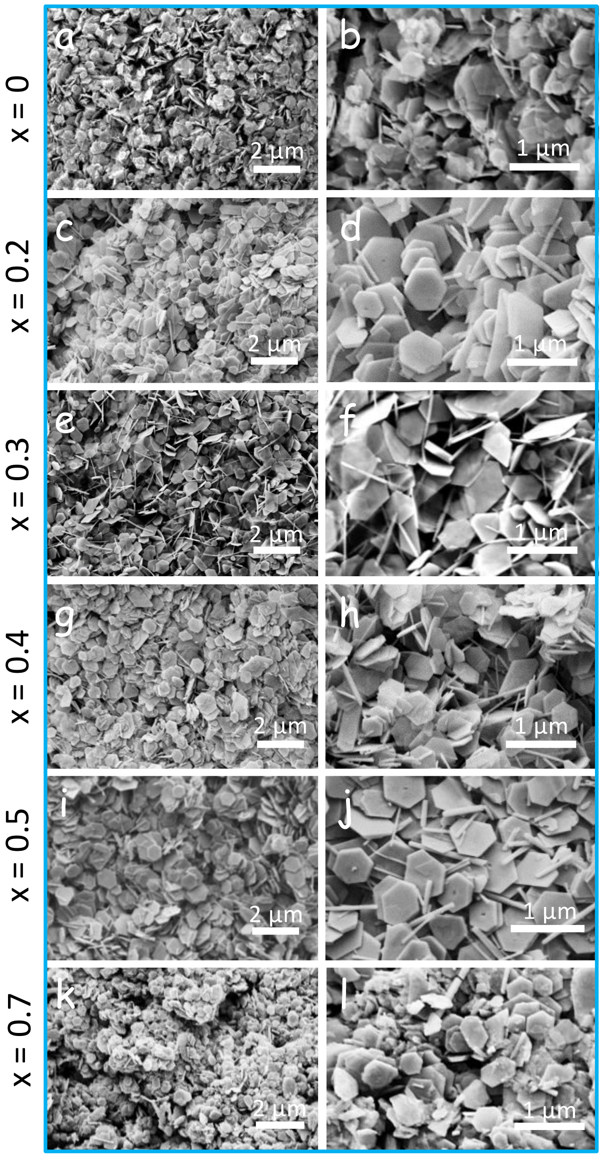

Figure 6.1. Representative SEM micrographs of $Bi_2Te_{3-x}Se_x$ NCs synthesized at the 25 mol% excess of Te: (a), (b) x = 0; (c), (d) x = 0.2; (e), (f) x = 0.3; (g), (h) x = 0.4; (i), (j) x = 0.5 and (k), (l) x = 0.7.

$Bi_2Te_{3-x}Se_x$ NCs with variable composition (x=0, 0.2, 0.3, 0.4, 0.5 and 0.7) were produced in EG at 185 °C by reacting bismuth (III) nitrate with sodium selenite and sodium tellurite in the presence of PVP. NC composition could be conveniently tuned by adjusting the initial ratios of Se and Te precursors (Table 6.1). This synthetic protocol, including the purification step, was characterized by material yields above 95 % and it was optimized to produce ca. 4 g of NCs per batch. Figure 6.1 shows representative SEM micrograph of the disk-shaped $Bi_2Te_{3-x}Se_x$ NCs obtained following this procedure. As measured from SEM, NCs had average lateral dimensions of around 480 ± 100 nm and an average thickness of 35 ± 8 nm. Excess amounts of Te, nominally 25 mol%, were introduced in the reaction mixture. This Te excess was found in the form of thin Te nanorods segregated from $Bi_2Te_{3-x}Se_x$ nanodisks (Figure 6.1).

$Bi_2Te_{3-x}Se_x$ NCs were purified by multiple precipitation and redispersion steps using different solvents, as detailed in the experimental section. Subsequently, they were dried and, to remove any remaining trace of surfactant, were annealed at 350 °C for 60 min under argon flow inside a tube furnace. The annealed nanopowders still consisted of disk-shaped $Bi_2Te_{3-x}Se_x$ NCs (Figure 6.2), but the NC edges became smoother and the lateral size and thickness slightly increased with the thermal treatment. The size of the Te nanorods particularly increased as observed in Figures 6.2d and 2f.

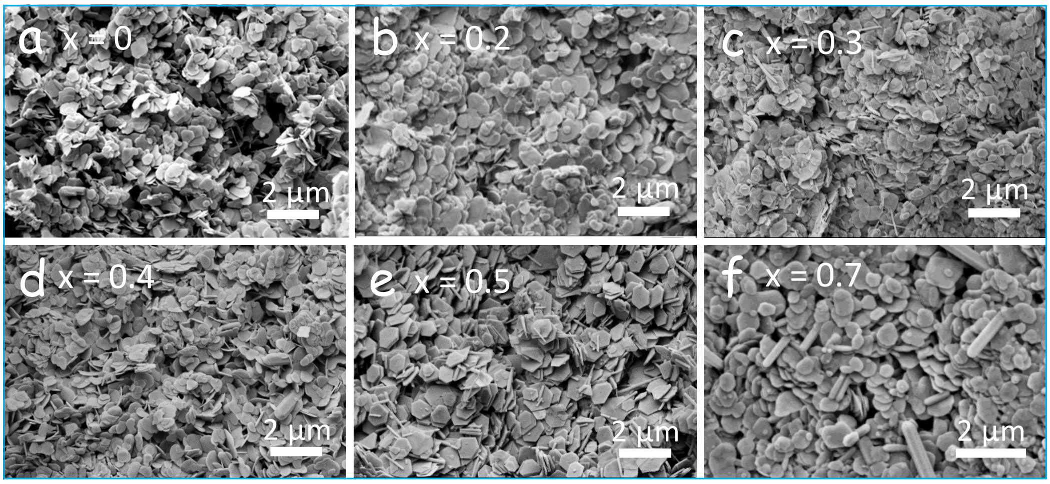

Figure 6.2. a-f) SEM images of $Bi_2Te_{3-x}Se_x$ (x=0, 0.2, 0.3, 0.4, 0.5 and 0.7) NCs with 25% excess tellurium after annealing at 350 ºC for 1 h.

SEM-EDX analysis showed the NC composition, particularly the Bi:Se ratios, to precisely follow the nominal values (Table 6.1), both before and after the annealing treatment. However, the excess of Te was measured at around 20 mol% instead of the nominal 25 mol% also both before and after annealing.

Table 6.1. SEM-EDX composition (related to Bi = 2) of $Bi_2Te_{3-x}Se_x$ (x=0, 0.2, 0.3, 0.4, 0.5 and 0.7) NCs, annealed nanopowders and consolidated pellets. Data was obtained from averaging several analyses, resulting in an estimated error of ca. 2 %.

Nominal / **Material**	x = 0		x = 0.2		x = 0.3		x = 0.4		x = 0.5		x = 0.7	
	Te	**Se**	**Te**	**Se**	**Te**	**Se**	**Te**	**Se**	**Te**	**Se**	**Te**	**Se**
NCs	3.60	0.0	3.19	0.19	3.12	0.29	3.09	0.40	3.01	0.50	2.90	0.71
Nanopowder	3.58	0.0	3.20	0.20	3.11	0.29	3.08	0.39	3.00	0.51	2.89	0.72
Pellet	3.04	0.0	2.79	0.20	2.73	0.30	2.61	0.39	2.48	0.46	2.30	0.73

XRD analyses of the initial NCs and the annealed nanopowder showed no secondary phases (Figure 6.3), not even elemental Te. XRD patterns clearly shifted to higher diffraction angles when increasing the Se concentration, as it corresponds to a lattice contraction due to the substitution of Te by Se atoms, which evidenced the presence of increasing amounts of Se within the alloy crystal lattice.

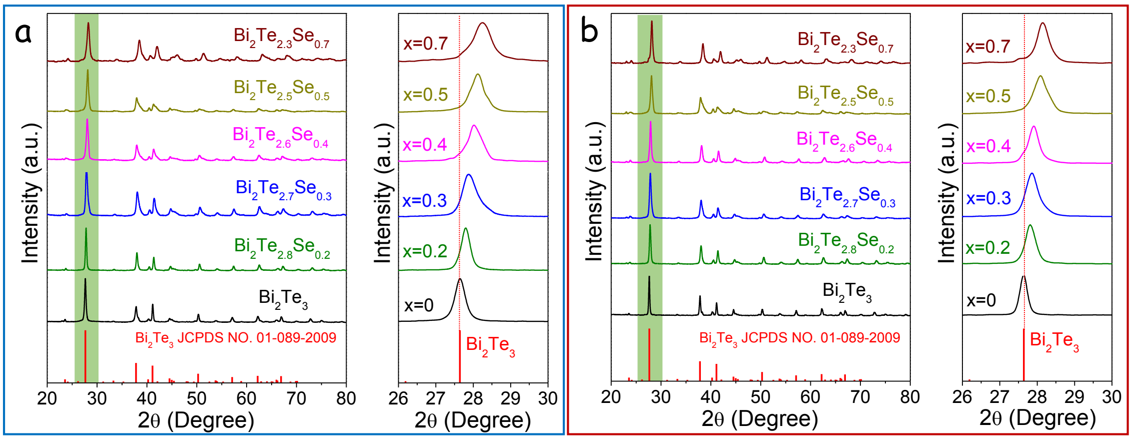

Figure 6.3. XRD patterns of $Bi_2Te_{3-x}Se_x$ (x=0, 0.2, 0.3, 0.4, 0.5 and 0.7) NCs before (a) and after (b) annealing at 350 °C for 60 min. Detail of the same XRD patterns showing the systematic shift of the (0 1 5) peak with the Se composition (x) is also provided. The standard Bi_2Te_3 diffraction pattern (JCPDS NO. 01-089-2009) is also included as reference.

Annealed $Bi_2Te_{3-x}Se_x$ nanopowders were hot-pressed within an inert atmosphere into cylindrical pellets (10 mm in diameter and 10 mm height). The process temperature was set at 480 °C. Pressure, 70 MPa, was applied and released for 5 times during the 210 s that the material was kept at 480 ºC. This overall process resulted in $Bi_2Te_{3-x}Se_x$ cylinders with relative densities of ca. 92 % of the theoretical value, as measured by the Archimedes' method.

XRD analysis of the cylindrical pellets hold in two perpendicular directions, with the cylinder plane normal and parallel to the diffraction plane, demonstrated the consolidated material to be characterized with a significant crystallographic texture, with the [001] crystallographic direction oriented along the pressing direction (Figure 6.4).

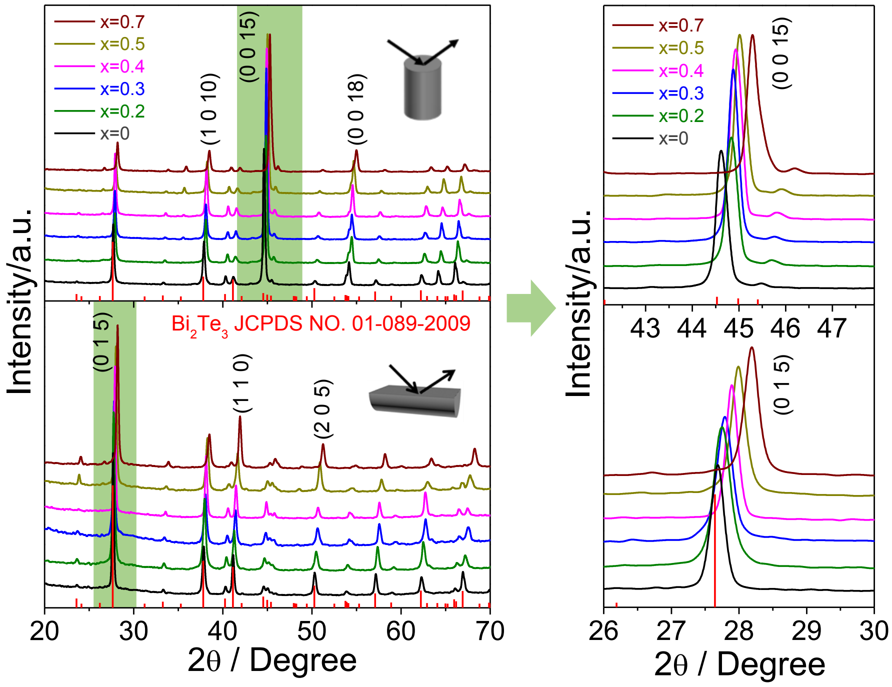

Figure 6.4. Left: XRD patterns of consolidated $Bi_2Te_{3-x}Se_x$ (X=0, 0.2, 0.3, 0.4, 0.5 and 0.7) pellets measured in the two directions, parallel and normal to the press direction; Right: detail of the same XRD patterns showing the systematic shift of the (0 0 $\underline{15}$) and (0 1 5) peaks with the Se composition (x).

SEM micrographs of the pellet cross-section along the pressing direction showed the consolidated material to have a laminar microstructure, with $Bi_2Te_{3-x}Se_x$ layers extending several microns in the cylinder plane directions and with thicknesses of ca. 50 nm (Figure 6.5). Top-view, from the pressing direction, SEM micrographs showed the grains to partially conserve the precursor disk-like geometry, but to have significantly grown in the lateral direction during the hot press process.

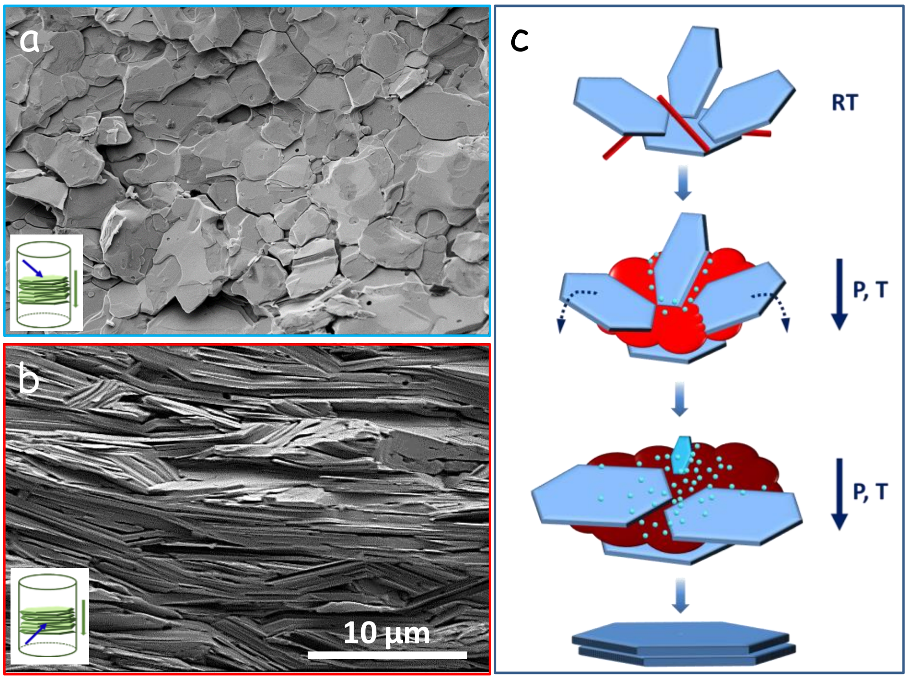

Figure 6.5. Top-view (a) and cross-section (b) SEM micrographs of a $Bi_2Te_{2.7}Se_{0.3}$ pellet. c) Cartoon of the mechanism of formation of the crystallographically textured polycrystalline material from the hot pressing of $Bi_2Te_{3-x}Se_x$ nanodisks under an excess of Te. The rotation of the disks aligned close to normal to the pressure axis and the dissolution and reprecipitation within the liquid Te of the disks aligned close to the pressing direction is represented.

The presence of an excess of Te during the hot press step was essential to produce highly textured nanomaterials. Te liquified during the consolidation process, aiding both the rotation of the $Bi_2Te_{3-x}Se_x$ disks and their dissolution and reprecipitation.

Under a uniaxial pressure, the alignment of the disks with the c direction along the pressure axis is driven by a minimization of both the system entropy and the energy related to the stress accommodation, being the c direction the one with the lowest elastic modulus.

On the other hand, Bi has a relatively high solubility within liquid Te at the hot pressing temperature (480 ºC), which promotes the dissolution and reprecipitation of the disks.[34] Dissolution takes place preferentially at the highest energy facets, i.e. those normal to the ab plane, and is aided in the pressing direction by the created stress.[35-36] When reprecipitating, $Bi_2Te_{3-x}Se_x$ crystals naturally grow forming plates that extend along the ab crystal plane. The presence of a uniaxial pressure favors growth in the direction normal to the pressure axis. At the same time, to minimize energy under the uniaxial pressure, reprecipitating crystals align with their minimum elastic modulus, i.e. the c direction, along the direction of the stress. Thus, plates with the c direction along the pressure axis are produced.

Overall, both mechanisms might have taken place simultaneously. Disk-shaped NCs already lying close to normal to the pressure axis might rotate and grow in the ab directions from ions present in the liquid tellurium that provide from the dissolution of NCs that lied mostly parallel to the pressure axis (Figure 6.5c).

While the presence of liquid Te was essential to obtain highly textured nanomaterials, materials with close to stoichiometric cation: anion ratios are required to achieve optimum TE properties. Therefore, the removal of the excess of Te during the consolidation process was critical. Conveniently, the excess amount of Te was expelled through the die-plunger interface during the hot pressing, as observed by careful analysis of the plunger insertion region of the die (Figure 6.6). However, the complete removal of Te required cycling up and down the pressure several times during the 210 s that the material was at 480 °C. This pressure cycling and Te removal also aided texturization. That is, higher texture degrees were obtained when cycling pressure than when maintaining it fixed. We hypothesize that better texturing with cycling and proper Te removal might be in part associated to a lower amount of liquid material randomly crystallizing during the cooling down process. Additionally, the overall compression and decompression of the pellet during each cycle, extending ca. 1 μm, could also help in the rotation and reorientation of the NCs.

Within its experimental error, EDX analysis of the consolidated samples showed them to have close to stoichiometric cation: anion ratios (Table 6.1) with Te: Se ratios closely following the nominal compositions once the excess of Te was removed. However, careful STEM-EELS analysis of a thinned cross section of the pellet demonstrated the presence of abnormally large amounts of Te at a significant number of crystal interfaces (Figure 6.7).

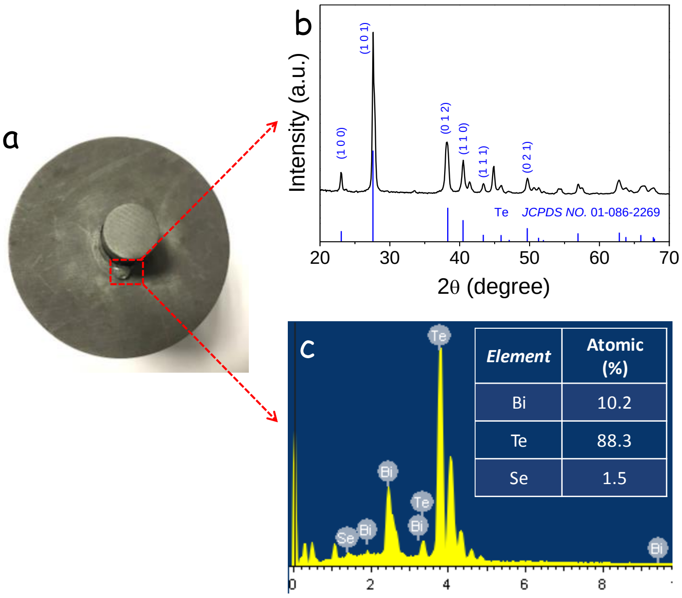

Element	Atomic (%)
Bi	10.2
Te	88.3
Se	1.5

Figure 6.6. a) Photograph of the graphite die and the carbon rod after hot press. As indicated by the red square, some material was expelled out from the die during the process. a-b) XRD (b) and EDX (b) data of the expelled material, confirming that, in a ~90%, consisted of tellurium.

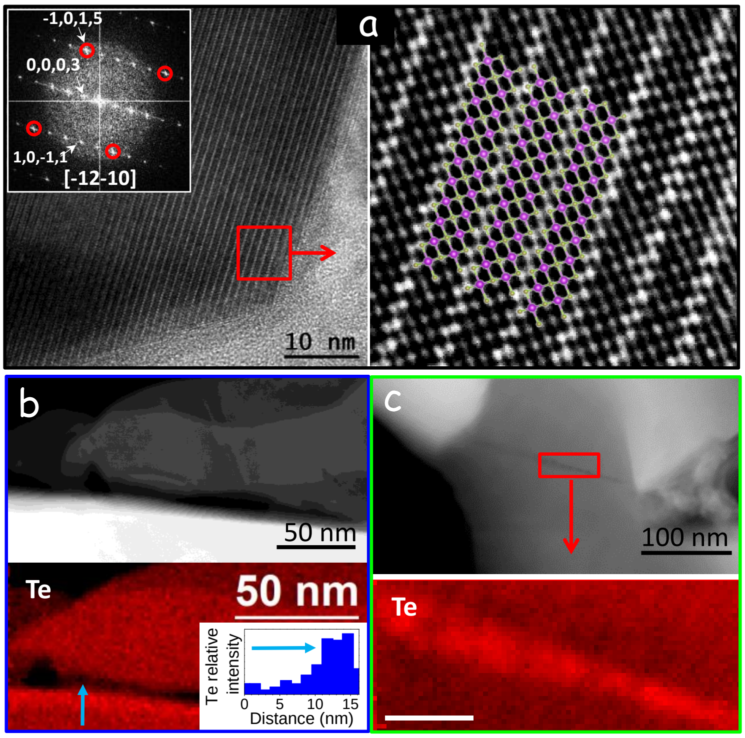

Figure 6.7. a) HRTEM image of a $Bi_2Te_{2.7}Se_{0.3}$ crystal within a consolidated pellet, with its corresponding powder spectrum as an inset, and detail of the squared region of the HRTEM image overlaid with the structure of $Bi_2Te_{2.7}Se_{0.3}$: Bi in purple, Se and Te in green, with partial occupations on the same sites. b) ADF-STEM (top) and STEM-EELS Te composition map (bottom) of the interface between two crystals. An inset displays the relative Te intensity profile calculated along the cyan arrow in the EELS map. c) ADF-STEM (top) and STEM-EELS Te

composition map (bottom) of an interface between two crystals within the consolidated pellet.

From the consolidated cylinders, rectangular bars were cut in two directions, along the pressing direction, i.e. the cylinder length, and within the plane normal to this axis, i.e. the cylinder disk plane (Figure 6.8).

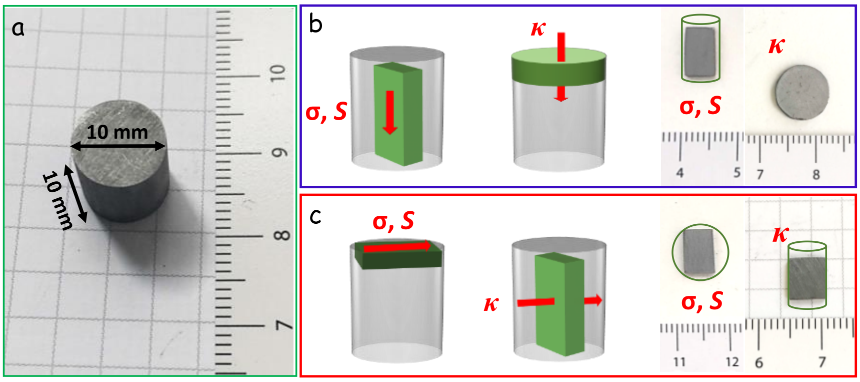

Figure 6.8. a) Photograph of a cylindrical pellet produced by hot pressing. b-c) Schematic illustrations and photographs of the samples obtained from the cylindrical pellets and used to measure TE properties in both direction, parallel (b) and normal (c) to the pressing direction. Electrical conductivities and Seebeck coefficients were always measured using rectangular samples. Thermal conductivities were measured from disk-shaped samples in the direction of the pressing direction and from rectangular samples in the direction normal to the pressing direction.

Figures 6.9 and 6.10 display the electrical conductivity (σ), Seebeck coefficient (*S*), power factor (PF), total thermal conductivity (κ), the total thermal conductivity once subtracted the electronic contribution ($\kappa - \kappa_e$), and the TE figure of merit (ZT) of the $Bi_2Te_{3-x}Se_x$ (x=0, 0.2, 0.3, 0.4, 0.5 and 0.7) pellets measured in the two directions. Figure 6.11 displays the dependence of the same parameters on the Se concentration, x. Additionally, Figure 6.12 displays the comparison between the TE properties of the best performing nanomaterial, $Bi_2Te_{2.7}Se_{0.3}$, and a commercial ingot measured in two normal directions, the cleavage plane and its normal.

All compositions displayed a degenerated semiconductor behavior, with σ monotonically decreasing with temperature in all the temperature range measured (Figures 6.9a and 6.10a). Te-rich Bi_2Te_3 has an n-type character because σ is dominated by positively charged antisite defects, Te_{Bi}.[37] Such defects are abundant due to the similar ionic radius of Te and Bi, what provides the material with large charge carrier concentrations, in the range 10^{18}-10^{20} cm^{-3}.[37] σ decreased with the amount of Se introduced (Figure 6.11a), which was related to a decrease of the concentration of the dominant n-type point defect, Te_{Bi}. This decrease is associated with the smaller radius of Se compared with Te and Bi, which makes the formation of Se_{Bi} antisites much less energetically favorable than Te_{Bi}. Actually, the dominant point defects in n-type Bi_2Se_3 are positively charged Se vacancies, which are not favored in an ambient with an excess of chalcogen as the one used to process our nanomaterials.

As expected, all samples exhibited much higher σ in the cylinder plane ($\sigma_\perp$) than in the pressing direction ($\sigma_{/\!/}$), e. g. $\sigma_\perp/\sigma_{/\!/} = 2.3$ for $Bi_2Te_{2.7}Se_{0.3}$ at 320 K, which was related to the higher charge carrier mobility in the ab crystal plane than in the c direction (Figures 9a and 10a). At first view surprisingly, σ was higher for nanomaterials than commercial samples (Figure 6.12a). This result was related to the higher charge carrier concentrations obtained in our nanomaterials compared with the commercial ingot. Hall measurements at room temperature showed the charge carrier concentration of $Bi_2Te_{2.7}Se_{0.3}$ nanomaterials, $n_H = 7 \pm 2 \times 10^{19}$ cm^{-3}, to be a 3.5 fold higher than in the commercial sample, $n_H = 2.0 \pm 0.5 \times 10^{19}$ cm^{-3}. These higher charge carrier concentrations were related to the tellurium excess environment where they were processed. The excess of tellurium introduced a large concentration of Te_{Bi} antisites. Additionally, Te traces in the final pellet could contribute to further increase n through the spillover of charge from Te domains to the $Bi_2Te_{3-x}Se_x$ matrix taking into account the lower work function of Te compared with $Bi_2Te_{3-x}Se_x$ (Figure 6.13). As expected, charge carrier mobilities in the commercial samples were sensibly higher than in the nanomaterial: μ_H = 286 cm^{2}V^{-1}s^{-1} for the commercial sample in the cleavage plane; μ_H = 136 cm^{2}V^{-1}s^{-1} for the nanomaterial in the direction normal to the pressure axis; μ_H = 71 cm^{2}V^{-1}s^{-1} for the commercial sample in the plane normal to the cleavage; μ_H = 61 cm^{2}V^{-1}s^{-1} for the nanomaterial in the pressing direction.

Negative *S* values were measured for all samples in the whole temperature range, in agreement with the n-type character of the materials. The absolute value of *S* increased gradually up to 450 K and flattened at higher temperatures, with the emergence of the bipolar contribution. *S* absolute values increased with the amount of Se, consistently with the decrease of the charge carrier concentration associated to the replacement of Te with Se. *S* values measured in the two directions were very similar, e.g. $S_{/\!/}/S_{\perp} = 1.1$ for $Bi_2Te_{2.7}Se_{0.3}$ at 320 K, which was consistent with the low anisotropy of this parameter (Figure 6.12b).[28] Absolute *S* values of the nanomaterials were significantly lower than those of commercial ingots, consistently with their higher charge carrier concentrations. These higher charge carrier concentrations also explained the lower absolute *S* decrease observed for the nanomaterial than for the commercial ingot in the high temperature region measured. That is, the bipolar contribution became significant at much higher temperature in the nanomaterials than in the commercial samples.

For nanomaterials, PFs calculated in the pressing direction were lower than those calculated in its normal (Figures 6.9c, 6.10c and 6.11c). In this last direction PFs up to 2.86 $Wm^{-1}K^{-2}$ at 350 K were reached. The highest PFs measured in the pressing direction were obtained for $Bi_2Te_{2.7}Se_{0.3}$ and $Bi_2Te_{2.8}Se_{0.2}$, and in the cylinder plane for Bi_2Te_3, $Bi_2Te_{2.8}Se_{0.2}$ and $Bi_2Te_{2.7}Se_{0.3}$. Compared with commercial ingots (Figure 6.12c), PFs of nanomaterials were lower than those measured in the cleavage plain of commercial ingots, due to the higher S of the later, but higher than in direction normal to the cleavage plane, due to the low σ of the commercial sample in this direction.

As expected from the microstructure of the nanomaterial pellet, κ in the pressing direction was much lower than in the cylinder plane for all samples, e.g. $\kappa_{\perp}/\kappa_{/\!/}= 2.5$ for $Bi_2Te_{2.7}Se_{0.3}$ at 320 K (Figure 6.112d). In the low temperature range, κ decreased with temperature to later slightly rise with the emergence of the bipolar contribution. This bipolar contribution strongly decreased with the amount of Se introduced due to the band gap increase, as observed in Figures 9e and 10e. κ also decreased with Se due to the higher lattice disorder.

After having subtracted the electronic contribution, thermal conductivities decreased with temperature in the low temperature range and stabilized or increased at higher temperatures, when the bipolar contribution, κ_{bi}, became significant (Figure 6.11e). Above the Debye temperature, ca. 145 K for Bi_2Te_3,[42] phonon scattering by Umklapp mechanism leads to a T^{-1} temperature dependence of κ_L. On the other hand, κ_{bi} displays an exponential relation with temperature and the material band gap, E_g:[43]

$$\kappa_{bi} \propto \exp(-\frac{E_g}{2\kappa_B T}) \quad (1)$$

To estimate κ_{bi}, we linearly fitted (κ - κ_e) vs. T^{-1} in the low temperature range and extrapolated data to higher temperatures (Figure 6.12e).

At room temperature, compared with commercial ingots, with κ_L ~1.1 $Wm^{-1}K^{-1}$ along the cleavage direction and κ_L ~ 0.43 $Wm^{-1}K^{-1}$ normal to this direction (Figure 6.12e), nanocrystalline $Bi_2Te_{3-x}Se_x$ samples displayed significantly lower κ_L, even when correcting for the smaller relative densities, ca. 92 %. Taking into account the porosity correction, i.e. ca. 20% modification, $Bi_2Te_{3-x}Se_x$ samples displayed κ_L~0.74 $Wm^{-1}K^{-1}$ in the cylinder plane and κ_L~0.25 $Wm^{-1}K^{-1}$ in its normal direction. These low κ_L were associated to the large density of grain boundaries, interphase Te and crystal defects such as stacking faults. Notice that the κ_L values obtained were still above the theoretical minimum calculated using the half-wavelength model proposed by Cahill κ_{Lmin} =0.14-0.18 $Wm^{-1}K^{-1}$,[38] and values reported for $Bi_2Te_{2.7}S_{0.3}/Bi_2Te_3$ hetero-nanosheets (0.2 $Wm^{-1}K^{-1}$ at 300 K),[39] highly defective Bi_2Te_3 (ca. 0.17 $Wm^{-1}K^{-1}$),[40] small Bi_2Te_3 nanograins (0.12 $Wm^{-1}K^{-1}$) and stacked Bi_2Te_3 2D films (0.1 $Wm^{-1}K^{-1}$).[41]

In commercial ingots, κ_{bi} became significant at ~350 K. In $Bi_2Te_{3-x}Se_x$ nanomaterials the κ_{bi} contribution was substantially lower and started to be appreciated at ~400 K (Figure 12e). The lower κ_{bi} contribution in $Bi_2Te_{3-x}Se_x$ nanomaterials and particularly $Bi_2Te_{2.7}S_{0.3}$ compared with commercial ingots was mainly attributed to the larger density of majority charge carriers of the former.[44-45] Potentially, a slightly higher Se concentrations in $Bi_2Te_{2.7}S_{0.3}$,[44, 46] and the selective scattering of minority carriers at intergrain energy barriers, particularly in the presence of elemental Te (Figure 6.13), could also contribute to the reduction of the bipolar contributions and particularly κ_{bi} in $Bi_2Te_{3-x}Se_x$ nanomaterials.[13, 47]

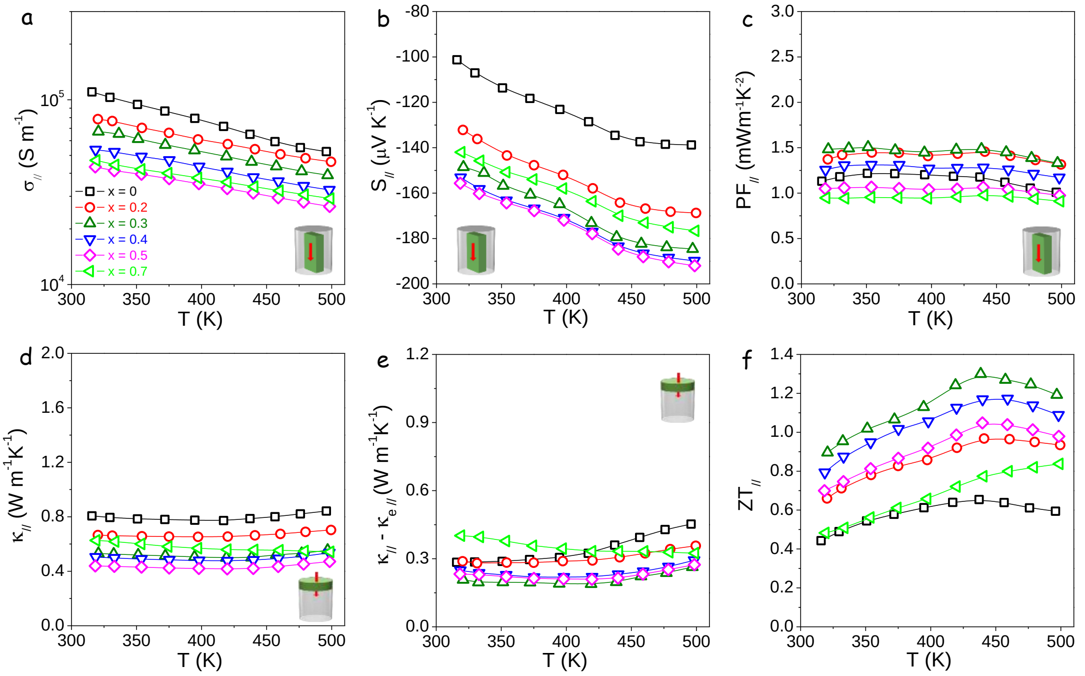

Figure 6.9. Thermoelectric properties of $Bi_2Te_{3-x}Se_x$ (x = 0, 0.2, 0.3, 0.4, 0.5 and 0.7) nanomaterials measured in the pressing direction (//): (a) electrical conductivity, $\sigma_{//}$; (b) Seebeck coefficient, $S_{//}$; (c) power factor, $PF_{//}$; (d) total thermal conductivity, $\kappa_{//}$; (e) thermal conductivity after subtraction of electronic component, $\kappa_{//}$- $\kappa_{e\,//}$; and (f) TE figure of merit, $ZT_{//}$.

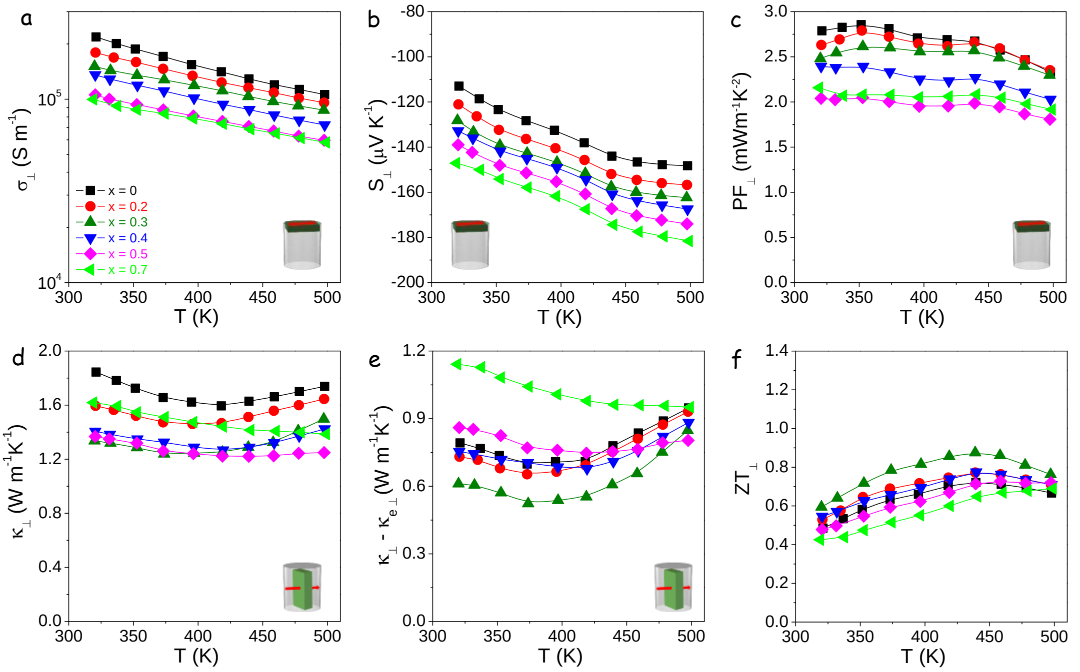

Figure 6.10. Thermoelectric properties of $Bi_2Te_{3-x}Se_x$ (x = 0, 0.2, 0.3, 0.4, 0.5 and 0.7) nanomaterials measured in the plane normal to the pressing direction (⊥): (a) electrical conductivity, $\sigma_{\perp}$; (b) Seebeck coefficient, $S_{\perp}$; (c) power factor, $PF_{\perp}$; (d) total thermal conductivity, $\kappa_{\perp}$; (e) thermal conductivity after subtraction of electronic component, $\kappa_{\perp}$- $\kappa_{e\,\perp}$; and (f) TE figure of merit, $ZT_{\perp}$..

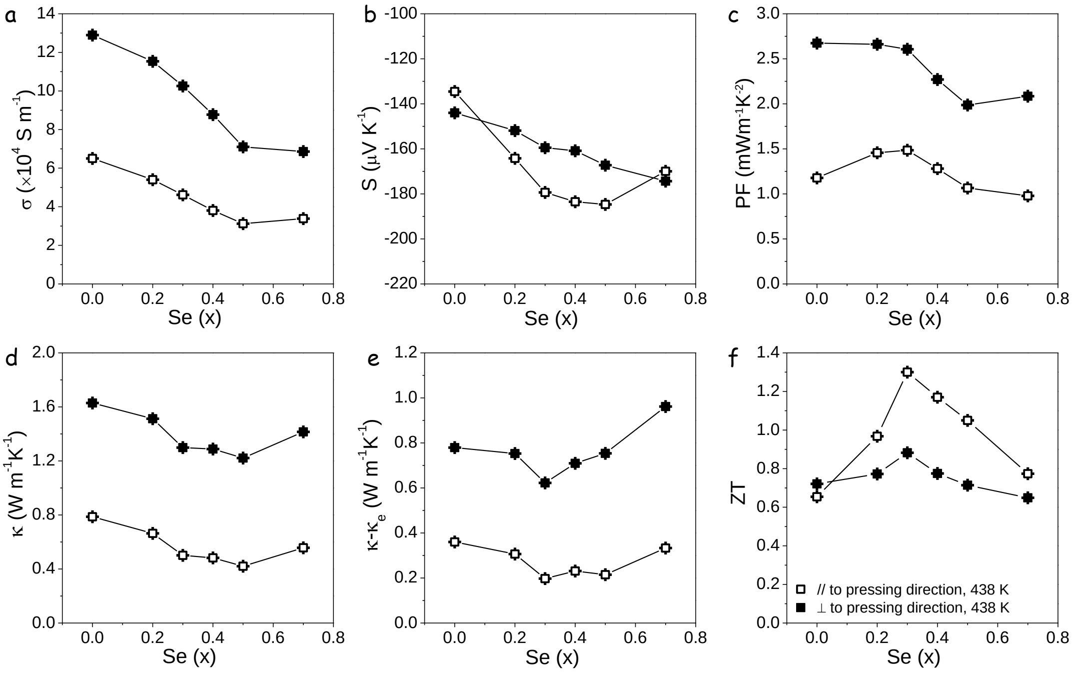

Figure 6.11. Dependence with the Se concentration (x) of the electrical conductivity, σ (a); Seebeck coefficient, *S* (b); power factor PF (c); total thermal conductivity κ (d); thermal conductivity after subtraction of electronic component, κ-κ$_e$ (e), and TE figure of merit ZT (f), of $Bi_2Te_{3-x}Se_x$ pellets measured in the two directions, parallel (//) (open symbols, □) and normal (⊥) (solid symbols, ■) to the pressing direction at 438 K.

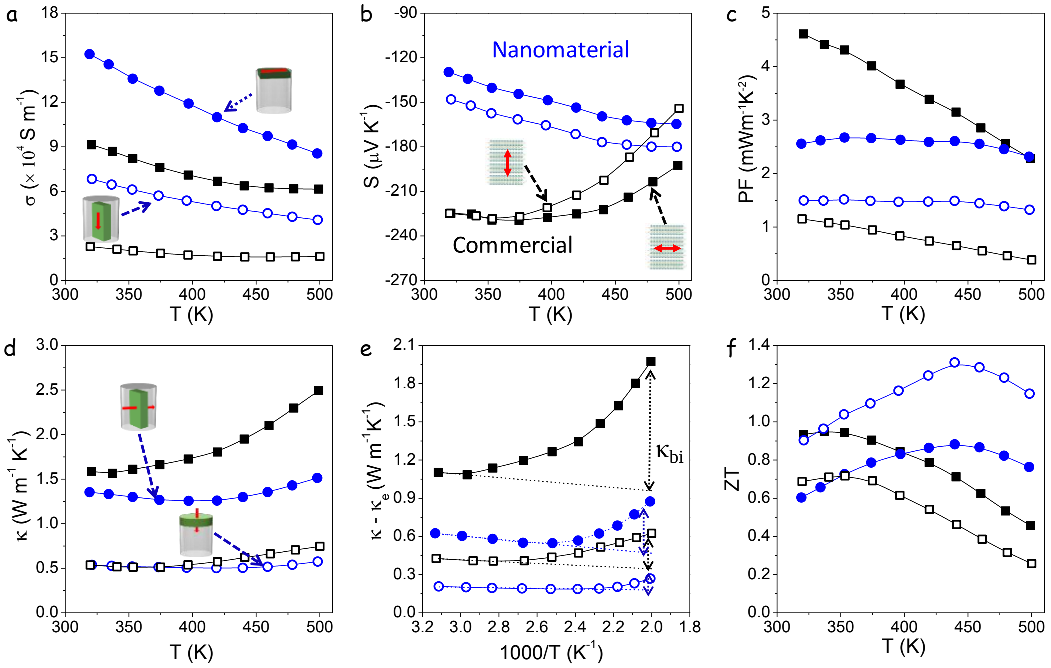

Figure 6.12. TE properties of $Bi_2Te_{2.7}Se_{0.3}$ nanomaterials hot pressed at 480 °C measured in two directions, parallel (//) (open blue circles, ○) and normal (⊥) (solid blue circles, ●) to the pressing direction; and a commercial ingot measured in two directions, parallel (solid black squares, ■)

and normal (open black squares, ☐) to the cleavage direction: (a) σ; (b) *S*; (c) PF; (d) κ; (e) κ-$κ_e$; and (f) ZT. Nanomaterial data was obtained from averaging the experimental results from 5 samples with the same composition.

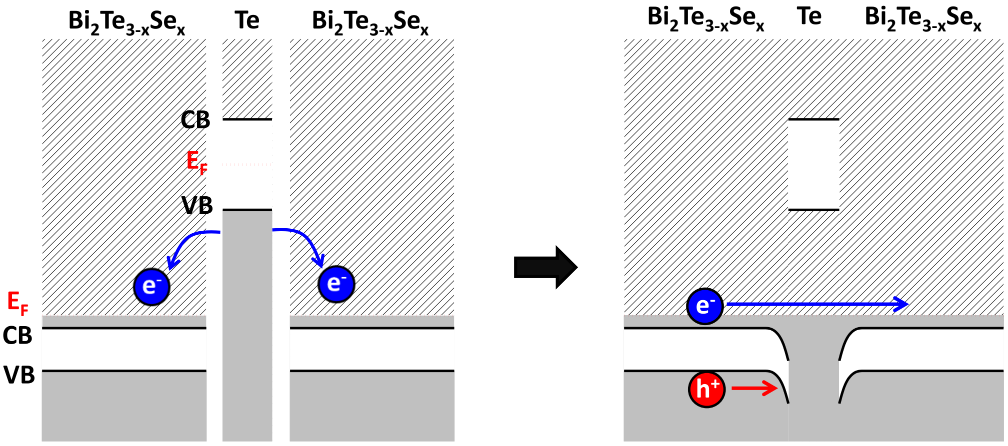

Figure 6.13. Scheme of the energy band alignment between Te (Φ= 4.7 eV; Eg = 0.33-0.36 eV)[48-50] and $Bi_2Te_{3-x,}Se_x$ (Bi_2Te_3: Φ= 5.30 eV; Eg = 0.17 eV),[51-52] underlying the charge injection from Te to $Bi_2Te_{3-x}Se_x$ and the barrier for hole transport that Te introduce within $Bi_2Te_{3-x,}Se_x$.

Overall, among the different compositions tested, $Bi_2Te_{2.7}Se_{0.3}$ displayed the highest ZT values (Figures 6.9f, 6.10f and 6.11f), which was consistent with the use of approximately this composition in commercial devices. ZT values in the pressing direction, that is in the direction of preferential c crystallographic orientation, were systematically higher than in its normal direction, the ab plane, due to the predominance of κ suppression in c over σ gain in ab (Figures 6.9d and 6.10d). Averaging the data measured from 5 pellets with very similar compositions, the highest ZT was reached at 438 K, ZT = 1.31, for $Bi_2Te_{2.7}Se_{0.3}$ in the pressing direction (Figure 6.14). This is the highest value reported for bulk n-type $Bi_2Te_{3-x}Se_x$ alloys (Figures 6.15a and 6.15b). Even more important, very high ZT values were sustained in an extended temperature range in nanomaterials, due to the lower bipolar contributions. The average ZT for $Bi_2Te_{2.7}Se_{0.3}$, calculated over 180 K, from 320 K to 500 K, was ZT_{ave}=1.15 (Figure 6.15c), which is 50% above the value calculated for the commercial ingot, ZT_{ave}=0.77. Additionally, nanocrystalline $Bi_2Te_{3-x}Se_x$ also showed good stability when maintained at relatively high temperature, 420 K, for long periods of time (> 60 h, Figure 6.16) or when cycling it between the room temperate and 500 K (Figure 6.17).

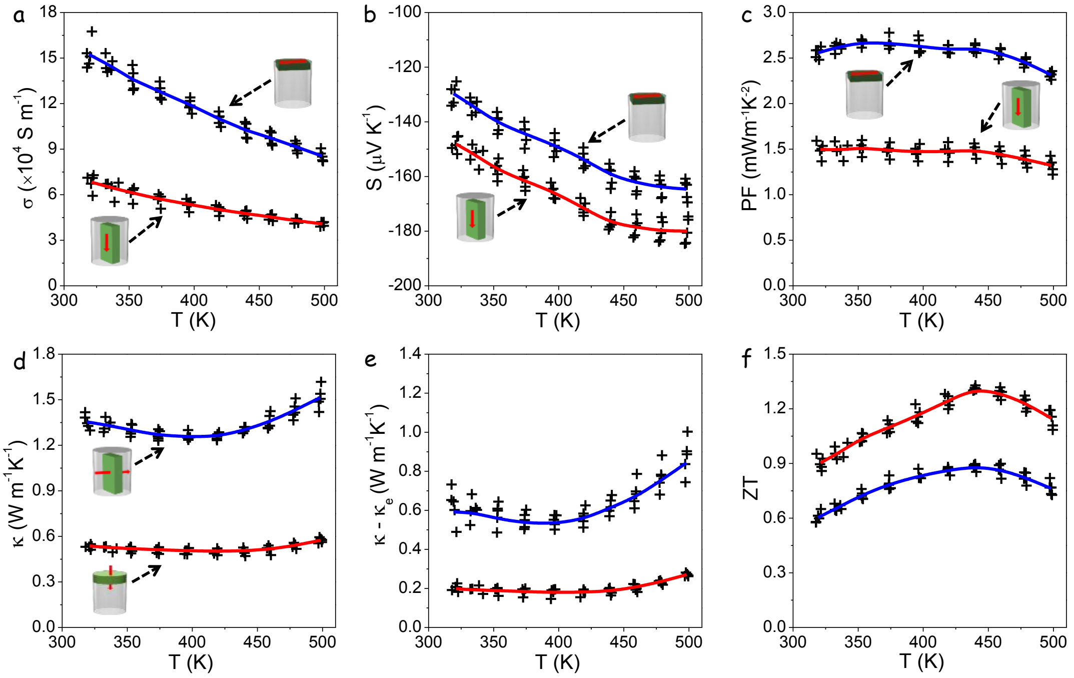

Figure 6.14. Temperature dependence of electrical conductivity, σ (a); Seebeck coefficient, S (b); thermal conductivity, κ (c); and TE figure of merit, ZT (d) of five $Bi_2Te_{2.7}Se_{0.3}$ pellets measured in the direction parallel and normal to the pressing direction. Data from 5 samples is plotted with black crosses, and red and blue lines display the average values in the parallel and normal directions, respectively.

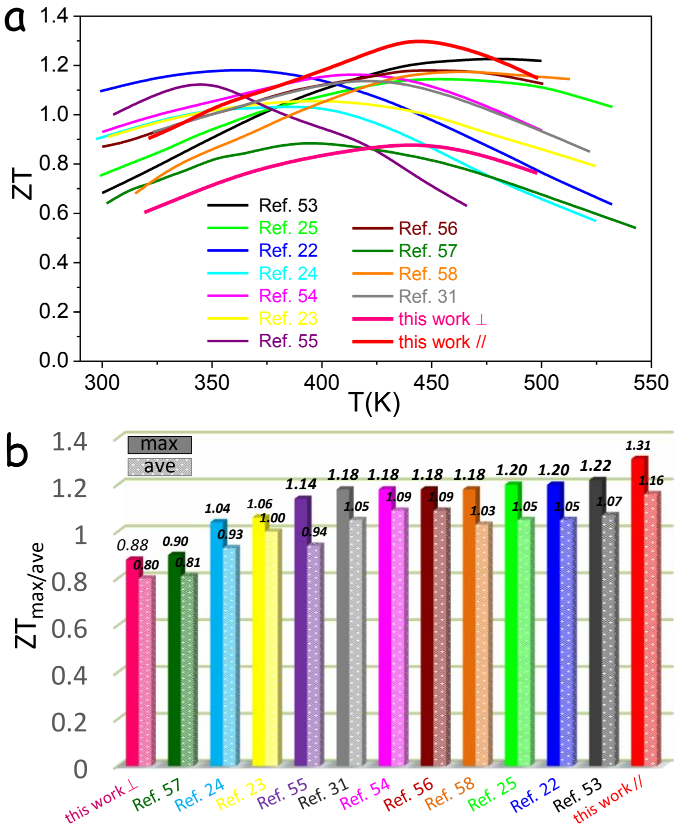

Figure 6.15. State-of-the-art ZT values and average ZT values for n-type Bi_2Te_3-based alloys.[22-]

[25, 31, 53-58] Our data is named as “this work ⊥”, “this work //”, orresponding to the values obtained from averaging the experimental data measured from 5 different samples in the two directions: perpendicular and parallel to the pressing direction, respectively. Average ZT values were calculated on the temperature range from 320 K to 500 K, except for reference 55 (320-465 K).

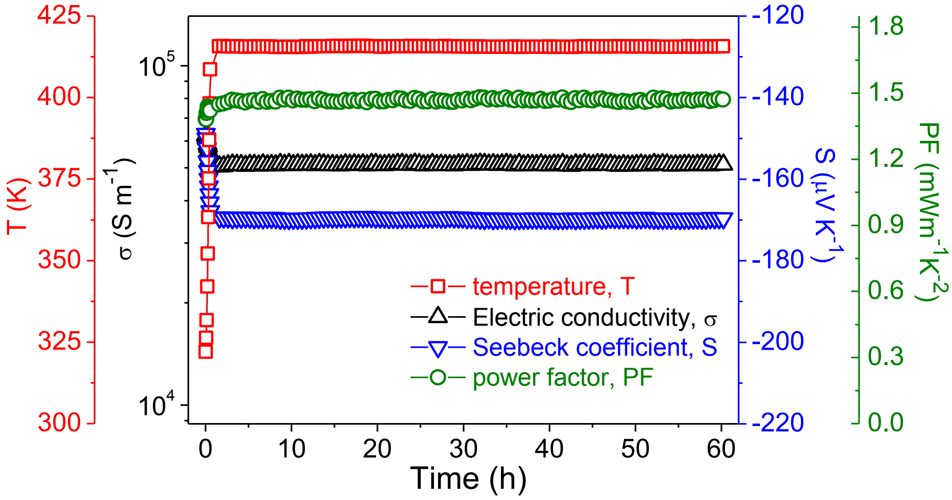

Figure 6.16. Evolution of the electrical conductivity (σ), Seebeck coefficient (*S*) and power factor (PF) of the $Bi_2Te_{2.7}Se_{0.3}$ sample measured in the // direction during a 60.2 h test at 420 K.

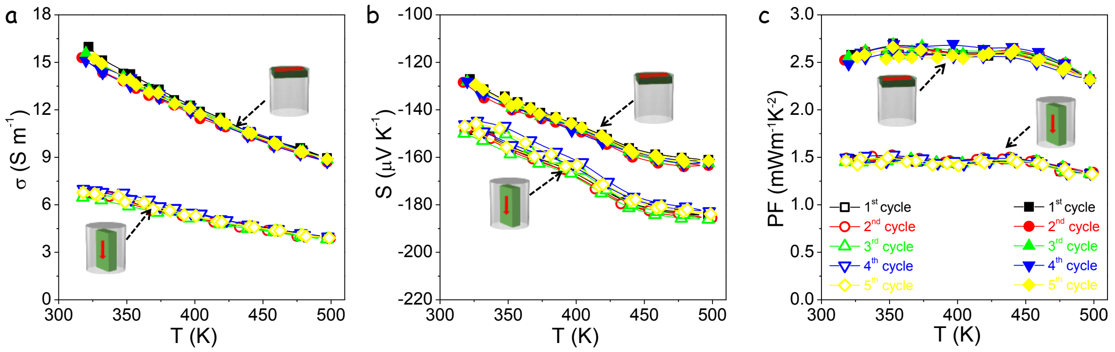

Figure 6.17. Temperature dependence of the electrical conductivity, σ (a), Seebeck coefficient, *S* (b), and power factor, PF (c) of a $Bi_2Te_{2.7}Se_{0.3}$ pellet measured in the // direction for 5 consecutive up-down cycles heating-cooling cycles from room temperature to 498 K. No pre-stabilization treatment was carried out before the first measurement.

6.5 Conclusions

In this chapter, n-type $Bi_2Te_{3-x}Se_x$ NCs with disk-like asymmetric shapes and tuned composition (x=0, 0.2, 0.3, 0.4, 0.5 and 0.7) were produced in solution. Excess amounts of Te were incorporated at the NC synthesis step. Such NCs were used to produce high density $Bi_2Te_{3-x}Se_x$ bulk nanomaterials with marked crystallographic texture through hot-pressing them at a temperature above Te melting point. The TE properties of NC-based bulk nanomaterials were measured in two perpendicular directions, along the pressure axis and normal to it. Nanomaterials were characterized by higher electrical conductivities but lower Seebeck coefficients than commercial materials, which was associated to the higher charge carrier concentrations of the former due to their processing in an excess of tellurium. Nanomaterials also showed notably lower bipolar contributions, which was in most part also related to the higher charge carrier concentrations, but it could be also influenced by a preferential scattering of minority charge carriers at Te-containing grain boundaries. Record TE figures of merit, ZT ~1.31 at 438 K were measured from the $Bi_2Te_{2.7}Se_{0.3}$ nanomaterial in the pressing direction. In addition, the high ZT values also extended over a larger temperature range, from 320 K to 500 K, resulting in ZT average values as high as $ZT_{ave} = 1.15$.

6.6 References

1. Bell, L. E. *Science* **2008,** 321, (5895), 1457-1461.
2. Snyder, G. J.; Toberer, E. S. *Nature materials* **2008,** 7, (2), 105-114.
3. Kim, S. I.; Lee, K. H.; Mun, H. A.; Kim, H. S.; Hwang, S. W.; Roh, J. W.; Yang, D. J.; Shin, W. H.; Li, X. S.; Lee, Y. H. *Science* **2015,** 348, (6230), 109-114.
4. Ibáñez, M.; Luo, Z.; Genç, A.; Piveteau, L.; Ortega, S.; Cadavid, D.; Dobrozhan, O.; Liu, Y.; Nachtegaal, M.; Zebarjadi, M.; Arbiol, J.; Kovalenko, M.V.; Cabot, A. *Nature communications* **2016**, 7, 10766.
5. Ortega, S.; Ibáñez, M.; Liu, Y.; Zhang, Y.; Kovalenko, M. V.; Cadavid, D.; Cabot, A. *Chemical Society Reviews* **2017**, 46, 3510-3528.
6. Mehta, R. J.; Zhang, Y.; Karthik, C.; Singh, B.; Siegel, R. W.; Borca-Tasciuc, T.; Ramanath, G. *Nature materials* **2012,** 11, (3), 233.
7. Kim, S.; Yin, F.; Kagawa, Y. *Journal of alloys and compounds* **2006,** 419, (1-2), 306-311.
8. Kim, S. S.; Aizawa, T. *Metals and materials international* **2006,** 12, (4), 317-322.
9. Liu, Y.; Cadavid, D.; Ibánez, M.; De Roo, J.; Ortega, S.; Dobrozhan, O.; Kovalenko, M. V.; Cabot, A. *Journal of Materials Chemistry C* **2016,** 4, (21), 4756-4762.
10. Liu, Y.; García, G.; Ortega, S.; Cadavid, D.; Palacios, P.; Lu, J.; Ibáñez, M.; Xi, L.; De Roo, J.; López, A.; Martí-Sánchez, S.; Cabezas, I.; Mata, M.; Luo, Z.; Dun, C.; Dobrozhan, O.; Carroll, D.; Zhang, W.; Martins, J.; Kovalenko, M.; Arbiol, J.; Noriega, G.; Song, J.; Wahnon, P.; Cabot, A. *Journal of Materials Chemistry A* **2017,** 5, (6), 2592-2602.
11. Ibáñez, M.; Korkosz, R. J.; Luo, Z.; Riba, P.; Cadavid, D.; Ortega, S.; Cabot, A.; Kanatzidis, M. G. *Journal of the American Chemical Society* **2015,** 137, (12), 4046-4049.
12. Ibáñez, M.; Zamani, R.; Gorsse, S.; Fan, J.; Ortega, S.; Cadavid, D.; Morante, J. R.; Arbiol, J.; Cabot, A. *ACS nano* **2013,** 7, (3), 2573-2586.
13. Poudel, B.; Hao, Q.; Ma, Y.; Lan, Y.; Minnich, A.; Yu, B.; Yan, X.; Wang, D.; Muto, A.; Vashaee, D. *Science* **2008,** 320, (5876), 634-638.
14. Venkatasubramanian, R.; Siivola, E.; Colpitts, T.; O'quinn, B. *Nature* **2001,** 413, (6856), 597.
15. Zhu, T.; Liu, Y.; Fu, C.; Heremans, J. P.; Snyder, J. G.; Zhao, X. *Advanced Materials* **2017**, 29, (14), 1605884.
16. Goldsmid, H.; Douglas, R. *British Journal of Applied Physics* **1954,** 5, (11), 386.
17. Liu, Y.; Zhang, Y.; Ortega, S.; Ibáñez, M.; Lim, K. H.; Grau Carbonell, A.; Martí-Sànchez, S.; Ng, K. M.; Arbiol, J.; Kovalenko, M. V.; Cadavid, D.; Cabot, A. *Nano letters* **2018**, 18, (4), 2557-2563.

18. Yu, Y.; He, D.-S.; Zhang, S.; Cojocaru-Mirédin, O.; Schwarz, T.; Stoffers, A.; Wang, X.-Y.; Zheng, S.; Zhu, B.; Scheu, C. *Nano energy* **2017,** 37, 203-213.
19. Hong, M.; Chen, Z. G.; Yang, L.; Zou, J. *Nano Energy* **2016,** 20, 144-155.
20. Zheng, Y.; Zhang, Q.; Su, X.; Xie, H.; Shu, S.; Chen, T.; Tan, G.; Yan, Y.; Tang, X.; Uher, C. *Advanced Energy Materials* **2015,** 5, (5), 1401391.
21. Kim, Y. M.; Lydia, R.; Kim, J.-H.; Lin, C.-C.; Ahn, K.; Rhyee, J.-S. *Acta Materialia* **2017,** 135, 297-303.
22. Hu, L.; Wu, H.; Zhu, T.; Fu, C.; He, J.; Ying, P.; Zhao, X. *Advanced Energy Materials* **2015,** 5, (17), 1500411.
23. Liu, W. S.; Zhang, Q.; Lan, Y.; Chen, S.; Yan, X.; Zhang, Q.; Wang, H.; Wang, D.; Chen, G.; Ren, Z. *Advanced Energy Materials* **2011,** 1, (4), 577-587.
24. Yan, X.; Poudel, B.; Ma, Y.; Liu, W.; Joshi, G.; Wang, H.; Lan, Y.; Wang, D.; Chen, G.; Ren, Z. *Nano letters* **2010,** 10, (9), 3373-3378.
25. Zhai, R.; Hu, L.; Wu, H.; Xu, Z.; Zhu, T.-J.; Zhao, X.-B. *ACS applied materials & interfaces* **2017,** 9, (34), 28577-28585.
26. Zhu, B.; Huang, Z.-Y.; Wang, X.-Y.; Yu, Y.; Yang, L.; Gao, N.; Chen, Z.-G.; Zu, F.-Q. *Nano Energy* **2017,** 42, 8-16.
27. Uher, C., *Materials Aspect of Thermoelectricity*. CRC Press: 2016.
28. Carle, M.; Pierrat, P.; Lahalle-Gravier, C.; Scherrer, S.; Scherrer, H. *Journal of Physics and Chemistry of Solids* **1995,** 56, (2), 201-209.
29. Seo, J.; Lee, C.; Park, K. *Journal of materials science* **2000,** 35, (6), 1549-1554.
30. Srinivasan, R.; McReynolds, K.; Gothard, N. W.; Spowart, J. E. *Materials Science and Engineering: A* **2013,** 588, 376-387.
31. Zhao, L.; Zhang, B.-P.; Li, J.-F.; Zhang, H.; Liu, W. *Solid State Sciences* **2008,** 10, (5), 651-658.
32. Bhame, S. D.; Pravarthana, D.; Prellier, W.; Noudem, J. G. *Applied Physics Letters* **2013,** 102, (21), 211901.
33. Hu, L.; Liu, X.; Xie, H.; Shen, J.; Zhu, T.; Zhao, X. *Acta Materialia* **2012,** 60, (11), 4431-4437.
34. Okamoto, H.; Tanner, L. *ASM* **1986**.
35. Kamb, W. B. *The Journal of Geology* **1959,** 67, (2), 153-170.
36. Abdullaev, N. *Physics of the Solid State* **2006,** 48, (4), 663-669.
37. Zhu, T.; Hu, L.; Zhao, X.; He, J. *Advanced Science* **2016,** 3, (7), 1600004.
38. Takashiri, M.; Tanaka, S.; Hagino, H.; Miyazaki, K. *Journal of Applied Physics* **2012,** 112, (8), 084315.
39. Li, S.; Xin, C.; Liu, X.; Feng, Y.; Liu, Y.; Zheng, J.; Liu, F.; Huang, Q.; Qiu, Y.; He, J. *Nano Energy* **2016,** 30, 780-789.
40. Termentzidis, K.; Pokropyvnyy, O.; Woda, M.; Xiong, S.; Chumakov, Y.; Cortona,

P.; Volz, S. *Journal of Applied Physics* **2013,** 113, (1), 013506.

41. Teweldebrhan, D.; Goyal, V.; Balandin, A. A. *Nano letters* **2010,** 10, (4), 1209-1218.
42. Walker, P. *Proceedings of the Physical Society* **1960,** 76, (1), 113.
43. Bahk, J.-H.; Shakouri, A. *Physical Review B* **2016,** 93, (16), 165209.
44. Liu, W.; Yan, X.; Chen, G.; Ren, Z. *Nano Energy* **2012,** 1, (1), 42-56.
45. Hu, L.-P.; Zhu, T.-J.; Wang, Y.-G.; Xie, H.-H.; Xu, Z.-J.; Zhao, X.-B. *NPG Asia Materials* **2014,** 6, (2), e88.
46. Zhao, L.; Wu, H.; Hao, S.; Wu, C.-I.; Zhou, X.; Biswas, K.; He, J.; Hogan, T. P.; Uher, C.; Wolverton, C. *Energy & Environmental Science* **2013,** 6, (11), 3346-3355.
47. Puneet, P.; Podila, R.; Karakaya, M.; Zhu, S.; He, J.; Tritt, T. M.; Dresselhaus, M. S.; Rao, A. M. *Scientific reports* **2013,** 3, 3212.
48. Agapito, L. A.; Kioussis, N.; Goddard III, W. A.; Ong, N. *Physical review letters* **2013,** 110, (17), 176401.
49. Kirchhoff, F.; Binggeli, N.; Galli, G.; Massidda, S. *Physical Review B* **1994,** 50, (13), 9063.
50. Rigaux, C. *Journal of Physics and Chemistry of Solids* **1962,** 23, (6), 805-817.
51. Kioupakis, E.; Tiago, M. L.; Louie, S. G. *Physical Review B* **2010,** 82, (24), 245203.
52. Haneman, D. *Journal of Physics and Chemistry of Solids* **1959,** 11, (3-4), 205-214.
53. Hong, M.; Chasapis, T. C.; Chen, Z.-G.; Yang, L.; Kanatzidis, M. G.; Snyder, G. J.; Zou, J. *ACS nano* **2016,** 10, (4), 4719-4727.
54. Prokofieva, L.; Pshenay-Severin, D.; Konstantinov, P.; Shabaldin, A. *Semiconductors* **2009,** 43, (8), 973-976.
55. Park, K.; Ahn, K.; Cha, J.; Lee, S.; Chae, S. I.; Cho, S.-P.; Ryee, S.; Im, J.; Lee, J.; Park, S.-D. *Journal of the American Chemical Society* **2016,** 138, (43), 14458-14468.
56. Hu, L.; Zhu, T.; Liu, X.; Zhao, X. *Advanced Functional Materials* **2014,** 24, (33), 5211-5218.
57. Yang, L.; Chen, Z.-G.; Hong, M.; Han, G.; Zou, J. *ACS applied materials & interfaces* **2015,** 7, (42), 23694-23699.
58. Xu, B.; Feng, T.; Agne, M. T.; Zhou, L.; Ruan, X.; Snyder, G. J.; Wu, Y. *Angewandte Chemie* **2017,** 129, (13), 3600-3605.

Conclusions

In this thesis, I detailed the bottom-up production and characterization of TE nanomaterials with significantly enhanced performances using colloidal NCs as building blocks. Development of TE nanomaterials with significantly improved figure of merit ZT come up not only from a precise control of the influence of each nanomaterial parameter on TE performance, but also a further accurate control over the crystallographic alignment of nanograins for highly anisotropic materials. The main results and conclusions reached are:

I–V–VI NCs at the gram scale with narrow size, shape and composition distributions could be produced using bottom-up approach. A simple and general process to displace the organic ligands from these ternary Ag/Cu-based NCs surface that use a low concentration of inorganic salt solution was developed. NCs were used as building blocks to produce high density nanomaterials. The influence of doping level during the synthesis on the TE performance of $AgSbSe_2$ and Cu_3SbSe_4 nanomaterials obtained was discussed. In Cu_3SbSe_4 system, Sn was demonstrated to be a p-type dopant which effectively helped to control charge carrier concentration, the replacement of Sb by Bi conveniently modified the electronic band structure of the compound leading to higher Seebeck values. Moreover, we optimized the amount of Sn in a Bi-doped material and finally the maximum ZT value was up to 1.26 at 673 K for $Cu_3Sb_{0.88}Sn_{0.10}Bi_{0.02}Se_4$. We further fabricated innovative ring-shaped TE generators, which provided 1 mW of electric power per TE element with a 160 °C temperature gradient. In $AgSbSe_2$ system, a preliminary optimization of the charge carrier concentration by 2% Bi-doping resulted in the maxmum ZT reaching ZT=1.1 at 640 K. Both of the results are among the best ZT values obtained with a Pb- and Te-free material in this middle temperature range, with the additional advantage of the high versatility and low cost associated to solution processing technologies.

The TE performances of PbS can be strongly improved by combining it with low work function nanoparticles, consistent with a spillover of electrons from the low work function metal to the semiconductor. So, in this work PbS-metal composites revealed much higher electrical conductivities and negative Seebeck coefficients in the whole temperature range. Furthermore, we compared the TE properties of PbS-Cu composites with commercial micrometer scale crystal domain sizes with our nanocomposites, it could be observed that with the same metal adding, higher electrical conductivities were obtained in the nanocomposite, but higher Seebeck coefficients were maintained in the commercial microcomposite. Correspondingly, the nanocomposite possessed much lower thermal conductivities. Finally, a 2-fold increase of figure of merit ZT in both composites were obtained over pristine PbS, but the nanocomposites showed higher ZT values in the higher temperature range.

P-type $Bi_xSb_{2-x}Te_3$ and n-type $Bi_2Te_{3-x}Se_x$ NCs with disk-like asymmetric shapes and tuned composition were produced by bottom-up engineering. Excess amount of Te were incorporated at the NC synthesis step. In this work, Bi–Sb–Se–Te nanomaterials with crystallographic texture could be obtained by the liquid phase sintering using an excess of Te. Orientation and solution-reprecipitation mechanisms under a uniaxial pressure were found to be responsible of the crystal texture. Nanomaterials were characterized by higher electrical conductivities but lower Seebeck coefficients than commercial ingots, which was associated to the much higher charge carrier concentrations of the former due to their processing in an excess of Te. Record ZT values, up to 1.96 for p-type $Bi_{0.5}Sb_{1.5}Te_3$ and 1.31 for n-type $Bi_2Te_{2.7}Se_{0.3}$ were reached in the press direction, thus potentially allowing up to more than 50% higher energy conversion efficiencies than that of commercial ingots.

Overall, the different strategies to improve the TE performance of bulk nanostructured materials produced from bottom-up engineering building blocks have been intensively revealed in this thesis. Additionally, it has been proven that the solution-processed synthesis approach is simple, low-cost, compatible with the scale up engineering, and also versatile in tuning the composition, microstructure or other parameters of TE materials to optimize their TE properties

Future Work

While the bottom-up engineering of TE nanomaterials using NCs is a well suited approach to reach high efficiencies, there is still much work and challenges to be completed to fully access the extremely exciting possibilities offered. As far as I am concerned, I will continue my research in the future in the following 3 main areas:

i) To accelerate the development of new TE materials based on metal chalcogenides, overcoming restrictions of the solution-based synthesis strategy.

ii) To fabricate bulk TE modules with versatile form factors. To develop organic – inorganic flexible composites for potential application in wearable TE devices based on high-performance p-type $Bi_{0.5}Sb_{1.5}Te_3$ and n-type $Bi_2Te_{2.7}Se_{0.3}$ NCs developed in the last two chapters of this thesis.

iii) To further improve the Bi_2Te_3-based TE performance. To produce n-type $Bi_2Te_{3-x}Se_x$ nanocomposites from the combination of this n-type host with low work function metal nanoparticles, e.g. Ag, Cu, etc. Additionally, the effectivity of p-type $Bi_xSb_{2-x}Te_3$ nanocomposites potentially produced by combining this p-type host with metal nanoparticles characterized by a large enough work function that need to be proven and revealed.

CURRICULUM VITAE

PERSONAL INFORMATION

Yu Liu

Birthday: 3rd August 1988
Nationality: China
Address: Jardins de les Dones de Negre 1, Pl 2 08930,
Sant Adria del Besos, Barcelona, Spain
E-mail: liuyu92525@gmail.com / yliu@irec.cat
Telephone: +34 651861699
Disciplines: Thermoelectricity, Nanoscience, Materials Science

DEGREE-ACADEMIC QUALIFICATIONS

- 2014.10-present: Ph.D. in Nanoscience, University of Barcelona, Spain
  Thesis: Bottom-up Engineering of Chalcogenide Thermoelectric Nanomaterials.
  Supervisors: Prof. Andreu Cabot and Prof. Doris Cadavid
- 2011.9-2014.6: M.S. in Applied Chemistry, Anhui University, China
  Thesis: Colloidal Synthesis of Ternary Copper-based Nanomaterials and Their Thermoelectric Properties
  Supervisor: Prof. Ji-Ming Song
- 2007.9-2011.7: B.S. in Material Chemistry, Shandong Agricultural University, China

RESEARCH INTEREST

- Synthesis, assembly and characterization of semiconductor and nanocomposites: solution phase synthesis, structural and spectroscopic characterization.
- Development of high performance nanostructured thermoelectric materials and understanding the parameters and their underlying mechanisms that enhance the thermoelectric performance.

RESEARCH EXPERIENCE

2014.10-present: Functional Nanomaterials Group, Catalonia Institute for Energy Research-IREC, Barcelona, Spain, Supervisors: Prof. Andreu Cabot and Dr. Doris Cadavid

- 2017.2-present: High thermoelectric performance in crystallographically textured nanomaterials and devices produced from the liquid phase sintering of Bi_2Te_3-based nanocrystal building blocks
- 2016.1-2017.1: Solution-based synthesis and processing of Sn-and Bi-doped Cu_3SbSe_4 nanocrystals, nanomaterials and ring-shaped thermoelectric generators
- 2015.7-2016.4: Colloidal $AgSbSe_2$ nanocrystals: surface analysis, electronic doping and processing into thermoelectric nanomaterials
- 2014.10-2016.4: Synthesis various nanoparticles and metal-semiconductor nanocomposites by nanoparticle blending for thermoelectric applications

2011.9-2014.6: The key laboratory of environment friendly polymer materials of Anhui province, school of chemistry & chemical engineering, Anhui University, Hefei, China, Supervisor: Prof. Ji-Ming Song

- 2013.1-2014.6: thermoelectric property characterization of ternary Cu-based selenides
- 2011.9-2012.12: Synthesis of different ternary Cu-based selenides nanoparticles, e.g. Cu_2SnSe_3, Cu_3SbSe_4 and $CuFeSe_2$, and their surface modification for thermoelectric applications

PUBLICATIONS LIST

1. **Y. Liu,** Y. Zhang, S. Ortega, M. Ibáñez, K. H. Lim, A. Grau Carbonell, S. Martí-Sànchez, K. M. Ng, J. Arbiol and M. V. Kovalenko, D. Cadavid,* A. Cabot,* "*Crystallographically Textured Nanomaterials Produced from the Liquid Phase Sintering of $Bi_xSb_{2-x}Te_3$ Nanocrystal Building Blocks."* ***Nano Letters*** 2018, 18, 2557-2563.
2. **Y. Liu,** G. García, S. Ortega, D. Cadavid,* P. Palacios, J. Y. Lu, M. Ibáñez, L. L. Xi, J. De Roo, A. M. López, S. Martí-Sánchez, I. Cabezas, M. Mata, Z. S. Luo, C. Dun, O. Dobrozhan, D. L. Caroll, W. Zhang, J. Martins, M. V. Kovalenko, J. Arbiol, G. Noriega, J. Song,* P. Wahnón* and A. Cabot,* "*Solution-Based Synthesis and Processing of Sn- and Bi-Doped Cu_3SbSe_4 Nanocrystals, Nanomaterials and Ring-Shaped Thermoelectric Generators."* ***Journal of Materials Chemistry A*** 2017, 5, 2592-2602.
3. **Y. Liu,** D. Cadavid,* M. Ibáñez, J. D. Roo, S. Ortega, O. Dobrozhan, M. V

Kovalenko, A. Cabot,* "*Colloidal $AgSbSe_2$ nanocrystals: Surface analysis, electronic doping and processing into thermoelectric nanomaterials.*" ***Journal of Materials Chemistry C*** 2016, 4, 4756-4762.

4. **Y. Liu,** D. Cadavid,* M. Ibáñez, S. Ortega, S. Martí-Sánchez, O. Dobrozhan, M.V. Kovalenko, J. Arbiol, A. Cabot,* "*Thermoelectric properties of semiconductor-metal composites produced by particle blending.*" ***APL Materials*** 2016; 4,104813.
5. **Y. Liu,** Y. Zhang, K. H. Lim, M. Ibáñez, S. Ortega M. Li, K. M. Ng, M. V. Kovalenko, D. Cadavid,* A. Cabot,* *"High Thermoelectric Performance in Crystallographically Textured n-type $Bi_2Te_{3-x}Se_x$ Produced from Asymmetric Colloidal Nanocrystals"* submitted.
6. B. Q. Zhang,# **Y. Liu,#** Y. Zuo, J. S. Chen, J. M. Song,* C. J. Mao, H. L. Niu, "*Colloidal Synthesis and Thermoelectric Properties of $CuFeSe_2$ Nanocrystals.*" ***Nanomaterials*** 2018, 8, 8; (contributed equally).
7. S. Ortega, M. Ibáñez,* **Y. Liu,** Y. Zhang, M. V Kovalenko, D. Cadavid,* A. Cabot,* "*Bottom-up engineering of thermoelectric nanomaterials and devices from solution-processed nanoparticle building blocks.*" ***Chemical Society Reviews*** 2017, 46, 3510-3528.
8. M. Ibáñez, R. Hasler, **Y. Liu,** O. Dobrozhan, O. Nazarenko, D. Cadavid, A. Cabot, M. V. Kovalenko,* "*Tuning P-type Transport in Bottom-Up-Engineered Nanocrystalline Pb Chalcogenides Using Alkali Metal Chalcogenides as Capping Ligands.*" ***Chemistry of Materials*** 2017, 29, 7093–7097.
9. M. Ibáñez, Z. S. Luo, A. Genç, L. Piveteau, S.Ortega, D. Cadavid, O. Dobrozhan, **Y. Liu,** M. Nachtegaal, M. Zebarjadi, J. Arbiol, M. V. Kovalenko, A. Cabot,* "*High-performance thermoelectric nanocomposites from nanocrystal building blocks.*" ***Nature Communications*** 2016, 7:10766.
10. Z. S. Luo, E. Irtem, M. Ibáñez, R. Nafria, S. Marti, A. Genç, M. Mata, **Y. Liu,** D. Cadavid, J. Llorca, J. Arbiol, T. Andreu, J. R. Morante, A. Cabot,* "*Mn_3O_4@$CoMn_2O_4$-Co_xO_y nanoparticles: partial cation exchange synthesis and electrocatalytic properties toward the oxygen reduction and evolution reactions.*" ***ACS Applied Materials & Interfaces*** 2016, 8, 17435–17444.
11. J. M. Song,* **Y. Liu,** H. L. Niu, C. J. Mao, L. J. Cheng, S. Y. Zhang, Y. H. Shen, "*Hot-injection synthesis and characterization of monodispersed ternary Cu_2SnSe_3 nanocrystals for thermoelectric applications.*" ***Journal of Alloys and Compounds*** 2013; 581: 646-652.

PARTICIPATION IN CONFERENCE

1. **Y. Liu,** S. Ortega, A. Massaguer, T. Pujol, D. Cadavid, A. Cabot. "*Bottom-up engineering of thermoelectric nanomaterials and devices from solution processed*

nanoparticles" EUROMAT 2017. 17th -22nd September 2017, Thessaloniki, Greece. Oral Presentation

2. **Y. Liu,** G. García, S. Ortega, D. Cadavid, P. Palacios, P. Wahnón, A. Cabot. "*Solution-Based Synthesis and Processing of I-V-VI Nanocrystals, Nanomaterials and Ring-Shaped Thermoelectric Generators*" EUROMAT 2017. 17th -22nd September 2017, Thessaloniki, Greece. Oral Presentation
3. **Y. Liu,** D. Cadavid, S. Ortega, G. García, P. Palacios, P. Wahnón, A. Cabot. "*Solution-Based Synthesis and Processing of Doped Cu-Based Nanocrystals, Nanomaterials and Thermoelectric Generators*" E-MRS Spring Meeting, 25th -30th May 2017, Strasbourg, France. Oral Presentation
4. **Y. Liu,** Doris Cadavid, Silvia.ortega, M. Ibáñez, Oleksandr Dobrozhan, Andreu Cabot. "*Thermoelectric properties of I-V-VI nanomaterials produced from the bottom up assembly of colloidal nanocrystal building blocks.*" The 35th Annual International Conference on Thermoelectrics (ICT 2016) and the 1st Asian Conference on Thermoelectrics, 28th May - 2nd June 2016, Wuhan, China. Oral Presentation
5. M. Ibáñez, Z. Luo, A. Genç, L. Piveteau, S. Ortega, D. Cadavid, O. Dobrozhan, **Y. Liu,** M. Nachtegaal, M. Zebarjadi, J. Arbiol, M. V. Kovalenko, A. Cabot. *"High-Performance Thermoelectric Nanocomposites from Nanocrystal Building Blocks"* The 35th Annual International Conference on Thermoelectrics (ICT 2016) and the 1st Asian Conference on Thermoelectrics, 28th May - 2nd June 2016, Wuhan, China. Oral Presentation
6. P. Orench, M. Meyns, N. J. O. Silva, Z. Luo, À. Carreté, D. Cadavid, **Y. Liu,** M. Ibañez, A. Cabot, *"Neutron diffraction study of CZTS nanoparticles"* European Conference on Neutron Scattering (ECNS), 30th August-4th September 2015, Zaragoza, Spain. Oral Presentation
7. G. García, **Y. Liu,** S. Ortega, D. Cadavid, P. Palacios A. Cabot, P. Wahnón. *Electronic and thermoelectric properties of Bi and Sn doped Cu_3SbSe_4 from first principles.* E-MRS Spring Meeting, 25th-30th May 2017, Strasbourg, France. Poster
8. D. Cadavid, **Y. Liu,** S. Ortega, M. Ibáñez, A. Cabot. *Bottom-up processing of silver chalcogenide nanocomposites.* The 35th Annual International Conference on Thermoelectrics (ICT 2015) and the 13th European Conference on Thermoelectrics. 28th June-2nd July 2015, Dresden, Germany. Poster

Annex

Journal of
Materials Chemistry C

PAPER

View Article Online
View Journal | View Issue

Cite this: *J. Mater. Chem. C*, 2016, 4, 4756

Colloidal $AgSbSe_2$ nanocrystals: surface analysis, electronic doping and processing into thermoelectric nanomaterials†

Yu Liu,[a] Doris Cadavid,*[a] Maria Ibáñez,[bc] Jonathan De Roo,[d] Silvia Ortega,[a] Oleksandr Dobrozhan,[a] Maksym V. Kovalenko[bc] and Andreu Cabot*[ae]

Received 1st March 2016,
Accepted 13th April 2016

DOI: 10.1039/c6tc00893c

www.rsc.org/MaterialsC

We present a high-yield and scalable colloidal synthesis to produce monodisperse $AgSbSe_2$ nanocrystals (NCs). Using nuclear magnetic resonance (NMR) spectroscopy, we characterized the NC surface chemistry and demonstrate the presence of surfactants in dynamic exchange, which controls the NC growth mechanism. In addition, these NCs were electronically doped by introducing small amounts of bismuth. To demonstrate the technological potential of such processed material, after ligand removal by means of $NaNH_2$, $AgSbSe_2$ NCs were used as building blocks to produce thermoelectric (TE) nanomaterials. A preliminary optimization of the doping concentration resulted in a thermoelectric figure of merit (*ZT*) of 1.1 at 640 K, which is comparable to the best *ZT* values obtained with a Pb- and Te-free material in this middle temperature range, with the additional advantage of the high versatility and low cost associated with solution processing technologies.

1. Introduction

I–V–VI_2 semiconductors, particularly $AgSbSe_2$, show very attractive and yet to be exploited functional properties. $AgSbSe_2$, with a rock-salt crystal structure, is highly suitable, for instance, as a phase change recording material in rewritable optical memories due to drastic resistance drop upon crystallization from an amorphous state.[1–6] Within the $AgSbSe_2$ structure, Ag and Sb are generally assumed to randomly occupy the Na sites of the NaCl-type lattice,[7–10] which is consistent with *ab initio* calculations showing the total energies of the various ordered structures to be very close, thus allowing the presence of a significant density of disorder defects and mixed phases. A careful structural characterization has shown domains of ordering, not only in $AgSbSe_2$,[11] but also in the related $AgSbTe_2$,[12] correlating well with calculations showing a rhombohedral ordering to be the most energetically favorable in $AgSbSe_2$.[13] Atomic ordering within the $AgSbSe_2$ crystal has a significant impact on the electronic structure near the band gap, which dominates the electronic properties[14] and provides the material with ferroelectric properties.[11]

$AgSbSe_2$ is a narrow, indirect band-gap semiconductor (0.03–0.10 eV) showing p-type conductivity.[15] However, an apparent optical bandgap of 0.6–1.1 eV[2,15–18] and a high optical absorption coefficient (10^4 cm^{-1}) have also motivated the use of $AgSbSe_2$ for photovoltaic applications.[2,17,19–21]

The $AgSbSe_2$ band structure is characterized by a multi-peak valence band maximum, which potentially results in a high effective mass for holes and thus a high Seebeck coefficient. In addition, $AgSbSe_2$ features a strong anharmonic bonding arrangement associated with the Sb $5s^2$ lone pair, which translates into strong phonon–phonon interactions that reduce the lattice thermal conductivity to values close to the amorphous limit. This intrinsically low thermal conductivity and the appropriate electronic band structure make $AgSbSe_2$ and $AgSbTe_2$ promising candidates for TE applications in the intermediate temperature range (500–700 K).[16,22–28] While $AgSbTe_2$ exhibits higher electrical conductivity, and its nanostructured alloys with GeTe (TAGS)[29] and PbTe (LAST-m)[30] are well known for their remarkable *ZT* values, $AgSbSe_2$ is advantageous in terms of thermal stability, abundance of constituting elements and cost. Bulk $AgSbSe_2$ is typically produced by the solid state reaction of its highly purified elements at temperatures above 1000 K. A relatively large variety of extrinsic electronic dopants, introduced

---

[a] *Catalonia Institute for Energy Research-IREC, Jardins de les Dones de Negre 1, 08930, Sant Adrià del Besos, Spain. E-mail: dcadavid@irec.cat, acabot@irec.cat*
[b] *Institute of Inorganic Chemistry, Department of Chemistry and Applied Biosciences, ETH Zürich, CH-8093, Switzerland*
[c] *Empa-Swiss Federal Laboratories for Materials Science and Technology, Dübendorf, CH-8600, Switzerland*
[d] *Ghent University, Department of Inorganic and Physical Chemistry, Krijgslaan 281 S3, 9000 Gent, Belgium*
[e] *Institució Catalana de Recerca i Estudis Avançats – ICREA, 08010 Barcelona, Spain*

† Electronic supplementary information (ESI) available: Additional experimental details and TEM, XRD, EDX, and NMR data. See DOI: 10.1039/c6tc00893c

as pure elements in the reaction mixture, have been tested, including the substitution of Sb^{3+} by monovalent Na^+,[28] divalent Pb^{2+},[16] Zn^{2+},[23] Sn^{2+},[24] Cd^{2+},[26] Mg^{2+},[27] Ba^{2+},[27] and peculiarly by trivalent Bi^{3+}.[16] Extrinsic dopants can also introduce additional disorder and point defect scattering reducing the material thermal conductivity. In some cases, *e.g.* Na^+, Zn^{2+} and Ba^{2+} can also introduce nanoprecipitates with modified stoichiometry, *e.g.* Na-rich $AgSbSe_2$ or even of secondary phases, *e.g.* ZnSe and $BaSe_3$, which further reduce thermal conductivity and allow reaching *ZT* values of up to ~1.1.[23,27] Besides, intrinsic doping strategies based on tuning the material stoichiometry by modifying, for instance, the Sb content[25] and reaching *ZT* values of up to ~1 have also been tested by solid state reaction methods.

The preparation of $AgSbSe_2$ with controlled properties by means of solution processing methods is especially appealing to investigate the structural and compositional dependent functional properties, optimize the material for relevant applications and develop high performance cost-effective products. In particular, the availability of $AgSbSe_2$ NCs with tuned size, shape, composition and phase would allow high density data storage systems, cost-effective photovoltaic devices and high performance thermoelectric modules to be produced by highly versatile, low-cost, high-throughput and high-yield solution-based bottom-up technologies.[31–36] However, to the best of our knowledge, no synthesis protocol to produce colloidal $AgSbSe_2$ NCs is currently available.

Here, we detail the first colloidal synthesis of monodisperse $AgSbSe_2$ NCs on the gram scale, determine the NC surface composition by NMR analysis and demonstrate the possibility of electronically doping this material with controlled amounts of bismuth. Finally, we elaborate upon a procedure to remove organic ligands and demonstrate the suitability of these NCs to produce high performance thermoelectric nanomaterials.

2. Experimental section

2.1. Chemicals and solvents

Silver nitrate ($AgNO_3$, ≥99%), antimony(III) chloride ($SbCl_3$, 99%), selenium powder (Se, 99.5%), bismuth(III) acetate ($Bi(CH_3CO_2)_3$, >99.99%), sodium amide ($NaNH_2$, 95%), 1-dodecanethiol (DDT, ≥98%), oleic acid (OA, 90%), 1-octadecene (ODE, 90%), and oleylamine (OLA, 70%) were purchased from Sigma-Aldrich. Analytical grade acetone and chloroform were obtained from various sources. All chemicals were used as received without further purification. Syntheses were carried out using a standard vacuum/dry argon Schlenk line.

2.2. Selenium precursor stock solution

A 0.5 M selenium stock solution was prepared by dissolving selenium powder (1.5792 g, 20 mmol) in 20 ml OLA and 20 ml DDT at room temperature, cycled between vacuum and argon to remove the oxygen in the flask, and then stirred under an Ar atmosphere until Se powder was completely dissolved.

2.3. Synthesis of $AgSbSe_2$ NCs

In a typical synthesis, $AgNO_3$ (5 mmol, 0.849 g), $SbCl_3$ (5 mmol, 1.141 g), 70 ml OLA and 10 ml OA were mixed in a 250 ml three-neck flask at room temperature under magnetic stirring for 30 min in order to remove low boiling point impurities. Afterwards, the solution was maintained at 80 °C under vacuum for 60 min. At around 70 °C the solution became yellowish and changed from ivory yellow to yellowish-brown during the time at 80 °C. Then the solution was heated to 120 °C for another 10 min under vacuum. After these steps, argon was introduced and the reaction was rapidly heated to 220 °C. At this temperature, 20 ml of a 0.5 M selenium solution were quickly injected. After injection, the color of the solution changed immediately from yellowish-brown to dark brown, indicating the NC nucleation. NCs were allowed to grow for 30 min at 220 °C. Afterwards, the colloidal solution was rapidly cooled to room temperature through a water bath. The resultant dark brown solution was cleaned by centrifugation at 6000 rpm for 5 min using chloroform as a solvent and acetone as a non-solvent.

2.4. Synthesis of Bi-doped $AgSbSe_2$ NCs

Bi-doped $AgSbSe_2$ NCs were synthesized by using the same process as the pristine NCs, but replacing the desired amount of $SbCl_3$ by $Bi(CH_3CO_2)_3$. To produce $AgSb_{0.98}Bi_{0.02}Se_2$, the precursor molar ratio was $SbCl_3/Bi(CH_3CO_2)_3$ = 0.98/0.02 (4.9 mmol/0.1 mmol).

2.5. Nuclear magnetic resonance (NMR)

NMR measurements were recorded on a Bruker Avance III HD spectrometer operating at a ^1H frequency of 500.26 MHz and equipped with a BBFO-Z probe. The sample temperature was set to 298.2 K. One dimensional (1D) ^1H and 2D NOESY (Nuclear Overhauser Effect Spectroscopy) spectra were acquired using standard pulse sequences from the Bruker library. For the quantitative 1D ^1H measurements, 64k data points were sampled with the spectral width set to 20 ppm and a relaxation delay of 30 s. The NOESY mixing time was set to 300 ms and 4096 data points in the direct dimension and 512 data points in the indirect dimension were sampled, with the spectral width set to 12 ppm. Diffusion measurements (2D DOSY) were performed using a double stimulated echo sequence for convection compensation and with monopolar gradient pulses.[37] Smoothed rectangle gradient pulse shapes were used throughout. The gradient strength was varied quadratically from 2–95% of the probe's maximum value in 64 increments, with the gradient pulse duration and diffusion delay optimized to ensure a final attenuation of the signal in the final increment of less than 10% relative to the first increment. For 2D processing, the spectra were zero filled until a 4096–2048 real data matrix. Before Fourier transformation, the 2D spectra were multiplied with a squared cosine bell function in both dimensions, and the 1D spectra were multiplied with an exponential window function. Concentrations were obtained using the Digital ERETIC method, as provided in the standard software of Bruker. The diffusion coefficients were obtained by fitting the appropriate Stejskal–Tanner equation to the signal intensity decay.[38]

2.6. NC ligand displacement (LD)

$NaNH_2$ was used to displace organic ligands from the $AgSbSe_2$ and $AgSb_{0.98}Bi_{0.02}Se_2$ NC surface. In a typical procedure, $AgSbSe_2$ NCs (500 mg) were dispersed in 15 ml of chloroform and mixed at room temperature with 5 ml of $NaNH_2$ solution (0.02 M) in methanol. The solution was shaken for 1–2 min to displace the organic ligands attached to the NC surface. This process was repeated twice. Afterward, NCs were precipitated by centrifugation and they were thoroughly purified using chloroform and acetone to remove the remaining organic surfactants and excess $NaNH_2$. Finally, $AgSbSe_2$ NCs were precipitated and dried under vacuum to obtain a fine nanopowder.

2.7. Bulk nanomaterials

$AgSbSe_2$ and $AgSb_{0.98}Bi_{0.02}Se_2$ nanopowders obtained from drying 15 nm NCs were loaded into graphite dies and compacted into pellets (Ø10 mm × ~1.5 mm) in an Ar atmosphere using a custom-made hot press. The process temperature was maintained between 350 °C and 360 °C for 30 min and the pressure was set to 70 MPa. In this system, heat is provided by an induction coil operated in the RF range applied directly to a graphite die, which acts as a susceptor, resulting in a heating ramp of about 20 °C per second. The density of the pressed pellets was always higher than 93% of their theoretical value.

2.8. Structural and chemical characterization

X-ray diffraction analyses were carried out on a Bruker AXS D8 ADVANCE X-ray diffractometer using Cu-Kα radiation (λ = 0.15406 Å). The size and shape of initial NCs were examined by transmission electron microscopy (TEM) using a ZEISS LIBRA 120, operating at 120 kV. High resolution TEM (HRTEM) images were recorded using a JEOL JEM-2200FS microscope operated at 200 kV. For TEM analysis colloidal nanoparticles in chloroform were supported by drop-casting the solution on a carbon-coated copper grid at room temperature and ambient atmosphere. For HRTEM characterization of the pellets, we manually ground a piece of the measured pellet and mixed the obtained powder with TCE (tetrachloroethylene). The powder suspension was drop casted onto a carbon coated copper grid at room temperature and ambient atmosphere. Field-emission scanning electron microscopy (SEM) was carried out on an Auriga Zeiss at 5.0 kV. Quantitative elemental analysis was made by means of an energy dispersive X-ray spectroscopy (EDX) detector attached to a SEM.

2.9. Thermoelectric measurements

Seebeck coefficient was measured by using a static DC method. Electrical resistivity data were obtained by a standard four-probe method. Both the Seebeck coefficient and the electrical resistivity were measured simultaneously in a LSR-3 LINSEIS system in the range between room temperature and 700 K, under a helium atmosphere. XFA 600 xenon flash equipment was used to determine the thermal diffusivities of the samples. The carrier concentration and mobility were measured using the Hall measurement system (PPMS-9T, Quantum Design Inc., USA) at room temperature under a magnetic field of 2 T. The thermal conductivity was calculated using $\kappa = \lambda C_p \rho$, where λ is the thermal diffusivity, C_p is the heat capacity, and ρ is the mass density of the specimen. The specific heat capacity (C_p) was measured by means of a differential scanning calorimetry method (DSC model T2000, TA Instruments), and the density (ρ) values used here were calculated using Archimedes' method.

3. Results and discussion

Fig. 1a shows a representative TEM micrograph of the spherical 15 ± 1 nm $AgSbSe_2$ NCs obtained following the above procedure. NCs could be dispersed in non-polar solvents such as toluene, hexane or chloroform to form a stable, dark brown dispersion (Fig. 1b). XRD analysis showed $AgSbSe_2$ NCs to have a cubic structure with a $Fm\bar{3}m$ space group (a = 5.78 Å) (Fig. 1d, JCPDS card No. 00-012-0379). No order between the Ag and Sb ions could be discerned from the XRD patterns, which is consistent with the similar scattering factors of Ag and Sb ions. Importantly, no secondary phases were detected in the XRD pattern, pointing towards the phase purity of the synthesized NCs. EDX analysis showed the composition of silver, antimony, and selenium to be consistent with stoichiometric $AgSbSe_2$, within the experimental error of ~2% (Fig. S1, ESI†).

The presence of OLA and OA in the precursor solution was required to dissolve $AgNO_3$ and $SbCl_3$, respectively.[39] The absence of OA prevented the incorporation of Sb and thus the formation of stoichiometric $AgSbSe_2$ NCs. Likewise, the absence of OLA resulted in a polydisperse mixture of $AgSbSe_2$ and Ag_2Se (Fig. S2 and S3, ESI†).

Although the reaction mixture already turned dark brown upon injection of the selenium precursor, relatively long reaction times were necessary to produce monodisperse NCs (Fig. 2 and Fig. S4, ESI†). Within the first 15 min, NCs with a bimodal size distribution were obtained. This bimodal distribution possibly originates from an extended nucleation time due to a relatively low reactivity of the precursor complexes, which

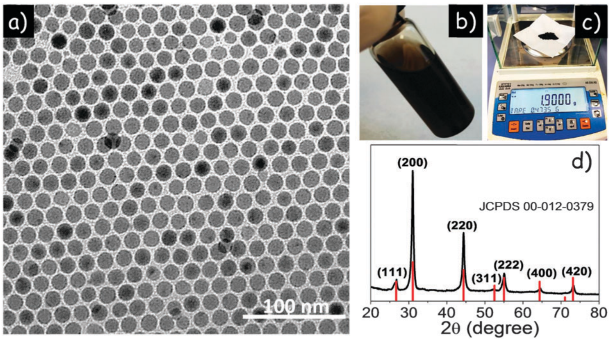

Fig. 1 (a) TEM micrograph of the $AgSbSe_2$ NCs. (b) NCs dispersed in chloroform. (c) The amount of NCs produced per batch. (d) The XRD pattern of $AgSbSe_2$.

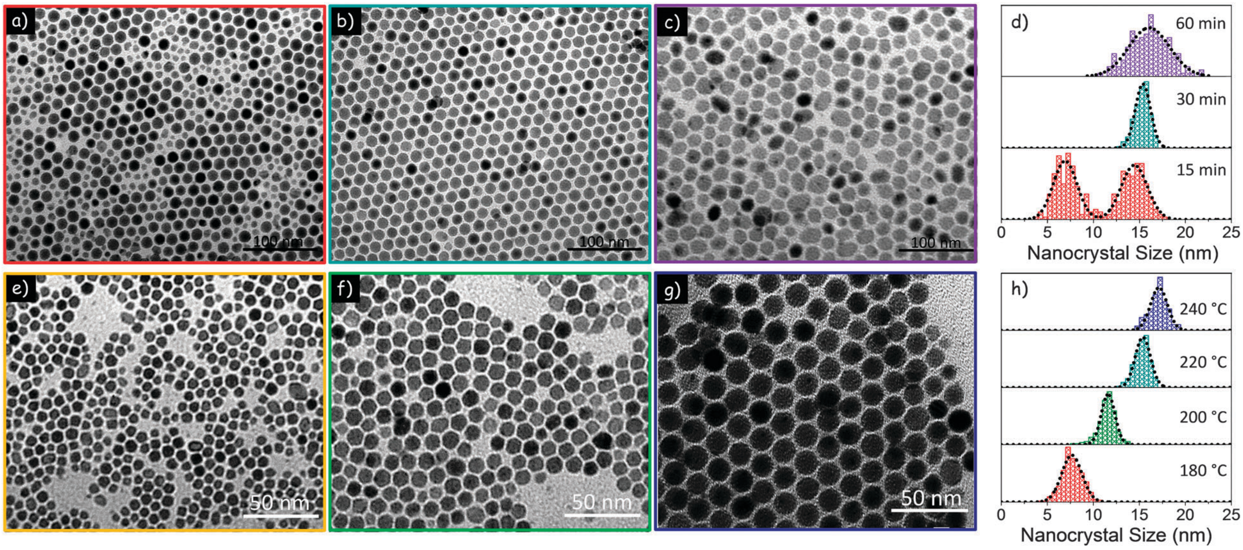

Fig. 2 (a–c) TEM micrographs of $AgSbSe_2$ NCs prepared at a fixed temperature, 220 °C, and different reaction times: (a) 15 min; (b) 30 min; and (c) 60 min. (d) Histogram of the particle size distribution for NCs produced at increasing reaction times. (e and f) TEM micrographs of $AgSbSe_2$ NCs prepared at different reaction temperatures and a fixed reaction time, 30 min: (e) 180 °C; (f) 200 °C; and (g) 240 °C (5 min). (h) Histogram of the measured particle size distribution for NCs produced at increasing reaction temperatures.

translates into a slow NC growth that prevents a rapid monomer reduction in the supersaturation.[40] A focusing of the size distribution, most probably mediated by an Ostwald ripening process, was observed up to 30 min of reaction time, when the narrowest size distribution was obtained. Larger reaction times resulted in a non-uniform growth of the NCs, increasing the size distribution width.

Consistent with this growth mechanism, an increase of the injection and reaction temperature and thus of the monomer reactivity resulted in larger NCs. Therefore, fixing the reaction time, the $AgSbSe_2$ NC size could be easily tailored in the range from 7 ± 1 nm to around 17 ± 2 nm by just adjusting the reaction temperature in the range from 180 to 240 °C (Fig. 2 and Fig. S5, ESI†). Reaction temperatures below 180 °C did not allow the growth of $AgSbSe_2$ NCs. Higher reaction temperatures resulted in highly polydisperse NCs.

In the ^1H nuclear magnetic resonance (NMR) spectrum of the resulting NC dispersion in deuteroform, slightly broadened resonances are observed which correspond to an oleyl chain (Fig. 3a). Since the integrations from the alkene resonance (5) and the CH_3 resonance (6) fit the expected 2 : 3 ratio we conclude that fully saturated molecules are not present. However, it is difficult to distinguish OA from OLA since the characteristic CH_2 resonances (1 and 2) next to the functional group are not detected, presumably due to the interaction of the ligand with the NC surface. The nuclear Overhauser effect spectrum (NOESY) (Fig. 3b) indeed confirms that the oleyl species interact with the surface since negative (black) nOe cross peaks are observed.[41] The total ligand concentration was determined to be 4.5 mM (based on resonance 6) and with the NC concentration and NC size, a rather low ligand density of 1.2 nm^{-2} was calculated. The diffusion ordered NMR spectrum (DOSY, Fig. 3c) features two sets of resonances (apart from acetone), with a different diffusion coefficient, *D*. This indicates that two species are present which diffuse with a different speed. However, none of the two species diffuses slow enough

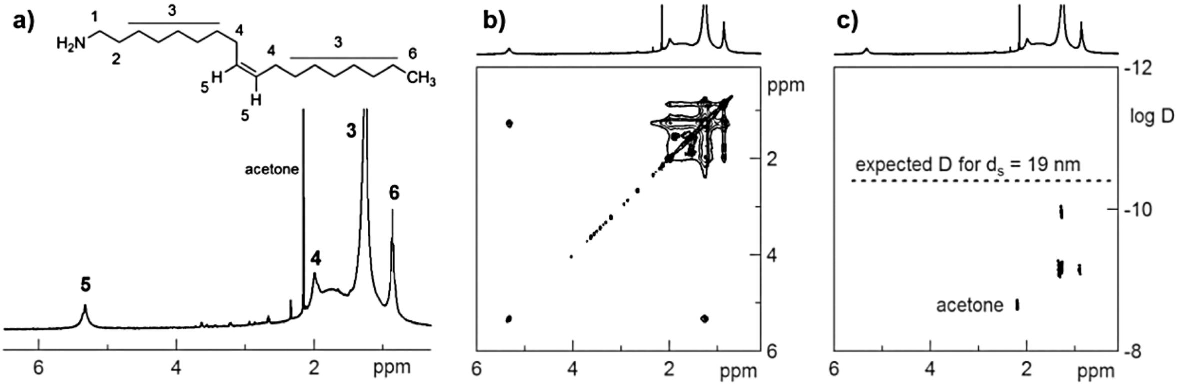

Fig. 3 (a) ^1H NMR spectrum of $AgSbSe_2$ 15 ± 2 nm NCs (4 μM) and the corresponding (b) NOESY and (c) DOSY spectra.

to correspond to a 15 nm nanocrystal plus a tightly bound ligand shell, which would yield a solvodynamic diameter, d_s = 19 nm. We thus infer that the ligands are not tightly bound but are in a dynamic exchange regime between a free state and a bound state. Therefore, the ligand density that was calculated earlier is a maximum value and, in reality, the ligands only spend part of their time on the surface. A low bond strength of the ligands to the NC surface and the observed ligand dynamic exchange are consistent with the NC growth not being limited by the surfactant concentration, but by the growth kinetics.

To elucidate the nature of the two species in DOSY, we stripped the ligands from the NC surface by the addition of TFA. After removal of the NCs by centrifugation, the supernatant was again measured using NMR (Fig. S6, ESI†) and the characteristic resonances of both OA and OLA were observed with a relative abundance of 18% and 82% respectively.

Controlled amounts of bismuth were incorporated within the $AgSbSe_2$ NCs by replacing a small amount of $SbCl_3$ by an equivalent amount of $Bi(CH_3COO)_3$ in the precursor solution. At relatively low Bi concentrations, [Bi] < 5%, EDX analysis showed the final Bi composition in the NCs to match, within the experimental error, the nominal concentration of introduced $Bi(CH_3COO)_3$. The incorporation of Bi ions within the $AgSbSe_2$ lattice was confirmed by a slight peak shift toward lower angles in the XRD pattern (Fig. 4b), pointing towards an increase of the lattice parameters. Bi-doping had also an evident influence on the size and shape distribution of the produced NCs (Fig. 4a).

To use $AgSbSe_2$ NCs in solid-state devices that require an efficient transport of charge carriers, original insulating organic ligands have to be removed. Among the different ligand displacement agents tested, $NaNH_2$ was the most effective one, as characterized by Fourier-transform infrared spectroscopy (FTIR). After ligand removal with a 0.02 M $NaNH_2$ solution, $AgSbSe_2$ could not be re-dispersed in non-polar solvents and the strong C–H vibration modes (2850–3000 cm^{-1}) and the bands corresponding to C–C, C–N and NH_2 (700–1650 cm^{-1}) had completely disappeared from the FTIR spectrum (Fig. 5), proving the effective removal of OLA and OA from the NC surface.

After ligand displacement, dried 15 nm $AgSbSe_2$ NCs were hot-pressed into 10 mm diameter and 1.5 mm thick pellets at 350 °C under 70 MPa pressure for 30 min. All pellets produced had a metallic lustre, were mechanically robust and had relative densities above 93% as measured by Archimedes' method. No secondary phases or changes in composition of the $AgSbSe_2$ and $AgSb_{0.98}Bi_{0.02}Se_2$ materials during the hot press process were detected by EDX and XRD (Fig. S7 and S8, ESI†). SEM and TEM characterization showed a very low porosity and large grains, up to several hundred nanometers, during the thermal processes (Fig. 6a and Fig. S9, ESI†). However, HRTEM characterization allowed discerning crystallographic order domains in the nanometer size regime (Fig. 6b).

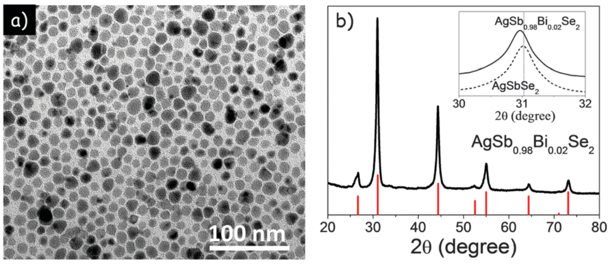

Fig. 4 (a) TEM micrograph of $AgSb_{0.98}Bi_{0.02}Se_2$ NCs and (b) their XRD pattern including the reference JCPDS 00-012-0379. The inset shows details of the (200) peak.

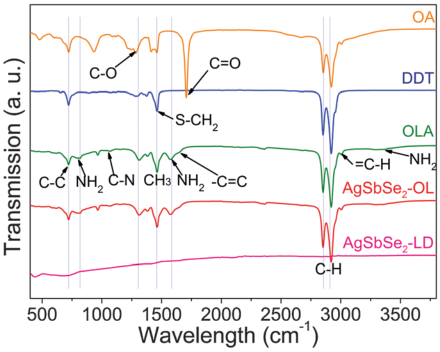

Fig. 5 From top to down, FTIR spectra of pure OA, DDT, OLA, as-produced $AgSbSe_2$ NCs ($AgSbSe_2$-OL) and $AgSbSe_2$ NC after ligand removal with $NaNH_2$ ($AgSbSe_2$-LD).

Fig. 7 shows the electrical conductivity (σ), Seebeck coefficient (S), thermal conductivity (κ), and thermoelectric figure of merit ($ZT = \sigma S^2 T/\kappa$) of $AgSbSe_2$ and $AgSb_{0.98}Bi_{0.02}Se_2$ pellets. Both materials showed a p-type electronic character. $AgSbSe_2$ was characterized by a relatively low σ, which increased from 1380 S m^{-1} at ambient temperature up to 1700 S m^{-1} at 600 K. It showed high Seebeck coefficients reaching up to 462 μV K^{-1} at 695 K, which relates with its flat valence band maximum and multipeak valence band structure.[16] The introduction of an atomic 0.5% Bi significantly enhanced the electrical conductivity, which increased from 4520 S m^{-1} at room temperature to 5970 S m^{-1} at 618 K in $AgSb_{0.98}Bi_{0.02}Se_2$. These values are slightly above those previously reported for bulk $AgSb_{0.98}Bi_{0.02}Se_2$ produced by solid state methods.[16] With Bi doping, the Seebeck coefficient decreased to values below 360 μV K^{-1}, which is consistent with an increase of carrier concentration. Overall, the

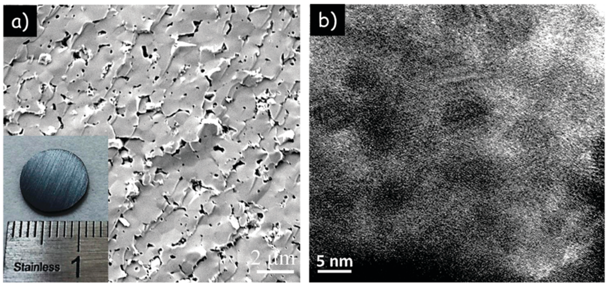

Fig. 6 (a) SEM micrograph of the fractured surface of a $AgSbSe_2$ pellet (inset); (b) HRTEM micrograph of the same $AgSbSe_2$ pellet showing several crystal nanodomains.

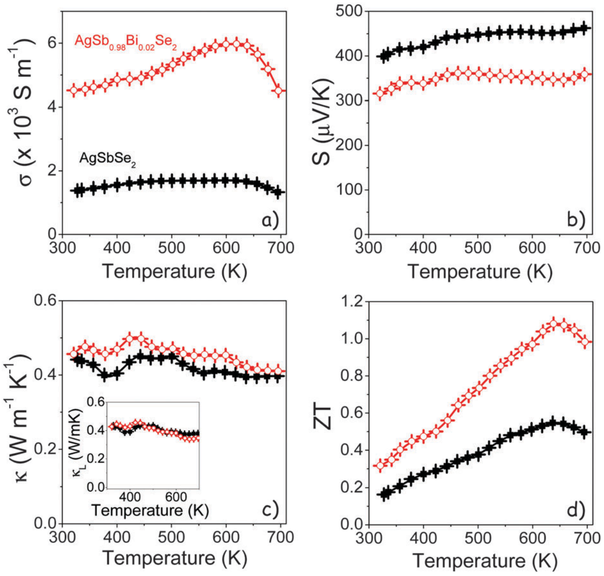

Fig. 7 Temperature dependence of: (a) electric conductivity (σ); (b) Seebeck coefficient (S); (c) thermal conductivity (κ) including lattice thermal conductivity (κ_L) in the inset; and (d) thermoelectric figure of merit (ZT) of $AgSbSe_2$ (■) and $AgSb_{0.98}Bi_{0.02}Se_2$ (○).

$AgSb_{0.98}Bi_{0.02}Se_2$ power factor (PF) was higher than that of $AgSbSe_2$, up to ~0.74 mW m^{-1} K^{-2} at 580 K (Fig. S10, ESI†), and slightly higher than previously reported for bulk $AgSb_{0.98}Bi_{0.02}Se_2$ (Fig. S12, ESI†).[16]

Room temperature Hall measurements provided hole concentrations $p = 4 \pm 2 \times 10^{19}$ cm^{-3} in $AgSbSe_2$ and 5-fold higher for $AgSb_{0.98}Bi_{0.02}Se_2$, $p = 2 \pm 1 \times 10^{20}$ cm^{-3}. As in related Cu_2SbSe_3[42,43] and $AgSbTe_2$[44–47] compounds, the origin of the p-type conductivity in $AgSbSe_2$ is found in its defect structure and non-stoichiometry, and it is generally associated with Ag vacancies. The introduction of a small amount of an impurity may perturb the $AgSbSe_2$ lattice and modify this defect concentration. In the particular case of substituting Sb^{3+} ions by the larger Bi^{3+} ions a compressive strain is introduced, which we hypothesize can in part be alleviated by a larger density of Ag vacancies and thus an increase of the hole concentration. The confirmation of this hypothesis needs in all cases a careful analysis of the defect formation energies within this compound in the presence of Bi, which is out of the scope of the present work. Besides, the relatively low Hall mobilities measured, 2.5 cm^2 V^{-1} s^{-1} and 1.9 cm^2 V^{-1} s^{-1} for $AgSbSe_2$ and $AgSb_{0.98}Bi_{0.02}Se_2$, respectively, are consistent with the large degree of disorder, the nanoscale precipitates and the intrinsically large effective mass of holes in this system. The mobility decrease with the introduction of Bi ions is also consistent with the presence of additional point defects scattering charge carriers.

Very low thermal conductivities ($\kappa_{total} = \lambda C_p \rho < 0.5$ W m^{-1} K^{-1}) were measured for both $AgSbSe_2$ and $AgSb_{0.98}Bi_{0.02}Se_2$ compounds in the whole studied temperature range of 300 to 700 K (Fig. 7c). These low thermal conductivities can be explained by an efficient multi-level phonon scattering; that is by nanometer scale precipitates, by the highly disordered lattice and by the strong phonon–phonon interactions from the high degree of anharmonicity of the Sb–Se bonds in this material.[18] In spite of the higher density of defects associated with the presence of Bi, thermal conductivities were slightly higher for $AgSb_{0.98}Bi_{0.02}Se_2$ due to the larger contribution from the electronic thermal conductivity (Fig. 7c inset).

As a result, ZT values of up to 1.1 at 640 K were obtained for $AgSb_{0.98}Bi_{0.02}Se_2$ (Fig. 7d), which represents a two-fold increase over pristine $AgSbSe_2$, and is among the best values obtained for a Pb- and Te-free material at this temperature (Table S1, ESI†).

4. Conclusions

In summary, a scalable colloidal synthesis of monodisperse $AgSbSe_2$ NCs and Bi-doped $AgSb_{1-x}Bi_xSe_2$ NCs was developed. We showed OLA and OA to be present in dynamic exchange at the surface of the NCs, rendering them soluble in non-polar solvents while allowing kinetic control of their growth. After displacing these surfactants, NCs were used as building blocks to produce 93% relative density nanomaterials. A preliminary optimization of the doping level resulted in $AgSb_{0.98}Bi_{0.02}Se_2$ nanomaterials reaching $ZT = 1.1$ at 640 K. This figure of merit is among the largest values reported for a tellurium-free material in the middle temperature range, with the additional advantage of the low-cost and convenient solution processability of the materials and related devices.

Acknowledgements

This work was supported by the European Regional Development Funds, the Framework 7 program under project UNION (FP7-NMP-2012-310250), the Swiss Federal Commission for Technology and Innovation (CTI, Project Nr. 14698.2 PFIW-IW) and the Spanish MINECO project BOOSTER (ENE2013-46624-C4-3-R). YL thanks the China Scholarship Council (CSC 201406500003) for scholarship support. MI, OD and SO thank AGAUR for their Beatriu de Pinós postdoctoral grant (2013 BP-A00344) and PhD grant, respectively. JDR thanks the FWO (Research Foundation Flanders) for financial support. M. V. K. acknowledges partial financial support from the European Union (EU) *via* FP7 ERC Starting Grant 2012 (Project NANOSOLID, GA No. 306733). The authors also acknowledge the funding from Generalitat de Catalunya 2014 SGR 1638.

Notes and references

1 K. Wang, C. Steimer, R. Detemple, D. Wamwangi and M. Wuttig, *Appl. Phys. A: Mater. Sci. Process.*, 2005, **81**, 1601–1605.

2 H. Soliman, D. Abdel-Hady and E. Ibrahim, *J. Phys.: Condens. Matter*, 1998, **10**, 847.

3 K. Wang, C. Steimer and M. Wuttig, *J. Optoelectron. Adv. Mater.*, 2007, **9**, 2008.

4 A. Patel and D. Lakshminarayana, *Thin Solid Films*, 1982, **98**, 59–63.

5 A. Patel, D. Lakshminarayana and K. Rao, *Thin Solid Films*, 1982, **94**, 51–57.
6 A. Abdelghany, S. Elsayed, D. Abdelwahab, A. A. El Ela and N. Mousa, *Mater. Chem. Phys.*, 1996, **44**, 277–280.
7 K. Wojciechowski and M. Schmidt, *Phys. Rev. B: Condens. Matter Mater. Phys.*, 2009, **79**, 184202.
8 S. Geller and J. Wernick, *Acta Crystallogr.*, 1959, **12**, 46–54.
9 J. Wernick and K. Benson, *J. Phys. Chem. Solids*, 1957, **3**, 157–159.
10 R. Wolfe, J. Wernick and S. Haszko, *J. Appl. Phys.*, 1960, **31**, 1959–1964.
11 L. Aggarwal, J. S. Sekhon, S. N. Guin, A. Arora, D. S. Negi, R. Datta, K. Biswas and G. Sheet, *Appl. Phys. Lett.*, 2014, **105**, 113903.
12 E. Quarez, K.-F. Hsu, R. Pcionek, N. Frangis, E. Polychroniadis and M. G. Kanatzidis, *J. Am. Chem. Soc.*, 2005, **127**, 9177–9190.
13 K. Hoang, S. Mahanti, J. R. Salvador and M. G. Kanatzidis, *Phys. Rev. Lett.*, 2007, **99**, 156403.
14 M. Salimi and S. J. Hashemifar, *J. Alloys Compd.*, 2015, **650**, 143–148.
15 K. Wojciechowski, J. Tobola, M. Schmidt and R. Zybala, *J. Phys. Chem. Solids*, 2008, **69**, 2748–2755.
16 S. N. Guin, A. Chatterjee, D. S. Negi, R. Datta and K. Biswas, *Energy Environ. Sci.*, 2013, **6**, 2603–2608.
17 J. Garza, S. Shaji, A. Rodriguez, T. D. Roy and B. Krishnan, *Appl. Surf. Sci.*, 2011, **257**, 10834–10838.
18 T. N. Asokan, K. Urmila, R. Jacob, R. R. Philip, G. Okram, V. Ganesan and B. Pradeep, *J. Semicond.*, 2014, **35**, 052001.
19 J. González, S. Shaji, D. Avellaneda, A. Castillo, T. D. Roy and B. Krishnan, *Mater. Res. Bull.*, 2013, **48**, 1939–1945.
20 K. Bindu, M. Nair, T. D. Roy and P. Nair, *Electrochem. Solid-State Lett.*, 2006, **9**, G195–G199.
21 K. Bindu, J. Campos, M. Nair, A. Sanchez and P. Nair, *Semicond. Sci. Technol.*, 2005, **20**, 496.
22 K. Wojciechowski, M. Schmidt, J. Tobola, M. Koza, A. Olech and R. Zybała, *J. Electron. Mater.*, 2010, **39**, 2053–2058.
23 S. N. Guin, D. S. Negi, R. Datta and K. Biswas, *J. Mater. Chem. A*, 2014, **2**, 4324–4331.
24 D. Li, X. Qin, T. Zou, J. Zhang, B. Ren, C. Song, Y. Liu, L. Wang, H. Xin and J. Li, *J. Alloys Compd.*, 2015, **635**, 87–91.
25 S. N. Guin and K. Biswas, *J. Mater. Chem. C*, 2015, **3**, 10415–10421.
26 S. N. Guin, A. Chatterjee and K. Biswas, *RSC Adv.*, 2014, **4**, 11811–11815.
27 Z. Liu, J. Shuai, H. Geng, J. Mao, Y. Feng, X. Zhao, X. Meng, R. He, W. Cai and J. Sui, *ACS Appl. Mater. Interfaces*, 2015, **7**, 23047–23055.
28 S. Cai, Z. Liu, J. Sun, R. Li, W. Fei and J. Sui, *Dalton Trans.*, 2015, **44**, 1046–1051.
29 E. M. Levin, S. L. Bud'ko and K. Schmidt-Rohr, *Adv. Funct. Mater.*, 2012, **22**, 2766–2774.
30 B. A. Cook, M. J. Kramer, J. L. Harringa, M. K. Han, D. Y. Chung and M. G. Kanatzidis, *Adv. Funct. Mater.*, 2009, **19**, 1254–1259.
31 D. V. Talapin, J.-S. Lee, M. V. Kovalenko and E. V. Shevchenko, *Chem. Rev.*, 2009, **110**, 389–458.
32 M. V. Kovalenko, L. Manna, A. Cabot, Z. Hens, D. V. Talapin, C. R. Kagan, V. I. Klimov, A. L. Rogach, P. Reiss and D. J. Milliron, *ACS Nano*, 2015, **9**, 1012–1057.
33 M. Ibáñez, R. Zamani, S. Gorsse, J. Fan, S. Ortega, D. Cadavid, J. R. Morante, J. Arbiol and A. Cabot, *ACS Nano*, 2013, **7**, 2573–2586.
34 M. Ibáñez, D. Cadavid, U. Anselmi-Tamburini, R. Zamani, S. Gorsse, W. Li, A. M. López, J. R. Morante, J. Arbiol and A. Cabot, *J. Mater. Chem. A*, 2013, **1**, 1421–1426.
35 M. Ibáñez, R. J. Korkosz, Z. Luo, P. Riba, D. Cadavid, S. Ortega, A. Cabot and M. G. Kanatzidis, *J. Am. Chem. Soc.*, 2015, **137**, 4046–4049.
36 D. Cadavid, M. Ibáñez, A. Shavel, O. J. Durá, M. L. de la Torre and A. Cabot, *J. Mater. Chem. A*, 2013, **1**, 4864–4870.
37 M. A. Connell, P. J. Bowyer, P. A. Bone, A. L. Davis, A. G. Swanson, M. Nilsson and G. A. Morris, *J. Magn. Reson.*, 2009, **198**, 121–131.
38 D. Sinnaeve, *Concepts Magn. Reson., Part A*, 2012, **40**, 39–65.
39 B. Zhou, M. Li, Y. Wu, C. Yang, W. H. Zhang and C. Li, *Chem. – Eur. J.*, 2015, **21**, 11143–11151.
40 J. Owen, *Science*, 2015, **347**, 615–616.
41 Z. Hens and J. C. Martins, *Chem. Mater.*, 2013, **25**, 1211–1221.
42 X. Li, D. Li, H. Xin, J. Zhang, C. Song and X. Qin, *J. Alloys Compd.*, 2013, **561**, 105–108.
43 Y. Zhang, L. Xi, Y. Wang, J. Zhang, P. Zhang and W. Zhang, *Comput. Mater. Sci.*, 2015, **108**, 239–249.
44 L.-H. Ye, K. Hoang, A. Freeman, S. Mahanti, J. He, T. M. Tritt and M. Kanatzidis, *Phys. Rev. B: Condens. Matter Mater. Phys.*, 2008, **77**, 245203.
45 B. Du, H. Li and X. Tang, *J. Alloys Compd.*, 2011, **509**, 2039–2043.
46 V. Jovovic and J. Heremans, *Phys. Rev. B: Condens. Matter Mater. Phys.*, 2008, **77**, 245204.
47 R. Mohanraman, R. Sankar, F.-C. Chou, C.-H. Lee, Y. Iizuka, I. P. Muthuselvam and Y.-Y. Chen, *APL Mater.*, 2014, **2**, 096114.

Journal of
Materials Chemistry A

PAPER

View Article Online
View Journal | View Issue

Cite this: *J. Mater. Chem. A*, 2017, **5**, 2592

Solution-based synthesis and processing of Sn- and Bi-doped Cu_3SbSe_4 nanocrystals, nanomaterials and ring-shaped thermoelectric generators†

Yu Liu,[a] Gregorio García,[bc] Silvia Ortega,[ad] Doris Cadavid,*[a] Pablo Palacios,[be] Jinyu Lu,[c] Maria Ibáñez,[fg] Lili Xi,[h] Jonathan De Roo,[ij] Antonio M. López,[k] Sara Martí-Sánchez,[l] Ignasi Cabezas,[dk] María de la Mata,[l] Zhishan Luo,[a] Chaochao Dun,[m] Oleksandr Dobrozhan,[a] David L. Carroll,[m] Wenqing Zhang,[h] José Martins,[j] Maksym V. Kovalenko,[fg] Jordi Arbiol,[ln] German Noriega,[d] Jiming Song,*[o] Perla Wahnón*[bc] and Andreu Cabot*[an]

Copper-based chalcogenides that comprise abundant, low-cost, and environmental friendly elements are excellent materials for a number of energy conversion applications, including photovoltaics, photocatalysis, and thermoelectrics (TE). In such applications, the use of solution-processed nanocrystals (NCs) to produce thin films or bulk nanomaterials has associated several potential advantages, such as high material yield and throughput, and composition control with unmatched spatial resolution and cost. Here we report on the production of Cu_3SbSe_4 (CASe) NCs with tuned amounts of Sn and Bi dopants. After proper ligand removal, as monitored by nuclear magnetic resonance and infrared spectroscopy, these NCs were used to produce dense CASe bulk nanomaterials for solid state TE energy conversion. By adjusting the amount of extrinsic dopants, dimensionless TE figures of merit (*ZT*) up to 1.26 at 673 K were reached. Such high *ZT* values are related to an optimized carrier concentration by Sn doping, a minimized lattice thermal conductivity due to efficient phonon scattering at point defects and grain boundaries, and to an increase of the Seebeck coefficient obtained by a modification of the electronic band structure with Bi doping. Nanomaterials were further employed to fabricate ring-shaped TE generators to be coupled to hot pipes, which provided 20 mV and 1 mW per TE element when exposed to a 160 °C temperature gradient. The simple design and good thermal contact associated with the ring geometry and the potential low cost of the material solution processing may allow the fabrication of TE generators with short payback times.

Received 29th September 2016
Accepted 19th December 2016

DOI: 10.1039/c6ta08467b

www.rsc.org/MaterialsA

1. Introduction

Tetrahedrally coordinated copper-based chalcogenides have emerged as realistic alternative materials for a number of energy conversion applications, including photovoltaics, photocatalysis and thermoelectricity.[1–7] Beyond the best studied ternary and quaternary Cu–Ga–In,[8–10] Cu–Zn–Sn,[11–15] and Cu–Zn–Ge[16,17] compounds, some I–V–VI tetrahedrally

---

[a] Catalonia Institute for Energy Research – IREC, 08930 Sant Adrià de Besòs, Barcelona, Spain. E-mail: dcadavid@irec.cat; acabot@irec.cat
[b] Instituto de Energía Solar, ETSI Telecomunicación, Universidad Politécnica de Madrid, 28040, Madrid, Spain. E-mail: perla@etsit.upm.es
[c] Departamento de Tecnología Fotónica y Bioingeniería, ETSI Telecomunicación, Ciudad Universitaria, s/n, 28040 Madrid, Spain
[d] Cidete Ingenieros S.L., Anselm Clavé 98, 08800 Vilanova i la Geltrú, Spain
[e] Departamento de Física aplicada a las Ingenierías Aeronáutica y Naval., ETSI Aeronáutica y del Espacio, Pz. Cardenal Cisneros, 3, 28040 Madrid, Spain
[f] Institute of Inorganic Chemistry, Department of Chemistry and Applied Biosciences, ETH Zürich, CH-8093, Switzerland
[g] Empa-Swiss Federal Laboratories for Materials Science and Technology, Dübendorf, CH-8600, Switzerland
[h] Materials Genome Institute, Shanghai University, Shanghai 200444, China
[i] Department of Inorganic and Physical Chemistry, Ghent University, B-9000 Ghent, Belgium
[j] Department of Organic and Marcromolecular Chemistry, Ghent University, B-9000 Ghent, Belgium
[k] Departament d'Enginyeria Electrònica, Universitat Politècnica de Catalunya, EPSEVG, 08800 Vilanova i la Geltrú, Barcelona, Spain
[l] Catalan Institute of Nanoscience and Nanotechnology (ICN2), CSIC and The Barcelona Institute of Science and Technology (BIST), Campus UAB, Bellaterra, 08193 Barcelona, Spain
[m] Center for Nanotechnology and Molecular Materials Wake Forest University, 501 Deacon Blvd., Winston Salem, NC 27109, USA
[n] ICREA, Pg. Lluis Companys 23, 08010 Barcelona, Spain
[o] School of Chemistry & Chemical Engineering, Anhui University, Hefei, Anhui, 230601, P. R. China. E-mail: jiming@ahu.edu.cn

† Electronic supplementary information (ESI) available: Additional experimental details and TEM, XRD, EDX and NMR data. See DOI: 10.1039/c6ta08467b

coordinated semiconductors also offer excellent functional properties, but remain largely underexplored. In particular, Cu_3SbSe_4 (CASe) is a semiconductor with a relatively small direct band gap of 0.3 eV and a defect-related carrier density on the order of 10^{18} cm^{-3} at ambient temperature.[18] It crystallizes in a zinc blende-type tetragonal superstructure that can be viewed as a three-dimensional Cu–Se framework of distorted [$CuSe_4$] tetrahedra with inserted one dimensional array of [$SbSe_4$] tetrahedra. It features two Cu sites with different Cu–Se bond lengths. The valence band maximum (VBM) is mainly formed by a hybridization of Cu-3d and Se-4p states, while the conduction band minimum (CBM) has a strong contribution from the Sb-5s and Se-4p hybridization. In such a structure, the Cu–Se framework provides avenues for hole transport with relatively high mobility, up to 135 cm^2 V^{-1} s^{-1} for undoped and 49 cm^2 V^{-1} s^{-1} for highly doped materials.[19–21] Furthermore, such a complex lattice structure is not effective for phonon propagation, resulting in low thermal conductivities. The high hole mobility and the low phonon mean free path combined with a suitable electronic band structure (including a large degeneracy at the VBM)[19,20] render CASe an excellent thermoelectric (TE) material. However, to maximize its TE performance, it is strictly necessary to optimize its charge carrier concentration either by adjusting the density of intrinsic defects that control hole concentration or by introducing an extrinsic p-type dopant, preferably in the non-conducting sub-lattice, *i.e.* by substituting Sb, to minimize the adverse effects on the hole mobility.

Nanoparticle-based bottom-up strategies offer several advantages to produce thin films and bulk nanostructured materials for a wide range of applications. From an engineering viewpoint, the unmatched compositional and interfacial control makes this route very robust and versatile, allowing the establishment of structure–property relationships and subsequently enabling the rational design of superior materials. From a commercial viewpoint, facile and inexpensive solution synthesis and processing allow for a low-cost and high throughput production with high material yields.[22–27] However, two major challenges in this technology are the incorporation of controlled amounts of electronic dopants and the removal of organics. Both of them are critical to optimize transport properties within such nanomaterials.[26]

Thus far, colloidal Cu_3SbS_4 [28–30] and $Cu_{12}Sb_4S_{13}$ [29–31] nanocrystals (NCs) have been primarily used for photoelectrochemical studies. Few reports have also detailed the production of bulk nanostructured CASe.[32–34] However, bottom-up strategies to cost-effectively produce efficient CASe NCs, nanomaterials and CASe-based devices remain to be demonstrated. Here, we report a solution-based scalable synthesis approach to produce several grams of monodisperse CASe NCs doped with controlled amounts of Sn and Bi. We demonstrate their bottom-up processing into bulk nanostructured materials with high relative density and excellent TE performances. We further use this material to fabricate ring-shaped TE devices, which provide improved thermal contact for heat recovery from pipes.

2. Experimental section

2.1. Chemicals and solvents

Copper(I) chloride (CuCl, ≥99%), antimony(III) chloride ($SbCl_3$, 99%), bismuth(III) acetate ($Bi(CH_3CO_2)_3$, 99.99%), selenium powder (Se, 99.5%), ammonium thiocyanate (NH_4SCN, ≥99%), dodecanethiol (DDT, 98%), 1-octadecene (ODE, technical grade 90%), oleic acid (OA, technical grade 99%), decanoic acid (DAc, ≥98%), and oleylamine (OLA, technical grade 70%) were purchased from Sigma Aldrich. Tin(II) chloride ($SnCl_2$, 98%) was purchased from Strem. Analytical grade methanol, ethanol and chloroform were obtained from various sources. All chemicals were used as received without further purification.

2.2. Se precursor solution

Se powder (23.69 g, 300 mmol) was dissolved in 300 ml OLA and 300 ml DDT at room temperature, cycled between vacuum and Ar to remove oxygen, and then stirred under an Ar atmosphere until Se powder was completely dissolved.

2.3. Synthesis of Cu_3SbSe_4 NCs

In a typical synthesis, 10.0 mmol CuCl, 4.0 mmol $SbCl_3$, 15 ml OLA, 10 ml OA and 100 ml ODE were mixed in a 500 ml three-neck flask and stirred for 20 min at room temperature. The solution was kept at 130 °C under vacuum and vigorous stirring for 30 min, and then heated to 180 °C. The colour of the solution changed from light green to yellowish-brown at ~170 °C. At 180 °C, 50 ml of the Se precursor solution was swiftly injected and the color of the solution changed immediately from brown to dark green, indicating the nucleation and subsequent growth of CASe NCs. After injection, the temperature of the reaction mixture dropped to around 165 °C, but it was allowed to recover to 180 °C. The overall reaction time after recovering to 180 °C was 30 min. Then the sample was rapidly cooled to room temperature using a water bath. NCs were collected by precipitation with ethanol. The final product could be dispersed in relatively non-polar solvents such as toluene or chloroform, forming a stable, dark-green dispersion (inset of Fig. S1b†). For subsequent chemical, structural and functional characterization, NCs were purified by multiple precipitation (6000 rpm for 5 min) and redispersion steps using chloroform as a solvent and ethanol as a non-solvent. The resulting powder was re-suspended in chloroform and stored for subsequent characterization and use. This synthesis protocol was optimized to produce more than 2.0 g of NCs per batch (Fig. S1a†), which was the amount required for a complete characterization of the material at the laboratory scale, including the fabrication of a ring-shaped prototype device.

2.4. Synthesis of $Cu_3Sb_{1-x}Sn_xSe_4$, $Cu_3Sb_{1-x}Bi_xSe_4$ and $Cu_3Sb_{1-x-y}Sn_xBi_ySe_4$ NCs

$Cu_3Sb_{1-x}Sn_xSe_4$, $Cu_3Sb_{1-x}Bi_xSe_4$ and $Cu_3Sb_{1-x-y}Sn_xBi_ySe_4$ NCs were produced following the above procedure, but replacing the desired amount of $SbCl_3$ by $SnCl_2$ and/or $Bi(CH_3CO_2)_3$.

2.5. Ligand displacement

Cu_3SbSe_4, $Cu_3Sb_{1-x}Sn_xSe_4$, $Cu_3Sb_{1-x}Bi_xSe_4$ and $Cu_3Sb_{1-x-y}Sn_xBi_ySe_4$ NCs produced in one batch were divided into 6 centrifuge tubes. In each of the tubes, containing ~350 mg in 10 ml of chloroform, 2 ml of a 50 mM NH_4SCN solution in acetone was added. Then the solution was shacked during 1–2 min to displace the organic ligands attached to the NC surface, followed by precipitation of the NCs by centrifugation. This process was repeated several times, adding chloroform and NH_4SCN in each step. Finally, NCs were precipitated and dried under vacuum to obtain a fine powder.

2.6. Bulk nanomaterial consolidation

The dried NCs were loaded into a graphite die and compacted into pellets (Ø 10 mm × ~1.5 mm). The process was carried out in an Ar atmosphere, using a custom-made hot press to simultaneously apply a pressure of 70 MPa and a temperature of 370–380 °C for 30 min. In this system, the heat was provided by an induction coil operated at 30–80 kHz and it was applied directly to a graphite die acting as a susceptor. Fast heating ramps of 20 °C s^{-1} were reached by this method with a 25 kW induction heater. The relative densities of all the pressed pellets were measured by the Archimedes' method and found to be ~90% of the theoretical values.

2.7. Ring thermoelectric generators

TE rings with an overall internal diameter of 28 mm and an external diameter of 39 mm were fabricated by placing the dried NCs between two concentric copper rings with 2 mm in thickness and hot-pressing the material at a temperature of 370–380 °C for 30 min and 20 MPa of pressure using a custom-made die.

2.8. Structural and chemical characterization

Crystallographic phases were characterized by X-ray diffraction (XRD, 2θ angle: 20° to 80°; scanning rate: 1° min^{-1}) on a Bruker AXS D8 ADVANCE X-ray diffractometer with Cu-Kα radiation ($\lambda = 0.15406$ Å). X-ray photoelectron spectroscopy (XPS) was performed on a VG ESCA scientific theta probe spectrometer in constant analyser energy mode with a pass energy of 28 eV and Al Kα (1486.6 eV) radiation as the excitation source. The size and shape of initial NCs were examined by transmission electron microscopy (TEM) using a ZEISS LIBRA 120, operating at 120 kV. In depth TEM analyses were performed in a FEI Tecnai F20 microscope operated at 200 keV with a point to point resolution of 0.19 nm. High-resolution TEM (HRTEM) analyses were combined with high angle annular dark field (HAADF) scanning TEM (STEM). We also examined elemental composition using spectroscopy analyses with nanometer resolution by means of electron energy loss spectroscopy (EELS) and energy dispersive X-ray spectroscopy (EDX) with a Gatan Quantum EELS and an Oxford EDX detector, respectively, both coupled to the FEI TEM. The grain size and morphology of the hot-pressed materials were characterized using field-emission scanning electron microscopy (SEM, Auriga Zeiss) at 5.0 kV. The overall material composition was analyzed by using an Oxford energy dispersive X-ray spectrometer (EDX) attached to the Zeiss Auriga SEM and by optical emission spectroscopy by means of inductively coupled plasma (ICP) on a Perkin Elmer Optima 3200 RL system. Fourier-transform infrared spectra (FTIR) were acquired by using an Alpha Bruker FTIR spectrometer with the platinum attenuated total reflectance (ATR) single reflection module.

2.9. Nuclear magnetic resonance (NMR)

NMR measurements were recorded on a Bruker Avance III Spectrometer operating at a ^1H frequency of 500.13 MHz and equipped with a BBI-Z probe. The sample temperature was set to 298.2 K. One dimensional (1D) ^1H and 2D NOESY (Nuclear Overhauser Effect Spectroscopy) spectra were acquired using standard pulse sequences from the Bruker library; zg and noesygpphpp respectively. For the quantitative 1D ^1H measurements, 64k data points were sampled with the spectral width set to 16 ppm and a relaxation delay of 30 s. The NOESY mixing time was set to 300 ms, with 2048 data points sampled in the direct dimension for 512 data points in the indirect dimension, with the spectral width set to 11.5 ppm. For 2D processing, the spectra were zero filled to a 4096 × 2048 real data matrix, followed by multiplication with a squared cosine bell function in both dimensions prior to Fourier transformation. The 1D spectra were apodized with an exponential window function. Concentrations were obtained using the Digital ERETIC method. Diffusion measurements (2D DOSY) were performed using a double stimulated echo sequence (dstegp2s)[35] for convection compensation and with monopolar gradient pulses.[35] Smoothed rectangle gradient pulse shapes were used throughout. The gradient strength was varied linearly from 2–95% of the probe's maximum value (calibrated at 50.2 G cm^{-1}) in 64 steps, with the gradient pulse duration and diffusion delay optimized to ensure a final attenuation of the signal in the final increment of less than 10% relative to the first increment. The diffusion coefficients were obtained by fitting the Stejskal–Tanner (ST) equation to the signal intensity decay. For the pulse sequence at hand, the appropriate ST equation is:[36]

$$I = I_0 e^{-(\gamma \delta g \xi)^2 D(\varDelta - 0.6\delta)} \tag{1}$$

with the gyromagnetic ratio of the observed ^1H nucleus γ, the gradient pulse length δ, the gradient strength g, the diffusion time $\varDelta$ and the diffusion coefficient D. The shape factor ξ depends on the gradient shape but this is usually already corrected for in the gradient strength value by the Bruker software, TOPSPIN. The ST equation for other pulse programs is only slightly different and the impact on the diffusion coefficient is very small in the case of long diffusion times ($\varDelta$ > 250 ms). In a real DOSY experiment, values of $\varDelta$ and δ are set while varying g to derive the decay curve.[36]

2.10. Thermoelectric property measurements

Seebeck coefficients were measured using a static DC method. Electrical resistivity data were obtained by a standard four-probe method. Both the Seebeck coefficient and the electrical resistivity were measured simultaneously in a LSR-3 LINSEIS system in the temperature range between room temperature and 673 K, under a helium atmosphere. At each temperature, 3 measurements were generally taken. Taking into account the system accuracy and the measurement precision, we estimate an error of *ca.* 4% in the measurement of the electrical conductivity and Seebeck coefficient. The thermal conductivity was calculated by $\kappa = \lambda C_p \rho$, where λ is the thermal diffusivity, C_p is the heat capacity, and ρ is the mass density of the specimen. A XFA 600 Xenon Flash apparatus from Linseis was used to determine the thermal diffusivities of the samples with an estimated error of 5%. The specific heat (C_p) was measured by means of the differential scanning calorimeter method (DSC model T2000 TA Instruments) with an associated error of *ca.* 2%. The density (ρ) values used here were calculated using the Archimedes' method with a measurement error of *ca.* 2%.

2.11. Hall measurement

Hall carrier concentrations and mobilities at room temperature were measured using a magnetic field of 2 T with a PPMS-9T (Quantum Design Inc., USA). Values reported correspond to the average of 5 consecutive measurements, from which an error of *ca.* 10% was estimated.

2.12. Device test

TE rings were tested in a custom-made test station. Temperature was monitored by two thermocouples attached at the copper electrodes and the open circuit voltage was measured by using a Keithley 2400. A heating cartridge within a cylindrical metal block was used to increase the temperature of the internal part of the ring, while the external part of the ring was kept at lower temperature by means of TE coolers. The maximum temperature reached at the hot side was 250 °C. At this point, the temperature at the cold side was 90 °C, which provided a maximum temperature gradient of 160 °C.

2.13. Density functional theory (DFT)

It is well known that common DFT methods fail to correctly predict the bandgap.[37,38] Unfortunately, accurate methods such as screened hybrid functional or quasi particle energy calculations are extremely time-consuming and computationally expensive.[37] D. Do *et al.* carried out electronic structure calculations for Cu_3SbSe_4 using GGA, GGA+U, m-BJ exchange potential and HSE06 exchange–correlation potential.[39–41] Only bandgap values calculated by using HSE06 and GGA+U were in agreement with experimental values (0.1–0.4 eV),[42,43] and a large effective value of U ($U_{\text{eff}} = 15$ eV) was necessary to get an accurate bandgap. Based on these results and to minimize computational cost, total energy calculations were carried out using the GGA+U approach. The PBE exchange correlation functional[44] along with the formalism proposed by Dudarev *et al.* was applied.[45] We use $U_{\text{eff}} = 15$ eV for the Cu-3d states. Total energy calculations were carried out with the plane-wave based Vienna *ab initio* simulation package (VASP),[46,47] along with projector augmented wave (PAW) potentials to represent the inert core electrons.[48,49] We used a plane-wave energy cutoff of 400 eV, an energy convergence criterion of 10^{-4} eV, and a Methfessel–Paxton first-order scheme with 0.1 eV of smearing to extract the occupations of Kohn–Sham eigenvalues.[50] For the Brillouin zone integration, we used a 12 × 12 × 12 Monkhorst–Pack scheme *k*-point mesh.[51] All the calculations were performed with the experimental lattice parameters of the native compound. The model system Cu_3SbSe_4 was studied through a tetragonal unit cell with 64 atoms ($Cu_{24}Sb_8Se_{32}$). Structures derived from Cu_3SbSe_4 due to the substitution with Bi or Sn were obtained by replacing one Sb atom by one Bi or Sn atom. In this way, the doping concentration was equal to $x = 0.125$, which is similar to the largest values experimentally produced and measured ($x = 0.10$). The transport properties were calculated using a semi-classical solution based on Boltzmann's transport theory within the constant scattering time and the rigid band approximations using the BoltzTraP code.[52]

3. Results and discussion

CASe NCs were produced from copper chloride, antimony chloride and selenium powder dissolved in OLA and DDT, as detailed in the experimental part. This synthesis protocol enabled a high batch-to-batch reproducibility and a 94% material yield. Fig. 1 and S2† show representative TEM and HRTEM micrographs with the respective indexed power spectrum of the 18 ± 2 nm CASe NCs produced following this procedure. From HRTEM analysis, the NC crystallographic phase was identified as tetragonal CASe (space group $I\bar{4}2m$ (121), Table S1†) with lattice constants $a = b = 0.566$ nm and $c = 1.128$ nm, which is in agreement with XRD data (Fig. 2a, JCPDS card no. 85-0003). No secondary phases were detected by HRTEM and XRD analysis, except for a minor peak at $2\theta \sim 34°$ in the XRD pattern, which could correspond to Cu_3SbSe_3 (JCPDS card no. 1-86-1751, Fig. S3†).

Within its experimental error, SEM-EDX analysis showed the metal and chalcogen ratios to match those of stoichiometric CASe (Cu_3SbSe_4, Fig. S4†). EELS was used for compositional

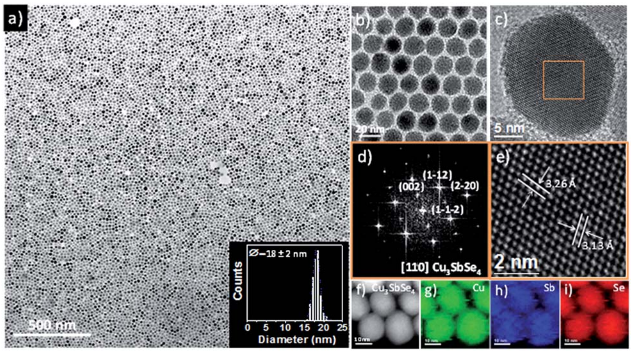

Fig. 1 (a) Representative TEM micrograph of CASe NCs. The inset shows the histogram for the measured particle size distribution (18 ± 2 nm). (b) Higher-magnification TEM micrograph; (c) HRTEM image of a single CASe NC. (d) Its respective power spectrum fitting with the CASe tetragonal phase. (e) Detail of the squared regions of the single CASe NCs. (f) Annular dark field scanning TEM (ADF-STEM) image of some CASe NCs and (g)–(i) areal density of each of the elements extracted from the EELS spectrum image.

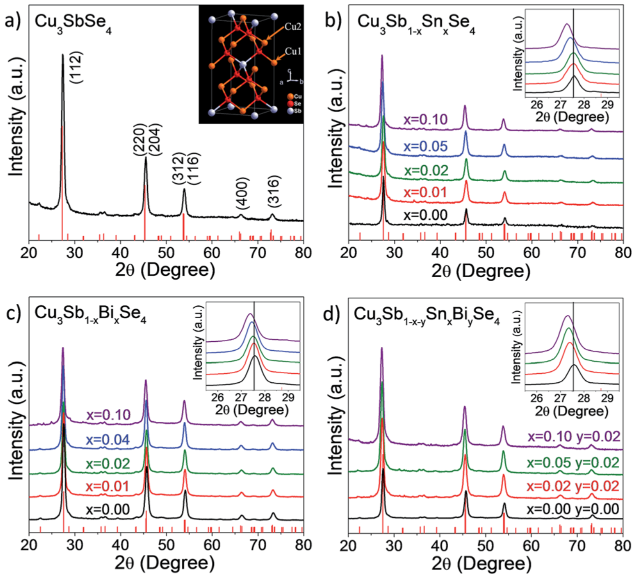

Fig. 2 (a) XRD pattern of CASe NCs including the JCPDS 85-0003 reference. The inset shows a unit cell of tetragonal CASe. (b) XRD patterns of $Cu_3Sb_{1-x}Sn_xSe_4$ ($x = 0.00, 0.01, 0.02, 0.05, 0.10$) NCs. (c) XRD patterns of $Cu_3Sb_{1-x}Bi_xSe_4$ ($x = 0.00, 0.01, 0.02, 0.04, 0.10$) NCs. (d) XRD patterns of $Cu_3Sb_{1-x-y}Sn_xBi_ySe_4$ ($x = 0.02, 0.05, 0.10$ and $y = 0.02$) NCs. The insets in graphs (b) and (c) show a detail of the (112) peak, at around $2\theta = 27.5°$.

analysis within each particle using Sb $M_{4,5}$, Cu $L_{2,3}$ and Se $L_{2,3}$ edges (Fig. 1f–i and S5†). In the central region of the NC, elemental quantification (in at%) showed the presence of around 12% Sb, 30% Cu and 48% Se, which is compatible with the CASe stoichiometry. In the outer part of the NCs, the relative composition of Sb and Cu were found to be slightly higher than that in the core and that of Se was slightly lower: 17% Sb, 40% Cu and 43% Se (Fig. S5†).

$Cu_3Sb_{1-x}Sn_xSe_4$ (Fig. S8†), $Cu_3Sb_{1-x}Bi_xSe_4$ (Fig. S9†) and $Cu_3Sb_{1-x-y}Sn_xBi_ySe_4$ (Fig. S10†) NCs showed quasi-spherical morphologies with an average size of around 18 nm. Increasingly broader size and shape distributions were obtained as the amount of doping was augmented (Fig. S8 and S9†). Doped CASe NCs were characterized by larger *a* and *c* lattice parameters, as evidenced by a slight peak shift toward lower angles in the XRD patterns (Fig. 2b–d). The lattice expansion is attributed to the substitution of Sb^{5+} (0.6 Å) by larger Sn^{4+} (0.69 Å) or Bi^{3+}/Bi^{5+} (≥0.76 Å) cations.[53,54] TEM-EDX analysis evidenced the presence of Sn and Bi in all Sn- and Bi-doped NCs, respectively. However, Sn and Bi signals were too weak to quantify (Fig. S11†). The overall NC composition was studied by ICP (Tables S2 and S3†). The composition of the consolidated materials used for TE characterization (see below) was also analysed by SEM-EDX (Tables S4–S6†). Within their experimental errors, both ICP and SEM-EDX results matched the nominal Bi and Sn concentrations.

CASe NCs were synthesized in the presence of OLA, OA and DDT. In order to identify which surfactants were finally present on the NC surface and establish their bonding nature, NMR analysis was performed. Fig. 3a shows a ^1H NMR spectrum of the as-synthesized NCs (unpurified) and the ^1H NMR spectrum of NCs purified four times by precipitation/redispersion with acetonitrile as a non-solvent and toluene as a solvent. In the spectrum of unpurified NCs we observe the characteristic resonances of a terminal alkene at 5.0 and 5.8 ppm, associated with ODE. The resonance around 5.5 ppm is associated with an internal alkene, from OLA and/or OA. The ODE resonances possess a fine structure, indicating the unbound nature of ODE. In contrast, the alkene resonance is a superposition of sharp and broad resonances, associated with free and bound ligands respectively.[55] After purification, the ODE features disappear completely together with the majority of the sharp resonance corresponding to the free molecules OLA or OA, indicating a successful purification of the NC solution. Further purification to remove the remaining free ligands in solution render the NCs completely insoluble in any solvent. The NOESY spectrum (Fig. S13†) contains negative (black) NOE cross peaks confirming the interaction of OLA/OA with the surface.[55] To discriminate whether OLA or OA (or both) is stabilizing the NC surface, we reproduced the exact same synthesis described above but instead of OA we used DAc. Although DAc and OA are both fatty acids and are expected to interact identically with NC surfaces, DAc has no alkene group and this allows us to distinguish OLA from OA. Fig. 3b shows the NMR spectra of CASe NPs synthesized with DAc. Since the ^1H NMR spectra are almost identical to spectra of the dispersions prepared with OA and because OLA is now the only molecule with an alkene resonance, we identify OLA as a ligand. Additionally, the intensity of the alkene resonance and CH_3 resonance features a 2 : 3 ratio. This excludes any other (fully saturated) ligands such as DDT or DAc, proving that OLA is the only ligand present. Since OLA is an L-type ligand and the NCs were found to be stoichiometric (*vide supra*), this NC system belongs to the earlier established class of binding motifs; NC (L).[56] To assess the dynamics of interaction, DOSY experiments were performed. A good fitting of the CH_3 signal decay was only obtained with two exponentials, indicating two populations (Fig. S14†). The small fraction with a high diffusion coefficient (552 $\mu m^2\ s^{-1}$) is attributed to free OLA while the fraction with a low diffusion coefficient (45 $\mu m^2\ s^{-1}$) is associated with bound OLA. Using the Stokes–Einstein equation, a solvodynamic diameter of 16.5 nm is calculated from the diffusion coefficient. Since this is close to the diameter from TEM (16–20 nm), we conclude that OLA is firmly attached to the NC surface and diffuses together with the NC. Considering the L-type nature of OLA,[56] it is usually involved in a more dynamic stabilization of the NC surface.[57] However, it was repeatedly reported that Cu-based NCs typically have tightly bound amines bound to the surface.[13,58] It should however be noted that OLA is quite easily desorbed during purification suggesting only a moderate binding affinity for the NC surface, in line with L-type ligand behaviour.

To facilitate charge transport/transfer, CASe NCs were thoroughly purified by multiple precipitation/re-dispersion steps and subsequently treated with NH_4SCN, which could efficiently displace remaining OLA. Fig. S15† shows FTIR spectra of dried

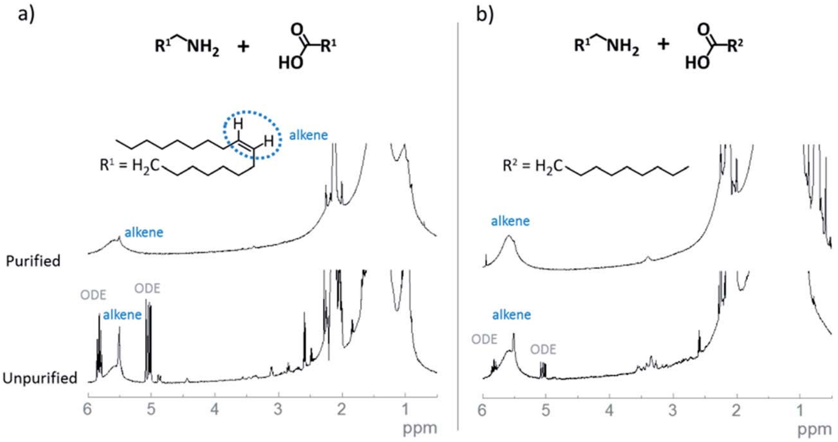

Fig. 3 ^{1}H NMR spectrum of CASe 18 ± 2 nm NPs synthesized with (a) OA and (b) DAc shown before (bottom) and after (top) purification.

CASe NCs before (CASe–OL) and after (CASe–LD) organic ligand displacement with a 50 mM NH_4SCN solution. The CASe–OL spectrum showed the characteristic features of OLA: C–H vibration modes have a strong band in the high-frequency region (2850–3000 cm^{-1}) and various peaks in the lower frequency region, between 700 cm^{-1} and 1650 cm^{-1}. These features completely disappeared from the CASe–LD spectrum, proving the effective organic ligand displacement.

Nanocrystalline disk-shaped CASe pellets (Ø 10 mm × ~1.5 mm) were prepared under an Ar atmosphere by hot-pressing ~700 mg of ligand-displaced NCs at ~380 °C, 70 MPa and for 30 min. The pellets had a metallic luster and were mechanically robust enough to endure polishing. Relative densities ~90% of the theoretical value were measured for all samples. XRD analysis of the CASe pellets showed no crystallographic or related compositional change after the hot-press process (Fig. S3 and S16†). However, during this process, CASe NCs coalesced to form larger crystalline domains with sizes ranging from tens to few hundred nanometers (Fig. S17†).

The electrical conductivity (σ), Seebeck coefficient (S), thermal conductivity (κ), and the dimensionless TE figure or merit ($ZT = \sigma S^2 T/\kappa$) of undoped and Sn- and Bi-doped CASe pellets are displayed in Fig. 4 and 5. Undoped CASe nanomaterials were characterized by relatively low σ, which increased with temperature up to 6.2×10^3 S m^{-1}, and positive S in the whole temperature range measured. Significantly higher σ, up to 9.0×10^4 S m^{-1} at room temperature, was obtained for Sn-CASe (Fig. 4a), which showed a degenerated semiconductor behavior with a decrease of σ with temperature. In contrast, S decreased with the Sn introduction (Fig. 4b). The observed increase of σ and decrease of S with the amount of Sn indicated Sn ions to act as a p-type dopant within CASe. This electronic role was confirmed by a one order of magnitude increase in the Hall charge carrier concentration with the Sn introduction, from $p = 5 \times 10^{18}$ cm^{-3} in CASe to $p = 9 \times 10^{19}$ cm^{-3} in $Cu_3Sb_{0.98}Sn_{0.02}Se_4$ (Table S7†). Overall, higher power factors ($PF = \sigma S^2$) were obtained for the Sn-doped samples, with a maximum PF of 1.14 mW m^{-1} K^{-2} at 673 K for the sample containing a 2% replacement of Sb by Sn, $Cu_3Sb_{0.98}Sn_{0.02}Se_4$ (Fig. S18a†).

Relatively low thermal conductivities, which as expected decreased with temperature, were obtained for all the analyzed materials. For undoped CASe, κ dropped from 1.60 W m^{-1} K^{-1} to 0.81 W m^{-1} K^{-1} (Fig. 4c) in the temperature range from 327 K

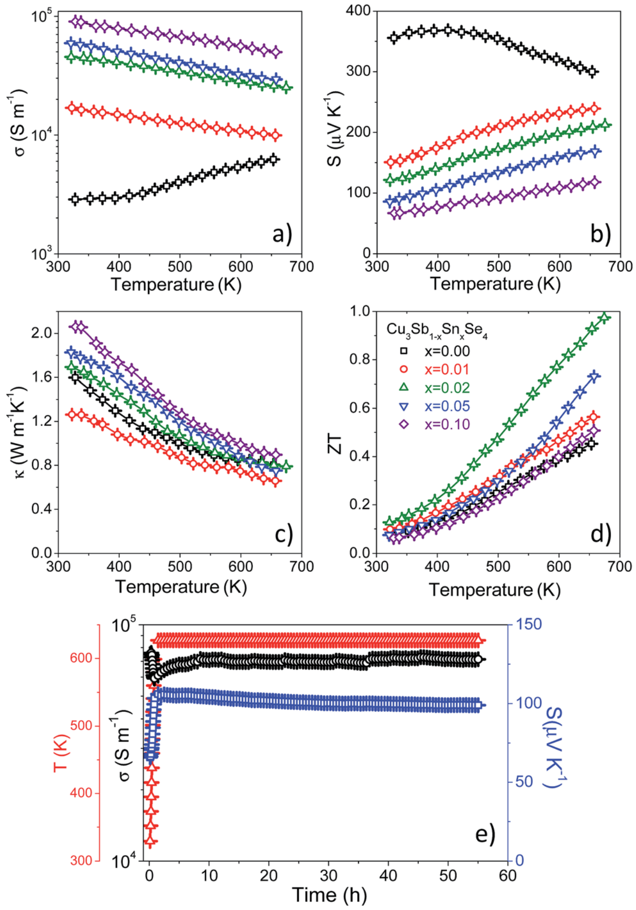

Fig. 4 (a–d) Temperature dependence of (a) electric conductivity (σ), (b) Seebeck coefficient (S), (c) thermal conductivity (κ), and (d) TE figure of merit (ZT) of $Cu_3Sb_{1-x}Sn_xSe_4$ ($x = 0.01$, 0.02, 0.05 and 0.10). (e) Time evolution of the electrical conductivity (σ, ○), Seebeck coefficient (S, □) and temperature (T, △) of $Cu_3Sb_{0.9}Sn_{0.1}Se_4$ during a 55 h test.

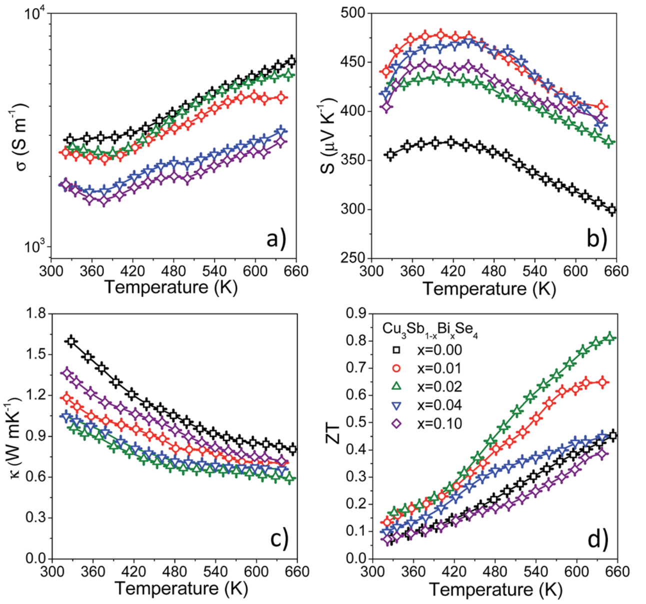

Fig. 5 Temperature dependence of (a) electric conductivity (σ), (b) Seebeck coefficient (S), (c) thermal conductivity (κ), and (d) TE figure of merit (ZT) of $Cu_3Sb_{1-x}Bi_xSe_4$.

to 653 K. These are lower κ values than those previously reported for bulk CASe,[19,20,53,59] but slightly higher than those reported for nanostructured CASe produced by co-precipitation,[32] and much higher than the estimated minimum κ of this material (0.26 W m^{-1} K^{-1}).[60,61] Lower lattice thermal conductivities (κ_L) were obtained with the incorporation of Sn due to the introduced lattice distortion and the increased density of point defects (Fig. S18d†). However, the associated increase of the electronic contribution to the thermal conductivity (κ_e) resulted in an overall increase of κ for most of the Sn-CASe pellets. Overall, ZT significantly increased with the introduction of relatively small amounts of Sn, reaching $ZT = 0.97$ at 673 K for $Cu_3Sb_{0.98}Sn_{0.02}Se_4$, which represents more than a 2-fold increase over undoped CASe (Fig. 4d).

Nanocrystalline CASe showed good stability even when maintained at relatively high temperatures for long periods of time. Fig. S21† shows the results obtained from 5 consecutive heating–cooling cycles. Minor differences were observed from cycle to cycle and mainly from the first cycle to the following ones. To account for the minor variations obtained from the first to the following cycles, all samples were measured at least 3 consecutive times and results from the first cycle were discarded. Fig. 4e shows the results obtained from $Cu_3Sb_{0.9}Sn_{0.1}Se_4$ during a 55 h test involving the heating of the sample from 323 to 626 K at a rate of 10 K min^{-1} and then maintaining the sample at 656 K for 54 h. During this time, the electrical conductivity and Seebeck coefficient changed by around 1% and 3%, respectively.

When replacing part of Sb by Bi, slightly lower σ was obtained (Fig. 5a), which correlated with a small decrease in the Hall hole concentrations ($p = 2 \times 10^{18}$ cm^{-3}, Table S7†). This was surprising experimental evidence if assuming Sb^{5+} to be replaced by Bi^{3+} as it have to be the case taking into account the very high energy required to oxidize Bi^{3+} to Bi^{5+}. As no increase of the hole concentration was observed, the difference in the oxidation state between Sb and Bi is probably compensated with the creation of an equivalent amount of Se^{2-} vacancies. The slight decrease in the measured charge carrier concentration could be further associated with an indirect diminution of the concentration of intrinsic defects acting as p-type dopants, *e.g.* the presence of Cu$^+$ at Sb^{5+} sites or Cu or Sb vacancies.

Significantly larger S values were measured for all Bi-CASe samples (Fig. 5b) when compared with CASe, which did not correlate well with the small decrease in electrical conductivity when just taking into account a slight modification of the charge carrier concentration (Table S7†).

Combining σ with S, the highest PF values for Bi-CASe were obtained with a composition $Cu_3Sb_{0.98}Bi_{0.02}Se_4$ (~0.77 mW m^{-1} K^{-2} at 608 K, Fig. S19a†). Additionally, Bi-doped CASe was characterized by lower κ than CASe due to slightly lower κ_e and κ_L contributions (Fig. 5c and S19d). Overall, higher ZT values, up to 0.81 for $Cu_3Sb_{0.98}Bi_{0.02}Se_4$ at 648 K, were obtained for Bi-CASe when compared with CASe (Fig. 5d).

To further determine the influence of Sn and Bi on the electronic band structure of CASe, DFT calculations were carried out. Fig. 6 shows the band structure of pure CASe, $Cu_3Sb_{0.875}Sn_{0.125}Se_4$ and $Cu_3Sb_{0.875}Bi_{0.125}Se_4$. Results indicate that pure CASe is a semiconductor with a direct band gap of 0.27 eV measured at Γ point, which is consistent with experimental values (0.1–0.4 eV).[38,42,62] The calculated bandgap was also in agreement with theoretical results from Do *et al.*[63] using the non-local exchange HS06 model (0.26 eV). As expected, the VBM in CASe is mainly composed of Cu-3d and Se-4p states and the CBM is mainly formed by Sb-5s and Se-4p states (Fig. 6a).

Fig. 7 shows the temperature dependence of the DFT-derived S for different concentrations of the majority charge carrier. For pure CASe, at moderate p levels ($p < 5 \times 10^{19}$ cm^{-3}) the Seebeck coefficient increases with temperature up to a maximum and then rapidly decreases. At higher hole concentrations ($p > 5 \times 10^{19}$ m^{-3}), S monotonously increases with temperature in the analysed range ($T \leq 700$ K). Calculated values matched relatively well with experimental results and qualitatively predicted the measured temperature evolution.

The introduction of small amounts of Sn at the Sb sites significantly reduced the band gap, to 0.16 eV, and shifted the Fermi level to within the valence band due to the p-type doping character of Sn^{4+} ions (Fig. 6b). Thus, only Seebeck coefficients for relatively high carrier concentrations $p \geq 5 \times 10^{19}$ cm^{-3} were reliably calculated. In agreement with experimental measurements, such large charge carrier concentrations resulted in an important diminution of S. A hole carrier concentration $p \approx 1 \times 10^{20}$ cm^{-3} was needed to match the experimental S values, which is consistent with the Hall charge carrier concentrations measured for the Sn-doped materials.

The partial substitution of Sb by Bi had little effect on the band structure at the VBM, but it significantly affected the CBM, decreasing the band gap and resulting in a divergence of the multi-valleys (Fig. 6c). Taking into account only the contribution of majority carriers, the DFT-derived S just slightly changed with the Bi introduction (Fig. 7) mainly due to the bandgap

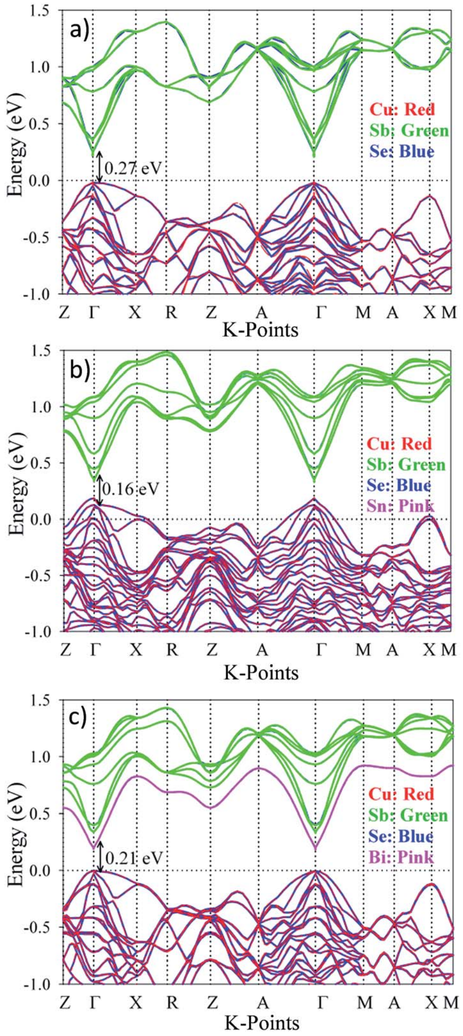

Fig. 6 Electronic band structure of (a) CASe, (b) $Cu_3Sb_{0.875}Sn_{0.125}Se_4$ and (c) $Cu_3Sb_{0.875}Bi_{0.125}Se_4$. The symbols stand for the main atomic contributions of the bands. Band energies were plotted with respect to the Fermi level.

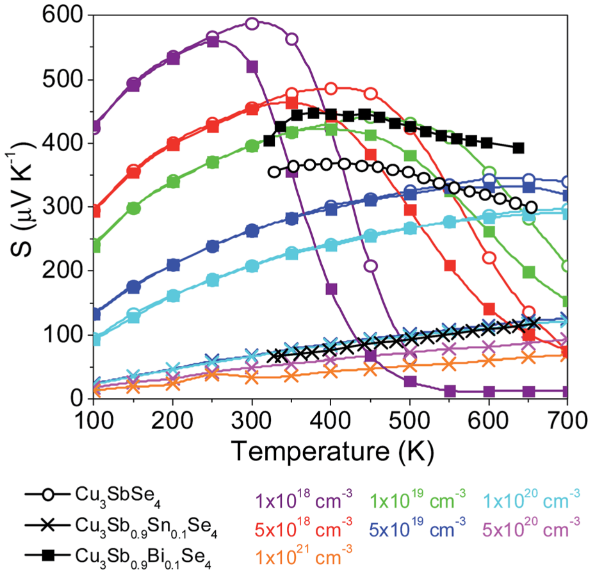

Fig. 7 Temperature dependence of DFT-calculated Seebeck coefficients (S) of pure CASe, $Cu_3Sb_{0.875}Bi_{0.125}Se_4$ and $Cu_3Sb_{0.875}Sn_{0.125}Se_4$ at different hole concentrations (colored lines and symbols). Experimental values for pure CASe, $Cu_3Sb_{0.9}Bi_{0.1}Se_4$ and $Cu_3Sb_{0.9}Sn_{0.1}Se_4$ are also plotted (in black).

reduction. However, the perturbation of the CBM associated with the Bi presence certainly had a strong influence on the contribution of the conduction electrons to the transport properties. In this regard, the splitting of the degenerated multivalleys at the CBM should translate in a reduction of a bipolar effect on S, thus resulting in overall higher S values. In this direction, our DFT analysis clearly showed a significant diminution of the effective mass of electrons with the introduction of Bi (Table S8, Fig. S22†). While the calculation of this effect is beyond the present work, we qualitatively analyzed the bipolar impact to S by calculating the contribution of thermally generated charge carriers (Fig. S23 and S24†).[64] Results obtained clearly showed that in spite of the lower bandgap of Bi-CASe, and thus the higher charge carrier concentrations associated with thermal generation, the reduced effective mass for electrons in this compound should translate in a lower contribution of the minority carriers to S and thus to an overall higher Seebeck coefficient. A bipolar contribution could also explain the differences in the temperature dependence of κ_L between Bi-CASe and pure CASe, but this point is to be confirmed.[65]

The introduction of Sn also translated into large differences in the effective masses of holes and electrons which in spite of the strong band gap decrease in this material also resulted in higher S values at moderate doping levels. However, the modification of the electronic band structure by means of sufficient amounts of Sn injected very large amounts of charge carrier, which inevitably resulted in overall lower S. Thus the introduction of both dopants, a small amount of Sn to control charge carrier concentration and Bi to modify the band structure, was necessary to optimize performance.

To take advantage of the carrier concentration control provided by Sn doping and the relative increase of S with the inclusion of Bi, we prepared a series of Sn,Bi-doped CASe samples. Fig. 8 shows the temperature dependence of the electrical and thermal transport properties of $Cu_3Sb_{0.98-x}Sn_x Bi_{0.02}Se_4$. These samples showed a degenerated electrical conductivity behavior, associated with a large level of doping. σ increased with the Sn content as in the Sn-CASe series. Surprisingly, σ of co-doped Sn,Bi-CASe was systematically larger than that of Sn-CASe samples with the same amount of Sn. Hall measurements showed the presence of high charge carrier concentrations, up to $p = 1 \times 10^{20}$ cm^{-3} for $Cu_3Sb_{0.88}Sn_{0.10}Bi_{0.02}Se_4$ (Table S7†). On the other hand, S decreased for all Sn,Bi-CASe samples when compared with plain CASe due to the large increase of charge carrier concentration. However, S values of co-doped materials slightly increased when compared with Sn-CASe with equivalent electrical conductivities, proving the positive effect of the Bi addition.

Overall, the PFs of co-doped Sn,Bi-CASe were significantly higher than those of Sn- or Bi-CASe, and reached up to around

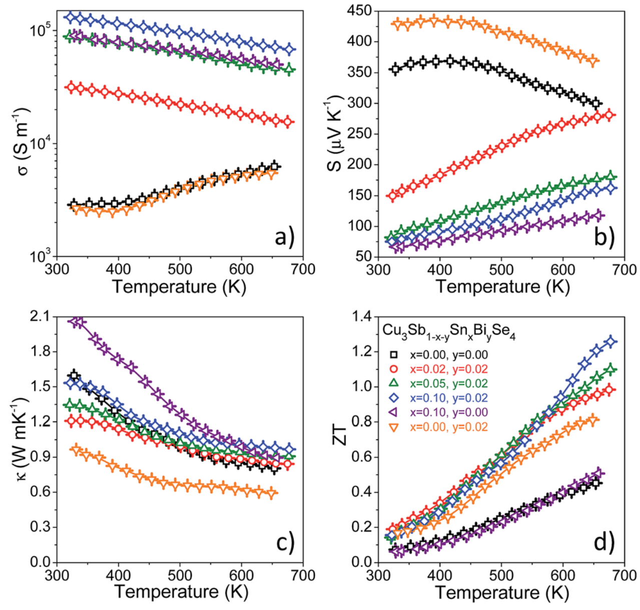

Fig. 8 Temperature dependence of (a) electric conductivity (σ), (b) Seebeck coefficient (*S*), (c) thermal conductivity (κ), and (d) TE figure of merit (*ZT*) of $Cu_3Sb_{0.98-x}Sn_xBi_{0.02}Se_4$.

1.81 mW m^{-1} K^{-2} at 654 K for $Cu_3Sb_{0.88}Sn_{0.10}Bi_{0.02}Se_4$ (Fig. S20a†). Like in the case of Sn-CASe, in Sn,Bi-CASe the dependence of κ with the dopant concentration showed a competition between the decrease of κ_L associated with the introduction of lattice defects and the increase of κ_e associated with the much higher carrier concentrations (Fig. 8c and S20d†). Overall, *ZT* values up to 1.26 at 673 K were obtained for $Cu_3Sb_{0.88}Sn_{0.10}Bi_{0.02}Se_4$, which is among the best *ZT* values obtained with a Pb- and Te-free material in this middle temperature range (Table S9†).

These materials were further employed to fabricate simple TE generator prototypes with ring geometry (Fig. 9). When compared with conventional flat devices, the ring design optimizes the thermal contact between the TE generator and the walls of a hot or cold pipe, and at the same time minimizes the module form factor and provides improved mechanical stability. In a ring-based module, rings with n and p type materials could be placed thermally in parallel and electrically in series to harvest radial heat fluxes (Fig. 9a). Alternatively, multiple n and p elements could be integrated within each ring (Fig. 9d). The module, containing multiple n- and p-type rings or several multi-element rings, makes use of thin thermal and electrical insulators between rings to alternatively contact the outer and inner rings as shown in Fig. 9a.

Single p-type $Cu_3Sb_{0.88}Sn_{0.10}Bi_{0.02}Se_4$ rings, with inner and outer diameter of 28 mm and 39 mm, respectively, and with copper ring thicknesses of 2 mm and thus a CASe thickness of 1.5 mm were assembled and tested in a custom made set-up as detailed in the experimental part (Fig. 9b). The inner ring temperature was increased up to 250 °C using a heat cartridge within a cylindrical metal block, while maintaining the outside ring at lower temperature using a metal block cooled using commercial thermoelectric devices. Fig. 9c shows the voltage obtained from a single p-type ring as a function of the temperature gradient. Open circuit voltages close to 20 mV were obtained for a single TE element exposed to a temperature gradient of 160 °C. Being the electrical resistance of the ring <0.4 Ω, this voltage translates into a >1 mW of generated electric power for each single TE element. The combination of several TE p–n pairs in each ring (Fig. 9d) and of several rings into a module (Fig. 9e) could provide electric powers on the order of 100 W for 200–300 °C temperature gradients as those available among other in exhaust gas pipes of vehicles with combustion engines. Such power could suffice to supply all the electric energy spent by the vehicle, allowing the alternator replacement and thus improving the vehicle fuel efficiency.

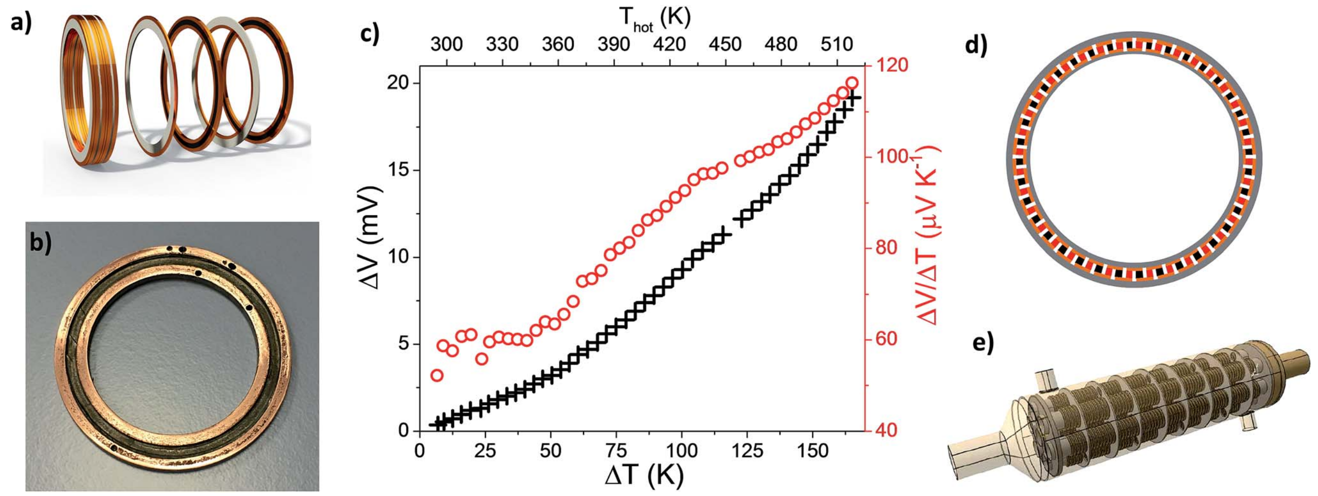

Fig. 9 (a) Scheme of a basic ring-based TE module, (b) $Cu_3Sb_{0.88}Sn_{0.10}Bi_{0.02}Se_4$-based ring, (c) voltage obtained from a single $Cu_3Sb_{0.88}Sn_{0.10}Bi_{0.02}Se_4$ ring as a function of the temperature gradient when increasing the temperature at the hot side (top axis). Red open circles display the effective Seebeck coefficient of the ring. (d) Scheme of a ring with multiple p and n type elements (in black and red). (e) Scheme of a multi-ring system to be coupled to a hot pipe including a jacket for the circulation of cooling fluid.

4. Conclusions

In summary, a novel solution-based strategy to produce monodisperse CASe NCs and Sn- and Bi-doped CASe NCs at the gram scale was presented. The effect of Sn- and Bi-doping on the TE performance of CASe nanomaterials obtained *via* hot press was discussed. Sn was demonstrated to be a p-type dopant which effectively helped to control charge carrier concentration. On the other hand, the introduction of Bi conveniently modified the electronic band structure of the compound resulting in higher S values. We tentatively associated the Bi effect to a reduction of the negative contribution of conduction electrons on the Seebeck coefficient, but further theoretical calculations and detailed experimental results are required to clarify the exact Bi role in such a complex system. Besides, the introduction of these impurities helped to reduce the material lattice thermal conductivity. By optimizing the amount of Sn in a Bi-doped material, ZT values up to 1.26 at 673 K were obtained for $Cu_3Sb_{0.88}Sn_{0.10}Bi_{0.02}Se_4$, which is among the best ZT values obtained with a Pb- and Te-free material in this middle temperature range, with the additional advantage of the high versatility and low cost associated with solution processing technologies. Taking advantage of this processability, we fabricated innovative ring-shaped TE generators, which provided 1 mW of electric power per TE element with a 160 °C temperature gradient.

Author contributions

The manuscript was prepared through the contribution of all authors. J. S., D. C. and A. C. conceived and guided the project, and supervised the work. Y. L. and D. C. designed the experiments, produced the nanomaterials, performed the thermoelectric characterization and wrote the manuscript. S. O. and G. N. designed, produced and tested the device. S. O., A. L. and I. C. designed and fabricated the device test station. M. I., J. R. and J. M. performed Hall and NMR measurements and analysed the results. S. M., M. M., and J. A. performed structural and morphological NCs characterization by means of HRTEM and EELS and discussed these results. L. X. and W. Z. performed and discussed preliminary DFT calculations. G. M., P. P., J. L. and P. W. performed and discussed detailed DFT calculations including related transport properties. C. D. and D. L. C. performed the C_p characterization. O. D. and Z. L. measured and discussed XPS data. The manuscript was corrected and improved by all authors.

Acknowledgements

This work was supported by the European Regional Development Funds, the Framework 7 program under project UNION (FP7-NMP-2012-310250), by the Spanish Ministerio de Economía y Competitividad through the projects BOOSTER (ENE2013-46624-C4-3-R) and e-TNT (MAT2014-59961-C2-2-R) and by the Comunidad de Madrid project MADRID-PV (S2013/MAE/2780). YL thanks the China Scholarship Council for scholarship support. MI and SO thank AGAUR for their Beatriu de Pinós postdoctoral grant (2013 BP-A00344) and PhD grant, respectively. JDR thanks the FWO (Research Foundation Flanders) for financial support. M. V. K. acknowledges partial financial support by the European Union (EU) *via* FP7 ERC Starting Grant 2012 (Project NANOSOLID, GA No. 306733). JM Song acknowledges financial support by the Natural Science Foundation of Anhui Province (Grant No. 1508085MB22) and major project of education department of Anhui Province (KJ2016SD63). The authors also acknowledge the funding from Generalitat de Catalunya 2014 SGR 1638. MI and JCM thank the FWO MULTIMAR scientific research network for financial support for a short research stay. The 500 MHz used in this work was funded by the Hercules foundation (AUGE009/06). SMS acknowledges funding from "Programa Internacional de Becas "la Caixa"-Severo Ochoa". ICN2 acknowledges support from the Severo Ochoa Program (MINECO, Grant SEV-2013-0295). Part of the present work has been performed in the framework of Universitat Autònoma de Barcelona Materials Science PhD program. The authors also acknowledge the computer resources, technical expertise and assistance provided by the Red Española de Supercomputación and the Centro de Supercomputación and Visualización de Madrid (CeSViMa).

Notes and references

1 M. Yuan, D. B. Mitzi, W. Liu, A. J. Kellock, S. J. Chey and V. R. Deline, *Chem. Mater.*, 2009, **22**, 285–287.
2 Y. Zhao and C. Burda, *Energy Environ. Sci.*, 2012, **5**, 5564–5576.
3 D. Aldakov, A. Lefrançois and P. Reiss, *J. Mater. Chem. C*, 2013, **1**, 3756–3776.
4 F.-J. Fan, L. Wu and S.-H. Yu, *Energy Environ. Sci.*, 2014, **7**, 190–208.
5 A. Singh, A. Singh, J. Ciston, K. Bustillo, D. Nordlund and D. J. Milliron, *J. Am. Chem. Soc.*, 2015, **137**, 6464–6467.
6 W. Van Der Stam, A. C. Berends and C. de Mello Donega, *ChemPhysChem*, 2016, **17**, 559–581.
7 M. Ibáñez, D. Cadavid, R. Zamani, N. García-Castelló, V. Izquierdo-Roca, W. Li, A. Fairbrother, J. D. Prades, A. Shavel, J. Arbiol, A. Pérez-Rodríguez, J. M. Morante and A. Cabot, *Chem. Mater.*, 2012, **24**, 562–570.
8 J. Shi, Z. Li, D. Zhang, Q. Liu, Z. Sun and S. Huang, *Prog. Photovoltaics*, 2011, **19**, 160–164.
9 X. Yu, X. An, A. Shavel, M. Ibáñez and A. Cabot, *J. Mater. Chem. A*, 2014, **2**, 12317–12322.
10 A. Chirilă, S. Buecheler, F. Pianezzi, P. Bloesch, C. Gretener, A. R. Uhl, C. Fella, L. Kranz, J. Perrenoud and S. Seyrling, *Nat. Mater.*, 2011, **10**, 857–861.
11 A. Shavel, D. Cadavid, M. Ibanez, A. Carrete and A. Cabot, *J. Am. Chem. Soc*, 2012, **134**, 1438–1441.
12 A. Carrete, A. Shavel, X. Fontané, J. Montserrat, J. Fan, M. Ibáñez, E. Saucedo, A. Pérez-Rodríguez and A. Cabot, *J. Am. Chem. Soc.*, 2013, **135**, 15982–15985.
13 A. Shavel, M. Ibáñez, Z. Luo, J. De Roo, A. Carrete, M. Dimitrievska, A. Genç, M. Meyns, A. Pérez-Rodríguez and M. V. Kovalenko, *Chem. Mater.*, 2016, **28**, 720–726.

14 X. Yu, A. Shavel, X. An, Z. Luo, M. Ibanez and A. Cabot, *J. Am. Chem. Soc.*, 2014, **136**, 9236–9239.

15 V. Lesnyak, C. George, A. Genovese, M. Prato, A. Casu, S. Ayyappan, A. Scarpellini and L. Manna, *ACS Nano*, 2014, **8**, 8407–8418.

16 L. Shi, P. Yin, H. Zhu and Q. Li, *Langmuir*, 2013, **29**, 8713–8717.

17 M. Ibáñez, R. Zamani, A. LaLonde, D. Cadavid, W. Li, A. Shavel, J. Arbiol, J. R. Morante, S. Gorsse and G. J. Snyder, *J. Am. Chem. Soc.*, 2012, **134**, 4060–4063.

18 L. I. Berger, *Ternary Diamond-Like Semiconductors,* Springer Science & Business Media, 2012.

19 T.-R. Wei, H. Wang, Z. M. Gibbs, C.-F. Wu, G. J. Snyder and J.-F. Li, *J. Mater. Chem. A*, 2014, **2**, 13527–13533.

20 C. Yang, F. Huang, L. Wu and K. Xu, *J. Phys. D: Appl. Phys.*, 2011, **44**, 295404.

21 L. I. Berger and V. D. Prochukhan, *Ternary Diamond-Like Semiconductors*, Consultants Bureau, New York, NY, 1969.

22 X. Pang, L. Zhao, W. Han, X. Xin and Z. Lin, *Nat. Nanotechnol.*, 2013, **8**, 426–431.

23 J. Chang and E. R. Waclawik, *RSC Adv.*, 2014, **4**, 23505–23527.

24 J. van Embden, A. S. Chesman and J. J. Jasieniak, *Chem. Mater.*, 2015, **27**, 2246–2285.

25 D. V. Talapin, J.-S. Lee, M. V. Kovalenko and E. V. Shevchenko, *Chem. Rev.*, 2009, **110**, 389–458.

26 M. Ibáñez, R. Zamani, S. Gorsse, J. Fan, S. Ortega, D. Cadavid, J. R. Morante, J. Arbiol and A. Cabot, *ACS Nano*, 2013, **7**, 2573–2586.

27 M. Ibáñez, Z. Luo, A. Genç, L. Piveteau, S. Ortega, D. Cadavid, O. Dobrozhan, Y. Liu, M. Nachtegaal, M. Zebarjadi, J. Arbiol, M. V. Kovalenko and A. Cabot, *Nat. Commun.*, 2016, **7**, 10766.

28 J. van Embden and Y. Tachibana, *J. Mater. Chem.*, 2012, **22**, 11466–11469.

29 J. van Embden, K. Latham, N. W. Duffy and Y. Tachibana, *J. Am. Chem. Soc.*, 2013, **135**, 11562–11571.

30 K. Ramasamy, H. Sims, W. H. Butler and A. Gupta, *Chem. Mater.*, 2014, **26**, 2891–2899.

31 K. Chen, J. Zhou, W. Chen, P. Zhou, F. He and Y. Liu, *Part. Part. Syst. Charact.*, 2015, **32**, 999–1005.

32 D. Li, R. Li, X.-Y. Qin, C.-J. Song, H.-X. Xin, L. Wang, J. Zhang, G.-L. Guo, T.-H. Zou and Y.-F. Liu, *Dalton Trans.*, 2014, **43**, 1888–1896.

33 Y. Wu, X. Qiao, X. Fan, X. Zhang, S. Cui and J. Wan, *J. Nanopart. Res.*, 2015, **17**, 1–7.

34 R. B. Balow, E. P. Tomlinson, M. M. Abu-Omar, B. W. Boudouris and R. Agrawal, *J. Mater. Chem. A*, 2016, **4**, 2198–2204.

35 M. A. Connell, P. J. Bowyer, P. A. Bone, A. L. Davis, A. G. Swanson, M. Nilsson and G. A. Morris, *J. Magn. Reson.*, 2009, **198**, 121–131.

36 D. Sinnaeve, *Concepts Magn. Reson., Part A*, 2012, **40**, 39–65.

37 M. Chan and G. Ceder, *Phys. Rev. Lett.*, 2010, **105**, 196403.

38 Y. Zhang, L. Xi, Y. Wang, J. Zhang, P. Zhang and W. Zhang, *Comput. Mater. Sci.*, 2015, **108**, 239–249.

39 D. Do, V. Ozolins, S. D. Mahanti, M.-S. Lee, Y. Zhang and C. Wolverton, *J. Phys.: Condens. Matter*, 2012, **24**, 415502.

40 D. T. Do and S. D. Mahanti, *J. Phys. Chem. Solids*, 2014, **75**, 477–485.

41 D. T. Do and S. Mahanti, *J. Alloys Compd.*, 2015, **625**, 346–354.

42 E. J. Skoug, J. D. Cain, P. Majsztrik, M. Kirkham, E. Lara-Curzio and D. T. Morelli, *Sci. Adv. Mater.*, 2011, **3**, 602–606.

43 H. Nakanishi, S. Endo and T. Irie, *Jpn. J. Appl. Phys.*, 1969, **8**, 443.

44 J. P. Perdew, K. Burke and M. Ernzerhof, *Phys. Rev. Lett.*, 1996, **77**, 3865.

45 S. Dudarev, G. Botton, S. Savrasov, C. Humphreys and A. Sutton, *Phys. Rev. B: Condens. Matter Mater. Phys.*, 1998, **57**, 1505–1509.

46 G. Kresse and J. Hafner, *Phys. Rev. B: Condens. Matter Mater. Phys.*, 1993, **47**, 558–561.

47 G. Kresse and J. Furthmüller, *Phys. Rev. B: Condens. Matter Mater. Phys.*, 1996, **54**, 11169–11186.

48 P. E. Blöchl, *Phys. Rev. B: Condens. Matter Mater. Phys.*, 1994, **50**, 17953–17979.

49 G. Kresse and D. Joubert, *Phys. Rev. B: Condens. Matter Mater. Phys.*, 1999, **59**, 1758–1775.

50 M. Methfessel and A. Paxton, *Phys. Rev. B: Condens. Matter Mater. Phys.*, 1989, **40**, 3616–3621.

51 H. J. Monkhorst and J. D. Pack, *Phys. Rev. B: Condens. Matter Mater. Phys.*, 1976, **13**, 5188–5192.

52 G. K. Madsen and D. J. Singh, *Comput. Phys. Commun.*, 2006, **175**, 67–71.

53 X. Li, D. Li, H. Xin, J. Zhang, C. Song and X. Qin, *J. Alloys Compd.*, 2013, **561**, 105–108.

54 R. D. Shannon, *Acta Crystallogr., Sect. A: Cryst. Phys., Diffr., Theor. Gen. Crystallogr.*, 1976, **32**, 751–767.

55 Z. Hens and J. C. Martins, *Chem. Mater.*, 2013, **25**, 1211–1221.

56 J. De Roo, K. De Keukeleere, Z. Hens and I. Van Driessche, *Dalton Trans.*, 2016, **45**, 13277–13283.

57 B. Fritzinger, I. Moreels, P. Lommens, R. Koole, Z. Hens and J. C. Martins, *J. Am. Chem. Soc.*, 2009, **131**, 3024–3032.

58 R. Dierick, F. Van den Broeck, K. De Nolf, Q. Zhao, A. Vantomme, J. C. Martins and Z. Hens, *Chem. Mater.*, 2014, **26**, 5950–5957.

59 Y. Li, X. Qin, D. Li, X. Li, Y. Liu, J. Zhang, C. Song and H. Xin, *RSC Adv.*, 2015, **5**, 31399–31403.

60 L. I. Berger, *Semiconductor Materials*, CRC Press, Boca Raton, FL, 1997, p. 267.

61 P. Pfitzner, *Z. Kristallogr.*, 1995, **209**, 685.

62 H. Nakanishi, S. Endo and I. Taizo, *Jpn. J. Appl. Phys.*, 1969, **8**, 443.

63 D. Do, V. Ozolins, S. D. Mahanti, M.-S. Lee, Y. Zhang and C. Wolverton, *J. Phys.: Condens. Matter*, 2012, **24**, 415502.

64 J. Gong, A. Hong, J. Shuai, L. Li, Z. Yan, Z. Ren and J.-M. Liu, *Phys. Chem. Chem. Phys.*, 2016, **18**, 16566–16574.

65 S. Wang, J. Yang, T. Toll, J. Yang, W. Zhang and X. Tang, *Sci. Rep.*, 2015, **5**, 10136.

Thermoelectric properties of semiconductor-metal composites produced by particle blending

Yu Liu, Doris Cadavid, Maria Ibáñez, Silvia Ortega, Sara Martí-Sánchez, Oleksandr Dobrozhan, Maksym V. Kovalenko, Jordi Arbiol, and Andreu Cabot

Citation: APL Materials **4**, 104813 (2016); doi: 10.1063/1.4961679
View online: https://doi.org/10.1063/1.4961679
View Table of Contents: http://aip.scitation.org/toc/apm/4/10
Published by the American Institute of Physics

APL MATERIALS **4**, 104813 (2016)

Thermoelectric properties of semiconductor-metal composites produced by particle blending

Yu Liu,[1] Doris Cadavid,[1,a] Maria Ibáñez,[2,3] Silvia Ortega,[1]
Sara Martí-Sánchez,[4] Oleksandr Dobrozhan,[1] Maksym V. Kovalenko,[2,3]
Jordi Arbiol,[4,5] and Andreu Cabot[1,5,a]
[1]*Catalonia Institute for Energy Reseach-IREC, Sant Adrià de Besòs, 08930 Barcelona, Spain*
[2]*Department of Chemistry and Applied Biosciences, Institute of Inorganic Chemistry, ETH Zürich CH-8093, Switzerland*
[3]*Empa-Swiss Federal Laboratories for Materials Science and Technology, Dübendorf CH-8600, Switzerland*
[4]*CSIC and The Barcelona Institute of Science and Technology, Catalan Institute of Nanoscience and Nanotechnology (ICN2), Bellaterra, 08193 Barcelona, Catalonia, Spain*
[5]*ICREA, Pg. Lluís Companys 23, 08010 Barcelona, Spain*

(Received 30 April 2016; accepted 15 August 2016; published online 29 August 2016)

In the quest for more efficient thermoelectric material able to convert thermal to electrical energy and vice versa, composites that combine a semiconductor host having a large Seebeck coefficient with metal nanodomains that provide phonon scattering and free charge carriers are particularly appealing. Here, we present our experimental results on the thermal and electrical transport properties of PbS-metal composites produced by a versatile particle blending procedure, and where the metal work function allows injecting electrons to the intrinsic PbS host. We compare the thermoelectric performance of composites with microcrystalline or nanocrystalline structures. The electrical conductivity of the microcrystalline host can be increased several orders of magnitude with the metal inclusion, while relatively high Seebeck coefficient can be simultaneously conserved. On the other hand, in nanostructured materials, the host crystallites are not able to sustain a band bending at its interface with the metal, becoming flooded with electrons. This translates into even higher electrical conductivities than the microcrystalline material, but at the expense of lower Seebeck coefficient values. [http://dx.doi.org/10.1063/1.4961679]

The cost-effective use of solid state thermoelectric devices to directly convert heat to electricity and vice versa requires designing and engineering thermoelectric materials that provide higher performance. In this direction, composites offer several advantages.[1–8] The thermal conductivity of composite materials can be strongly reduced with respect to their components by effective phonon scattering at the interfaces of two dissimilar materials. Additionally, high charge carrier concentrations can be reached while conserving high carrier mobilities by modulation doping, that is, by introducing electronic dopants in just one of the phases and spilling the carriers over from this phase to the host semiconductor. This doping strategy minimizes the influence of ionized doping impurities on charge carrier transport when this takes place through the other phase.[9] Furthermore, higher Seebeck coefficients can be obtained by selectively scattering low energy charge carriers at interfaces.[10] Alternatively, by properly selecting the constituent materials and precisely engineering the composite, the minority phase can become invisible to charge carriers.[11–13] Besides, in particular cases, inclusions can even improve charge carrier mobility by reducing intergrain potential barriers in the matrix material, as recently observed in semiconductor-metal nanocomposites.[14]

---

[a] Authors to whom correspondence should be addressed. Electronic addresses: dcadavid@irec.cat and acabot@irec.cat

This last type of composite, obtained from combining a semiconductor host having a large Seebeck coefficient with metal inclusions, is particularly interesting. A potentially strong acoustic impedance mismatch between the semiconductor and the metal provides a very efficient interface phonon scattering. Besides, the very high density of free carriers in metals represents a convenient charge pool to adjust the host charge carrier concentration if a proper band alignment for charge spillover exists.[14,15] Additionally, Schottky metal-semiconductor interfaces may effectively and preferentially scatter low energy carriers.[10,16] The interest that semiconductor-metal composites has evoked is such that in the last decade a wide spectrum of experimental results, not always obviously consistent between each other, has been reported for several different combinations (Table I).

The proper design and engineering of a semiconductor-metal composite requires not only to select materials with a suitable band alignment but also to use production approaches that allow tuning the material composition and properly distributing the different phases. In this regard, the blending of metal and semiconductor particles in a controlled atmosphere represents an extremely simple methodology to produce composites with a huge compositional versatility and an excellent control over a number of parameters, such as distribution and composition of the phases. Within this approach, the particle sizes of both metal and semiconductor are the key parameters as they determine the final metal and semiconductor domain size in the composite and the metal domain density at a set overall composition. These parameters not only determine the extent of phonon scattering, charge spillover, or potential energy filtering but also the extent that the metal influences the host semiconductor Fermi level, especially when employing intrinsic semiconductors as those required to take full advantage of the modulation doping strategy.

TABLE I. Effect of the metal on semiconductor-metal composites as reported in the literature. Red: worsens; green: improves; yellow: unchanged; blue: no data.[14,15,17–35] κ is thermal conductivity, S the Seebeck coefficient, σ the electrical conductivity and, n and p are the carrier density according to the type of the semiconductor N or P.

Semiconductor	Metal	κ	S	σ	n/p	μ	Reference
PbS (N)	Ag	🟥	🟥	🟩	🟩	🟩	14
PbTe (P)	Pb	🟦	🟩	🟩	🟩	🟥	17
Bi_2Te_3 (N)	Au	🟩	🟥	🟩	🟩	🟥	18
Bi_2Te_3 (N)	Cu	🟩	🟩	🟥	🟥	🟩	19
Bi_2Te_3 (N)	Ag	🟩	🟩	🟩	🟩	🟥	20
Bi_2Te_3 (N)	Bi	🟩	🟥	🟩	🟩	🟥	21
Sb_2Te_3 (P)	Ag	🟦	🟥	🟩	🟥	🟩	22
Sb_2Te_3 (P)	Pt	🟦	🟩	🟥	🟩	🟥	22
$Bi_{0.5}Sb_{1.5}Te_3$ (N)	Cu	🟩	🟥	🟩	🟩	🟥	23
$Bi_{0.5}Sb_{1.5}Te_3$ (P)	Ag	🟩	🟥	🟩	🟩	🟥	24
$Bi_{0.5}Sb_{1.5}Te_3$ (P)	Cu	🟩	🟥	🟩	🟩	🟥	24
$Bi_2Te_{2.7}Se_{0.3}$ (N)	Pt	🟩	🟩	🟩	🟩	🟥	25
$Bi_2(Te_{0.9}Se_{0.1})_3$ (P)	Cu	🟩	🟥	🟩	🟩	🟥	26
$Bi_2(Te_{0.9}Se_{0.1})_3$ (P)	Zn	🟥	🟥	🟩	🟩	🟥	26
GaAs (N)	Bi	🟩	🟩	🟥	🟥	🟦	27
GaAs (N)	In	🟩	🟩	🟥	🟥	🟦	28
$FeSb_2$ (N)	Cu	🟩	🟥	🟩	🟩	🟩	15
$FeSb_2$ (N)	AgSb	🟩	🟥	🟩	🟩	🟦	29
$Ba_{0.3}Co_4Sb_{12}$ (N)	Ag	🟩	🟩	🟩	🟨	🟩	30
Na_xCoO_2 (P)	Au	🟦	🟥	🟩	🟦	🟦	31
$Bi_2Sr_2Co_2O_y$ (P)	Ag	🟥	🟨	🟩	🟦	🟦	32
$Ca_3Co_40_{9+\delta}$ (P)	Ag	🟩	🟩	🟩	🟦	🟦	33
$Ca_3Co_40_9$ (P)	Ag	🟥	🟥	🟩	🟦	🟦	34
$Na_xCo_2O_4$ (P)	Ag	🟥	🟩	🟩	🟦	🟦	35

We recently demonstrated that low work function metals such as Ag are able to inject electrons to a quasi-intrinsic and nanostructured PbS host.[14] We also observed that the presence of Ag at the interfaces allowed reducing the energy barriers for charge transport between PbS grains, thus not only minimizing the influence over mobility, as in a conventional modulation-doping scenario, but actually also improving it. In the present work, we demonstrate that combinations of intrinsic PbS with low work function non-noble metals, such as copper and tin, can also provide higher thermoelectric performances. Besides, here we compare the results obtained from a nanocrystalline semiconductor host, which Fermi level may be pinned to the metal's, with those of a microcrystalline host, which supports the band bending at the metal-semiconductor interface. We demonstrate that while higher electrical conductivities can be reached with a more extensive distribution of metal nanoparticles within the host semiconductor, larger Seebeck coefficients can be maintained with the microcrystalline host.

Cubic PbS nanocrystals with a mean edge size of ~10 nm were prepared following our previously reported procedure.[36] Cu nanocrystals with an average diameter of ~5 nm were prepared following the approach developed by Yang *et al.*[37] Sn nanocrystals with an average diameter of ~13 nm were prepared using the method developed by Kovalenko *et al.*[38]

The blending of nanocrystals was performed by wetting 750 mg of dried PbS nanocrystals with different amounts of a solution of metal nanocrystals in anhydrous chloroform. Subsequently, the solvent was allowed to evaporate under the argon atmosphere.

Proper amounts of commercial PbS and Cu powders were mixed inside an argon-filled glovebox by manually grinding them with an agate mortar.

PbS-metal blends were annealed at 450 °C for 60 min under an Ar flow inside a tube furnace. Then, the annealed powder was loaded into a graphite die and compacted into pellets (Ø10 mm × 1.5 mm) in an Ar atmosphere using a custom-made hot press for 5 min at 420 °C and under 70 MPa pressure. The relative density of the obtained pellets was higher than 85% of the theoretical value in all cases.

X-ray diffraction (XRD) patters were obtained on a Bruker AXS D8 ADVANCE X-ray diffractometer with Cu–Kα radiation ($\lambda = 0.154\,06$ Å). Transmission electron microscopy (TEM) characterization was carried out on a Zeiss Libra 120, operating at 120 kV. High resolution TEM (HRTEM) images were obtained using a Jeol 2010F field-emission gun microscope at 200 keV. Field-emission scanning electron microscopy (SEM) micrographs were obtained on Zeiss Auriga at 5.0 kV. Composition was analyzed by means of an Oxford energy dispersive X-ray (EDX) spectrometer coupled to the SEM.

Both the Seebeck coefficient and the electrical resistivity were measured simultaneously in a LSR-3 LINSEIS system under helium atmosphere. Thermal conductivities were calculated by $\kappa = \lambda C_P \rho$, where λ is the thermal diffusivity, C_p is the heat capacity, and ρ is the mass density of the specimen. Thermal diffusivities were measured using XFA 600 Xenon Flash apparatus. The specific heat (C_P) was calculated by the Dulong-Petit approximation, and the density values used were obtained using the Archimedes' method. Error bars were estimated from the repeatability of the experimental result obtained, calculated after measuring each parameter 3 times. Hall carrier concentrations were measured using a PPMS-9T from Quantum Design, Inc. at room temperature under a magnetic field of 2 T.

Figures 1(a)-1(d) display representative TEM micrographs and the corresponding particle size histograms of the 10 nm cubic PbS, the 5 nm spherical Cu, and the 13 nm spherical Sn nanocrystals obtained following the above procedures and used to produce semiconductor-metal nanocomposites. Figure 1(e) shows the nanocrystals XRD patterns. Importantly, no secondary phases, including the corresponding oxides, were detected when carefully producing, manipulating, and purifying the nanocrystals in air-free conditions.

PbS-Cu and PbS-Sn nanocomposites with adjusted metal concentrations were produced by combining purified PbS nanocrystals with different amounts of a suspension of colloidal Cu or Sn nanocrystals, respectively. To remove residual organic compounds and chemically and structurally stabilize the material, nanocomposites were annealed at 450 °C for 60 min under an Ar flow. Subsequently, the annealed powder was consolidated into disk-shaped pellets using a hot-press. EDX analysis showed the amount of Cu and Sn in the final nanocomposite to be consistent, within the

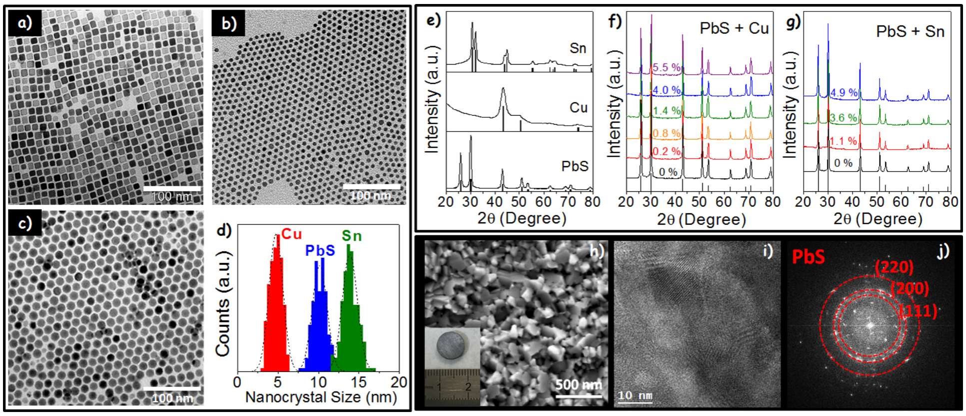

FIG. 1. (a)-(d) TEM micrographs of PbS (a), Cu (b), and Sn (c) nanocrystals and the corresponding size histograms (d). (e) XRD patterns of PbS, Cu, and Sn nanocrystals. The respective reference patterns are also plotted as follows: PbS: JCPDS 00-005-0592; Cu: JCPDS 03-065-9026; Sn: JCPDS 01-086-2265. (f)-(g) XRD patterns for different concentrations of Cu in the PbS-Cu (f) and PbS-Sn (g) nanocomposite pellets. (h) Representative SEM micrograph of a PbS-Sn nanocomposite showing 100-200 nm grains. Inset shows an image of the actual pellet. (i) HRTEM micrograph and (j) power spectra of the PbS-Sn nanocomposite showing the material polycrystallinity with crystal domain sizes in the range between 10 and 20 nm.

experimental error, with the nominal composition of the nanocomposites prepared. This result was to be expected as no additional purification process was performed after the nanocrystal combination, and processing temperatures were not high enough for metal evaporation.

Figures 1(f) and 1(g) show the XRD patterns of PbS-Cu and PbS-Sn nanocomposite pellets, respectively. Because of the low amount of metal introduced and the coincidence of the main x-ray diffraction peaks of the metal with those of PbS, the presence of metallic Cu and Sn phases was not detected by XRD. During the annealing processes, PbS grains were observed to grow from the initial 10 nm to around 100-200 nm (Figure 1(h)). However, careful HRTEM analysis showed the grains to be highly polycrystalline, with crystal domain sizes in the range 10–20 nm (Figures 1(i) and 1(j)). The coincidence of interplanar spacings did not allow obtaining evidences of the presence of metallic Cu or Sn crystals from HRTEM and electron diffraction.

The electrical conductivities (σ), Seebeck coefficients (S), thermal conductivities (κ), and dimensionless thermoelectric figure of merit $ZT = \sigma S^2 T/\kappa$ of nanocrystalline PbS and a series of PbS-Cu and PbS-Sn nanocomposites with metal concentrations up to 5 mol% are displayed in Figure 2. The pristine PbS material was characterized by low electrical conductivity at ambient temperature, which, as it corresponds to an intrinsic or poorly doped semiconductor, strongly

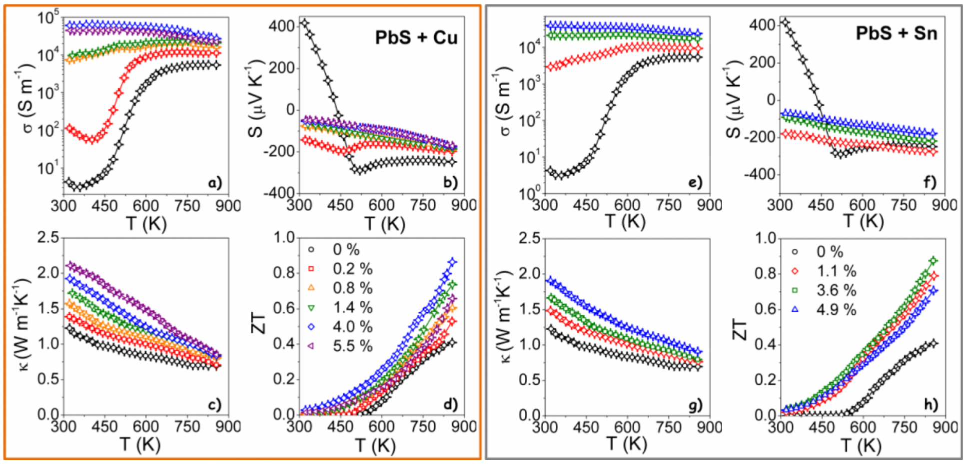

FIG. 2. Temperature dependence of the (a), (e) electrical conductivity, σ; (b), (f) Seebeck coefcient, S; (c), (g) thermal conductivity, κ; and (d), (h) thermoelectric figure of merit (ZT) for PbS-Cu (a)-(d) and PbS-Sn (e)-(h) nanocomposites.

increased with temperature. Consistently, relatively high Seebeck coefficients were measured for PbS at ambient temperature. Besides, a sign inversion in the Seebeck coefficient was observed at around 450 K, corresponding to a change from p-type to n-type conductivity. PbS–Cu and PbS-Sn nanocomposites showed significantly higher electrical conductivities, which increased with the metal content. For the nanocomposites with the highest metal contents, electrical conductivities decreased with temperature, as it corresponds to a degenerated semiconductor. This result demonstrates the important electronic role that Cu and Sn play on the final material. Over the entire temperature range measured, both PbS–Cu and PbS-Sn nanocomposites exhibited negative Seebeck coefficients and their absolute values increased with temperature. This n-type behavior pointed towards an injection of electrons from the metal to the host semiconductor. Consistently with the higher electrical conductivities measured, lower Seebeck coefficients were generally obtained for the nanocomposites when compared with pristine PbS.

Hall charge carrier concentration measurements provided further evidence of the charge carrier increase, of up to 3 orders of magnitude, obtained with the introduction of metal nanocrystals. The Hall charge carrier concentrations at room temperature for PbS, PbS-Cu 4 mol%, and PbS-Sn 3.6 mol% were $p = 2 \times 10^{16}$ cm^{-3}, $n = 3 \times 10^{19}$ cm^{-3}, and $n = 1 \times 10^{19}$ cm^{-3}, respectively. The majority carrier mobilities directly calculated from the measured electrical conductivities were $\mu_p = 14\ \mathrm{cm}^2 \cdot \mathrm{V}^{-1} \cdot \mathrm{s}^{-1}$, $\mu_n = 130\ \mathrm{cm}^2 \cdot \mathrm{V}^{-1} \cdot \mathrm{s}^{-1}$, and $\mu_n = 130\ \mathrm{cm}^2 \cdot \mathrm{V}^{-1} \cdot \mathrm{s}^{-1}$, for PbS, PbS-Cu 4 mol%, and PbS-Sn 3.6 mol%, respectively.

With the metal addition, higher thermal conductivities, which increased with the metal content, were obtained in the whole temperature range. This increase is associated with the higher electronic component of the thermal conductivity. Overall, nanocomposites displayed significantly higher power factors ($PF = \sigma S^2$) and figures of merit than pristine PbS. Maximum ZT values were obtained for PbS-Cu 4.0 mol% and PbS-Sn 3.6 mol% nanocomposites, which reached ZT values up to 0.86 and 0.88 at 855 K, respectively, which represents a twofold increase over pristine PbS. Higher metal concentrations provided either a too large reduction in the Seebeck coefficient or a too large increase on thermal conductivity, thus decreasing the overall thermoelectric figure of merit. To estimate measurement accuracy and have a first assessment of the sample stability, all measurements were repeated at least three times for each sample, providing minimal variations.

Figure 3 displays the results obtained from the thermoelectric characterization of microcrystalline PbS and PbS-Cu 4.0 mol% composites produced from commercial powders. Results are compared with those obtained from nanocrystalline PbS and the PbS-Cu 4.0 mol% nanocomposite produced from colloidal nanoparticles. Electrical conductivities of the pristine microcrystalline PbS were low, similar to those of the PbS nanomaterial. In the high temperature range, higher electrical conductivities were obtained for the nanocrystalline PbS, which we associate to a higher density of

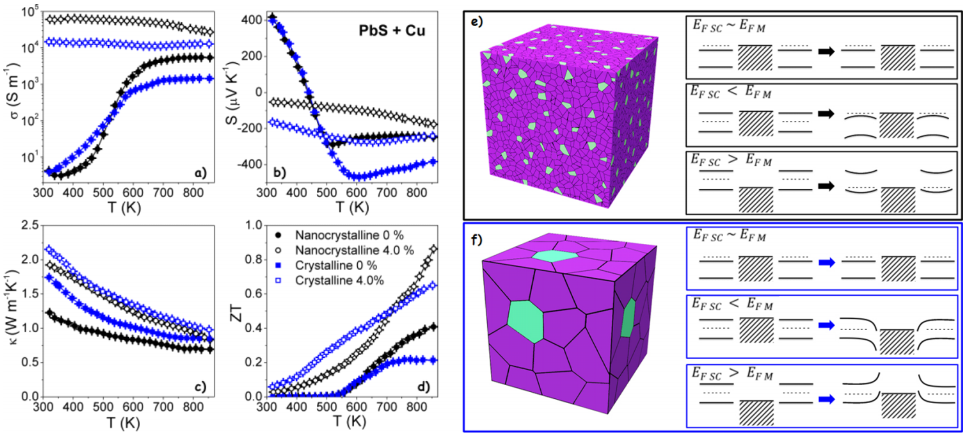

FIG. 3. Temperature dependence of the (a) electrical conductivity; (b) Seebeck coefficient; (c) thermal conductivity; and (d) thermoelectric figure of merit for microcrystalline PbS–Cu composites (blue squares) and PbS-Cu nanocomposites (black circles). (e)-(f) Scheme of a semiconductor-metal nanocomposite and a microcomposite and the band alignments in three scenarios depending on the relative position of the semiconductor ($E_{F\ SC}$) and metal Fermi Energy levels ($E_{F\ M}$).

surface defects, susceptible to be ionized in the high temperature range and thus providing higher charge carrier concentrations. With the Cu introduction, the electrical conductivities of the microcrystalline composite increased several orders of magnitude, up to 10^4 S m^{-1}, but remained a factor 4 lower than those of the PbS-Cu nanocomposite.

On the other hand, the Seebeck coefficients of the pristine PbS microcrystalline material showed a similar temperature evolution as the nanocrystalline PbS, but reached higher values in the high temperature range, which is consistent with the relatively lower electrical conductivities measured in this temperature range for the microcrystalline material. In the presence of copper, negative Seebeck coefficients were measured in the whole temperature range, which, together with the large increase of electrical conductivity, points toward a spillover of electrons from the metal to the host semiconductor, as in the case of the PbS-Cu nanocomposite. In the microcrystalline composite however, much higher Seebeck coefficients than in the nanocomposite were obtained, even when comparing with nanocomposites having lower Cu loads and similar electrical conductivities. We associate the relatively lower Seebeck coefficients obtained in the nanocrystalline material to the nanocrystals charge flooding, not being able to sustain a sufficient band bending due to their small size and low electronic doping. In the microcrystalline compound, the injection of charge from copper to PbS introduces a band bending in the semiconductor, but still most of the PbS crystal remains quasi-intrinsic, thus overall providing much larger Seebeck coefficients (Figures 3(e) and 3(f)).

In microcrystalline PbS, the measured Hall charge carrier concentration at room temperature was $p = 9 \times 10^{15}$ cm^{-3}, just slightly lower than for nanocrystalline PbS. The related charge carrier mobility was $\mu_p = 28\ cm^2 \cdot V^{-1} \cdot s^{-1}$, twofold higher than in nanocrystalline PbS. When introducing a 4 mol% of Cu, the microcrystalline PbS-Cu 4 mol% composite displayed a charge carrier concentration of $n = 2 \times 10^{18}$ cm^{-3}, which was one order of magnitude lower than when blending the same amount of Cu with nanocrystalline PbS. From this carrier concentration value, the calculated mobility in the microcrystalline composite was 3-fold larger than that of the nanocomposite, which is consistent with the higher crystallinity of the former.

As expected, the thermal conductivities of the microcrystalline PbS and the PbS-Cu composite were larger than those of the nanocrystalline PbS and PbS-Cu. Overall, while larger ZT values were obtained for the microcrystalline compound in the low temperature range measured, due to the much higher Seebeck coefficients provided, in the high temperature range, the nanocomposite was characterized by higher ZT values related to the lower lattice thermal conductivity due to more efficient phonon scattering and the higher electrical conductivities associated to a more efficient charge carrier injection from the metal to the semiconductor.

PbS-Cu and PbS-Sn composites were prepared by a facile and extremely versatile approach consisting on blending the proper amount of particles of each components and subsequently hot-pressing the resulting mixture. Compared with pristine PbS, PbS-metal composites exhibited much higher electrical conductivities and negative Seebeck coefficients in the whole temperature range, consistent with a spillover of electrons from the low work function metal to the semiconductor. Due to the strong contribution of the electronic thermal conductivity, the metal addition had associated an increase of the thermal conductivity. When comparing the thermoelectric properties of PbS-Cu composites with crystal domain sizes in the micrometer scale with those of nanocomposites with dimensions of both components in the nanometer size regime, we observed that with the same metal loading, higher electrical conductivities were reached in the nanocomposite, but higher Seebeck coefficients were maintained in the microcomposite. Both results were associated to a more efficient charge transfer from the metal to the semiconductor in the nanocrystalline materials. As expected, lower thermal conductivities were also measured in the nanocomposite. Overall, higher ZT values were measured on the microcomposite in the low temperature range, but higher ZT values were measured from the nanocomposites in the higher temperature range. Both in microcomposites and nanocomposites, a 2-fold increase of ZT was obtained over pristine PbS.

This work was supported by the European Regional Development Funds, the Framework 7 program under project UNION (No. FP7-NMP-2012-310250), and the Spanish MINECO Project BOOSTER (No. ENE2013-46624-C4-3-R). Y.L. thanks the China Scholarship Council (No. CSC 201406500003) for the scholarship support. M.I., O.D., and S.O. thank AGAUR for their Beatriu de Pinós postdoctoral Grant No. (2013 BP-A00344) and Ph.D. grants. M.V.K. acknowledges the partial financial support from the European Union (EU) via FP7 ERC Starting Grant 2012 (Project NANOSOLID, GA No. 306733). Authors also acknowledge the funding from Generalitat de Catalunya 2014 SGR 1638.

[1] A. M. Dehkordi, M. Zebarjadi, J. He, and T. M. Tritt, Mater. Sci. Eng., R **97**, 1–22 (2015).
[2] C. J. Vineis, A. Shakouri, A. Majumdar, and M. G. Kanatzidis, Adv. Mater. **22**, 3970–3980 (2010).
[3] M. Ibáñez, R. Zamani, S. Gorsse, J. Fan, S. Ortega, D. Cadavid, J. R. Morante, J. Arbiol, and A. Cabot, ACS Nano **7**, 2573–2586 (2013).
[4] J. R. Sootsman, D. Y. Chung, and M. G. Kanatzidis, Angew. Chem., Int. Ed. **48**, 8616–8639 (2009).
[5] Y. Zhang and G. D. Stucky, Chem. Mater. **26**, 837–848 (2013).
[6] Y. Lan, A. J. Minnich, G. Chen, and Z. Ren, Adv. Funct. Mater. **20**, 357–376 (2009).
[7] J. He, M. G. Kanatzidis, and V. P. Dravid, Mater. Today **16**, 166–176 (2013).
[8] L.-D. Zhao, V. P. Dravid, and M. G. Kanatzidis, Energy Environ. Sci. **7**, 251–268 (2014).
[9] M. Zebarjadi, G. Joshi, G. Zhu, B. Yu, A. Minnich, Y. Lan, X. Wang, M. Dresselhaus, Z. Ren, and G. Chen, Nano Lett. **11**, 2225–2230 (2011).
[10] S. V. Faleev and F. Léonard, Phys. Rev. B **77**, 214304 (2008).
[11] M. Zebarjadi, B. Liao, K. Esfarjani, M. Dresselhaus, and G. Chen, Adv. Mater. **25**, 1577–1582 (2013).
[12] W. Shen, T. Tian, B. Liao, and M. Zebarjadi, Phys. Rev. B **90**, 075301 (2014).
[13] J. Y. Lee and R.-K. Lee, Phys. Rev. B **89**, 155425 (2014).
[14] M. Ibáñez, Z. Luo, A. Genc, L. Piveteau, S. Ortega, D. Cadavid, O. Dobrozhan, Y. Liu, M. Nachtegaal, M. Zebarjadi, J. Arbiol, M. V. Kovalenko, and A. Cabot, Nat. Commun. **7**, 10766 (2016).
[15] M. Koirala, H. Zhao, M. Pokharel, S. Chen, T. Dahal, C. Opeil, G. Chen, and Z. Ren, Appl. Phys. Lett. **102**, 213111 (2013).
[16] J. M. O. Zide, J.-H. Bahk, R. Singh, M. Zebarjadi, G. Zeng, H. Lu, J. P. Feser, D. Xu, S. L. Singer, Z. X. Bian, A. Majumdar, J. E. Bowers, A. Shakouri, and A. C. Gossard, J. Appl. Phys. **108**, 123702 (2010).
[17] J. P. Heremans, C. M. Thrush, and D. T. Morelli, J. Appl. Phys. **98**, 063703 (2005).
[18] E. Lee, J. Ko, J.-Y. Kim, W.-S. Seo, S.-M. Choi, K. H. Lee, W. Shim, and W. Lee, J. Mater. Chem. C **4**, 1313–1319 (2016).
[19] F. R. Sie, C. H. Kuo, C. S. Hwang, Y. W. Chou, C. H. Yeh, Y. L. Lin, and J. Y. Huang, J. Electron. Mater. **45**, 1927–1934 (2016).
[20] Q. Zhang, X. Ai, L. Wang, Y. Chang, W. Luo, W. Jiang, and L. Chen, Adv. Funct. Mater. **25**, 966–976 (2015).
[21] S. Sumithra, N. J. Takas, D. K. Misra, W. M. Nolting, P. F. P. Poudeu, and K. L. Stokes, Adv. Energy Mater. **1**, 1141–1147 (2011).
[22] Y. Zhang, M. L. Snedaker, C. S. Birkel, S. Mubeen, X. Ji, Y. Shi, D. Liu, X. Liu, M. Moskovits, and G. D. Stucky, Nano Lett. **12**, 1075–1080 (2012).
[23] I.-H. Kim, S.-M. Choi, W.-S. Seo, and D.-I. Cheong, Nanoscale Res. Lett. **7**, 1–6 (2012).
[24] K.-H. Lee, H.-S. Kim, S.-I. Kim, E.-S. Lee, S.-M. Lee, J.-S. Rhyee, J.-Y. Jung, I.-H. Kim, Y. Wang, and K. Koumoto, J. Electron. Mater. **41**, 1165–1169 (2012).
[25] T. Sun, M. K. Samani, N. Khosravian, K. M. Ang, Q. Yan, B. K. Tay, and H. H. Hng, Nano Energy **8**, 223–230 (2014).
[26] S. Wang, H. Li, R. Lu, G. Zheng, and X. Tang, Nanotechnology **24**, 285702 (2013).
[27] M. V. Warren, J. C. Canniff, H. Chi, F. Naab, V. A. Stoica, R. Clarke, C. Uher, and R. S. Goldman, J. Appl. Phys. **117**, 065101 (2015).
[28] M. V. Warren, J. C. Canniff, H. Chi, E. Morag, F. Naab, V. A. Stoica, R. Clarke, C. Uher, and R. S. Goldman, J. Appl. Phys. **114**, 043704 (2013).
[29] H. Zhao, M. Pokharel, S. Chen, B. Liao, K. Lukas, C. Opeil, G. Chen, and Z. Ren, Nanotechnology **23**, 505402 (2012).
[30] X. Zhou, G. Wang, L. Zhang, H. Chi, X. Su, J. Sakamoto, and C. Uher, J. Mater. Chem. **22**, 2958–2964 (2012).
[31] X. Zhao, H. Wang, S. Wang, D. Elhadj, J. Wang, and G. Fu, RSC Adv. **4**, 57148–57152 (2014).
[32] J. Zheng, J. Peng, Z. Zheng, M. Zhou, E. Thompson, J. Yang, and W. Xiao, Front. Chem. **3**, 53 (2015).
[33] N. Van Nong, N. Pryds, S. Linderoth, and M. Ohtaki, Adv. Mater. **23**, 2484–2490 (2011).
[34] Y. Wang, Y. Sui, J. Cheng, X. Wang, and W. Su, J. Alloys Compd. **477**, 817–821 (2009).
[35] M. Ito and J. Sumiyoshi, J. Jpn. Soc. Powder Powder Metall. **55**, 90–95 (2007).
[36] M. Ibáñez, R. J. Korkosz, Z. Luo, P. Riba, D. Cadavid, S. Ortega, A. Cabot, and M. G. Kanatzidis, J. Am. Chem. Soc. **137**, 4046–4049 (2015).
[37] L.-I. Hung, C.-K. Tsung, W. Huang, and P. Yang, Adv. Mater. **22**, 1910–1914 (2010).
[38] K. Kravchyk, L. Protesescu, M. I. Bodnarchuk, F. Krumeich, M. Yarema, M. Walter, C. Guntlin, and M. V. Kovalenko, J. Am. Chem. Soc. **135**, 4199–4202 (2013).

NANO LETTERS
Letter
Cite This: *Nano Lett.* 2018, 18, 2557−2563
pubs.acs.org/NanoLett

Crystallographically Textured Nanomaterials Produced from the Liquid Phase Sintering of $Bi_xSb_{2-x}Te_3$ Nanocrystal Building Blocks

Yu Liu,[†] Yu Zhang,[†] Silvia Ortega,[†] Maria Ibáñez,[‡,§] Khak Ho Lim,[∥] Albert Grau-Carbonell,[⊥] Sara Martí-Sánchez,[⊥] Ka Ming Ng,[∥] Jordi Arbiol,[⊥,#] Maksym V. Kovalenko,[‡,§] Doris Cadavid,[*,†,○] and Andreu Cabot[*,†,#]

[†]Catalonia Energy Research Institute - IREC, Sant Adria de Besòs, 08930 Barcelona, Spain

[‡]Institute of Inorganic Chemistry, Department of Chemistry and Applied Biosciences, ETH Zürich, Vladimir Prelog Weg 1, CH-8093 Zürich, Switzerland

[§]Empa-Swiss Federal Laboratories for Materials Science and Technology, Dübendorf, Überlandstrasse 129, CH-8600 Dübendorf, Switzerland

[∥]Department of Chemical and Biological Engineering, Hong Kong University of Science and Technology, Hong Kong, China

[⊥]Catalan Institute of Nanoscience and Nanotechnology (ICN2), CSIC and BIST, Campus UAB, Bellaterra, 08193 Barcelona, Catalonia, Spain

[#]ICREA, Pg. Lluis Companys 23, 08010 Barcelona, Spain

[○]Departamento de Física, Universidad Nacional de Colombia, 111321 Ciudad Universitaria, Bogotá, Colombia

Supporting Information

ABSTRACT: Bottom-up approaches for producing bulk nanomaterials have traditionally lacked control over the crystallographic alignment of nanograins. This limitation has prevented nanocrystal-based nanomaterials from achieving optimized performances in numerous applications. Here we demonstrate the production of nanostructured $Bi_xSb_{2-x}Te_3$ alloys with controlled stoichiometry and crystallographic texture through proper selection of the starting building blocks and the adjustment of the nanocrystal-to-nanomaterial consolidation process. In particular, we hot pressed disk-shaped $Bi_xSb_{2-x}Te_3$ nanocrystals and tellurium nanowires using multiple pressure and release steps at a temperature above the tellurium melting point. We explain the formation of the textured nanomaterials though a solution−reprecipitation mechanism under a uniaxial pressure. Additionally, we further demonstrate these alloys to reach unprecedented thermoelectric figures of merit, up to ZT = 1.96 at 420 K, with an average value of ZT_{ave} = 1.77 for the record material in the temperature range 320−500 K, thus potentially allowing up to 60% higher energy conversion efficiencies than commercial materials.

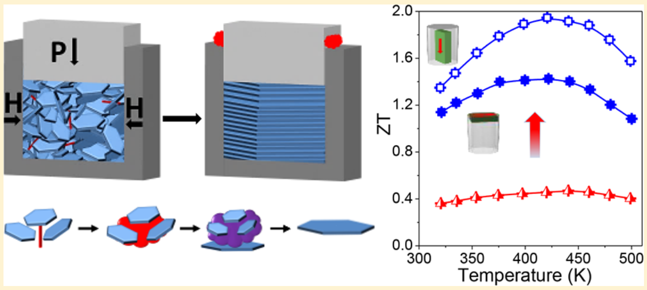

KEYWORDS: *$Bi_xSb_{2-x}Te_3$, nanocrystal, crystal texture, liquid phase sintering, thermoelectric, energy conversion*

Nanostructured materials hold the key to the cost-effective use of thermoelectric devices in a broad range of applications. Nanomaterials are characterized by reduced thermal conductivities attributed to phonon scattering at grain boundaries;[1,2] the potential to simultaneously combine high charge carrier concentrations with large charge carrier mobilities through modulation doping;[3−5] and the possibility to maximize the Seebeck coefficient by modifying the electronic band structure or through electron energy filtering at interphases.[6,7] However, to optimize all of these properties, an exquisite control over nanomaterial parameters in three dimensions is necessary. Such a level of control cannot be reached by current high throughput bulk nanomaterial fabrication technologies, such as mechanical grinding. Alternative vacuum-based thin film technologies are able to produce compositionally tuned films but with limited thickness and at expenses of high production costs and low throughputs.

Bottom-up assembly strategies that use nanocrystals as starting building blocks allow producing bulk nanomaterials with parameters tuned at the nanometer scale and in a cost-effective manner. This approach has been successful to produce a plethora of nanocrystalline materials with exceptional thermoelectric properties.[1,3,8−10] However, this methodology faces limitations in the production of highly anisotropic materials with proper crystallographic alignment, as required in numerous application fields, including thermoelectrics.[1]

Received: January 19, 2018
Revised: March 9, 2018
Published: March 16, 2018

DOI: 10.1021/acs.nanolett.8b00263

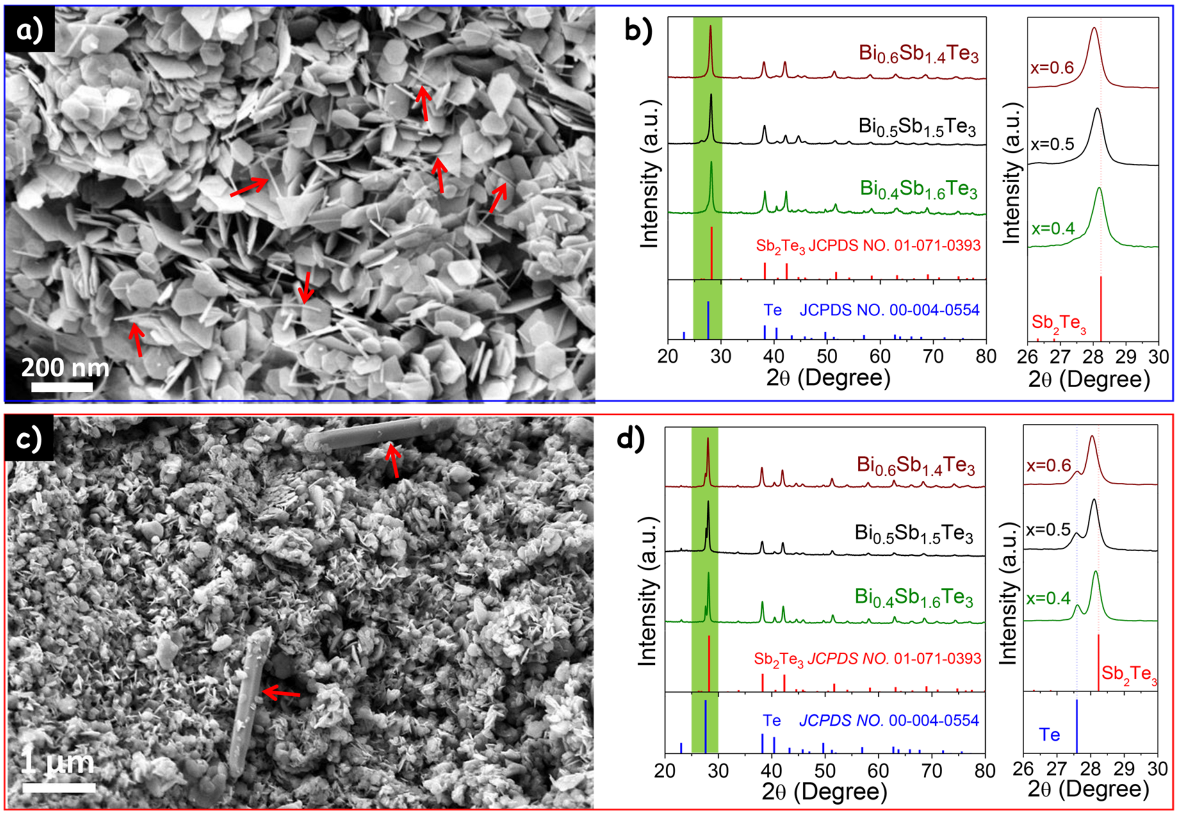

Figure 1. Representative SEM micrographs (a, c) and XRD patterns (b, d) of the $Bi_xSb_{2-x}Te_3$ disk-shaped nanocrystals used in this work, before (a, b) and after (c, d) annealing. Tellurium nanorods were present in samples prepared with a nominal excess of tellurium and some of them are pointed out by arrows in the SEM images of the sample before and after annealing. The presence of large tellurium nanorods in the annealed sample is also evidenced from the XRD peak at $2\theta = 27.6°$.

In particular, n-type $Bi_2Te_{3-x}Se_x$ and p-type $Bi_xSb_{2-x}Te_3$ alloys, the most ubiquitous thermoelectric materials operated at ambient temperature, have layered structures consisting of stacks of covalently bonded quintuple atomic layers, Te−Bi/Sb−Te−Bi/Sb−Te, that are held together by weak van der Waals interactions (Figure S1). Such layered materials are characterized by strongly anisotropic transport properties. In single crystals, the electrical conductivities in the *ab* plane are higher than those in the *c* direction, up to factors of 4.38 and 2.65 for $Bi_2Te_{2.6}Se_{0.4}$ and $Bi_{0.5}Sb_{1.5}Te_3$, respectively.[11,12] Similarly, 2-fold higher thermal conductivities are measured within the *ab* plane. Even though the Seebeck coefficient is nearly isotropic, overall, higher thermoelectric figures of merit, up to factors of 2.17 and 1.42 for $Bi_2Te_{2.6}Se_{0.4}$ and $Bi_{0.5}Sb_{1.5}Te_3$, are measured in the *ab* plane when compared with the *c* direction. Such strong anisotropy requires producing crystallographically textured $Bi_2Te_{3-x}Se_x$ and $Bi_xSb_{2-x}Te_3$ nanomaterials to optimize their thermoelectric properties.

To generate crystallographically textured polycrystalline materials, severe plastic deformation approaches, such as particular extrusion strategies[13,14] and high pressure torsion,[15] have been used with some success. More conventional processes, such as hot press and spark plasma sintering, have also been effective in producing $Bi_2Te_{3-x}Se_x$ and $Bi_xSb_{2-x}Te_3$ polycrystalline materials with significant degrees of crystallographic alignment.[16−18] Combining these methodologies with micropowders produced by ball milling, polycrystalline pellets with relatively thick layered structures, ca. 0.5−1 μm, have been obtained. To optimize such consolidation processes, most parameters have been investigated, but some controversy has arisen. As an example, it is generally assumed that anisotropy is stimulated by severe pressures and temperatures, but in some cases, less orientation at higher processing temperatures has been reported.[17] In other works, the size of the die was considered as the main parameter determining the degree of crystallographic texture.[16] Overall, three main conclusions have been generally accepted: (i) crystallographically aligned $Bi_2Te_{3-x}Se_x$ and $Bi_xSb_{2-x}Te_3$ alloys are produced with the *c* direction oriented along the pressing direction; (ii) in such materials, improved thermoelectric properties are measured or assumed within the *ab* plane when compared with the *c* direction; and (iii) much room is left for improvement through optimizing these processes.

Here, we detail a liquid phase sintering strategy to systematically produce crystallographically textured $Bi_xSb_{2-x}Te_3$ materials with thin layered structures. We further prove that these nanomaterials are characterized by record thermoelectric figures of merit, although not in the *ab* plane but in the *c* direction.

$Bi_xSb_{2-x}Te_3$ nanocrystals with controlled composition were used as precursor building blocks to produce bulk nanocrystalline pellets. Figure 1a shows a representative scanning electron microscopy (SEM) micrograph of the disk-shaped $Bi_xSb_{2-x}Te_3$ nanocrystals produced in diethylene glycol from bismuth(III) nitrate, antimony(III) chloride, and sodium tellurite in the presence of hydrazine and polyvinylpyrrolidone at 190 °C (see details in the Supporting Information). Over 5 g of nanocrystals per batch was produced using this synthetic protocol (Figure S2a). Composition could be easily tuned around its optimum value for thermoelectric applications ($x = 0.5$) by adjusting the

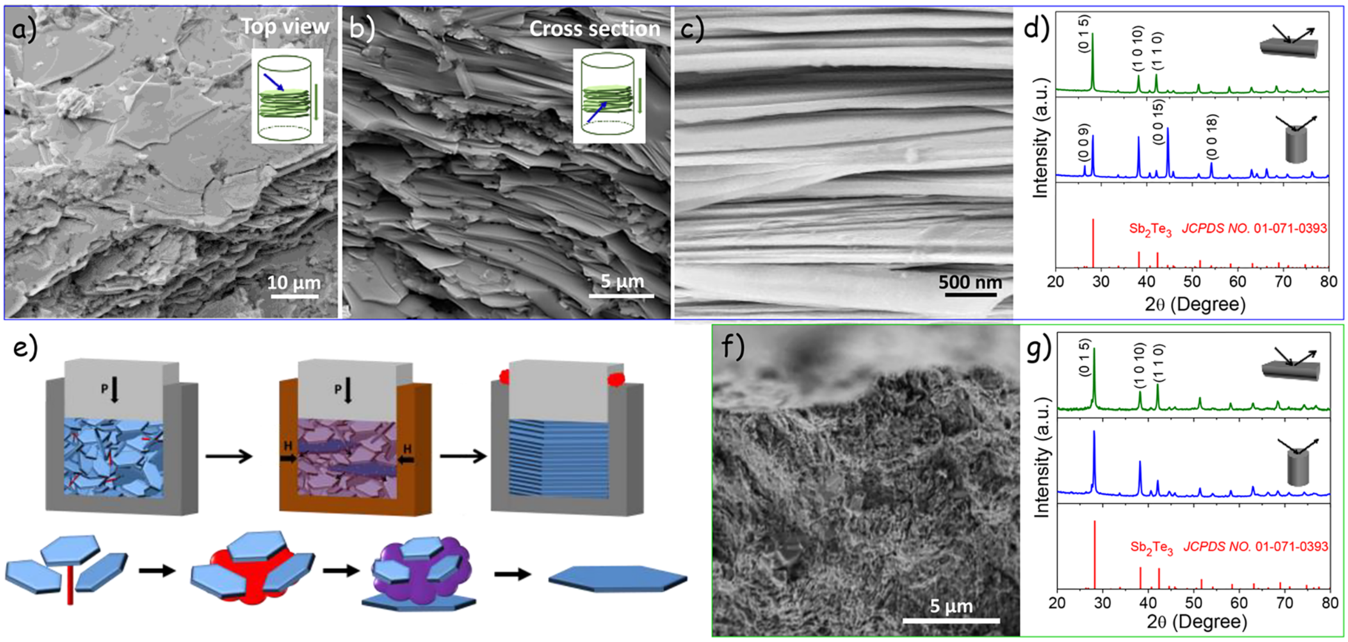

Figure 2. (a) Top-view SEM micrograph of a $Bi_xSb_{2-x}Te_3$ pellet produced at 480 °C. (b) Cross-section SEM micrograph of the same pellet. (c) Detail of the cross-section SEM micrograph. (d) XRD patterns of the pellet placed to have the press axis within the diffraction plane (green) and normal to it (blue). (e) Cartoon of the liquid-assisted sintering of the nanocrystals under uniaxial pressure. (f) Cross-section SEM micrograph of a pellet hot pressed at 300 °C. (g) XRD patterns of the pellet hot pressed at 300 °C placed to have the press axis within the diffraction plane (green) and normal to it (blue).

initial ratios of the bismuth and antimony precursors (Figure 1b and Table S2 and S3). In all samples, excess amounts of tellurium, nominally Te/(Bi + Sb) = 1.875, were introduced in the reaction mixture. The produced nanocrystal ensemble systematically conserved the nominal Bi/Sb ratios and an excess of tellurium: Te/(Bi + Sb) ∼ 1.7. Excess tellurium was found in the form of thin tellurium nanorods, segregated from $Bi_xSb_{2-x}Te_3$ nanodisks, as pointed out by red arrows in Figure 1a.

$Bi_xSb_{2-x}Te_3$ nanocrystals were purified by multiple precipitation and redispersion steps (Supporting Information). Subsequently, they were dried and annealed at 350 °C for 60 min under argon flow inside a tube furnace to remove remaining organics. The annealed nanopowders still consisted of disk-shaped $Bi_xSb_{2-x}Te_3$ nanocrystals (Figure 1c and Figure S2b−d), and contained large tellurium nanorods, grown during the annealing step from the excess amounts of this element in the original sample, as observed by SEM (Figure 1c) and X-ray diffraction (XRD, Figure 1d).

The annealed nanopowders were hot pressed for 210 s within an inert atmosphere into cylindrical pellets (10 mm in diameter and 10 mm length) using 80 MPa of pressure. The whole procedure, lasting less than 5 min and requiring no vacuum and moderate processing temperatures, resulted in $Bi_xSb_{2-x}Te_3$ cylinders with relative densities ca. 90% of the theoretical value, as measured by the Archimedes method. From these cylinders, rectangular bars of about $8 \times 6 \times 1$ mm^3 were cut in two directions: along the press axis, i.e., the cylinder length, and within the plane normal to this axis, i.e., the cylinder disk plane (Figure S6).

The uniaxial hot press of the materials at temperatures below 400 °C resulted in relatively isotropic pellets containing small nanograins with random orientations (Figure 2f,g). On the other hand, when hot pressing the annealed nanopowders at temperatures above 450 °C, pellets with strong crystallographic texture, with the [001] crystallographic direction oriented along the press axis, were produced (Figure 2a−d). Figure 2a−c shows top-view and cross-section SEM micrographs of a pellet produced from hot pressing $Bi_xSb_{2-x}Te_3$ nanodisks at 480 °C. A laminar structure, with layer thicknesses of around 40 nm and extending several tens and even hundreds of microns in the disk plane, was systematically observed in all of the samples produced at this temperature. These layers displayed a homogeneous distribution of Bi and Sb and contained numerous stacking faults as observed from STEM-EELS and HRTEM characterization of a pellet cross-section (Figures S4 and S5). Figures 2d and S3 display the XRD patterns measured in two perpendicular orientations of the cylinder, along and normal to the press axis. The XRD pattern of the pellet held with the press axis normal to the support showed a clear increase of the diffraction peaks corresponding to the [001] crystallographic directions with respect to the pattern obtained from the cylinder held planar (Figure 2d).

The excess of tellurium in the initial nanopowder was essential to produce highly crystallographically textured nanomaterials (Figure S7). During the hot press process at 480 °C, the excess of tellurium, ca. 8% in volume, liquefied (tellurium melting point is 449.5 °C), creating a solid−liquid interface with two main potential consequences. The liquid interface reduced the interparticle friction, potentially facilitating the reaccommodation of the solid nanocrystals. In a pure nanocrystal rearrangement scenario, the final pellet would consist of disk-shaped nanocrystals identical to those observed in the precursor nanopowders but all aligned in one preferential direction dictated by the press axis. However, this was not the observed pellet nanostructure (Figure 2a−c).

The tellurium liquid phase could also dissolve the randomly oriented $Bi_xSb_{2-x}Te_3$ nanocrystals, allow a fast atomic diffusion of the alloy elements, and feed, when oversaturated, the nucleation and growth of new $Bi_xSb_{2-x}Te_3$ crystals oriented in a

DOI: 10.1021/acs.nanolett.8b00263
Nano Lett. 2018, 18, 2557−2563

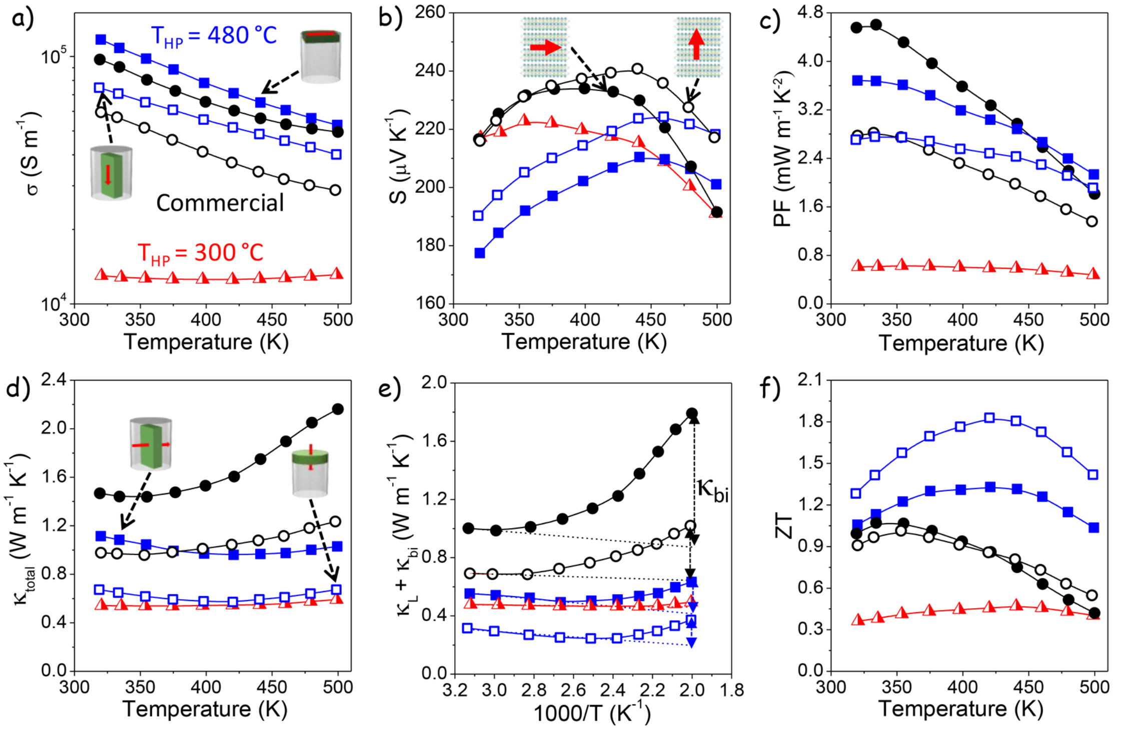

Figure 3. Thermoelectric properties of $Bi_{0.5}Sb_{1.5}Te_3$ nanomaterial hot pressed at 480 °C (blue squares) measured in two directions, parallel (open squares) and normal (solid squares) to the press axis (data were obtained from averaging the data values experimentally measured from five samples); $Bi_{0.5}Sb_{1.5}Te_3$ nanomaterial hot pressed at 300 °C (red triangles); and a commercial ingot (black circles) measured in two directions, parallel (solid circles) and normal (open circles) to the cleavage direction. (a) Electrical conductivity, σ; (b) Seebeck coefficient, S; (c) power factor, PF; (d) thermal conductivity, κ; (e) lattice and bipolar thermal conductivity, $\kappa_L + \kappa_{bi} = \kappa_{total} - \kappa_e$; and (f) thermoelectric figure of merit, ZT.

preferential direction dictated by the press axis. In the liquid phase sintering literature, this sintering mechanism is known as the solution−reprecipitation stage.[19] Indeed, at 480 °C, liquid tellurium can dissolve around 15% of Sb and 25% of Bi. Actually, both the Sb−Te and Bi−Te systems have eutectic points: at 422 °C for Sb−Te with 7.4% of Sb and at 413 °C with 10% of Bi in the Bi−Te system.[20,21] The dissolution of the solid in the liquid phase varies inversely with the crystal size; thus, smaller grains and higher energy surfaces preferentially dissolve, contributing to the formation of larger grains. In this Ostwald ripening scenario, randomly oriented small disk-shaped nanocrystals are rapidly dissolved and larger and crystallographically oriented structures are produced, strongly reducing the material porosity.[19,22] Such a nanostructure matched well with the results obtained.

The presence of a uniaxial hydrostatic pressure during the liquid phase sintering decisively influenced the orientation of the growing crystals. During the solution and reprecipitation step, the preferred orientation of the precipitating crystals is the one that minimizes the chemical potential required for equilibrium across the plane normal to the pressure axis.[23] Such an orientation depends on the elasticity of the material in each crystallographic direction, in such a way that in rather elastically anisotropic materials, such as $Bi_xSb_{2-x}Te_3$, crystals align with the weakest crystallographic plane normal to the pressure axis. The layered structure of $Bi_xSb_{2-x}Te_3$ crystals, with a strong bonding between atoms inside the *ab* plane and weak bonding between the layers in the *c* direction, results in a rather strong anisotropy of the elastic constants.[24] In particular, the Young modulus of Bi_2Te_3 crystals in the *a* and *b* axes is close to 30% larger than that in the *c* axis.[25,26] Thus, during the liquid phase sintering under a uniaxial pressure, reprecipitated crystals would be oriented with the *c* direction parallel to the press axis, as we observed experimentally.

The presence of a uniaxial pressure during the liquid phase sintering may not only introduce a preferential orientation of the reprecipitated crystals, but it may also influence their geometry.[23,24] In the presence of a liquid phase able to partially dissolve and reprecipitate the crystals, the uniaxial pressure promotes growth in their normal directions and aids the dissolution of the crystals in the direction parallel to this axis.[23,24] In the particular case of $Bi_xSb_{2-x}Te_3$, already in solution, at moderate temperatures and in the absence of a uniaxial pressure, nanocrystals grow faster in the *ab* plane than in the *c*-axis, thus acquiring flat, disk-shaped, morphologies. During the hot press process, the relative growth in the *ab* plane is much more accentuated and plates with much higher aspect ratios are finally obtained.

The initial shape of the pressed nanocrystals could influence the direction and even existence of a predominant orientation of the crystal domains in the final material.[27] Actually, in a previous work, no significant crystallographic texture was observed in pellets obtained from the hot press of ball milled $Bi_xSb_{2-x}Te_3$ containing an excess of tellurium, even when using processing temperatures above the tellurium melting point.[28] To determine the role of the geometry of the precursor nanocrystals, we hot pressed Bi_2Te_3 nanorods with the same excess of tellurium, Te/Bi ∼ 1.7, and following the exact same steps as in the case of $Bi_xSb_{2-x}Te_3$ nanodisks (Figure S8).[29] The polycrystalline material produced had a significant crystallographic texture ($I_{(00\underline{15})}/I_{(110)}$ = 5.6, Figures S9 and S10) but lower than that obtained with the $Bi_xSb_{2-x}Te_3$ nanodisks ($I_{(00\underline{15})}/I_{(110)}$ = 7.3, Figure 2d). We also produced pellets by hot pressing a powder obtained from the ball milling of a commercial ingot and adding an excess of elemental tellurium to it. These pellets also showed some crystallographic alignment ($I_{(00\underline{15})}/I_{(110)}$ = 3.1, Figures S11 and S12) but also lower than the pellets produced from nanodisks (Figure 2d).

To produce consolidated nanomaterials with stoichiometric composition and having the finest crystallographic texture and optimum thermoelectric properties, it was essential to completely remove the excess amount of tellurium. Conveniently, during the hot press, while the temperature was above the tellurium melting point, the excess of this element was expelled through the plunger rod (Figure S13). However, in just one pressure and release step, the tellurium excess was not completely removed from the sample, probably due to the blocking of the escape paths within the layered structure or the plunger rod (Figures S14−S16). Only upon multiple pressure and release steps the excess of tellurium could be totally ejected. Specifically, we used five pressure and release steps during the 210 s that the temperature was set at 480 °C to completely get rid of the tellurium excess. A similar cycling uniaxial pressure was previously reported to improve crystal alignment in spark plasma sintered $Bi_xSb_{2-x}Te_3$, having no tellurium excess.[18] No inside of the involved mechanism was reported in this previous work.

Among the different compositions tested, $Bi_{0.5}Sb_{1.5}Te_3$ provided the highest thermoelectric figures of merit (Figures S17−S20). We associated this experimental fact to a more optimum charge carrier concentration in this sample. This result is consistent with previous reports and with the use of this composition in commercial devices. Figure 3 shows the electrical conductivity, σ; Seebeck coefficient, S; power factor, PF; thermal conductivity, κ_{total}; lattice and bipolar thermal conductivity, $\kappa_L + \kappa_{bi} = \kappa_{total} - \kappa_e$, and overall thermoelectric figure of merit, $ZT = S^2\sigma T/\kappa$, of the $Bi_{0.5}Sb_{1.5}Te_3$ nanomaterial hot pressed at 480 °C and measured in two directions, parallel and normal to the press axis (Figure S6). Displayed results were obtained from averaging experimental data from five different pellets (Figures S25 and S26). These results are compared in Figure 3 with those obtained from a pellet produced with the exact same material but hot pressed at a lower temperature, 300 °C, and a commercial ingot measured in the cleavage plane (*ab*) and its normal direction (*c*).

The nanomaterials hot pressed at 300 °C showed relatively low electrical conductivities (Figure 3a). Such low electrical conductivities were associated with a strong scattering of charge carriers at the ubiquitous grain interfaces of these materials. Additionally, these materials had lower relative densities than materials hot pressed at higher temperatures and contained an excess amount of tellurium which had not been expelled during the hot press step. On the other hand, nanomaterials hot pressed at 480 °C showed very high electrical conductivities, comparable to those of the commercial sample. As expected, the electrical conductivities measured in the disk plane were higher than those obtained in the press direction (σ_{ab}/σ_c = 1.6 at 320 K). Such high electrical conductivities have been previously measured in samples processed in an excess of tellurium and were related to two main factors:[27,30] (i) an increase (over materials with similar Bi/Sb ratios) of the hole concentration associated with a modification of the antisite and vacancy defects due to the tellurium excess;[29] (ii) formation during the liquid phase sintering of semicoherent grain boundaries having a minimal effect on hole scattering.[27]

Hall measurements of a series of five hot pressed $Bi_{0.5}Sb_{1.5}Te_3$ nanomaterials measured three times showed the average charge carrier concentrations to be $p = (5 \pm 3) \times 10^{19}$ cm^{-3}, i.e., sensibly higher than that of the commercial material, $p = (1.0 \pm 0.5) \times 10^{19}$ cm^{-3}. The mobilities measured in the plane normal to the press axis were on average a factor of 1.6 higher than those measured in the press axis direction.

The Seebeck coefficients of the bottom-up assembled nanomaterials were significantly lower than those of the commercial sample, especially for the nanomaterial hot pressed at 480 °C (Figure 3b). These lower Seebeck coefficients were associated with the higher charge carrier concentrations present in the bottom-up nanomaterials. The higher charge carrier concentrations also explained that the Seebeck coefficients started to decrease at a higher temperature in the nanomaterial hot pressed at 480 °C when compared with the commercial sample. On top of this retard of the bipolar effect associated with the higher charge carrier concentration, the excess of tellurium during the consolidation step could also reduce the density of tellurium vacancies, an n-type defect, thus additionally decreasing the extent of the bipolar effect and shifting the ZT maximum to an even higher temperature. Seebeck coefficients measured in each of the two directions were very similar (S_c/S_{ab} = 1.07 at 320 K), as expected from the reduced anisotropy of this parameter already reported for single crystals (S_c/S_{ab} = 1.02).[11] Nevertheless, the coefficients measured in the press axis direction were slightly higher, which could point at some extent of selective scattering of the minority carriers at the crystal interfaces in the *c* direction.

As expected, the thermal conductivities of the nanomaterials were significantly lower than those of the commercial sample, due to effective scattering at grain boundaries and crystal defects such as stacking faults (Figure 3d). For the nanomaterial hot pressed at 480 °C, the thermal conductivity was particularly low in the direction of the press axis (κ_{ab}/κ_c = 1.64 at 320 K), where a higher density of interfaces and stacking faults existed. In this direction, the thermal conductivity of this nanomaterial became comparable to that measured on the pellet hot pressed at 300 °C containing a random distribution of very small crystals. When taking into account the correction for the 10% porosity measured, i.e., a factor 1.33, the lowest lattice thermal conductivities that we measured at room temperature (0.43 W m^{-1} K^{-1}) were slightly above the amorphous limit for Bi_2Te_3 (0.31 W m^{-1} K^{-1}),[31] and clearly above those estimated for highly defective Bi_2Te_3 (ca. 0.17 W m^{-1} K^{-1}),[32] or for very small Bi_2Te_3 nanograins (0.12 W m^{-1} K^{-1})[33] and those measured for stacked Bi_2Te_3 2D films at room temperature (0.1 W m^{-1} K^{-1}).[33]

Thermal conductivities decreased with increasing temperature in the low temperature range and stabilized or increased in the high temperature range, when the bipolar contribution became significant (Figures 3e and S21). Consistent with previous observations,[34] the bipolar contribution to the thermal conductivity was lower in the nanomaterial than in the commercial sample, which was attributed to a combination of the higher majority carrier concentration, the suppression of a source of minority carriers, such as tellurium vacancies, and the scattering of minority carriers at crystal interfaces or planar defects such as stacking faults.

Overall, the thermoelectric figures of merit of the nanomaterial hot pressed at 480 °C were significantly higher than those of the commercial sample (Figure 3f). In particular, in the direction of the press axis, i.e., *c*, the combination of a high electrical conductivity, a notable Seebeck coefficient, and a very low thermal conductivity resulted in thermoelectric figures of

DOI: 10.1021/acs.nanolett.8b00263
Nano Lett. 2018, 18, 2557−2563

merit up to ZT = 1.96 at 420 K for the record material and ZT = 1.83 when averaged for five pellets. Dispersion of results was provided from a dispersion of the charge carrier concentration in the samples. These values are the highest thermoelectric figures of merit reported in the ambient temperature range (Figure S22). Importantly, these high thermoelectric figures of merit were sustained in an extended temperature range. The average thermoelectric figure of merit, calculated over 180 K, from 320 to 500 K, was ZT_{ave} = 1.77 for the record material and ZT_{ave} = 1.65 when averaging for five pellets. These values translated in potential energy conversion efficiencies up to 60% higher than those of commercial materials (Supporting Information).[35,36]

Notice that the figures of merit measured from the nanomaterial in the *ab* plane were systematically lower than those in the *c* direction (Figure 3f). This was somehow unexpected, since higher ZT values have been generally measured or assumed in the *ab* plane for single crystals and partially oriented polycrystalline materials.[11,15] The general assumption that the figures of merit in the *ab* plane must be higher than those in the *c* direction explains that in several previous works only the thermoelectric properties in the *ab* plane were measured, when possibly higher figures of merit would have been obtained in the normal direction.[34,37]

Finally, we want to highlight that the nanocrystalline $Bi_xSb_{2-x}Te_3$ materials presented here showed good stability even when heated up to relatively high temperature (500 K) and during prolonged periods of time, as can be seen in Figures S23 and S24.

Conclusions. We demonstrated the production of crystallographically textured $Bi_xSb_{2-x}Te_3$ bulk nanomaterials with record thermoelectric figures of merit: ZT = 1.96 for the record sample and ZT = 1.83 when averaged over five materials at 420 K. These high ZT values also extended over a larger temperature range, resulting in ZT values averaged over 180 K as high as ZT_{ave} = 1.77 for the record material and ZT_{ave} = 1.65 as the mean value from five samples. These unprecedented figures of merit were obtained in the *c* direction, in contrast with most previous works measuring or assuming better thermoelectric performances in the *ab* plane. Our procedure was based on several key parameters: (i) the use of p-type $Bi_xSb_{2-x}Te_3$ disk-shaped nanocrystals having controlled composition; (b) the uniaxial hot press of the nanocrystals containing an excess of tellurium homogeneously distributed across the material; and (c) the use of a proper hot press temperature and processing steps to ensure a proper liquid-assisted sintering and the complete removal of the tellurium excess.

■ ASSOCIATED CONTENT

Ⓢ Supporting Information

The Supporting Information is available free of charge on the ACS Publications website at DOI: 10.1021/acs.nanolett.8b00263.

> Details of the chemicals used, NC synthesis, pellet fabrication, additional materials characterization (X-ray diffraction patterns, HRTEM, SEM, electrical and thermal characterization), stability measurement, repeatability, comparison with litterature values (PDF)

■ AUTHOR INFORMATION

Corresponding Authors

*E-mail: dycadavidr@unal.edu.co.
*E-mail: acabot@irec.cat.

ORCID

Yu Liu: 0000-0001-7313-6740
Maria Ibáñez: 0000-0001-5013-2843
Jordi Arbiol: 0000-0002-0695-1726
Maksym V. Kovalenko: 0000-0002-6396-8938
Andreu Cabot: 0000-0002-7533-3251

Author Contributions

The manuscript was prepared through the contribution of all authors. D.C. and A.C. guided the project and supervised the work. Y.L., D.C., M.I., M.V.K., and A.C. conceived and prepared the manuscript. Y.L., S.O., and D.C. designed the experiments, produced the nanomaterials, and performed the thermoelectric characterization. Y.Z. and K.H.L. produced the bulk samples. M.I., K.H.L., and K.M.N. performed Hall measurement and analyzed the results in this manuscript. A.G.-C., S.M.-S., and J.A. performed HRTEM and STEM-EELS and discussed these results. The manuscript was corrected and improved by all authors.

Notes

The authors declare no competing financial interest.

■ ACKNOWLEDGMENTS

This work was supported by the European Regional Development Funds. Y.L. and Y.Z. thank the China Scholarship Council for scholarship support. M.V.K. acknowledges partial financial support by the European Union (EU) via FP7 ERC Starting Grant 2012 (Project NANOSOLID, GA No. 306733). S.M.-S. acknowledges funding from “Programa Internacional de Becas ‘la Caixa’-Severo Ochoa”. IREC and ICN2 acknowledge funding from Generalitat de Catalunya 2014 SGR 1638. ICN2 acknowledges support from the Severo Ochoa Programme (MINECO, Grant No. SEV-2013-0295) and is funded by the CERCA Programme/Generalitat de Catalunya. Part of the present work has been performed in the framework of Universitat Autònoma de Barcelona Materials Science PhD program.

■ REFERENCES

(1) Ortega, S.; Ibáñez, M.; Liu, Y.; Zhang, Y.; Kovalenko, M. V.; Cadavid, D.; Cabot, A. *Chem. Soc. Rev.* **2017**, *46*, 3510−3528.
(2) Zhu, T.; Hu, L.; Zhao, X.; He, J. *Adv. Sci.* **2016**, *3*, 1600004.
(3) Ibáñez, M.; Luo, Z.; Genç, A.; Piveteau, L.; Ortega, S.; Cadavid, D.; Dobrozhan, O.; Liu, Y.; Nachtegaal, M.; Zebarjadi, M.; Arbiol, J.; Kovalenko, M. V.; Cabot, A. *Nat. Commun.* **2016**, *7*, 10766.
(4) Liu, Y.; Cadavid, D.; Ibáñez, M.; Ortega, S.; Martí-Sánchez, S.; Dobrozhan, O.; Kovalenko, M. V.; Arbiol, J.; Cabot, A. *APL Mater.* **2016**, *4*, 104813.
(5) Zebarjadi, M.; Joshi, G.; Zhu, G.; Yu, B.; Minnich, A.; Lan, Y.; Wang, X.; Dresselhaus, M.; Ren, Z.; Chen, G. *Nano Lett.* **2011**, *11*, 2225−2230.
(6) Ko, D.-K.; Kang, Y.; Murray, C. B. *Nano Lett.* **2011**, *11*, 2841−2844.
(7) Zhang, Q.; Ai, X.; Wang, L.; Chang, Y.; Luo, W.; Jiang, W.; Chen, L. *Adv. Funct. Mater.* **2015**, *25*, 966−976.
(8) Ibáñez, M.; Zamani, R.; Gorsse, S.; Fan, J.; Ortega, S.; Cadavid, D.; Morante, J. R.; Arbiol, J.; Cabot, A. *ACS Nano* **2013**, *7*, 2573−2586.

(9) Ibáñez, M.; Korkosz, R. J.; Luo, Z.; Riba, P.; Cadavid, D.; Ortega, S.; Cabot, A.; Kanatzidis, M. G. *J. Am. Chem. Soc.* **2015**, *137*, 4046−4049.
(10) Liu, Y.; García, G.; Ortega, S.; Cadavid, D.; Palacios, P.; Lu, J.; Ibáñez, M.; Xi, L.; De Roo, J.; López, A.; Martí-Sánchez, S.; Cabezas, I.; Mata, M.; Luo, Z.; Dun, C.; Dobrozhan, O.; Carroll, D.; Zhang, W.; Martins, J.; Kovalenko, M.; Arbiol, J.; Noriega, G.; Song, J.; Wahnon, P.; Cabot, A. *J. Mater. Chem. A* **2017**, *5*, 2592−2602.
(11) Caillat, T.; Carle, M.; Pierrat, P.; Scherrer, H.; Scherrer, S. *J. Phys. Chem. Solids* **1992**, *53*, 1121−1129.
(12) Carle, M.; Pierrat, P.; Lahalle-Gravier, C.; Scherrer, S.; Scherrer, H. *J. Phys. Chem. Solids* **1995**, *56*, 201−209.
(13) Kim, S.; Yamamoto, S.; Aizawa, T. *J. Alloys Compd.* **2004**, *375*, 107−113.
(14) Fan, X.; Yang, J.; Zhu, W.; Bao, S.; Duan, X.; Xiao, C.; Li, K. *J. Alloys Compd.* **2008**, *461*, 9−13.
(15) Santamaría, J. A.; Alkorta, J.; Sevillano, J. G. *J. Mater. Res.* **2015**, *30*, 2593−2604.
(16) Yan, X.; Poudel, B.; Ma, Y.; Liu, W.; Joshi, G.; Wang, H.; Lan, Y.; Wang, D.; Chen, G.; Ren, Z. *Nano Lett.* **2010**, *10*, 3373−3378.
(17) Han, L.; Spangsdorf, S. H.; Nong, N.; Hung, L.; Zhang, Y.; Pham, H. N.; Chen, Y.; Roch, A.; Stepien, L.; Pryds, N. *RSC Adv.* **2016**, *6*, 59565−59573.
(18) Kitagawa, H.; Takimura, K.; Ido, S.; Morito, S.; Kikuchi, K. *J. Alloys Compd.* **2017**, *692*, 388−394.
(19) German, R. M. *Liquid phase sintering*; Springer Science & Business Media: Boston, Mass, 2013.
(20) Ghosh, G. *J. Phase Equilib.* **1994**, *15*, 349−360.
(21) Okamoto, H.; Tanner, L. E. Bi-Te (Bismuth-Tellurium) Phase Diagram, ASM, 1986.
(22) German, R. M.; Pavan, S.; Seong, J. *J. Mater. Sci.* **2009**, *44*, 1−39.
(23) Kamb, W. B. *J. Geol.* **1959**, *67*, 153−170.
(24) Abdullaev, N. *Phys. Solid State* **2006**, *48*, 663−669.
(25) Feng, S.; Li, S.; Fu, H. *Comput. Mater. Sci.* **2014**, *82*, 45−49.
(26) Jenkins, J.; Rayne, J.; Ure, R., Jr *Phys. Rev. B* **1972**, *5*, 3171.
(27) Paterson, M. *Rev. Geophys.* **1973**, *11*, 355−389.
(28) Kim, S. I.; Lee, K. H.; Mun, H. A.; Kim, H. S.; Hwang, S. W.; Roh, J. W.; Yang, D. J.; Shin, W. H.; Li, X. S.; Lee, Y. H. *Science* **2015**, *348*, 109−114.
(29) Zhang, G.; Kirk, B.; Jauregui, L. A.; Yang, H.; Xu, X.; Chen, Y. P.; Wu, Y. *Nano Lett.* **2012**, *12*, 56−60.
(30) Kim, Y. M.; Lydia, R.; Kim, J.-H.; Lin, C.-C.; Ahn, K.; Rhyee, J.-S. *Acta Mater.* **2017**, *135*, 297−303.
(31) Chiritescu, C.; Mortensen, C.; Cahill, D. G.; Johnson, D.; Zschack, P. *J. Appl. Phys.* **2009**, *106* (7), 073503.
(32) Termentzidis, K.; Pokropyvnyy, O.; Woda, M.; Xiong, S.; Chumakov, Y.; Cortona, P.; Volz, S. *J. Appl. Phys.* **2013**, *113* (1), 013506.
(33) Teweldebrhan, D.; Goyal, V.; Balandin, A. A. *Nano Lett.* **2010**, *10* (4), 1209−1218.
(34) Zhang, C.; de la Mata, M.; Li, Z.; Belarre, F. J.; Arbiol, J.; Khor, K. A.; Poletti, D.; Zhu, B.; Yan, Q.; Xiong, Q. *Nano Energy* **2016**, *30*, 630−638.
(35) Kim, H. S.; Liu, W.; Chen, G.; Chu, C.-W.; Ren, Z. *Proc. Natl. Acad. Sci. U. S. A.* **2015**, *112*, 8205−8210.
(36) Kim, H. S.; Liu, W.; Ren, Z. *Energy Environ. Sci.* **2017**, *10*, 69−85.
(37) Park, K.; Ahn, K.; Cha, J.; Lee, S.; Chae, S. I.; Cho, S.-P.; Ryee, S.; Im, J.; Lee, J.; Park, S. D. *J. Am. Chem. Soc.* **2016**, *138*, 14458−14468.

■ NOTE ADDED AFTER ASAP PUBLICATION

This paper was published ASAP on March 20, 2018 with errors in the text. The corrected version was reposted on March 22, 2018.